Microscopic Investigation of Self-Organizing Water-Monoalcohol Mixtures for the Design of Green Solvents

Firoz Malayil Kalathil

THÈSE

Pour obtenir le grade de

DOCTEUR DE L'UNIVERSITÉ GRENOBLE ALPES

École doctorale : PHYS - Physique
Spécialité : Physique de la Matière Condensée et du Rayonnement
Unité de recherche : Institut LAUE LANGEVIN

Etudes microscopique de mélanges auto-organisés d'eau et de monoalcools pour la conception de solvants verts

Microscopic Investigation of Self-Organizing Water-Monoalcohol Mixtures for the Design of Green Solvents

Présentée par :

Firoz MALAYIL KALATHIL

Direction de thèse :

Marie PLAZANET DIRECTRICE DE RECHERCHE, CNRS DELEGATION ALPES	Directrice de thèse
Ingo HOFFMANN SCIENTIST, INSTITUT LAUE-LANGEVIN	Co-encadrant de thèse

Rapporteurs :

FABIENNE TESTARD
DIRECTRICE DE RECHERCHE, CEA CENTRE DE PARIS-SACLAY
JEAN-FRANÇOIS DUFRÊCHE
PROFESSEUR DES UNIVERSITES, UNIVERSITE DE MONTPELLIER

Thèse soutenue publiquement le **7 mai 2025**, devant le jury composé de :

JEAN-LOUIS BARRAT, PROFESSEUR DES UNIVERSITES, UNIVERSITE GRENOBLE ALPES	Président
FABIENNE TESTARD, DIRECTRICE DE RECHERCHE, CEA CENTRE DE PARIS-SACLAY	Rapporteure
JEAN-FRANÇOIS DUFRÊCHE, PROFESSEUR DES UNIVERSITES, UNIVERSITE DE MONTPELLIER	Rapporteur
MICHIHIRO NAGAO, SCIENTIST, NIST CENTER FOR NEUTRON RESEARCH	Examinateur
TILO SEYDEL, SENIOR SCIENTIST, INSTITUT LAUE-LANGEVIN	Examinateur

Microscopic Investigation of Self-Organizing Water-Monoalcohol Mixtures for the Design of Green Solvents

A thesis submitted for the degree of

PhD

in Soft Matter Physics by:

MALAYIL KALATHIL Firoz

Supervisors:

Marie PLAZANET

Ingo HOFFMANN

Université Grenoble Alpes

Institut Laue-Langevin

Grenoble, France

This doctoral research was funded by the IDEX-UGA and ILL PhD program

Acknowledgements

First and foremost, I thank God for everything I hold dear and for guiding me through this journey—because, let's be honest, divine intervention was probably needed more than once.

To my parents, brother, and sister, your unwavering support, patience, and understanding of my (many) concerns have been my foundation. Without you, I wouldn't be here—literally and figuratively.

A huge thanks to my supervisors, Marie P. *and* Ingo H.*, whose constant availability, knowledge-sharing, and guidance have been invaluable. Ingo, your wit and cheer made even the toughest tasks bearable, while Marie's generosity and ever-helpful nature made everything seem manageable. From beam times to sleepless nights, your support went beyond science, and I truly appreciate all the effort you put in to help me.*

Special thanks to Christiane A.*,* Thomas Z.*, and* Sylvain P. *for their invaluable support over the years, their scientific insights and discussions, and their constant guidance and encouragement throughout this work.* Bela F. *and* Frederic P.*, I truly appreciate your patience in enduring our CSI-style meetings, navigating endless reports, and hearing my research story on repeat each year—your resilience deserves its own study. Thanks also to* Peter F. *and* Dominik H. *for their contributions through experimental and simulation work. Research is always a team effort, and I'm grateful to be a small part of this incredible team.*

To my incredible friends — thank you for making these three years unforgettable and bearable. Diagu*,* Furhu*, and* Paingu*—my real-life ternary phase system—your unwavering presence has meant the world to me. From travel and cooking adventures to lunch breaks, coffee breaks (and yet another coffee break) at ILL, intense board games, and scenic hikes, every moment with you all has been a joy.* Riccardo*, for your expert travel recommendations and never-ending twisted questionnaires.* Hridya *and* Maneesha Chechi*, for our deep intellectual exchanges and heartfelt conversations. And of course, a special mention to* Christ *and* Mahip*, my ever-reliable 'phone-a-friend' lifelines, always ready with advice and the latest happenings.*

Finally, a big thank you to the staff at ILL, LIPHY, and ESRF. Your support made this phase of the journey not only smoother but also much more rewarding. To everyone who played a role in this, knowingly or unknowingly—thank you!

Microscopic Investigation of Self-Organizing Water-Monoalcohol Mixtures for the Design of Green Solvents

Abstract

Surfactant-free microemulsions (SFME) are an emerging class of self-organized ternary systems that exhibit mesoscale structuration despite the absence of conventional surfactants. Understanding their phase behavior and dynamics is essential for applications in drug delivery, extraction, and chemical engineering. In this work, we aim to clarify key aspects such as origins of macroscopic properties and boundaries of the so-called pre-Ouzo region, the impact of temperature on phase structuring, and the universality of Lifshitz line predictions.

We investigate the ternary systems octanol, ethanol & water and 2-ethyl hexanol, ethanol &water using small-angle X-ray scattering (SAXS) to resolve their structural organization upon dilution and temperature variation. Additionally, pulsed-field gradient NMR (PFG-NMR), neutron spin echo (NSE), and viscosity measurements are employed to analyze the dynamical changes associated with structural evolution. Our goal is to characterize structural and dynamic transitions in these systems, with a particular focus on pre-Ouzo mesostructuration.

We identify distinct regions of the ternary diagram, delineating the pre-Ouzo regions on one side, and chain like structures driven by the long hydrophobic tail of the 1-octanol on the other side. SAXS data reveal the frontier of the pre-Ouzo organization delimited by a curved Lifshitz line. The binodal line varies with temperature, but pre-Ouzo aggregates are shown to persist in response to variable thermodynamic conditions. A detailed analysis of the diffusion coefficients provides insight into the underlying dynamics, revealing a transition in the measured correlation times. The lifetime of the diffusing entities shifts across the Lifshitz line, from 20 ns when pre-Ouzo structures dominate to less than 70 ps in the presence of a water-in-oil dynamically connected network. This transition highlights the influence of mesoscale structuration on molecular mobility. Eventually, viscosity measurements confirm macroscopic effects related to pre-Ouzo aggregates, far from ideal solution behaviour. These findings advance the understanding of SFME ternary systems and will help refining theoretical descriptions in order to expand their potential applications.

Etudes microscopique de mélanges auto-organisés d'eau et de monoalcools pour la conception de solvants verts

Résumé

Les microémulsions sans surfactants (SFME) sont une classe émergente de systèmes ternaires auto-organisés qui présentent une structuration à l'échelle mésoscopique malgré l'absence de tensioactifs conventionnels. La compréhension de leurs diagrammes de phase et des dynamiques est essentielle pour les applications dans les domaines de la délivrance de médicaments, de l'extraction ou encore de l'ingénierie chimique. Dans ce travail, nous visons à clarifier des aspects essentiels tels que les origines des propriétés macroscopiques et les limites de la région dite pré-Ouzo, l'impact de la température sur la nano ou méso-structuration et l'universalité des prédictions théoriques telles que la ligne de Lifshitz.

Nous étudions les systèmes ternaires octanol, éthanol & eau et 2-éthyl hexanol, éthanol & eau en utilisant la diffusion des rayons X aux petits angles (SAXS) pour caractériser leur organisation structurale lors de la dilution et de la variation de la température. De plus, la RMN à gradient de champ pulsé (RMN-PFG), l'écho de spin de neutrons (NSE) et les mesures de viscosité sont utilisés pour analyser les changements dynamiques associés à l'évolution structurale. Notre objectif est de caractériser les transitions structurales et dynamiques dans ces systèmes, en mettant l'accent sur la mésostructuration de la zone pré-Ouzo.

Nous identifions des régions distinctes du diagramme ternaire, délimitant les régions pré-Ouzo d'un côté, et des structures en chaîne formées par la longue queue hydrophobe du 1-octanol, de l'autre côté. Les données SAXS révèlent la frontière de l'organisation pré-Ouzo délimitée par une ligne de Lifshitz courbée. La binodale varie avec la température, et nous montrons que les agrégats pré-Ouzo persistent en réponse à des conditions thermodynamiques variables. Une analyse détaillée des coefficients de diffusion fournit un aperçu des dynamiques sous-jacentes, révélant une transition dans les temps de corrélation mesurés. La durée de vie des entités diffusantes évolue à travers la ligne de Lifshitz, passant de 20 ns lorsque les structures pré-Ouzo dominent à moins de 70 ps en présence d'un réseau dynamique d'eau dans l'huile. Cette transition met en évidence l'influence de la structuration à l'échelle mésoscopique sur la mobilité moléculaire. Enfin, les mesures de viscosité confirment les effets macroscopiques liés aux agrégats pré-Ouzo, loin du comportement idéal de la solution. Ces résultats font progresser la compréhension des systèmes ternaires auto-organisés et permettront d'affiner les descriptions théoriques afin d'élargir leurs applications potentielles.

Contents

List of Figures

List of Tables

General Introduction

Nanoscale self-organization in surfactant-based systems has captivated scientific research for decades, with foundational contributions laying the groundwork for our understanding of these complex structures. Early milestones include the discovery of lyotropic liquid crystals in the late 19th century and the pioneering work of JW McBain and HE Martin in the 1930s, where they introduced the concept of micelles [1]. Micelles, aggregates of surfactant molecules that form above a critical micelle concentration (CMC), represent a strategy to minimize the unfavorable interactions between hydrophobic tails and water. These closed structures, consisting of a hydrophobic core and a hydrated shell, provided a crucial framework for the development of surfactant-based systems and have been central to advancing the field of colloidal science [2].

The study of emulsions (size range from a few μm to tens of μm), which involves the dispersion of one immiscible liquid phase within another, shares some similarities with the study of micelles. While micelles are self-organized aggregates of surfactant molecules, emulsions consist of two liquid phases—such as oil and water—that are stabilized by emulsifiers or surfactants. In an emulsion, the dispersed liquid phase forms droplets within the continuous liquid phase. Emulsions are categorized based on the relationship between these phases: oil-in-water (o/w) emulsions, like milk, mayonnaise, and vinaigrette, and typically thicker water-in-oil (w/o) emulsions, such as butter, sunscreen, and other skincare products.

Emulsions are inherently unstable due to the thermodynamic incompatibility between the two liquid phases. This instability drives the droplets to merge and eventually separate into different phases. To prevent phase separation, surfactants or emulsifiers—amphiphilic molecules that form protective barriers around the dispersed droplets—are employed [3, 4].

Microemulsions, isotropic mixtures of oil, water, and surfactants, differ from emulsions due to their self-assembled equilibrium state, resistance to phase separation, small droplet sizes (< 20 nm), and thermodynamic stability. These unique properties have led to various applications, including pharmaceuticals for targeted drug delivery, solubilizing poorly soluble drugs, and enhancing pharmacokinetic properties through self-emulsifying drug delivery systems (SEDDS) [5–10]. They

also serve as colloidal drug carriers, improving skin drug delivery [11]. In the food industry, microemulsions aid in solubilizing nutrients in non-polar solvents [12], and in industrial applications, they enhance oil solubilization for cleaning, wastewater treatment, and soil remediation [13–15].

Building on these discoveries, the concept of surfactant-free microemulsions (SFME) emerged, offering a fresh perspective that challenged traditional views on micelles and emulsions. SFME is a homogeneous system composed of oil and water, two immiscible liquids, along with an 'amphi-solvent' or 'hydrotrope' that is soluble in both. The potential for understanding SFME emerged from systems like *Pastis* (France), *Sambuca* (Italy), and *Ouzo* (Greece), alcoholic beverages made by soaking plants in an ethanol solution containing water-insoluble components. Scattering studies utilizing light, X-rays, and neutrons [16, 17] provided experimental evidence confirming the existence of structures similar to classical microemulsions in hydrotrope-based systems, while also demonstrating their thermodynamic stability.

A key question arises: why switch to a surfactant-free model when established surfactant-based systems are already performing well in fields like extraction, recovery, and pharmaceutics? The answer lies in the drawbacks of surfactants: they are foaming by nature, have a strong affinity for adsorption at interfaces, and pose challenges in recovery. Moreover, many surfactants are poorly biodegradable, and some can even form liquid crystalline phases, which can hinder the process. In contrast, hydrotropes, which generally do not exhibit these issues, present a viable alternative. Hydrotrope-based systems, such as those utilizing short-chain aliphatic alcohols, can achieve phase separation relatively easily, for instance, by adding water or adjusting the temperature. Thus, a significant advantage of surfactant-free microemulsions (SFMEs) over conventional surfactant-based microemulsions (SBMEs) is their simpler purification and separation processes. Furthermore, SFMEs are increasingly being used in green solubilization and extraction techniques as an alternative to pure organic solvents [18–20].

The transition from emulsions and micelles to spontaneously forming microemulsions marks a significant advance in understanding nanoscale self-assembly. These developments have enhanced theoretical knowledge and opened new possibilities in fields like drug delivery and food science, where precise control over nanoscale structures is essential. This manuscript presents findings on two SFME ternary systems, focusing on their molecular-scale structure and dynamics. It offers a quantitative analysis of these microscopic properties and establishes a connection between composition, organization, and dynamics across different regions of the phase diagram.

Chapter 1

Introduction to Ternary Systems and SFME

1.1 Solutions and Phase Separation

The ability of liquids to dissolve solids, other liquids, or gases is a fundamental natural phenomenon that plays a crucial role in both everyday life and industrial processes. From the simple demixing of oil and water to sophisticated liquid extraction techniques in chemical engineering, phase separation and multiphase coexistence are widely observed and harnessed for practical applications.

At the heart of these processes is the concept of solutions—homogeneous mixtures where the composition remains uniform on a molecular scale. This contrasts with suspensions, where discrete particles remain dispersed in a continuous fluid. The extent to which a substance dissolves, known as solubility, depends on its chemical nature and is often influenced by temperature and, in some cases, pressure. Understanding these factors is key to optimizing dissolution and separation techniques.

One of the most important applications of solubility control is in separation processes, particularly extraction, where a dissolved substance is selectively transferred between liquids. A common example is the removal of phenolic pollutants from industrial aqueous waste streams, which pose environmental risks. By treating the waste with a water-insoluble solvent, such as a high-boiling hydrocarbon, phenolic compounds can be effectively extracted [21]. The efficiency of this process is determined by the distribution coefficient—the ratio of the pollutant's solubility in the solvent to that in water—with higher values indicating more effective removal.

Building on the principles of selective solute transfer, liquid-liquid extraction (LLE) is a key technique used to separate solutes between immiscible liquids,

facilitating applications across multiple industries. In addition to waste-water treatment, where LLE effectively removes heavy metals and pollutants, it is employed in pharmaceutical purification, environmental waste remediation, and food safety. Advanced LLE methods, including solvent extraction and miniaturized techniques like dispersive liquid-liquid microextraction (DLLME), offer enhanced efficiency while supporting green chemistry principles. For example, DLLME minimizes the use of organic solvents by dispersing them into fine droplets, enabling the effective extraction of pharmaceuticals and environmental pollutants [22–30].

The growing emphasis on sustainability has spurred innovations in eco-friendly extraction methods. LLE focuses on reducing solvent consumption and toxicity while maintaining high efficiency, aligning with green chemistry goals. In food safety, it ensures the detection of contaminants like antibiotics in dairy and seafood, while in environmental monitoring, it tracks pollutants in water, soil, and air. Additionally, LLE supports resource recovery, such as extracting valuable compounds like oleuropein from olive oil processing wastewater. By integrating green chemistry principles and automation, LLE continues to evolve as a vital tool across healthcare, environmental, and industrial domains, advancing innovation with minimal environmental impact [31–33].

1.2 Ternary Phase Diagram

A ternary phase diagram, or phase triangle, is a useful tool for analyzing the phase behavior of three-component mixtures. It provides a visual representation of phase boundaries, distinguishing between single-phase (homogeneous) and multi-phase (heterogeneous) regions. The diagram also indicates several key points, helping to identify key transitions such as phase separation or self-organization. When additional factors like temperature are considered, the diagram extends into a 3D phase prism, typically visualized as 2D slices for clarity.

Figure 1.1 illustrates a ternary plot comprising a solubilizing agent (e.g., solute, surfactant, or hydrotrope), oil, and water. It highlights several characteristic cuts: the *fish cut* (red), which maintains a constant water-to-oil ratio while varying the surfactant concentration; the *Lund cut* (orange), where the surfactant-to-oil ratio remains constant, and water content varies; the *Shinoda cut* (green), with a fixed surfactant concentration and a varying water-to-oil ratio; and the *formulator's cut* (blue), where the water concentration is held constant while the oil-to-surfactant ratio changes [34].

In a ternary plot, each vertex corresponds to 100% of a specific component, while the side opposite to it represents 0% of that component. The composition percentages are indicated along the sides, starting from 100% at the vertex and

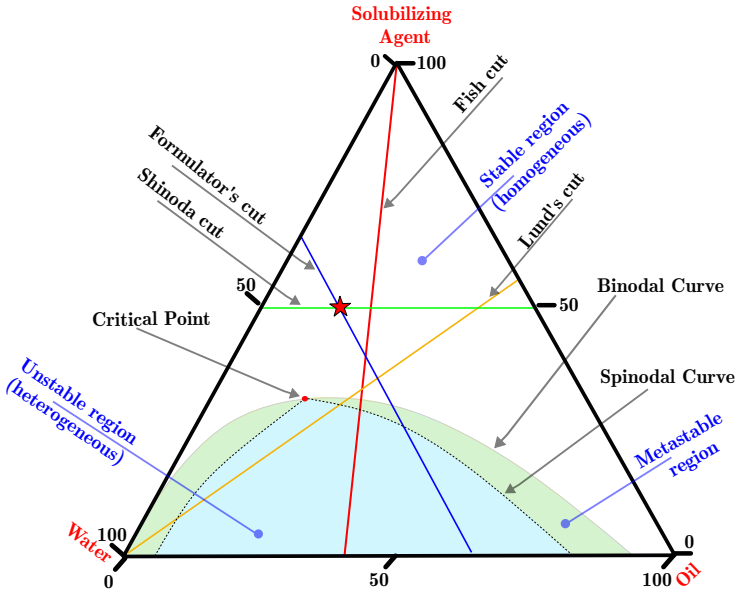

Figure 1.1: *Introduction to a basic ternary plot representing a three-component system (oil, water, and a solubilizing agent). The binodal line (also known as the coexistence line) and the spinodal line (stability line) serve as boundaries separating different phases. Various standard lines or cuts are displayed, including the critical point (red circle).* *(Adapted from [34])*

decreasing to 0% along the edge. Each side of the triangle represents a binary mixture of two components, where moving towards a vertex increases the proportion of one component while decreasing the other. To determine the composition at a specific point, such as the red star in Figure 1.1, draw lines parallel to the opposite sides of the vertices passing through the point. These lines indicate the proportion of each component: 50% solubilizing agent, 40% water, and 10% oil.

Further, in a phase triangle, the binodal line, also known as the coexistence curve, represents the thermodynamic solubility limit, marking the boundary between the region where the system exists as a single homogeneous phase and the region where it separates into two or more distinct phases. In many systems, this transition can be observed visually when phase separation occurs, manifesting as turbidity or distinct phase boundaries. The binodal curve defines the equilibrium compositions of coexisting phases, determined using the common tangent construction of the Gibbs free energy. In a ternary system, it encloses the miscibility gap, the area where two phases coexist. The shape and position of the binodal curve depend on the interactions among the components, as well as temperature and pressure conditions.

Inside the binodal curve lies the spinodal curve, which defines the absolute stability limit against phase separation. This curve corresponds to compositions where the second derivative of the Gibbs free energy with respect to composition

is zero, marking an inflection point in the free energy-composition curve. Within the spinodal region, the system is inherently unstable, and even infinitesimally small fluctuations in composition or density can lead to phase separation through spinodal decomposition. In contrast, the region between the binodal and spinodal curves is metastable, meaning that the system can remain in a single-phase state unless disturbed by larger fluctuations [35].

The binodal and spinodal curves converge at a critical point, where the differences between mixing entropy and mixing enthalpy vanish, resulting in a single critical composition and temperature. This critical point is of great significance in many systems, marking the transition zone where microemulsions and emulsion structures form. The emulsion region lies below the binodal curve near the critical point, where cloudy oil droplets in an aqueous medium begin to develop. In contrast, the microemulsion region represents an earlier stage, with smaller, transparent microemulsions forming upon dilution, as will be explained in the following sections.

Beyond this, other ternary systems may exhibit different structural arrangements, leading to variations in the phase diagram. The previously discussed case, where a single homogeneous phase, one critical point (CP), and a single biphasic region are present, is categorized as a Type 1 ternary system. In contrast, a Type 2 ternary system, such as the ethyl acetate–butanol–water system, contains two distinct homogeneous phases separated by a biphasic region. Meanwhile, a Type 0 system, like the water–dimethylsulfoxide–tetrahydrofuran system, features a biphasic region enclosed within a homogeneous phase [36].

1.3 Introduction to Emulsions

An emulsion is a mixture of two or more immiscible liquids, where one liquid (the dispersed phase) forms droplets within the other (the continuous phase). While emulsions can form without emulsifiers, the presence of emulsifiers stabilizes the droplets, preventing them from merging. Droplet sizes typically range from 1 to $20\mu m$, and emulsions are generally turbid and thermodynamically unstable. This instability arises due to the incompatibility between the oil and water phases, which naturally tend to separate. To stabilize emulsions, energy input and emulsifying agents are required to reduce the interfacial tension and prevent coalescence of the droplets [3, 4, 37, 38].

Emulsions can be classified based on the arrangement of their phases into oil-in-water (O/W), water-in-oil (W/O), or more complex systems such as multiple emulsions and nanoemulsions. Most food systems, such as milk, soup, and salad dressing, are oil-in-water emulsions, while water-in-oil emulsions are found in prod-

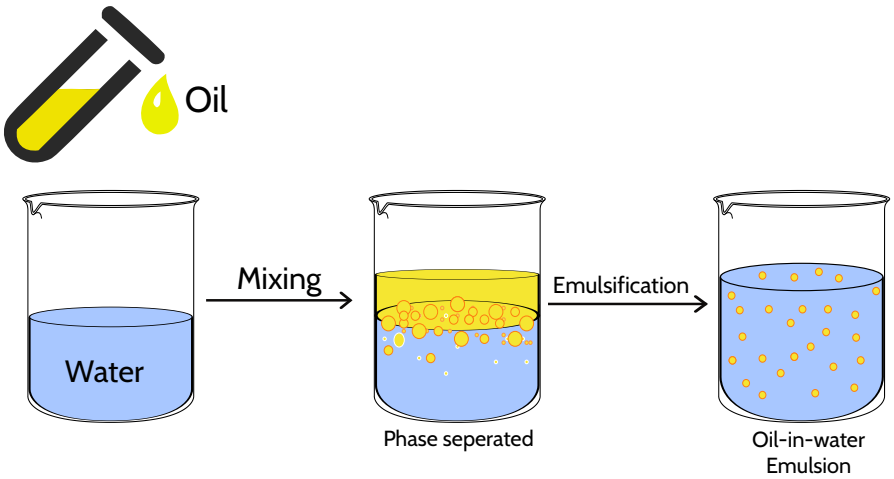

Figure 1.2: *The emulsification process: Initially, oil and water are mixed, leading to phase separation. Through agitation and the addition of an appropriate emulsifier and/or surfactants, the mixture forms a stable oil-in-water emulsion.*

ucts like margarine and butter [39, 40]. Multiple emulsions, such as oil-in-water-in-oil (O/W/O) and water-in-oil-in-water (W/O/W), contain larger droplets that encapsulate another phase and offer potential for controlled ingredient release and protection of sensitive compounds like probiotics [41].

The stability of an emulsion is largely governed by the choice of emulsifiers or surfactants. Surfactants are substances that lower the surface tension between two liquids or between a liquid and a solid. They are amphiphilic, comprising a hydrophilic (water-loving) head and a hydrophobic (water-repelling or oil-attracting) tail. This unique structure enables them to adsorb at interfaces, such as oil-water boundaries, effectively reducing surface tension. When their concentration in a solvent exceeds the critical micelle concentration (CMC), surfactants can spontaneously form micelles. As a broad category, surfactants encompass emulsifiers and detergents.

Emulsifiers are a subset of surfactants that facilitate emulsion formation [42]. The hydrophilic-lipophilic balance (HLB) of a surfactant provides a useful quantitative measure to classify emulsifiers based on their affinity for water and oil. Depending on the overall HLB value—determined by the contributions of various hydrophilic and lipophilic groups—a surfactant can function as a w/o emulsifier (HLB number: 3-6), wetting agent (HLB: 7-9), o/w emulsifier (HLB: 8-14), detergent (HLB: 9-13), solubilizer (HLB: 10-13), or dispersant (HLB: 12-17) [43]. Additional stabilizing agents include lecithin and pectin, commonly used in food products, as well as proteins like β-lactoglobulin, which provide long-term stability by reinforcing the interface and preventing droplet coalescence [44].

However, emulsions are not immune to destabilization, a process known as age-

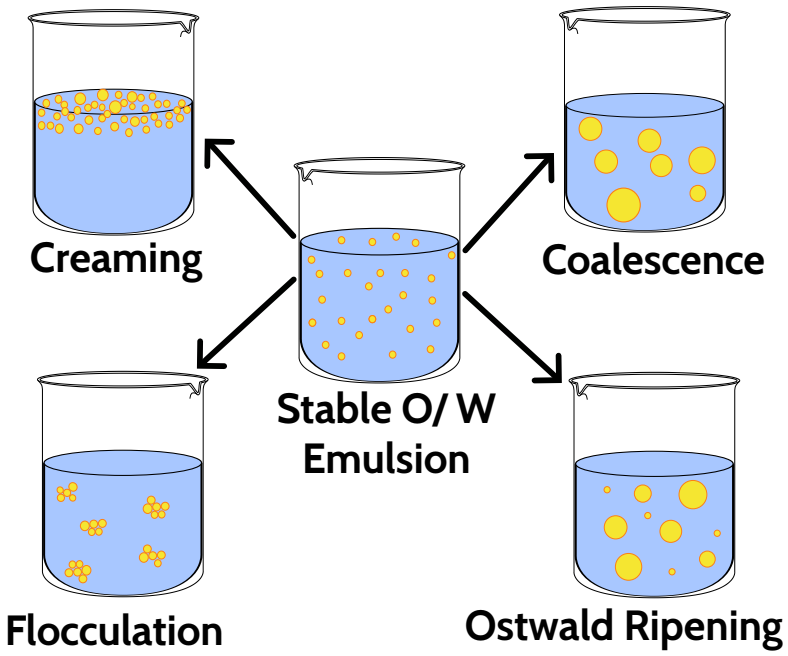

Figure 1.3: *Destabilization processes in emulsions: Creaming (separation of phases due to density differences), Flocculation (aggregation of droplets without fusion), Coalescence (merging of droplets into larger ones), and Ostwald ripening (growth of larger droplets as smaller ones dissolve).*

ing [45]. Emulsions are inherently unstable due to the unfavorable thermodynamic interaction between oil and water phases. This instability drives the droplets to merge and separate, a process that can be influenced by factors such as droplet size, type of emulsion, and the concentration of fat or water [38]. The destabilization of emulsions can occur in several ways, each with distinct characteristics. The simplest form involves creaming in o/w emulsions, where lighter oil droplets rise to the surface, or sedimentation in w/o emulsions, where heavier water droplets settle at the bottom. These phenomena arise from the density difference between the water and oil phases, and importantly, they do not alter the original droplet size distribution [46, 47]. A more complex form of destabilization is flocculation, which is a seemingly straightforward extension of creaming or sedimentation. In flocculation, droplets associate with each other, forming a weakly bound floc of larger average size, thus creating larger clusters without merging [48]. When considering the breakdown of individual droplets, two main mechanisms are widely discussed. First, in the case of coalescence, the interfacial film ruptures when two droplets collide, forming one larger droplet. This leads to the continuous merging of droplets, resulting in larger droplets and the eventual separation of the emulsion into distinct phases [48–50]. The second mechanism is Ostwald ripening, where the bigger droplets grow at the expense of smaller droplets, with the dispersed phase being transported through the continuous phase [51].

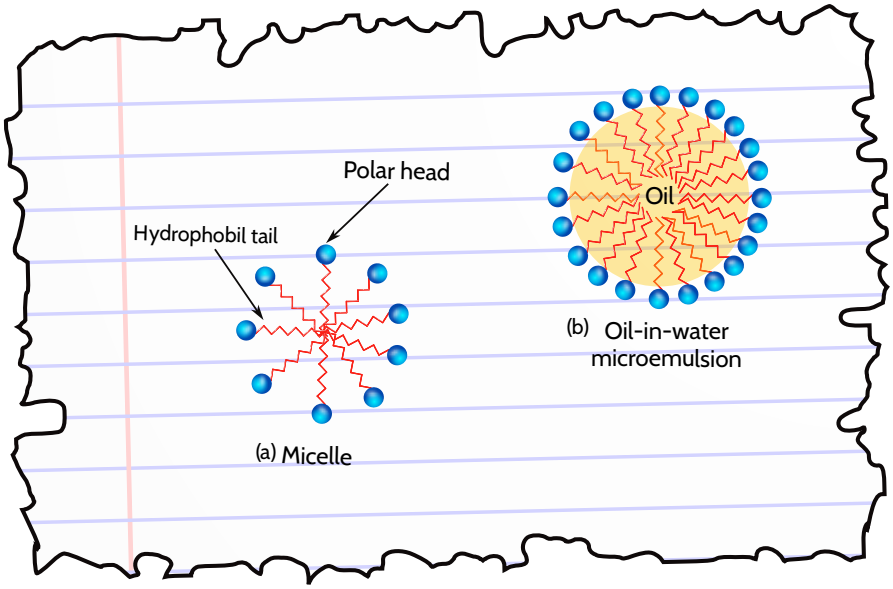

Figure 1.4: ***(a)*** *Surfactants, with hydrophilic heads and hydrophobic tails, can form micelles when the Critical Micelle Concentration (CMC) is reached.* ***(b)*** *Under appropriate conditions, including the correct surfactant concentration, oil-to-water ratio, and temperature, surfactants, oil, and water self-assemble into droplets, forming a microemulsion.*

1.4 Microemulsions

Microemulsions (MEs) are unique systems composed of water, oil, and surfactants, defined by their thermodynamic stability, transparency, and homogeneity. First introduced by P.A. Winsor in 1948 [52], these three components can form one of four types of equilibrium systems: Type I refers to a two-phase system where an organic phase floats on an oil-in-water phase, with the surfactant predominantly dissolved in water. Type II describes another two-phase system, where a water-in-oil phase containing the surfactant floats on an aqueous phase, with the surfactant primarily dissolved in the organic phase. Type III is a three-phase system in which a surfactant-rich intermediate layer forms between the aqueous and organic phases. Type IV represents a single-phase system without excess aqueous or organic phases, consisting entirely of microemulsions.

Unlike conventional emulsions that require external energy, microemulsions form spontaneously through surfactant self-assembly at the oil-water interface, reducing interfacial tension and enhancing stability (figure 1.4). Traditional surfactant-based microemulsions (SBMEs) rely on surfactants with polar head(s) and apolar tail(s) to stabilize immiscible mixtures. With droplet sizes typically spanning from around 20 nm down to just a few nanometers, SBMEs exhibit remarkable solubilization capacity and structural adaptability, including swollen micelles and bicontinuous phases, making them valuable in pharmaceuticals, cosmetics, and chemical industries [53].

Microemulsions play a crucial role in liquid-liquid extraction (LLE) by solubilizing and transporting a wide variety of hydrophobic and hydrophilic substances. Their small droplet size provides a significantly larger interfacial area between the dispersed and continuous phases, which enhances mass transfer efficiency. The high surface-to-volume ratio accelerates the dissolution and transport of solutes. Additionally, microemulsions are thermodynamically stable, maintaining a uniform dispersion of extractants and preventing phase separation, thus ensuring consistent efficiency [54–56]. By adjusting parameters like temperature or dilution, microemulsions can efficiently extract and concentrate specific compounds. In addition to their use in LLE, microemulsions are increasingly being utilized as carriers for drug delivery, as they allow the encapsulation of drugs in oily droplets, improving drug solubilization, minimizing toxicity, and reducing clearance rates. This makes them particularly valuable for enhancing the oral bioavailability and topical permeation of drugs. For instance, in a water-in-oil microemulsions, water acts as miniature reactors that exert control over the growth and formation of substances within the system by constraining the available space and resources [57]. This unique characteristic enables the production of nanoparticles.

Moreover, MEs are used in various extraction processes, accelerating the extraction of aqueous metal ions [58, 59] and in oil recovery through microemulsion flooding in the oil and gas sector, where they reduce interfacial tension in reservoirs [60]. Additionally, microemulsions contribute to solar energy production by facilitating hydrogen generation via UV-induced water decomposition [61]. These systems can exist in different structures, such as droplet-like swollen micelles and bicontinuous phases, offering versatility for applications in cosmetics, chemicals, and even the preservation of cultural artifacts like frescoes and monuments. Their phase behavior, viscosity, and solubilizing power can be adjusted by dilution or the evaporation of volatile components, further enhancing their utility [62].

Microemulsions are used for the controlled formation of nanoparticles and other materials in various scientific and industrial applications. The tunable properties of microemulsions, influenced by factors such as surfactant type and system composition, underscore their growing importance in modern technological advancements [63–67].

Phase Behavior in Surfactant-Based Ternary Systems: In oil-surfactant-water ternary systems, surfactants induce phase behaviors that go beyond what is seen in binary oil/water systems, which typically show only a two-phase region. Surfactants facilitate the formation of various phase regions, including one-phase, two-phase, and three-phase regions, which may involve isotropic or liquid crystalline phases (figure 1.5). Near the phase boundary, these systems are commonly classified into oil-in-water, water-in-oil, and bicontinuous (BC) structures. In bicontinuous microemulsions, oil and water domains are interconnected, exhibiting zero average curvature when the volumes of hydrophobic and hydrophilic phases are balanced. At higher surfactant concentrations, liquid crystalline phases can form near the microemulsion regions.

It is important to note that no clear-cut boundary exists between swollen micelles

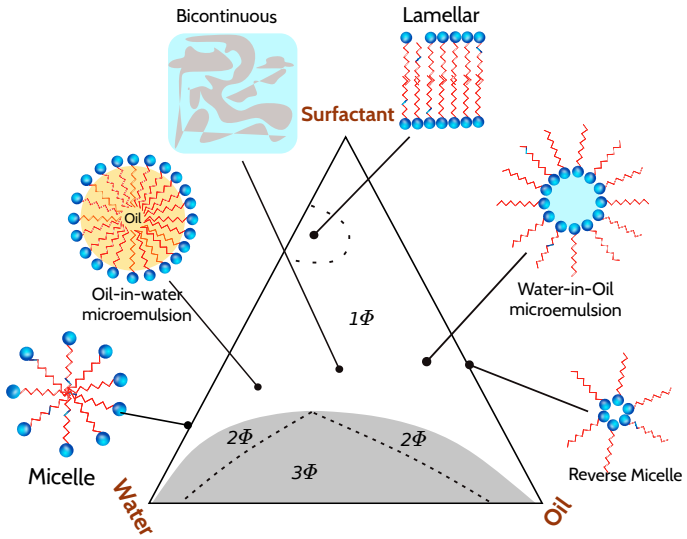

Figure 1.5: *Ternary phase diagram illustrating a typical system consisting of oil, surfactant, and water. The behavior of the system depends on the ratio of these components, resulting in either a monophasic (1ϕ) or multiphasic (2ϕ or 3ϕ) structure, i.e., phase separation. While the single-phase region appears macroscopically homogeneous, it may contain microscopically structured arrangements of the components, leading to the formation of micelles, microemulsions, or bicontinuous phases. Additionally, the depiction of micelles and reverse micelles on the same phase diagram is for reference only, as it is uncommon for a single system to form both micelles (in water) and reverse micelles (in oil).* *(Inspired by the figure drawn in [34])*

and microemulsions. In O/W systems with a surfactant-to-oil ratio exceeding seven, the system behaves more like swollen micelles rather than a true microemulsion. Similarly, in W/O systems, reverse micelles gradually transition into nanodroplets as the water content increases [68].

1.5 Hydrotropy

Hydrotropy, first introduced by Carl A. Neuberg in 1916 [70], refers to the molecular phenomenon where a hydrotropic agent—a non-toxic, water-soluble compound—enhances the aqueous solubility of poorly soluble solutes. Poor drug solubility in water is a significant challenge in pharmaceutical design, as nearly 70% of newly discovered drug candidates suffer from poor aqueous solubility [71–74]. This solubility issue directly impacts bioavailability and therapeutic effectiveness, making it one of the most critical factors in achieving the desired pharmacological response. While various formulation technologies exist to enhance solubility and improve oral bioavailability, one particularly promising technique is hydrotropy.

Hydrotropes are amphiphilic molecules that increase the solubility of hydrophobic substances in water through mechanisms distinct from micellar solubilization. Unlike surfactants, hydrotropes do not form micelles because their small hydrophobic region is inadequate for spontaneous aggregation [75, 76]. These include simple amphiphiles

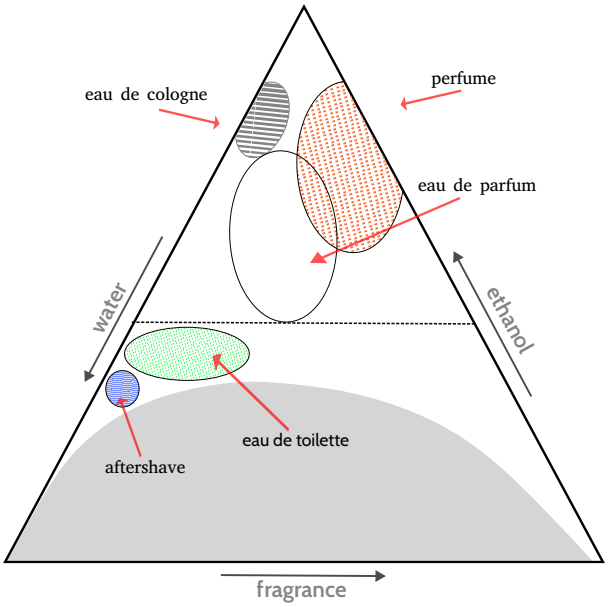

Figure 1.6: *Various applications of hydrotropy in the fragrance industry: the example above illustrates how the hydrotrope ethanol is used to solubilize fragrance in different commercial applications.* *(adapted from [69])*

like ethanol, n-propanol, iso-propanol, and tetrahydrofuran, which primarily interact with solutes via weak Van der Waals forces to enhance solubility [77–79]. Surfactants aggregate at millimolar concentrations (critical micellar concentration, CMC), whereas hydrotropes require molar concentrations (minimum hydrotrope concentration, MHC) to reduce surface tension [80]. However, certain hydrotropes, like those containing benzene rings, may gradually aggregate in a stepwise fashion [80], with the process involving less free energy. An example that illustrates the influence of chain length on hydrotropes is the case of alkyl chain benzoates and sulfonates. Short alkyl chain versions act as hydrotropes, while longer alkyl chain alkylbenzoates are classified as regular surfactants. This shows how the transition from hydrotropes to surfactants occurs as the chain length increases [81].

The efficiency of hydrotropic solubilization depends on the balance between the hydrophobic and hydrophilic portions of the hydrotrope molecule. A larger hydrophobic fraction typically enhances solubilization, while the charge on the hydrophilic portion is less influential. Hydrotropes can be organic or inorganic, ionic or neutral, and may exist in liquid or solid forms. By leveraging these unique properties, hydrotropes have proven highly effective in addressing solubility challenges in drug design, with solubility enhancements reported up to several orders of magnitude [82].

Despite their practical utility, the mechanism of hydrotropy has long been debated due to the lack of a reliable connection between solubility and the molecular interactions in aqueous solutions. Recent advances in Fluctuation Solution Theory (FST) have provided a rigorous, model-free framework derived from statistical thermodynamics, offering a deeper understanding of hydrotropy [83].

1.6 Ouzo Emulsions

The Ouzo effect, closely related to common emulsions and microemulsions, describes the formation of metastable droplets when water is added to specific mixtures, such as the anise-flavored liqueurs Ouzo or Pastis. This process leads to turbidity, marking emulsification as water dilutes the mixture beyond the phase boundary (see figure 3.1). Ouzo emulsions form rapidly when water addition moves the solution into the metastable region between the binodal and spinodal curves of the phase diagram. Supersaturation arises when solubility decreases non-linearly with increasing water, triggering homogeneous nucleation where nuclei spontaneously form due to local fluctuations in solute concentration.

These nuclei, enriched in solute, deplete nearby regions, halting nucleation in areas of reduced supersaturation. Droplet dispersion occurs uniformly on millisecond timescales, followed by slower growth via Ostwald ripening. During this process, smaller droplets dissolve while larger ones grow, governed by differences in their saturation levels [84]. This mechanism is exemplified in systems like ethanol-anethole diluted with water, where phase separation occurs spontaneously, creating stable emulsions without surfactants, stabilizers, or mechanical agitation. By fine-tuning the proportions of components, their densities, solubility, and temperature, control over droplet size, distribution, and number density can be achieved.

Certain polymer nanoparticles are synthesized via emulsion-solvent evaporation, where polymers dissolved in a good solvent precipitate as the solvent evaporates. This technique, leveraging the Ouzo effect, is widely used for encapsulating drugs in biodegradable polymers and preparing nanoparticles in nanoemulsions [85, 86].

Spontaneous emulsification via the Ouzo effect is a versatile method for producing emulsions, enhancing the stability and bioavailability of hydrophobic compounds like essential oils. This capability enables applications in food formulations, active packaging, and pharmaceuticals, optimizing activity, controlled release, and stability. Furthermore, sequential solvent transitions allow fine-tuning for higher oil content emulsions [87–90].

1.7 Surfactant Free MicroEmulsions

Surfactant-free microemulsions (SFMEs) have emerged as a promising alternative to SBMEs, replacing traditional surfactants with amphi-solvents or hydrotropes. An amphi-solvent, partially miscible with both oil and water, does not form micelles or ordered interfacial films. The first reported SFME, with a W/O structure, was discovered in a ternary system of hexane, water, and iso-propanol [94]. Subsequent research has confirmed that SFMEs can form structural analogs to SBMEs, including O/W and BC configurations (figure 1.7).

W/O surfactant-free microemulsions (SFMEs) have demonstrated significant potential in various applications. They serve as ideal media for chemical reactions. In early

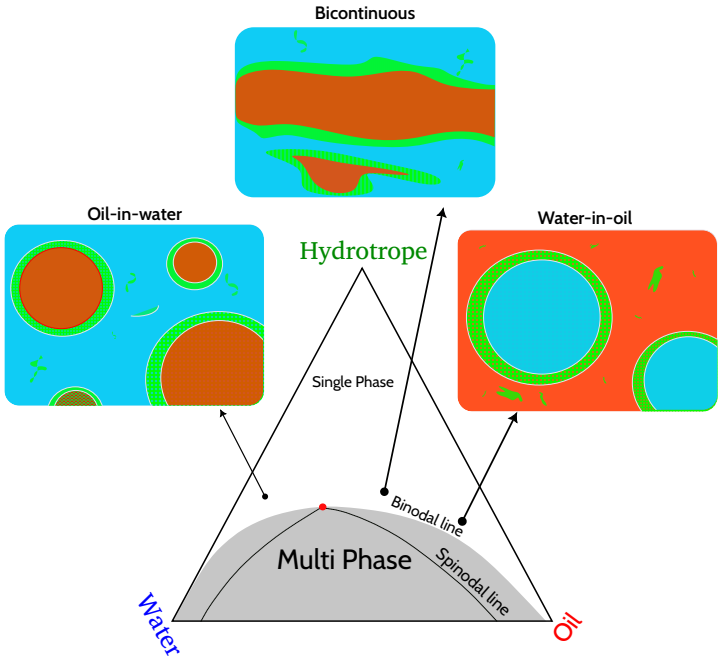

Figure 1.7: *Ternary phase diagram of a typical oil-hydrotrope-water SFME system, illustrating oil-in-water, bicontinuous and water-in-oil structures. Red represents oil, green denotes the hydrotrope, and blue corresponds to water. The hydrotrope forms a shell-like interface between the oil and water phases, albeit less structured compared to a surfactant. Unlike surfactants, the hydrotrope exhibits dynamic behavior, intermittently interacting with and detaching from the droplet interfaces.* *(derived from simulation results by [91–93].)*

studies on ester hydrolysis and chlorophyll degradation, higher reaction rates were observed in W/O SFMEs compared to surfactant-containing systems [95, 96]. Additionally, Keiser and Holt [97] reported elevated metalation rates in small aggregate and ternary solutions. SFMEs provide a cost-effective and straightforward approach for nanoparticle synthesis. For example, CdS nanoparticles synthesized in W/O SFMEs were larger compared to those formed in SBMEs [98]. Similarly, Mg_2Al-Cl layered double hydroxide nanosheets synthesized in SFMEs were free of organic coatings, unlike those produced in SBMEs, underscoring their utility in functional material development [99].

SFMEs are also advantageous for enzymatic reactions, overcoming challenges like catalyst reuse and surfactant separation, which are common in conventional SBMEs [95, 96]. Enzymes such as laccase and lipase exhibit higher catalytic activity and stability in W/O SFMEs, with activity patterns varying depending on the SFME composition, highlighting the medium's flexibility [100–103]. Enzyme recovery is efficient; by adding excess solvent, the aqueous phase containing the enzyme can be easily separated and reused [100]. Moreover, enzyme-containing organogels fabricated using SFMEs have shown high catalytic activity and stability in processes like esterification [103]. Finally, SFMEs have been explored for innovative applications like developing long-lasting insect repellent formulations, showcasing their versatility and potential [104].

SFMEs have also found applications driven by necessity, such as the solubilization of

electrolytes, which forms the basis for metal recycling—a critical component of the expanding circular economy. Additionally, the push to reduce reliance on fossil fuel-based products in formulations has gained momentum in recent years. This has spurred efforts to minimize or replace surfactants, which are often challenging to remove and recycle after industrial processes. Over the past two decades, these efforts have resulted in numerous studies focusing on developing innovative solubilization and separation techniques that eliminate the need for traditional surfactants, further advancing the principles of green chemistry [105–107]. Moreover, in oil recovery, the use of surfactant-co-surfactant mixtures (e.g., short-chain alcohols) is often undesirable, as the porous rock formations act like an extended chromatography column, causing the surfactant and co-surfactant to separate along the way. This challenge presents an opportunity for the application of SFMEs, which offer a more stable alternative [43, 54].

SFMEs offer considerable potential for applications similar to SBMEs, with the added benefits of cost efficiency and the ability to produce larger nanoparticles, thanks to the greater volume available within these systems [98]. For example, SFMEs have been used to create unique products such as biodegradable nanocapsules. Additionally, green SFMEs, made entirely of food-approved components, present significant industrial prospects, particularly within the food industry. Zhang et al. [108] investigated replacing traditional petroleum-based extraction solvents with SFMEs consisting of 1-octen-3-ol, ethanol (EtOH), and water.

Pre-Ouzo microemulsion refers to SFMEs, named in reference to the Ouzo effect. Within a conventional phase triangle absent of surfactants, the area where microemulsions form is designated as the pre-Ouzo region. In the pre-Ouzo region the system is macroscopically homogeneous, stable, and transparent, with a structured organization revealed, for example in the case of the octanol-ethanol-water mixtures, by O. Diat et al. [17, 109]. This region is characterized by sufficiently low water content to maintain a single-phase system, yet it exhibits an unanticipated structuring phenomenon. Drawing a parallel with the Ouzo effect—where metastable fine emulsions form without surfactants—the term "pre-Ouzo" describes the organization occurring prior to phase separation caused by water dilution.

This emergence of a pseudo-phase within a macroscopically homogeneous phase, driven by mesoscopic inhomogeneities, is known as mesoscopic solubilization [75, 110, 111]. Unlike the Ouzo effect, which occurs between the binodal and spinodal lines, mesoscopic solubilization takes place within a single-phase region.

This unique structuring is observed in ternary systems comprising two immiscible liquids and a third component, typically short-chain alcohols. Unlike surfactants, these alcohols do not form micelles but act as hydrotropes, enabling the dissolution of otherwise immiscible liquids.

Forces Stabilizing the Pre-Ouzo Structures: Zemb et al. [109] describe how the stability of pre-Ouzo structures emerges from a balance between *entropy-driven dispersion*, *hydration forces*, and other effects, which collectively stabilize dynamic aggregates

in the absence of surfactants. The *entropy of dispersion* promotes smaller, polydisperse domains, preventing large-scale phase separation and maintaining the coexistence of microdomains in dynamic equilibrium, thereby minimizing the system's free energy. *Hydration energy*, or more generally *solvation energy* for non-water species, plays a crucial role in interactions between octanol-rich domains, originating from the structured arrangement of water molecules at the high-density OH interfaces of octanol. These forces create a repulsive barrier that prevents the coalescence of microdomains. The role of hydration is highly system-specific, as evidenced by the absence of pre-Ouzo structuration in octane, which lacks sufficient OH group density to support hydration forces.

Van der Waals forces, while traditionally significant in other systems, are negligible here compared to the dominant hydration and entropy contributions due to their weaker interaction strength. Additionally, the *bending energy* associated with the curvature of the domains is minimal.

In summary, the stabilization of pre-Ouzo structures is primarily governed by the *entropy-hydration balance*, further influenced by solvation effects (see Table A.3). This mechanism is generalizable across various ternary systems where a hydrotrope mediates the compatibility of immiscible liquids, exemplifying a universal principle in soft matter systems [52, 73, 112–114].

Furthermore, when measuring the size of pre-Ouzo aggregates, **critical fluctuations** play a significant role. Near a critical point, two distinct mesoscopic length scales emerge: the size of the pre-Ouzo aggregates and the correlation length of critical fluctuations. Distinguishing between these can be challenging, especially in light scattering experiments like DLS, where critical opalescence dominates the signal, masking mesoscopic structures. Moreover, the correlation length of critical fluctuations in these mesoscopic systems can extend to 20–30 nm, further complicating the detection of smaller structures. Since DLS measurements are often taken at lower q values, large-scale critical fluctuations can overshadow contributions from smaller pre-Ouzo aggregates. In contrast, Small-Angle Scattering methods, by typically operating at higher q values, can mitigate this issue, ensuring a clearer distinction between different length scales. For instance, Robertson et al. [115] used deuterated solvents in SANS experiments, effectively reducing the overlap between critical fluctuations and pre-Ouzo structuration, thereby improving the accuracy of size measurements.

Lifshitz line

The **Lifshitz line** is a boundary in phase transition theory that originates from the *Lifshitz point*, where a system transitions from a uniform phase to a modulated phase. While the Lifshitz point is a singular critical point on the phase diagram, the Lifshitz line extends as a continuous boundary within a specific phase, marking the onset of modulation and structural changes in the system [116].

In the context of binary mixtures, such as those of water and surfactants, the Lifshitz line defines regions with distinct structural properties. For instance, in mixtures

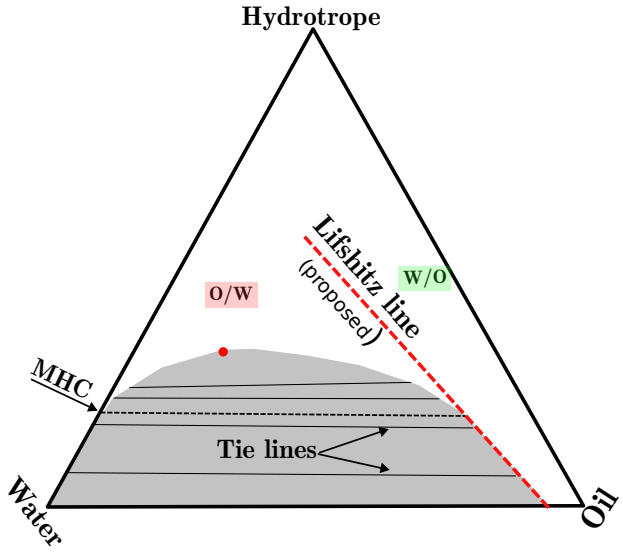

Figure 1.8: *Ternary phase diagram of an oil-hydrotrope-water system, illustrating the Lifshitz line (LL) proposed by Prevost et al. [120], which distinguishes between oil-in-water and water-in-oil emulsions. The diagram also highlights the Minimum Hydrotrope Concentration (MHC), which denotes the lowest hydrotrope concentration needed to solubilize oil and water in the system. The tie line from the MHC intersects with the LL, and eventually the tie lines converge at the critical point (red dot).*

like water/C_4E_1, it separates areas where the microstructures vary, influencing phenomena such as surfactant-less microemulsion formation and cluster behavior [117]. In ternary systems like homopolymer/diblock copolymer blends, the Lifshitz line exhibits non-monotonic behavior with respect to temperature, a result of fluctuational corrections influenced by wave vectors and studied through re-normalization group methods [118, 119].

The Lifshitz line is also associated with the *structure factor* $S(q)$, which is used to describe the periodicity of the system. As the system approaches the Lifshitz line, a peak in $S(q)$ shifts from zero wave vector to a nonzero value, indicating the onset of periodic structures [119]. This transition is characterized by the shift from a uniform phase to a modulated phase.

In addition to its definition in binary and ternary mixtures, the Lifshitz line is also helpful in characterizing self-assembly in amphiphilic systems. In these systems, the Lifshitz line demarcates regions where the microstructure transitions, often revealing intricate patterns of self-organization [116]. This line's position can be predicted theoretically using approaches like the Landau-Ginzburg theory, which accounts for fluctuational corrections and interactions in the system [119].

In the context of surfactant-free microemulsions in simple monoalcohol–water ternary systems, as explored in this project, the Lifshitz line represents a critical transition in the phase diagram. It defines the maximum swelling of alcohol-based reverse aggregates before the formation of a different pseudo-phase, namely the pre-Ouzo, where water is the

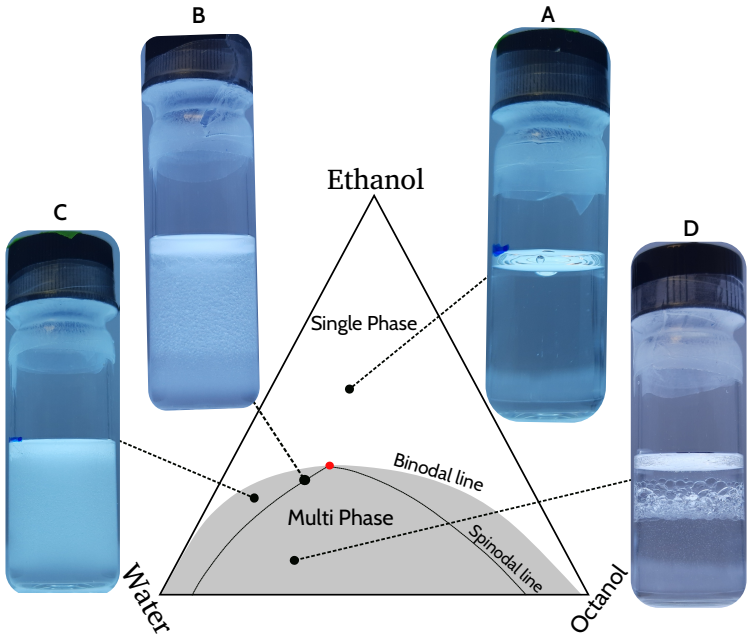

Figure 1.9: *Ternary phase diagram of an octanol-ethanol-water system illustrating various samples with different compositions. Sample **A** appears macroscopically homogeneous. Samples **B** and **C** correspond to Ouzo emulsions, while Sample **D** shows phase separation into two distinct phases.*

continuous phase. Initially stabilized in the oil-rich region, these reverse aggregates have a segregation of aliphatic and polar domains. As water hydrates the hydroxyl groups, the polar domains expand until reaching a limit—the Lifshitz line—beyond which the system undergoes a structural shift. This transition delineates the point where the reverse aggregates dissolve into a water-rich phase, representing a fundamental change in self-assembly. The Lifshitz line proposed tangential to the two-phase domain at low hydrotrope concentration, with its deviation from the binodal line is linked to the Minimum Hydrotrope Concentration (MHC) via a tie-line (see Figure 1.8).[117, 121, 122].

In summary, for a surfactant-free system, the Lifshitz line marks the transition from one pseudo phase to another. Starting with an oil-rich phase containing reverse aggregates with water cores, adding water causes these aggregates to swell. Beyond a certain point, the system shifts, with water becoming the continuous pseudo-phase, indicating a fundamental change in its microstructure [121].

Octanol-Ethanol-Water SFME

The octanol-ethanol-water ternary system, previously discussed, has been widely studied for its well-defined structural transitions, including pre-Ouzo phases characterized by mesoscopic organization at the nanometer scale, as well as Ouzo phases. Its straightforward preparation and safe handling make it an ideal model for exploring pre-Ouzo structuration. Figure 1.9 illustrates four samples with varying compositions of this ternary system. Sample A resides in the macroscopically homogeneous single-phase region, while

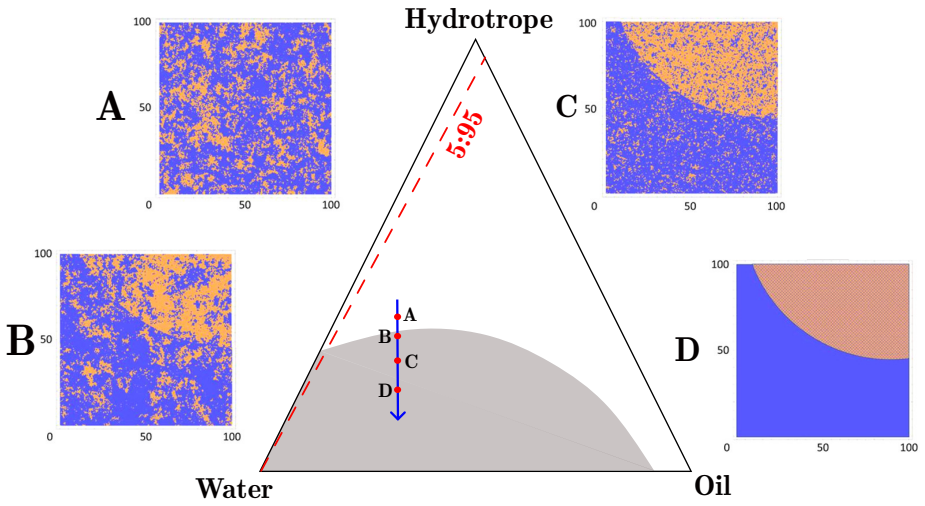

Figure 1.10: *Pictorial representation of the change in structural organization of a hydrotrope-based ternary system as it transitions from the single-phase region to the biphasic region. Sample **A** lies in the homogeneous region of the phase diagram, where SFME structures are observed. Samples **B**, **C**, and **D** are located in the two-phase region, where the upper oil-rich phase begins to form. Point **C** corresponds to a sample with a composition near the Minimum Hydrotrope Concentration (MHC), indicating the minimum concentration of hydrotrope required to start solubilizing the oil and water phases. The red dashed line in the phase triangle depicts autodilution line followed for SAXS and blue line with red circles corresponds to the SANS study (Adapted from [120]).*

samples B and C are in the metastable region, where Ouzo emulsions form. Finally, sample D represents a fully phase-separated state, with an oil-rich phase atop a water-rich phase, both containing ethanol.

The octanol–ethanol–water ternary system was studied by Prévost et al. [120], who employed *in situ* SAXS along a single dilution line, starting with a 5:95 w/w% octanol–ethanol mixture and progressively diluting the sample. They also carried out SANS experiments on four samples along a vertical line in the ternary phase diagram, as shown in Figure 1.10. Their study revealed the presence of spontaneous metastable Ouzo emulsions coexisting with pre-Ouzo aggregates in dynamic equilibrium within the bulk. They also found that the size of these emulsions depended on the amount of water added, highlighting a balance between molecular diffusion, interfacial diffusion, and coalescence-driven ripening [90, 123].

Additionally, the system was shown to be sensitive to temperature, which influences the phase boundary of the pre-Ouzo state. Importantly, the amount of water in the Ouzo droplet and octanol in the bulk plays a critical role in maintaining dynamic equilibrium and metastability. Below the Minimum Hydrotrope Concentration (MHC), metastability ceases. The MHC serves as a critical threshold, marking the point where emulsification stops or where the hydrotrope concentration becomes sufficient to solubilize oil and water (see Figure 1.8).

SANS and SAXS studies have provided insights into the structure of pre-Ouzo aggregates, which consist of globular domains enriched in octanol within the water-rich

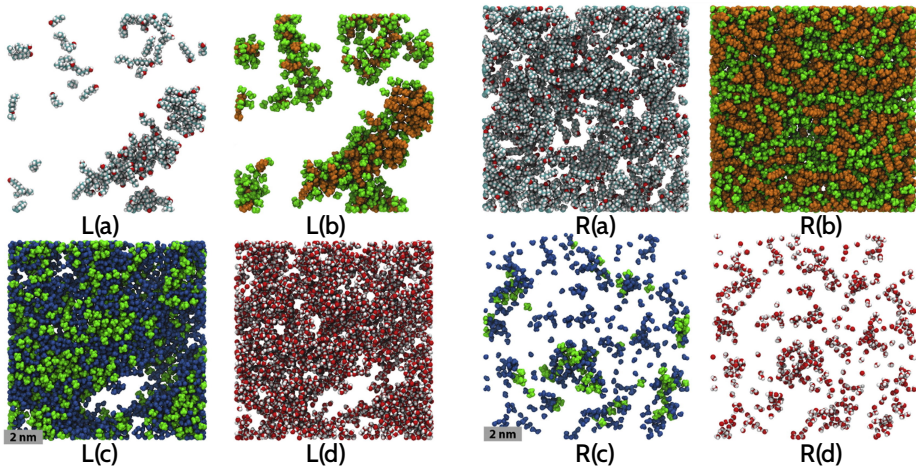

Figure 1.11: *Snapshots from molecular dynamics simulations illustrating the (**Left**) pre-Ouzo structuration in the water-rich side and (**Right**) reverse aggregates in the oil-rich side of phase triangle, of the octanol-ethanol-water ternary system. The images show (a) octanol molecules, (b) strongly interacting ethanol and octanol molecules, (c) ethanol molecules interacting with water and (d) water molecules (from [93]).*

phase. Ethanol is distributed between the two phases, with a slight excess forming a nanometer-thick layer at the interface [124–126]. Additionally, molecular dynamics simulations of the octanol-ethanol-water ternary system by Schöttl et al. [127] confirmed this structuration pattern. As illustrated in Figure 1.11, pre-Ouzo aggregates on the water-rich side exhibit a distinct arrangement, with octanol molecules forming the inner core, surrounded by a region enriched with strongly interacting ethanol molecules, all embedded within a continuous phase of water mixed with some ethanol. In contrast, on the oil-rich side, the reverse aggregate structures feature a smaller polar, water-rich domain enclosed within a network of octanol-ethanol chains.

In this thesis, we investigate surfactant-free monoalcohol–water systems, emphasizing mesoscale structuration and the formation of pre-Ouzo aggregates. Our study explores mixtures where one of the alcohols acts as a hydrotrope, promoting miscibility between water and a second, oil-like alcohol. By systematically varying component ratios, we examine how molecular organization evolves within the system. Utilizing Small-Angle X-ray Scattering, Neutron Spin Echo, and PFG-NMR, we probe the microscopic structural and dynamic properties of these mixtures, aiming to establish a quantitative framework for distinguishing the pre-Ouzo region from other pseudo-phases. Furthermore, we analyze the effect of temperature, contributing to a deeper understanding of water-alcohol systems and their potential applications in designing novel solvents.

Chapter 2

Experimental Techniques and Sample Preparation

2.1 Scattering Theory

Scattering of X-rays or neutrons involves the transfer of momentum (ΔP) and energy (ΔE) from the incident beam upon interaction with the sample. An incoming wave with energy E_i and wave vector k_i scatters off the sample, resulting in a scattered wave characterized by E_f and k_f. This scattering event encodes structural and dynamical information about the sample.

$$\textbf{Momentum transfer:} \quad \Delta P = \hbar k_i - \hbar k_f = \hbar q \tag{2.1}$$

$$\textbf{Energy transfer:} \quad \Delta E = E_i - E_f = \hbar \Delta\omega \tag{2.2}$$

where $q = k_i - k_f$ is the momentum transfer vector, and $\Delta\omega = \omega_i - \omega_f$ is the angular frequency change.

The scattering process is described by the *scattering law*, $S(\Delta P, \Delta E)$, which defines the transfer of energy and momentum. It is commonly represented as $S(q, E)$ or $S(q, \omega)$ and is known as the *dynamic structure factor*, an experimentally accessible quantity.

The dynamic structure factor is the Fourier transform of the space-time correlation function, given by:

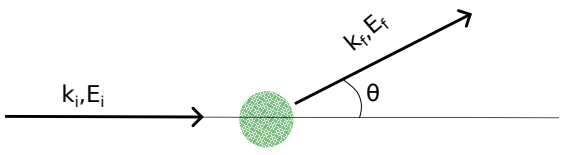

Figure 2.1: *Scattering of a wave (e.g., visible light, X-rays, neutrons, electrons) from a sample occurs with an incident energy E_i and wave number k_i. After interaction with the sample, the scattered wave exits at an angle θ relative to the initial wave direction, possessing energy E_f and wave number k_f.*

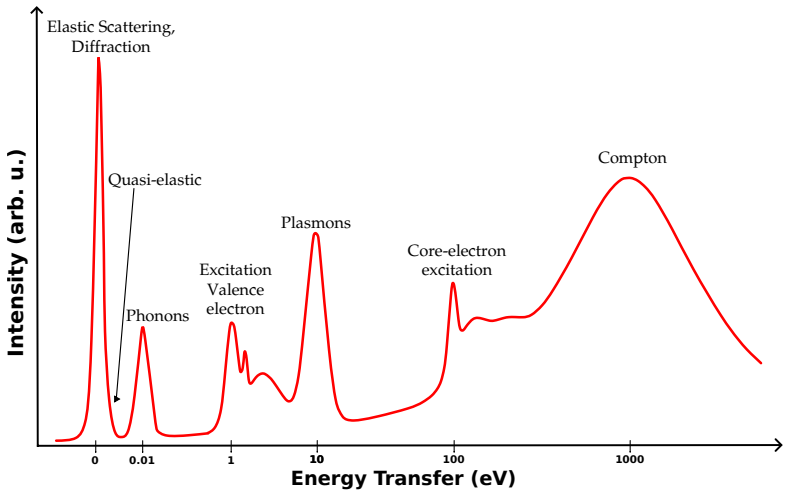

Figure 2.2: *Schematic illustration of different scattering phenomena and their associated energy transfer values (in eV), based on a hypothetical scatterer, $S(Q_0, \omega)$ integrated over Q.* *(Adapted from [129])*

$$S(q, E) = \mathscr{F}_T \left\{ \langle \exp[-iq(r(t) - r(0))] \rangle \right\} = \mathscr{F}_T \{ I(q, t) \} \tag{2.3}$$

$$S(q, E) = \mathscr{F}_{ST} \{ G(r, t) \} \tag{2.4}$$

where:

- $I(q, t)$ is the *intermediate scattering function*; its Fourier transform in time yields the dynamic structure factor.
- $G(r, t)$ is the *correlation function*; its Fourier transform in both space and time gives the dynamic scattering function [128].

Elastic scattering occurs when particles interact with a sample without exchanging energy, preserving both their wavelength and energy. This process provides insights into the static structure of a material. In elastic scattering, the energy transfer ($E = 0$) in the scattering function $S(q, E)$ implies that there are no temporal variations in the scattered signal. As a result, the magnitudes of the initial and final wavevectors (k_i and k_f) are equal, as there is no energy exchange between the scatterer and the scattering particle:

$$|k_i| = |k_f| = \frac{2\pi}{\lambda} \tag{2.5}$$

Thus, the magnitude momentum transfer q is given by:

$$q = \frac{4\pi \sin\theta}{\lambda} \tag{2.6}$$

Additionally, there is a reciprocal relationship between ω and t, expressed as:

$$\tau \sim \frac{1}{\Delta\omega} = \frac{\hbar}{\Delta E} \tag{2.7}$$

In the case of elastic scattering, low-resolution energy data is sufficient to obtain information about rapid motions within the system. Small Angle Scattering (SAS) techniques can be employed to analyze this phenomenon.

Quasi-elastic Scattering: Building on the elastic scattering case, where no energy exchange occurs, quasi-elastic scattering arises when there are small fluctuations in energy. These fluctuations lead to peaks at $\pm\omega_0$, corresponding to oscillations at a frequency ω_0. Random changes over a characteristic time scale τ cause a broadening of the elastic peak, creating a new peak centered at $\omega = 0$ with a width determined by $1/\tau$. This is illustrated in the broadening of the elastic peak in figure 2.2, marked as quasi-elastic.

$$\left| \int_0^\infty e^{-t/\tau} e^{i\omega t} dt \right|^2 = \frac{1}{\omega^2 + (1/\tau)^2} \tag{2.8}$$

where, in the Lorentzian term, the case of $T \to \infty$ corresponds to the elastic case.

For quasi-elastic scattering, which reveals information about diffusive translational and reorientational motions within the sample (where energy transfer is minimal), higher resolution is needed (eq. 2.7). This can be achieved using the Neutron Spin-Echo (NSE) technique.

Further, In contrast to elastic scattering, inelastic scattering involves interactions with dynamic processes such as phonon or magnon, where neutrons exchange energy with oscillatory motions, resulting in a finite energy transfer [130].

Scattering of X-ray Photons and Neutrons

The fundamental difference between X-ray and neutron scattering arises from their interaction mechanisms with matter.

The *scattering length density* (SLD) characterizes how a material interacts with incident radiation, whether X-rays or neutrons. In **X-ray scattering**, the SLD is directly proportional to the electron density $\rho_e(\mathbf{r})$, as X-rays interact with the electron cloud of atoms. This relationship is expressed as:

$$f_{\text{X-ray}}(\mathbf{r}) = \rho_e(\mathbf{r}) \tag{2.9}$$

In contrast, **neutron scattering** is governed by interactions with atomic nuclei. The neutron SLD depends on the distribution of nuclear scattering lengths b_i, which vary based on atomic species and isotope. It is given by:

$$f_{\text{neutron}}(\mathbf{r}) = \sum_i b_i \delta(\mathbf{r} - \mathbf{r}_i) \tag{2.10}$$

where b_i is the scattering length of the i-th nucleus, and the summation extends over all nuclei in the sample. As a result, *X-ray scattering* primarily probes the electron distribution, whereas *neutron scattering* provides information on nuclear positions and isotope-dependent contrast.

Coherent and Incoherent Scattering: In the specific case of *neutron scattering*, which differs fundamentally from X-ray and electron scattering, the elastically scattered neutron intensity consists of two main contributions: **coherent** and **incoherent** scattering. The total elastic scattering intensity is given by:

$$I_{\text{elastic}}(\mathbf{q}) \propto \left\langle |F(\mathbf{q}) + \delta F(\mathbf{q})|^2 \right\rangle \tag{2.11}$$

where $F(\mathbf{q})$ is the Fourier transform of the SLD function $f(\mathbf{r})$. Expanding this expression leads to the decomposition:

$$I_{\text{elastic}}(\mathbf{q}) = I_{\text{coherent}}(\mathbf{q}) + I_{\text{incoherent}}(\mathbf{q}) \tag{2.12}$$

Coherent scattering, or 'in-phase' scattering, arises from the ordered arrangement of scattering centers within a sample, resulting in interference effects that provide insights into collective phenomena. The corresponding scattered intensity is given by:

$$I_{\text{coherent}}(\mathbf{q}) \propto \left| \int_V f(\mathbf{r}) e^{i\mathbf{q}\cdot\mathbf{r}} \, d^3\mathbf{r} \right|^2 \tag{2.13}$$

where $f(\mathbf{r})$ represents the SLD as a function of position, and $\mathbf{q}$ is the scattering vector. This formulation essentially describes the scattering of a single neutron from all nuclei in the sample, incorporating their spatial correlations, with interference effects arising between different nuclei ($i \neq j$) in the case of coherent scattering.

Incoherent scattering arises from random variations in the scattering lengths of individual nuclei, without any long-range order. It involves interference only from the same nucleus ($i = j$) at different times, meaning it carries no spatial information. The intensity of incoherent scattering is given by:

$$I_{\text{incoherent}}(\mathbf{q}) \propto \langle (\Delta b)^2 \rangle \tag{2.14}$$

Incoherent scattering provides insight into temporal fluctuations of individual particles but does not contribute to structural information.

Diffusion

Diffusion is one of the simplest forms of quasielastic scattering. It refers to the stochastic motion of particles driven by thermal energy, which leads to their redistribution over time and plays a fundamental role in transport phenomena across gases, liquids, and complex fluids. The diffusion of particles is often described by Fick's First Law, which relates the flux J of a substance to its concentration gradient:

$$J = -D \frac{\partial C}{\partial x} \tag{2.15}$$

where D is the diffusion coefficient, and $\frac{\partial C}{\partial x}$ represents the concentration gradient. The negative sign indicates that diffusion occurs from regions of higher to lower concen-

tration.

In an isotropic medium, the probability density function for the displacement of a diffusing particle follows a Gaussian distribution. The mean square displacement (MSD) $\langle r^2 \rangle$ of a molecule over time t is given by:

$$\langle r^2 \rangle = 6Dt \tag{2.16}$$

For a Brownian particle undergoing free diffusion, the intermediate scattering function (ISF) $S(q,t)$ exhibits an exponential decay:

$$S(q,t) = S(q,0)e^{-Dq^2t} \tag{2.17}$$

where q is the scattering vector. This q^2 dependence is characteristic of purely diffusive behavior and is observed in many systems under dilute or weakly interacting conditions.

A key theoretical framework connecting diffusion to molecular properties is the Stokes-Einstein equation, which relates D to the hydrodynamic radius R of the diffusing species:

$$D = \frac{k_B T}{6\pi\eta R} \tag{2.18}$$

where k_B is the Boltzmann constant, T is the temperature, and η is the viscosity of the medium.

As mentioned above, in systems exhibiting simple Brownian motion, the decay of $S(q,t)$ typically follows the expected q^2 dependence. However, deviations from this behavior can indicate additional dynamic contributions. For instance, viscoelastic effects in complex fluids often cause the relaxation function to deviate from a simple exponential form, resulting in stretched or compressed exponential. Similarly, collective dynamics arising from intermolecular interactions or transient network formations can lead to non-Fickian diffusion, where $S(q,t)$ follows a power-law dependence different from e^{-Dq^2t}. Confinement effects in microemulsions and structured fluids may also lead to deviations, often manifesting as subdiffusive or oscillatory behavior in $S(q,t)$. As indicated above, these deviations provide crucial insights into mesoscale organization and dynamical heterogeneity in systems such as pre-Ouzo microemulsions, where competing interactions shape transport properties. Neutron spin echo (NSE) spectroscopy is particularly useful in such cases, as it enables the direct measurement of intermediate scattering functions over nanosecond to microsecond timescales, making it well-suited for probing slow collective and confined dynamics in soft matter systems.

2.2 Small-Angle Scattering

Small-angle scattering (SAS) provides a versatile method for characterizing structures indirectly, particularly in systems where direct visualization using microscopy poses

challenges. Microscopy, while effective for obtaining localized structural images, often requires sample conditions that deviate from their natural states, such as freezing, desiccating, or immobilizing liquid samples. Additionally, microscopy techniques are constrained by their limited field of view. Moreover, scattering experiments yield reliable and meaningful averages, offering a representative picture of the entire system. Small angle scattering is one of the methods which is used to indirectly characterize a sample.

A SAS experiment closely resembles a diffraction experiment, but the key difference is that SAS focuses on much smaller angles. In X-ray diffraction (XRD), the angles are typically much larger, as described by Bragg's law, which governs the diffraction of X-rays by periodic atomic planes. Bragg's law is expressed as:

$$n\lambda = 2d \sin\theta \tag{2.19}$$

This relationship indicates that larger angles are required to satisfy the diffraction condition for smaller interatomic distances (on the order of Ångströms), making XRD ideal for studying crystals with well-defined periodic structures. In contrast, SAS is used to probe larger structures, such as polymers, colloidal solutions, or micelles—ranging from hundreds of Angstroms to a few hundred nanometers—where smaller scattering angles are required to capture the scattering information from these larger systems [131].

Small-Angle Scattering (SAS), which includes well-established techniques like Small-Angle X-ray Scattering (SAXS) and Small-Angle Neutron Scattering (SANS), is a powerful method for probing the structural properties of materials at the nanoscale. There is also Small-Angle Light Scattering (SALS), a less frequently used technique compared to SAXS and SANS, which employs visible lasers as the scattering source. In typical SAS experiments, a monochromatic beam of either X-rays or neutrons, with a wavelength λ, is directed at a sample. The scattered intensity at low angles provides detailed information about the size, shape, and spatial arrangement of particles and macromolecules, making SAS invaluable for studying soft matter, biological materials, polymers, and colloidal systems.

The scattered intensity, $I(\mathbf{q})$, is governed by the differential scattering cross-section, $\frac{\mathrm{d}\sigma}{\mathrm{d}\Omega}$, which describes the probability of scattered particles appearing within a solid angle $\mathrm{d}\Omega$. For isotropic systems, $I(\mathbf{q})$ depends on the contrast in scattering length density (SLD) between different components of the sample and its surrounding medium.

A typical SAS instrument consists of several key components that work together to enable precise measurements (see Figure 2.3). The source emits a beam of X-rays or neutrons, which is then tuned to a specific wavelength essential for determining scattering angles and extracting structural information. A collimation system, composed of slits or apertures, ensures the beam remains parallel or collimated, producing a well-defined and uniform profile necessary for accurate scattering measurements. The sample holder positions the sample in the beam path and can be adjusted for various angles or orientations. Depending on the experiment, it may also incorporate temperature control or a rotating stage for enhanced precision. Finally, the detector captures the scattered beam,

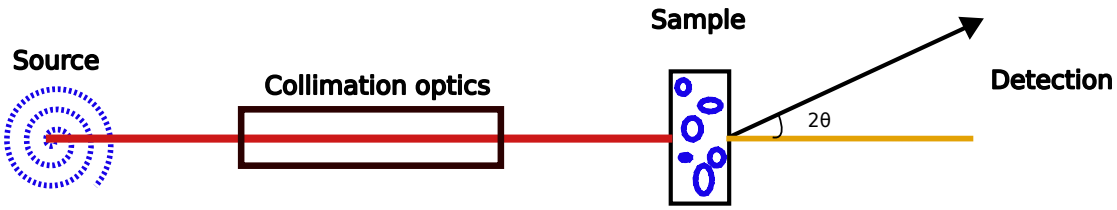

Figure 2.3: *Schematic diagram of a basic SAS instrumentation setup*

while a beamstop blocks the direct beam, allowing for accurate measurement of scattered photons at low angles. SAS can probe structural information across a wide range of scales using different angular ranges and geometries, with applications in studying aggregation, dispersion, and hierarchical organization of materials

While SAXS and SANS share many similarities in their data interpretation and applications, their primary distinction arises from contrast mechanisms. SAXS is sensitive to electron density differences, whereas SANS relies on nuclear contrast variations. This fundamental difference dictates their respective advantages in different experimental scenarios, making them complementary tools for nanoscale structural investigations.

SAXS utilizes X-rays to probe electron density variations within the sample, making it highly effective for studying amphiphiles, micelles, emulsions, and other nanoscale assemblies. It is particularly useful in pharmaceutical research, food science, and battery development [132]. The technique can be applied to different sample forms (liquid, solid, or powder) with minimal preparation and offers insights into both bulk and surface structures.

SANS, on the other hand, leverages the interaction of neutrons with atomic nuclei to probe scattering length density contrasts. This allows for enhanced contrast manipulation through isotopic substitution (e.g., deuteration), making it especially valuable in polymer science, biology, and soft matter physics. Overall, SAS is capable of extracting a broad range of structural information, such as size, shape, volume, mass, radius of gyration (R_g), and fractal dimensions of objects. [133–135].

2.2.1 Data interpretation for SAS

In a hypothetical perfectly homogeneous medium, no scattering would occur in directions other than the incident one. Scattering fluctuations in the medium are necessary to generate a scattering signal. This signal arises from the contrast between the scatterer and the surrounding medium, such as the contrast between a scattering particle and the solvent, or between different phases in the absence of distinct particles, as seen in a bicontinuous phase. In SAXS, this contrast is determined by the difference in electronic density ($\Delta\rho = |\rho_{scatterer} - \rho_{solvent}|$) between the scattering phase and the surrounding medium. Since X-rays interact with the electron cloud of atoms, the scattering intensity depends on variations in electron density. As a result, SAXS is particularly effective for studying systems containing heavier elements or components with significant elec-

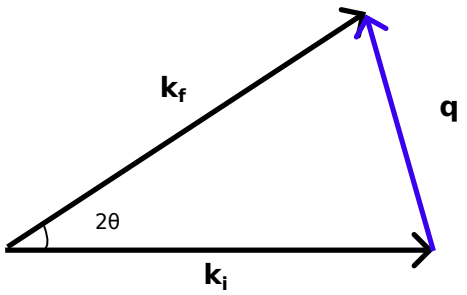

Figure 2.4: *Scattering vector q in terms of incident and scattered wave vectors.*

tron density contrast. However, SAXS struggles to differentiate between materials with similar electron densities, such as light hydrocarbons and biological macromolecules in aqueous solutions, due to minimal contrast.

SANS, on the other hand, involves the scattering of neutrons by atomic nuclei, and the scattering length density for neutrons, ρ_N, arises from nuclear interactions rather than electron clouds. Unlike SAXS, ρ_N is not directly correlated with the atomic number and varies irregularly between isotopes. For example, hydrogen (^{1}H) and deuterium (^{2}H) exhibit vastly different neutron scattering lengths, making SANS particularly powerful for contrast variation experiments. By selectively substituting hydrogen with deuterium in specific components, researchers can tailor the contrast to highlight or suppress specific features in a sample. This flexibility is a unique advantage of SANS that SAXS cannot achieve.

SANS is inherently non-destructive because the neutrons typically used for studying these systems have lower energy (in the meV range), compared to X-rays, which possess much higher energies (on the order of keV). This makes SANS ideal for investigating delicate systems like biological samples or soft matter.

When represented as I versus q, the scattering vector q defines the spatial range of the experiment, corresponding to the inverse length scale of the probed structures. For elastic scattering, it is given by $q = \frac{4\pi}{\lambda} \sin\theta$. The shape of the scattering curve reflects the spatial organization of the sample, resolving structural features across multiple length scales—from atomic or molecular arrangements (e.g., crystalline regions) to larger assemblies (e.g., micelles, clusters, or networks). The characteristics of the $I(q)$ curve, such as slope and oscillations, depend on the size, shape, and distribution of the structures within the sample.

Figure 2.5-left illustrates an example of a SAXS scattering curve plotted on an I vs. q scale. The intensity at a given q-value represents the contribution of scatterers in the sample at a corresponding real-space length scale (see Figure 2.5-right). For instance, a specific q-value, such as q_2, corresponds in real space to a green circle with a diameter $D_2 = \frac{2\pi}{q_2}$. Whenever this "window" (circle) encompasses a region with non-zero

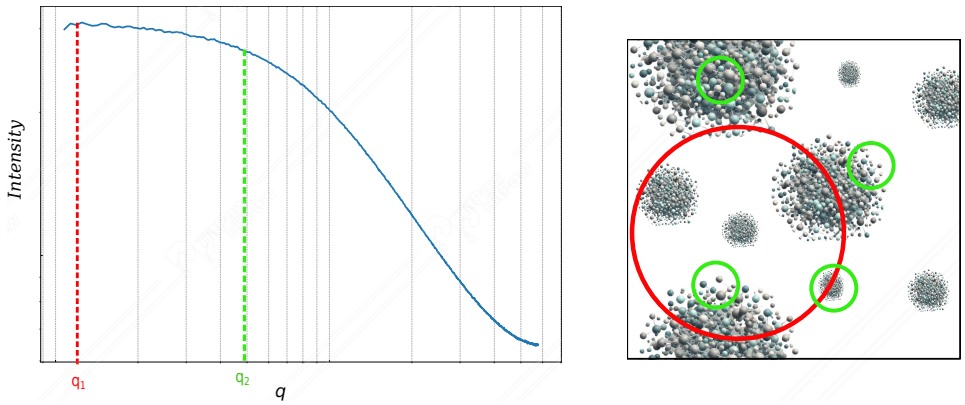

Figure 2.5: *(**Left**) Example scattering curve from a SAS experiment. (**Right**) Illustration of the q-range in real space for a sample. The red circle corresponds to a lower q_1 value, indicating a larger real-space region, while the green circle represents a higher q_2 value, indicating a smaller real-space region. Lower q values provide insights into interactions between system components, whereas higher q values offer details about individual components or interface of the structures.*

contrast—i.e., where the difference in scattering density is non-zero—a corresponding scattering intensity is observed. As the q-value decreases from q_2 to q_1 (where $q_2 > q_1$), the diameter increases, providing a broader view of the sample volume.

As we progressively move from lower to higher q values, the information obtained from the scattering intensity varies, depending on the relative size of the scatterers and the distances between them. At relatively low q values, where the "real-space window" is large, the intensity provides insights into the interactions and arrangements between different particles in the sample, captured by the structure factor $S(q)$. As we increase q, making the real-space window smaller, the intensity begins to reveal information about the individual scatterers, described by the form factor $P(q)$. At even higher q values, with much smaller real-space windows, the scattering intensity provides details about the interface between the scatterers and the surrounding medium.

Form Factor and Structure Factor

The *form factor* ($P(q)$) characterizes the scattering intensity of an individual scatterer—whether it be a micelle, colloidal particle, polymer molecule, or any entity with similar scattering properties—while accounting for its shape, size, and internal structure. Mathematically, it is derived from the Fourier transform of the particle's density distribution, offering insights into the geometry and dimensions of individual scatterers. However, extracting a well-defined form factor from experimental data is only feasible when discrete scatterers can be clearly identified. In highly polydisperse or dynamic systems, where particles exhibit significant size fluctuations or lack a well-defined shape, separating the form factor from the total scattered intensity may become ambiguous.

Experimentally, form factors can only be measured in the dilute regime, where par-

ticles are considered independent scatterers with negligible interactions. For a system of N identical particles, each with an inhomogeneous scattering length density (SLD) $\rho(\mathbf{r})$, located at different positions, the total scattered intensity $I(q)$ is given by the sum of the intensity contributions from individual scatterers.

The normalized amplitude scattered by a single particle is given by:

$$a(q) = \int_{V_{\text{particle}}} \rho(\mathbf{r}) e^{-i\mathbf{q}\cdot\mathbf{r}}\, d\mathbf{r} \tag{2.20}$$

resulting in the intensity:

$$I_{\text{particle}}(q) = a(q)a^*(q) = V_{\text{particle}}^2 P(q) \tag{2.21}$$

where $P(q)$ is the form factor, and V_{particle} represents the volume of the particle. The form factor is given by:

$$P(q) = \frac{1}{V_{\text{particle}}^2} \iint_{V_{\text{particle}}} \rho(\mathbf{u})\rho(\mathbf{v}) e^{-i\mathbf{q}\cdot(\mathbf{u}-\mathbf{v})}\, d\mathbf{u}\, d\mathbf{v} \tag{2.22}$$

Thus, the intensity per unit volume for a suspension containing N particles is:

$$I_V(q) = \frac{N}{V} V_{\text{particle}}^2 P(q) = \phi V_{\text{particle}} P(q) \tag{2.23}$$

where $\phi = NV_{\text{particle}}/V$ is the volume fraction of the particles in the suspension. The *structure factor* ($S(q)$) describes the spatial arrangement of particles in a system, incorporating inter-particle interactions and ordering. It quantifies interference effects arising from the organization of scatterers within the material, providing insights into particle spacing, correlations, and interaction effects. In complex systems, inter-particle interactions—whether attractive, repulsive, electrostatic, or non-electrostatic—contribute to the formation of $S(q)$. Additionally, factors such as temperature, salt concentration, and pressure influence the equilibrium structure, leading to variations in the structure factor.

When measuring the scattering intensity $I(q)$ for a system of centrosymmetric identical particles in solution, the total intensity reflects both the scattering from individual particles and the interference effects due to inter-particle correlations. In the absence of multiple scattering, the total intensity can be expressed as the product of the form factor $P(q)$ and the structure factor $S(q)$:

$$I(q) = \phi V_{\text{particle}} P(q) S(q) \tag{2.24}$$

Further, for a system of particles with homogeneous scattering length density ρ, the form factor $P(q)$ can be expressed as:

$$P(q) = (\Delta\rho)^2 P_0(q) \tag{2.25}$$

where $P_0(0) = 1$. Consequently, the scattering intensity simplifies to:

$$I(q) = \phi V_{\text{particle}} (\Delta\rho)^2 P_0(q) S(q) \tag{2.26}$$

Experimentally, the structure factor can be extracted by dividing the measured intensity $I(q)$ by the form factor $P(q)$. For instance, by applying a model that considers both electrostatic repulsion and Van der Waals attraction, it is possible to fit the experimental data to quantify the interaction potential. The limit $S(q = 0)$ corresponds to the osmotic compressibility of the sample, which is accessible only if absolute intensities are measured.

However, in many complex liquid systems, especially those lacking well-defined discrete scatterers (e.g., bicontinuous phases or highly dynamic emulsions), the separation of scattering intensity into distinct $P(q)$ and $S(q)$ components becomes ambiguous. In such cases, the direct interpretation of scattering data may require alternative approaches, such as correlation function analysis or simulations, rather than relying on the traditional $I(q) \propto P(q)S(q)$ factorization [131].

2.2.2 Porod Invariant

The *invariant*, also known as the *Porod invariant*, is a fundamental scattering property derived by integrating the scattering intensity across the entire range of the scattering vector q. It represents a fixed quantity independent of q and is directly related to the total contrast within a system. The invariant Q_I is mathematically expressed as:

$$Q_I = \int_0^\infty q^2 I(q)\, dq, \tag{2.27}$$

where $I(q)$ is the scattered intensity as a function of q. This integral corresponds to the area under the Kratky curve, which is obtained by plotting $I(q) \cdot q^2$ versus q.

For a two-phase system, the invariant can also be related to the scattering length density (SLD) contrast and the volume fractions of the phases as:

$$Q_I = 2\pi^2 (\Delta\rho)^2 \phi_1 \phi_2, \tag{2.28}$$

where $\Delta\rho = (\rho_1 - \rho_2)$ is the SLD contrast, and ϕ_1 and ϕ_2 are the volume fractions of the phases ($\phi_1 + \phi_2 = 1$).

The invariant has extensive applications in small-angle scattering experiments and serves multiple purposes. It is used to calculate the volume fractions of phases in a system when the contrast is known. By comparing experimental results with theoretical predictions, the invariant helps validate the contrast between phases. Additionally, it can cross-validate scattering patterns from different instruments, ensuring consistency across measurements. The invariant is also valuable for studying bulk properties, such as porosity, density fluctuations, and aggregation states.

The calculation of the invariant is closely related to Kratky analysis, which involves plotting $I(q) \cdot q^2$ versus q. This representation highlights specific features of the scat-

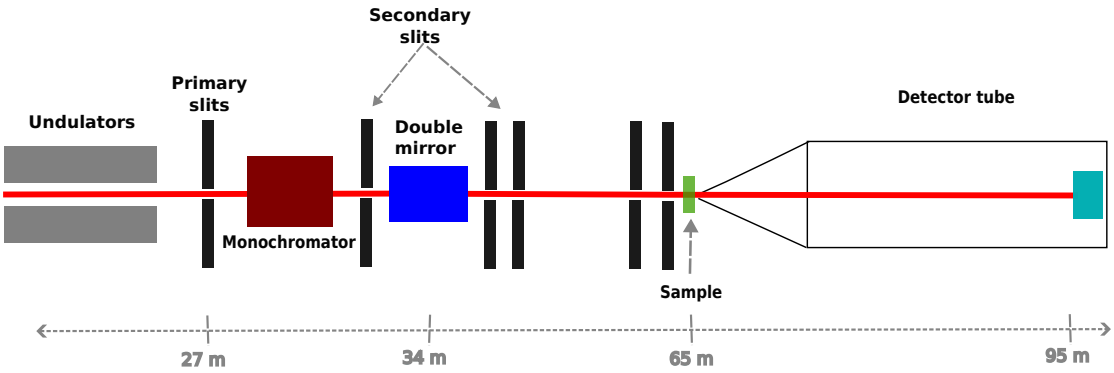

Figure 2.6: *Schematic diagram of the ID02 instrument at ESRF. The X-ray beam passes through a series of slits and a monochromator before reaching the sample. After interacting with the sample in transmission mode, the scattered X-ray photons travel through the detector tube and are detected by the detector.* *(Redrawn from [136])*

tering data that are not apparent in standard plots of $I(q)$ versus q. Kratky plots are particularly useful for studying polymer solutions, where the curve's shape reveals the polymer chain's conformation. A rise to a plateau indicates an unfolded chain (random coil), while a distinct peak suggests a compact or folded conformation, such as a folded protein. A pseudo-linear rise is characteristic of a rod-like conformation, and a high-q upturn from the plateau implies a worm-like chain. In polymer gels, a peak may indicate inhomogeneities, such as clustering.

In practice, the invariant is challenging to compute directly because experimental data rarely spans the entire range $0 \leq q \leq \infty$. As such, extrapolation is required. For the low-q region, the Guinier function $I_0 \exp(-q^2 R_g^2/3)$ or a power law is typically used. For the high-q region, a power law of the form A/q^m is employed, with m typically ranging between 3 and 4, depending on interface sharpness.

2.2.3 SAXS: ESRF ID02 Instrument

The Small-Angle X-ray Scattering (SAXS) experiment was conducted at the ID02 beamline at the ESRF, France, using a setup detailed in Figure 2.6. The incident X-ray beam from the synchrotron source is first passed through a monochromator, ensuring a monochromatic beam that then strikes the sample. The sample is held in a quartz capillary tube, and the measurement is performed in transmission mode. In this mode, scattering data from the empty capillary holder is subtracted from the scattering data of the sample to isolate the relevant information.

The SAXS setup consists of several key components: the synchrotron source, monochromator, sample holder (quartz capillary), and detector. The sample-to-detector distance can be varied from 0.8 m to 31 m, allowing the detector to cover a q-range from $10^{-3}\,\mathrm{nm}^{-1}$ to $60\,\mathrm{nm}^{-1}$. This adaptability enables fine-tuning of the measurements, providing flexibility in probing different length scales in the sample.

In this configuration, the detector system plays a crucial role in capturing the scat-

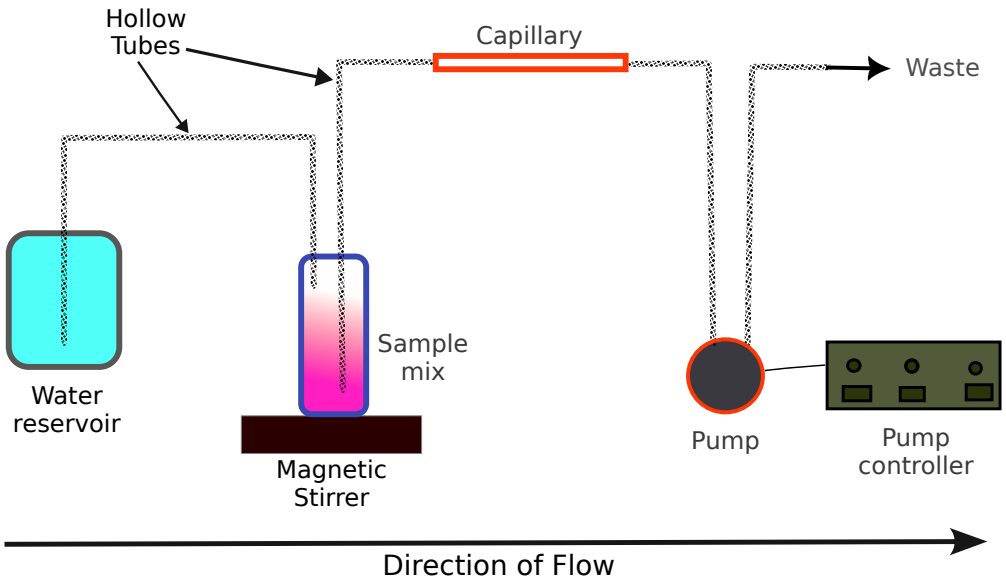

Figure 2.7: *Schematics of the pump flow setup used for the autodilution experiment at ID02*

tering data. By moving the detectors inside the detector tube, the experimental setup allows for a precise range of scattering angles and an enhanced understanding of the sample's structure at various scales [136, 137].

The instrument has an energy range of 8-20 keV out of which we used 12.46keV corresponding to a wavelength of 0.0995 nm. The detector employed was a Rayonix MX170-HS CCD camera, and The samples to detector distance was set to 1.5m which allowed us to scan the Q range from 1.077×10^{-1} to $1.086 \times 10^{1}\,\mathrm{nm}^{-1}$

2.2.4 Pump Flow Setup for Autodilution Experiments

For the *in situ* Small-Angle X-ray Scattering (SAXS) autodilution experiments, a flow setup was implemented, as illustrated in the schematic (Figure 2.7) and the photograph (Figure 2.8). The binary stock solution, prepared in a 20 mL glass vial, contained oil (octanol or 2-ethyl hexanol) and ethanol in a specific ratio. This vial was placed on a magnetic stirrer, while a water reservoir was connected as an inlet to the vial. The outlet of the vial was linked to a quartz capillary tube (approximately 2 mm in thickness), which was further connected to a micro-peristaltic pump operating at a constant flow rate. The pump, a WMC model rated at 9–30V DC and capable of operating at 7600 rpm at 12V (controlled via a 2.5A DC motor electronic box), was used to drive the flow of the sample.

Once the pump was activated and set to an appropriate voltage to achieve optimal flow, water from the reservoir was gradually pumped into the stock solution vial. Inside the vial, the water mixed with the binary oil-ethanol solution under the agitation of the magnetic stirrer, resulting in a ternary mixture. This autodilution method allowed for continuous monitoring as the composition of the ternary mixture changed. The resulting

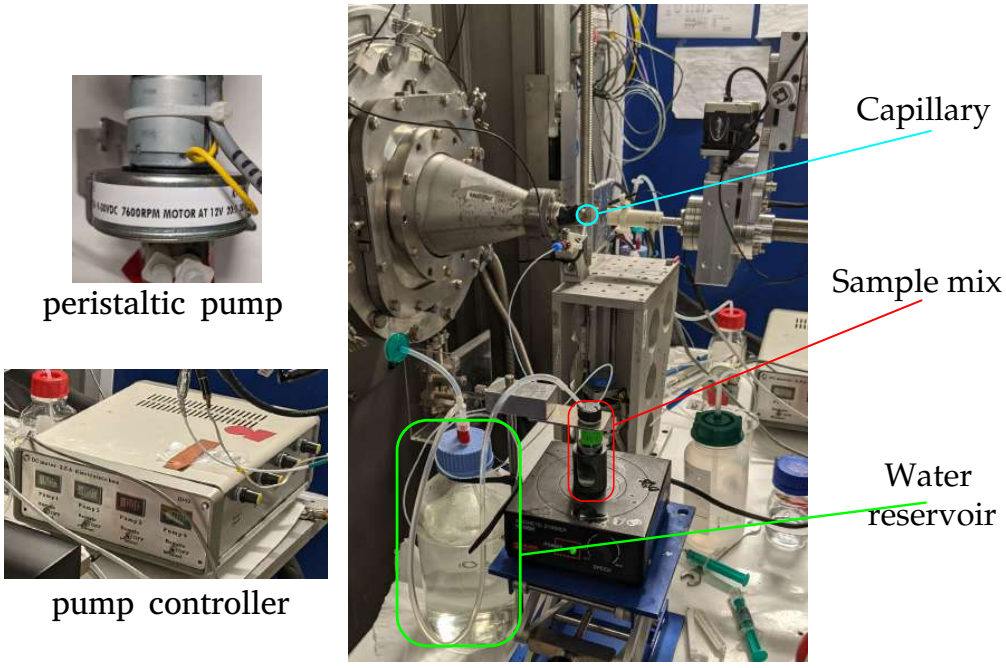

Figure 2.8: *Image of the auto-dilution experimental setup for in situ SAXS at ID02, ESRF, France. The X-ray beam passes through the capillary containing the flowing sample. The peristaltic pump and its controller are also shown.*

mixture was then passed through the quartz capillary, where X-ray photons interacted with the sample, providing *in situ* SAXS measurements. Finally, the mixture exited into a waste container.

This process continued until the entire ternary sample mix passed through the capillary, leaving only pure water flowing through the system, marking the end of the experiment for that particular oil-ethanol dilution line. A total of 20 such autodilution lines were selected, each corresponding to a different initial oil-to-ethanol ratio. The sample vial was then replaced with a new vial containing a binary mixture with a different oil-to-ethanol ratio, and the process was repeated.

2.2.5 Experimental Setup: Temperature Dependant SAXS

Temperature-dependent SAXS measurements were conducted using a Peltier sample cell (see figure 2.9-left) comprising a capillary housed within a frame, allowing the temperature to be controlled within a range of 5°C to 80°C. The cell's temperature was regulated using a Wavelength Electronics temperature controller (Model: LFI3751, see figure 2.9-right). The X-ray beam passed through the capillary tube, and the scattered radiation was detected by a detector positioned 1.5 meters from the sample. This configuration enabled the measurement of scattering data over a q-range from 0.1 to 10 nm^{-1}

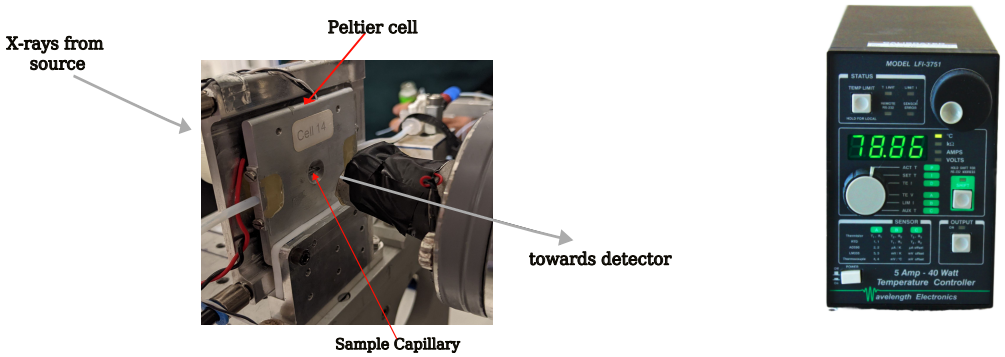

Figure 2.9: *(**Left**) Peltier cell used for temperature dependent SAXS experiment. (**Right**) Wavelength electronics LFI3751 temperature controller.*

2.3 Neutron Spin Echo

2.3.1 Principle of Neutron Spin Echo

Neutron Spin Echo (NSE) is a powerful technique used to investigate the dynamics of materials, particularly at very small energy transfers and long time scales. NSE measures the intermediate scattering function, operating in the time domain. It is particularly suited for studying quasielastic scattering, where the energy change due to sample interaction is close to elastic rather than purely inelastic. The NSE method relies on the principle of *Larmor precession* of neutrons in magnetic fields to encode and measure energy changes during neutron scattering.

Neutrons are particles with spin $S = \frac{1}{2}$ and a magnetic moment $\boldsymbol{\mu}$, which makes them behave like tiny classical magnetic dipoles. When neutrons enter a magnetic field $\mathbf{B}$ perpendicular to their magnetic moment, they undergo Larmor precession. The precession frequency, also known as the *Larmor frequency*, is given by:

$$\omega_L = \gamma B \tag{2.29}$$

where ω_L is the Larmor precession frequency, γ is the gyromagnetic ratio of the neutron ($\gamma = 2.916\,\mathrm{kHz/Oe}$), and B is the strength of the magnetic field. The gyromagnetic ratio relates the neutron's magnetic moment to its angular momentum, and the precession causes the neutron's spin orientation to rotate about the direction of the magnetic field.

Now consider a polarized neutron beam entering a magnetic field region B of length l. The total precession angle ϕ of the neutron spin depends on the neutron's velocity v and is given by:

$$\phi = \omega_L t = \frac{\gamma \mathbf{B} \mathbf{l}}{v} \tag{2.30}$$

Here, v represents the velocity of the neutron. This equation indicates that the pre-

cession angle depends on the magnetic field integral and the neutron's velocity. The velocity influences the amount of time the neutron spends in the magnetic field, which in turn affects the precession angle. If the neutron beam has a finite velocity distribution, the neutrons will accumulate different precession angles as they pass through the magnetic field, leading to an apparent depolarization of the neutron beam.

To recover the polarization in NSE, the neutron beam passes through a second magnetic field region (B_2) of length l_2. Before entering B_2, the neutron spins are flipped by 180°, and since the field direction in B_2 is the same as in B_1, this second field restores the polarization. The total precession angle after passing through both regions is:

$$\phi_{\text{total}} = \frac{\gamma B_1 l_1}{v_1} - \frac{\gamma B_2 l_2}{v_2} \tag{2.31}$$

In the case of elastic scattering, where the neutron velocity remains unchanged ($v_1 = v_2$), and if the magnetic field strengths and lengths satisfy $B_1 l_1 = B_2 l_2$, the precession angles cancel out:

$$\phi_{\text{total}} = 0 \tag{2.32}$$

Thus, the neutron beam regains its initial spin state, creating a *spin echo*. This recovery of polarization forms the foundation of the NSE technique.

If a neutron scatters with a small energy transfer $\hbar\omega$ between the B_1 and B_2 regions, the total precession angle becomes:

$$\phi_{\text{total}} = \frac{\gamma \hbar B l \omega}{m v^3} \tag{2.33}$$

where m is the mass of the neutron. Placing an analyzer after the second magnetic field region allows measurement of the angle ϕ between the neutron's polarization and the analyzer direction. The transmission probability of a neutron is proportional to $\cos\phi$ and the polarization (P), the average of this quantity, is related to $S(q,\omega)$ (the *dynamic structure factor* at momentum transfer q):

$$P = \langle \cos\phi \rangle = \langle \cos(\omega t) \rangle = \frac{\int \cos(\omega t) S(Q,\omega) d\omega}{\int S(Q,\omega) d\omega} \tag{2.34}$$

The Fourier transform of $S(q,\omega)$ gives the *intermediate scattering function* $S(q,t)$, which is directly measured in NSE:

$$S(q,t) = \int e^{-i\omega t} S(q,\omega)\, d\omega \tag{2.35}$$

Here, the time t is related to the neutron's wavelength λ by:

$$t = \frac{\phi}{\omega} = \frac{m^2 \gamma \int \mathbf{B}\cdot\mathbf{l}}{2\pi h^2} \lambda^3. \tag{2.36}$$

The resolution in time t increases rapidly with the neutron wavelength λ, as:

$$t \propto \lambda^3. \tag{2.37}$$

This strong dependence on λ allows NSE to achieve extremely high time resolution, making it an ideal tool for studying slow dynamics in materials. [138, 139]

The primary advantage of Neutron Spin Echo (NSE) lies in its ability to measure the intermediate scattering function $S(Q,t)$ directly in Fourier time, decoupling instrumental resolution from the measured signal. Unlike conventional neutron spectroscopy techniques that analyze $S(Q,\omega)$ in the energy domain—where the signal is convoluted with the resolution and requires complex deconvolution to extract meaningful results—NSE provides a direct measurement of the normalized intermediate scattering law $S(Q,t)/S(Q)$. While resolution effects are still present in NSE, the convolution in $S(Q,\omega)$ transforms into a simple multiplication in $S(Q,t)$, allowing it to be easily divided out. This Fourier time-based approach significantly improves energy resolution without being constrained by the energy distribution of incident neutrons, making NSE particularly well-suited for studying slow dynamics in soft matter, polymers, and complex fluids. The observed spin echo amplitude, $P_{\mathrm{NSE}}(Q,t)$, is corrected for instrumental resolution broadening through a simple and model-independent operation:

$$P'_{\mathrm{NSE}}(Q,t) = \frac{P_{\mathrm{NSE}}(Q,t)}{P_E(Q,t)}, \tag{2.38}$$

where $P_E(Q,t)$ is the experimentally measured resolution function.

In summary, an NSE experiment begins with neutron monochromatization and polarization, followed by controlled spin precession in a magnetic field. Spin flippers and precession coils manipulate neutron spins, encoding dynamical information about the sample (see Figure 2.10). Elastically scattered neutrons fully rephase, while quasielastically scattered ones do not. By detecting fully rephased neutrons, NSE provides high-resolution insights into microscopic dynamics. This direct approach, combining exceptional resolution with simplified analysis, minimizes interpretative bias and makes NSE particularly well-suited for studying slow dynamical processes in complex systems.

2.3.2 Spin-Flip Phenomenon and Its Impact on NSE

The difference in NSE measurements arises from the fact that, unlike most experimental setups where the sum of coherent and incoherent signals is measured, NSE specifically separates these contributions by measuring the coherent signal minus one-third of the incoherent signal.

Spin-incoherent scattering, a subset of incoherent scattering, arises from interactions with the random orientations of nuclear spins. This type of scattering flips the neutron spin with a probability of $\frac{2}{3}$, converting a significant portion of the scattered intensity into "non-polarized" background [139, 140]. The remaining $\frac{1}{3}$ contributes to the measurable signal but is associated with a factor of $-\frac{1}{3}$ in the cosine Fourier integral. This reduces the observable NSE signal and introduces a subtractive component to the coherent echo

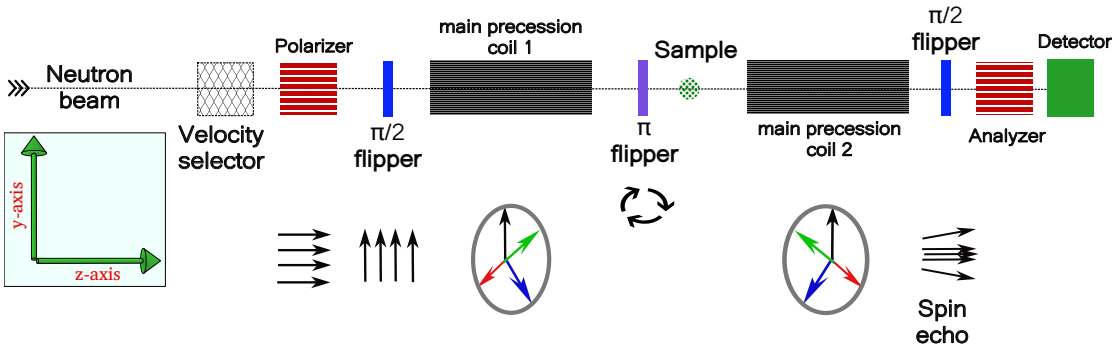

Figure 2.10: *A schematic representation of a typical Neutron Spin Echo (NSE) instrument, illustrating all major components. The instrument includes a velocity selector for monochromatizing the beam, a polarizer for aligning neutron spins, and a series of spin flippers ($\pi/2$ and π) to manipulate the neutron spin orientation. The precession coils generate strong magnetic fields that enable spin precession. The sample region, analyzer, and detector are also depicted.*

signal. The spin-flip (SF) and non-spin-flip (NSF) scattering intensities can be expressed as:

$$I_{\mathrm{NSF}} = I_{\mathrm{coh}} + I_{i-\mathrm{inc}} + \frac{1}{3} I_{s-\mathrm{inc}}, \tag{2.39}$$

$$I_{\mathrm{SF}} = \frac{2}{3} I_{s-\mathrm{inc}}. \tag{2.40}$$

The total intensity, I_{total}, and the separation of non-spin flip and spin flip contributions are given by:

$$I_{\mathrm{total}} = I_{\mathrm{coh}} + I_{i-\mathrm{inc}} + I_{s-\mathrm{inc}} = I_{\mathrm{NSF}} + I_{\mathrm{SF}}, \tag{2.41}$$

$$I_{\mathrm{coh}} + I_{i-\mathrm{inc}} = I_{\mathrm{NSF}} - \frac{1}{3} I_{\mathrm{SF}}, \tag{2.42}$$

$$I_{s-\mathrm{inc}} = \frac{3}{2} I_{\mathrm{SF}}. \tag{2.43}$$

where I_{NSF} is the non-spin-flip (NSF) intensity, I_{SF} is the spin-flip (SF) intensity, I_{coh} is the coherent scattering intensity, $I_{i-\mathrm{inc}}$ is the isotope-incoherent intensity, $I_{s-\mathrm{inc}}$ is the spin-incoherent intensity, and I_{total} is the total intensity.

The spin-flip process has significant implications for NSE measurements. Samples often exhibit both coherent and incoherent scattering, with the incoherent component becoming more prominent at higher momentum transfers (q). Hydrogen, in particular, has a larger incoherent scattering cross section compared to its coherent scattering and compared to other elements, making it a significant contributor to the incoherent scattering in samples. Despite the challenges posed by incoherent scattering, NSE remains effective in measuring coherent dynamics, particularly at low q, where the coherent contrast outweighs the incoherent background. Thus, while the spin-flip phenomenon introduces

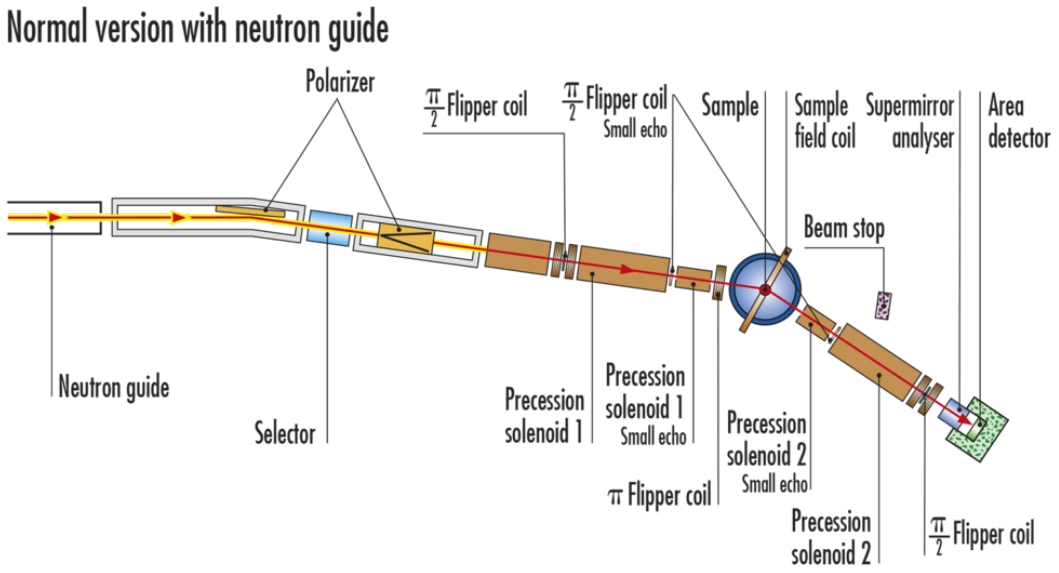

Figure 2.11: *Schematic diagram of the IN15 Neutron Spin Echo instrument at ILL ([142])*

challenges in separating coherent and incoherent contributions, it also underscores the precision and versatility of NSE in probing a wide range of materials, from structured systems to dynamically disordered ensembles [141].

2.3.3 NSE Instruments: IN15 and WASP

The **IN15** neutron spin-echo spectrometer at ILL is designed to study slow dynamics, covering relaxation times from 0.005 to 1000 ns and spatial scales from 1 to 500 Å. It utilizes long-wavelength neutrons (6 Å $< \lambda <$ 27 Å) to achieve high energy resolution and access small q values. This makes it suitable for investigating collective motions, polymer reptation, molecular diffusion in confined environments, and magnetic excitations.

The **WASP** (Wide Angle Spin-Echo) spectrometer extends the accessible q-range to 0.05 Å^{-1}–3.6 Å^{-1} and offers a higher signal rate. Its coil geometry, centered on the sample, generates a symmetrical field for all incoming and scattered neutrons, supporting large detector coverage (150° × 2.5°). WASP is suited for studying confined molecular motion, fast diffusion, and glassy dynamics within the timescale range of 0.6 ps to 18 ns, complementing the capabilities of IN15.

2.4 Pulse Field Gradient NMR

2.4.1 Nuclear Magnetic Resonance (NMR) Theory

Nuclear magnetic resonance (NMR) spectroscopy is based on the manipulation of nuclear spins in a magnetic field to probe molecular structure and dynamics. Initially, the net

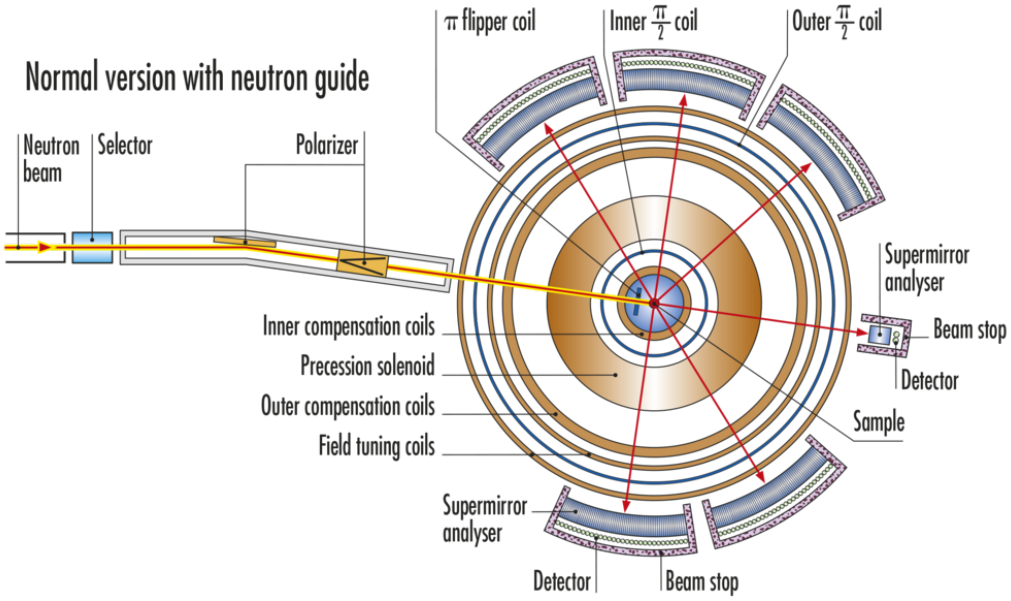

Figure 2.12: *Schematic diagram of the WASP Neutron Spin Echo instrument at ILL ([143])*

magnetization of the sample is aligned along the z-axis (parallel to the external magnetic field, B_0). When a 90° radio frequency (RF) pulse is applied, it tips the magnetization into the xy-plane. However, due to variations in the local magnetic field, such as chemical shift differences and inhomogeneities, the spins start to dephase, leading to a loss of coherence.

To refocus this dephasing and measure the relaxation times, the Hahn echo technique is used. A 180° RF pulse is applied at a time τ after the initial pulse, which inverts the phase of each spin. This inversion causes the spins to reconverge at a time 2τ, forming an echo. By analyzing the decay of the echo amplitude as a function of 2τ, the T_2 relaxation time—representing the decay of transverse magnetization due to spin-spin interactions—can be determined [144].

Additionally, NMR makes use of chemical shifts to probe molecular composition. These shifts arise due to the variation in the local magnetic field experienced by a nucleus as influenced by surrounding electrons. This variation alters the effective field at the nucleus and provides insights into the molecular structure [145–149].

2.4.2 Theory of Pulsed Field gradient NMR

Pulsed-field gradient (PFG) NMR is a powerful extension of traditional NMR spectroscopy, designed to probe molecular diffusion. Similar to neutron spin echo (NSE) experiments, the principle of spin manipulation is fundamental to PFG NMR. While NSE relies on neutrons traveling along a flight path where their spin precession evolves and is later rephased, PFG NMR induces dephasing using magnetic field gradients. After a specific delay, the spins are rephased, allowing for the recovery of the signal and

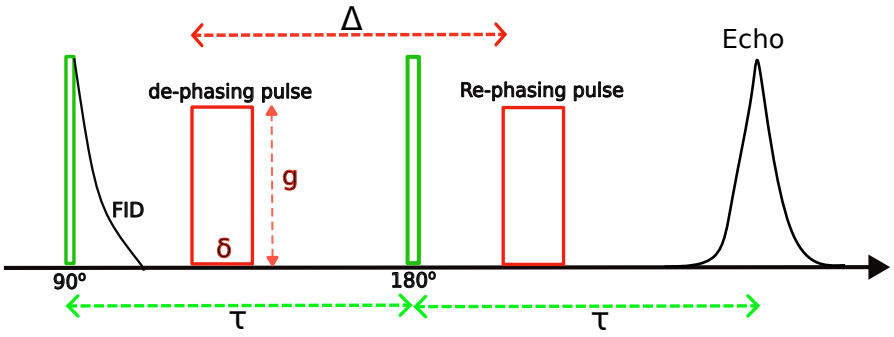

Figure 2.13: *Schematic of the PFG NMR experiment. Magnetic field gradient pulses (red) of duration δ and strength g are applied, with a diffusion time Δ between them. The 90° and 180° RF pulses (green) are separated by a time interval τ, and the spin echo occurs at 2τ. The dephasing gradient pulse is applied immediately after the 90° RF pulse, while the rephasing gradient pulse is applied after the 180° RF pulse.*

enabling molecular dynamics measurements.

In a typical PFG NMR experiment, a magnetic field gradient is applied along the static field B_0, which causes the spins to precess at different rates depending on their position. The relationship between the precession frequency and the spatial position of the spins is given by the Larmor frequency:

$$\omega = \gamma(B_0 + Gz) \tag{2.44}$$

where ω is the Larmor frequency, γ is the gyromagnetic ratio, B_0 is the static magnetic field, G is the gradient strength, and z is the spatial coordinate along the gradient direction. This spatial coordinate z encodes the position information of the spins, which is crucial for determining the diffusion properties of the sample. By manipulating this gradient, PFG NMR measures the rate at which the spins (and thus the molecules they represent) diffuse through the material.

The experiment involves two gradient pulses. The first gradient pulse causes dephasing, and spins at different positions within the sample precess at different rates. After a 180° RF pulse, a second rephasing gradient pulse is applied, which causes the spins to realign, effectively refocusing the magnetization. This process encodes spatial information in the NMR signal, allowing for the measurement of molecular diffusion.

The total spin echo attenuation signal, S, arising from all spins, is expressed as:

$$S = \exp\left(-q^2 t_{\text{eff}} D\right), \tag{2.45}$$

where $q = \gamma\delta G$, $t_{\text{eff}} = \Delta - \frac{\delta}{3}$ denotes the effective diffusion time, and D is the diffusion coefficient. Here, δ is the duration of the gradient pulse application, while Δ corresponds to the time delay between the two pulses during which diffusion occurs.

In comparison to NSE, PFG NMR operates at much lower wave vectors (q), making it more suitable for probing larger length scales and slower diffusion processes. This capability allows PFG NMR to effectively measure self-diffusion at the micrometer and

millisecond scale, whereas NSE is more sensitive to collective diffusion at shorter length scales, probing faster dynamics.

This technique has widespread applications across fields such as polymer science, biology, materials science, and food science, offering valuable insights into molecular dynamics, transport properties, and structural characteristics [150, 151].

Further, to enhance spectral resolution and suppress solvent interference, deuterated compounds (e.g., D_2O, $CDCl_3$) are often used in NMR. Since ^2H has a distinct Larmor frequency compared to ^1H, its substitution minimizes unwanted background signals, allowing better isolation of target molecular dynamics.

2.4.3 Experimental Setup: PFG NMR

We conducted NMR experiments for the octanol-ethanol-water and 2-ethyl hexanol-ethanol-water ternary at $25°C$. The experiment was performed using a Bruker Minispec mq20, which was equipped with a pulsed gradient unit capable of generating gradients up to 4 T/m. A standard Hahn Echo sequence was utilized, with a delay time (Δ) of 7.5 ms between the 90° and 180° pulses, and a gradient pulse length (δ) of 0.6 ms. The relationship between echo amplitudes and the field gradient can be described by a single exponential function:

$$y = a \cdot \exp\left(-D \cdot q\left(\Delta - \frac{\delta}{3}\right)\right) \tag{2.46}$$

where a is the amplitude, $q = (\gamma\delta G)^2$, with $\gamma = 26.7 \times 10^7$ rad/T/s, and G ranging from 0 to 3.2 T/m. D is the diffusion coefficient. Further details on the use of deuterated components to isolate the signal of individual species, as well as the calculation procedure, are provided in Appendix A.4.

2.5 Experimental Setup: Rheology

Viscosity measurements were performed using a rheometer (Anton Paar, Physica MCR 301) equipped with a Couette or concentric cylinder geometry, featuring inner and outer radii of 23.82 mm and 24.65 mm, respectively. The samples used were Newtonian liquids, and the rheometer's stage temperature was maintained at 298 K using a Peltier temperature control system. The variable shear-rate method was employed, where the shear rate was logarithmically increased from 10 s^{-1} to 200 s^{-1} across 20 measurement points, each lasting 20 seconds. The resulting shear rate vs. viscosity curve was analyzed to determine the average viscosity. A schematic representation of the viscosity behavior for Newtonian and non-Newtonian fluids is shown in Figure 2.14.

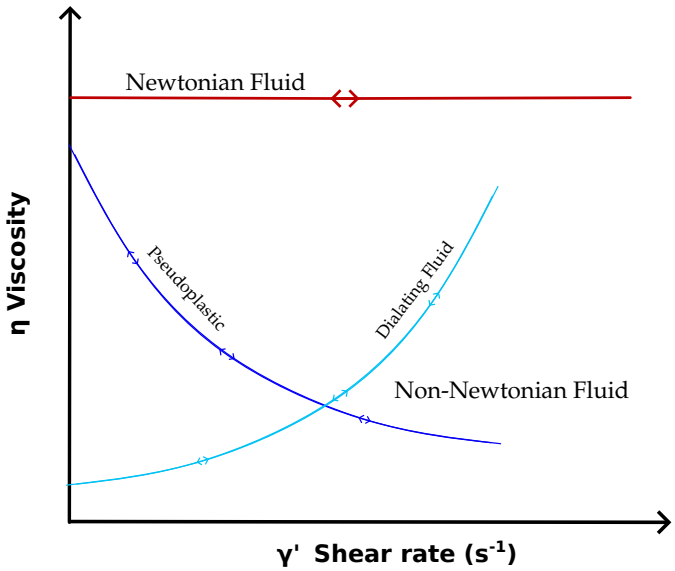

Figure 2.14: *Viscosity vs shear rate for Newtonian and non-Newtonian fluids. For Newtonian fluids (e.g., water), viscosity remains constant with shear rate, while non-Newtonian fluids, such as pseudoplastics (e.g., paint, emulsions) and dilatant fluids (e.g., clay sludge, corn starch in water), show shear-rate dependent viscosity—decreasing for pseudoplastics and increasing for dilatants.*

2.6 Sample Preparation

SAXS Autodilution: Octanol and 2-ethyl hexanol, both purchased from Sigma Aldrich, had densities of 0.827 g/mL and 0.833 g/mL at 25°C, respectively. Ethanol, acting as a hydrotrope, was also obtained from Sigma Aldrich. The experiments utilized Milli-Q water with a resistivity of 18.2 MΩ·cm. A total of 40 samples were prepared as initial binary mixtures: 20 containing octanol and 20 containing 2-ethyl hexanol. These mixtures were stored in 20 mL glass vials, referred to as stock solutions, each consisting of oil (either octanol or 2-ethyl hexanol) and ethanol in varying proportions, starting from 5% oil and 95% ethanol, with incremental steps up to 95% oil and 5% ethanol.

NMR and Viscosity: Samples of the octanol-ethanol-water ternary system were prepared by weighing the components and mixing them thoroughly. Octanol, sourced from Sigma Aldrich, had a density of 0.827 g/mL at 25°C. Ethanol, used as a hydrotrope, was also obtained from Sigma Aldrich. The water used in these experiments was Milli-Q water, with a resistivity of 18.2 MΩ·cm. The corresponding deuterated compounds were used as received.

NSE: Samples of octanol and 2-ethyl hexanol ternary systems were prepared by simple mixing. The 2-ethyl hexanol (Sigma Aldrich) had a density of 0.833 g/mL at 25°C. For the ethyl acetate+sodium salicylate+water system, hydrogenated compounds were used as received. While ethyl acetate-D8 is commercially available, deuterated sodium salicylate was synthesized in-house using hydrogenated salicylic acid and NaOD.

Chapter 3

Investigation of SFME Ternary Using Autodilution *In-Situ* SAXS

3.1 Introduction

This study aimed to investigate key structural parameters within octanol-based and 2-ethyl hexanol (EH)-based ternary systems, focusing on three primary objectives: (a) understanding the overall structural transitions as the system shifts from a low-water regime to a high-water regime, (b) exploring the presence of pre-Ouzo structures, which represent intermediate mesoscale organizations, and (c) identifying and mapping the trajectory of the Lifshitz line, which marks the boundary between different pseudo-phases. To achieve these goals, an *in situ* Small-Angle X-ray Scattering (SAXS) experiment was performed using the ID02 beamline at the European Synchrotron Radiation Facility (ESRF). The experiment, conducted over three days, involved twenty dilution lines for each of octanol and 2-ethyl hexanol based ternary (Figure 3.1). Each line began with different oil-to-hydrotrope ratios, allowing for a thorough mapping of the ternary phase diagram and an in-depth analysis of the structural transitions within these systems.

Furthermore, the composition corresponding to each individual SAXS scan was determined using transmission values directly obtained from the experiment. This approach simplified the in situ measurement setup, eliminating the need for separate real-time calculations of the volumes of added components, as the transmission values were inherently recorded alongside the scattering data (as detailed in Appendix A.1.2).

3.1.1 Pre-peak and Mean-Peak: Characteristics of Alcohol Scattering Curves

The scattering curves of pure alcohols, like octanol or ethanol (see Figure 3.2), exhibit a distinct feature: a *mean-peak* centered around $q = 10\text{–}15\,\mathrm{nm}^{-1}$. This peak, studied through diffraction methods [152], has a characteristic bell shape. In case of bulk alcohol, the mean-peak is the center of mass distance between the molecules.

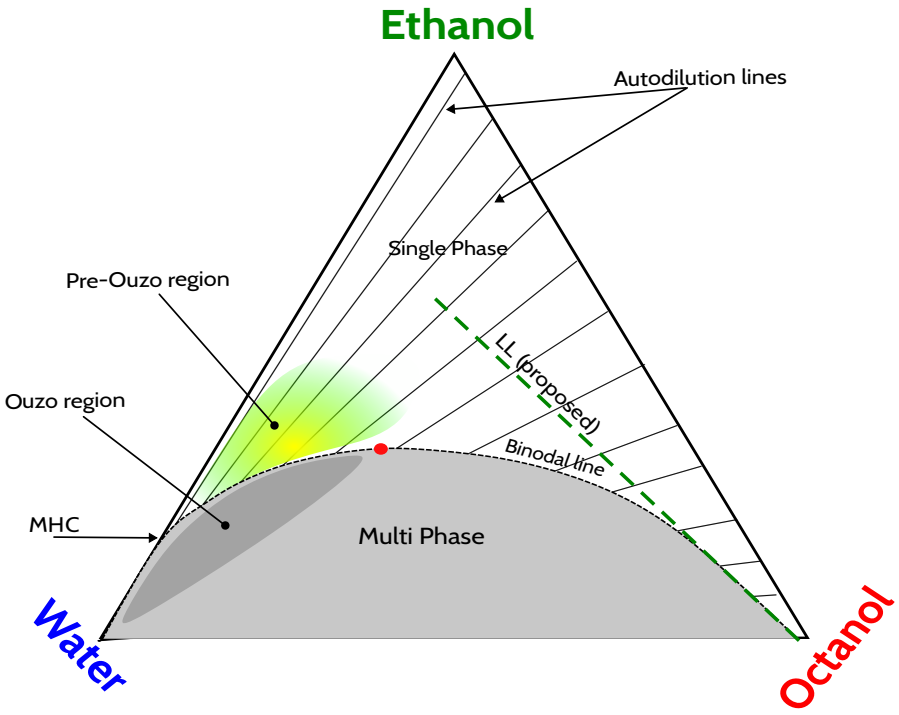

Figure 3.1: *Sketch of a ternary phase diagram showing the critical point (red dot) on the binodal line, which separates the biphasic and monophasic regions, with the Ouzo and pre-Ouzo regions nearby. The Lifshitz line (green dashed) marks the transition between ordered and disordered states. Autodilution lines (gray), along which in-situ SAXS experiments were conducted, extend from the octanol-ethanol edge toward the water vertex.*

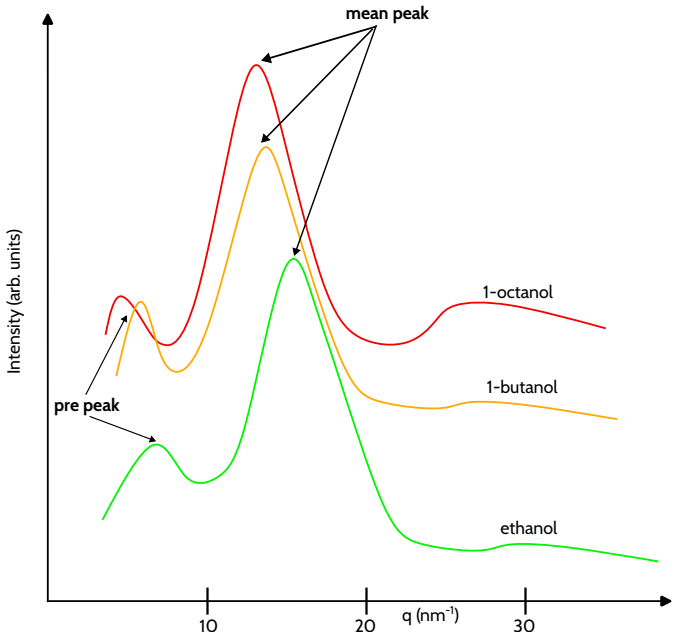

Figure 3.2: *Scattering curves of pure alcohols (octanol, butanol, and ethanol) highlighting the mean-peak and pre-peak features.* (Adapted from Ref. [152])

In addition to the mean-peak, a *pre-peak* (often referred to as a *broad-peak*) is observed in the range of q = 4–8 nm^{-1}. This feature arises due to pair correlations between hydroxyl groups separated by the aliphatic chains [152, 153]. Such peaks are consistently present not only in pure or bulk alcohols but also in mixtures of alcohol and water. The pre-peak specifically stems from hydrogen bonding interactions between the alcohol molecules, leading to the formation of a shell-like structure where water occupies the core of the alcohol-based assembly. As these systems are further diluted, these 'reverse' structure undergoes swelling due to the incorporation of additional water into the polar domains [92, 109].

The q range in our experiments extends up to 10 nm^{-1}, which leads to some residual influence from the mean peak (located at a higher q than our current window). In our case, the *broad peak* (BP) sometimes appears on the tail shoulder of the mean peak, making the fitting process more challenging. To mitigate this, we trimmed the data to focus exclusively on the key features associated with the pre-Ouzo aggregates and the BP. Additionally, these peaks can be effectively described using a simple Lorentzian function:

$$I = \frac{I_{BP}}{1 + ((q - q_{BP})^2 \cdot \xi_{BP}^2)} \tag{3.1}$$

where I_{BP} is the intensity of the pre-peak, q_{BP} is the corresponding q value for the peak, and ξ_{BP} is related to the peak width.

3.1.2 Ornstein-Zernike function

The Ornstein-Zernike (OZ) function is a fundamental concept in statistical mechanics that characterizes particle interactions in fluids. The OZ equation establishes a relationship between two key correlation functions: the direct correlation function, which is short-ranged, and the total correlation function, which captures long-range interactions. These functions play a crucial role in determining various experimental properties, including partial molar volume, excess Helmholtz free energy, chemical potential, isothermal compressibility, pressure, and the structure factor [154, 155].

In the context of SAS data, the Ornstein-Zernike term is often applied to describe composition fluctuations within a system, offering information about the size of pseudo-phase domains. Mesoscale aggregation within the system leads to an increase in scattering intensity at specific q-values, which can be described using a Lorentzian function derived from the OZ term. This Lorentzian is centered at $q = 0$. Such a peak at low q-values is indicative of structural correlations arising from mesoscale organizations like pre-Ouzo aggregates, expressed mathematically as:

$$I = \frac{I_{OZ}}{1 + (q \cdot \xi_{OZ})^2} \tag{3.2}$$

where I_{OZ} represents the scattering intensity at $q = 0$, q is the scattering vector, and ξ_{OZ} is the correlation length that quantifies the extent of structural correlations.

The characteristic length parameter ξ_{OZ} can be further simplified to estimate the cluster size, as derived by Schottl et al. [93]. Interpreting ξ as the diameter D of an equivalent sphere, the OZ function can be expanded as:

$$I_{OZ_0}\left(1 - q^2\xi^2 + \dots\right) \tag{3.3}$$

and compared with the Guinier approximation of the McLaurin series:

$$I(0)\left(1 - q^2 R_G^2/3 + \dots\right) \tag{3.4}$$

This leads to the relation:

$$\xi_{OZ} = \frac{R_G}{\sqrt{3}} \tag{3.5}$$

For a homogeneous sphere, where $R = \sqrt{\frac{5}{3}}R_G$, we get the diameter:

$$D \approx 4.5\xi_{OZ} \tag{3.6}$$

Thus, for the pre-Ouzo clusters, the size of the domains is of the order of $4\xi_{OZ}$, and the volume is proportional to:

$$V \sim \frac{4}{3}\pi\left(\frac{D}{2}\right)^3 \sim 33\xi_{OZ}^3 \tag{3.7}$$

3.2 Result and Discussion

3.2.1 Preliminary Interpretation of Reduced Scattering Curve

Among the various autodilution lines analyzed, Figure 3.3-Top displays a single sample point from two distinct autodilution lines. The blue line in the phase triangle, starting from a 80% ethanol to 20% octanol ratio (by weight), gradually enters the pre-Ouzo region with dilution. The corresponding reduced scattering curve (Figure 3.3-Bottom Left) from SAXS, taken at point A on the blue line within the pre-Ouzo region, exhibits the characteristic Ornstein-Zernike (OZ) feature at lower q values ($\sim 0.1\,\mathrm{nm}^{-1}$).

Similarly, the scattering curve corresponding to point B on the red dilution line (with an initial octanol-to-ethanol ratio of 35:65) (Figure 3.3-Bottom Right) prominently displays a pre-peak (or broad peak, as explained in the previous section). These pre-peaks appear at relatively higher q values ($\sim 3 - 4\,\mathrm{nm}^{-1}$) compared to the OZ feature.

In contrast, Figure 3.4 presents reduced scattering curves for three distinct points along the same dilution line, highlighting the progression of I-q behavior as the system undergoes continuous dilution. The experiment begins with a binary mixture of 25% octanol and 75% ethanol by weight. As water is added, the initial scattering curve

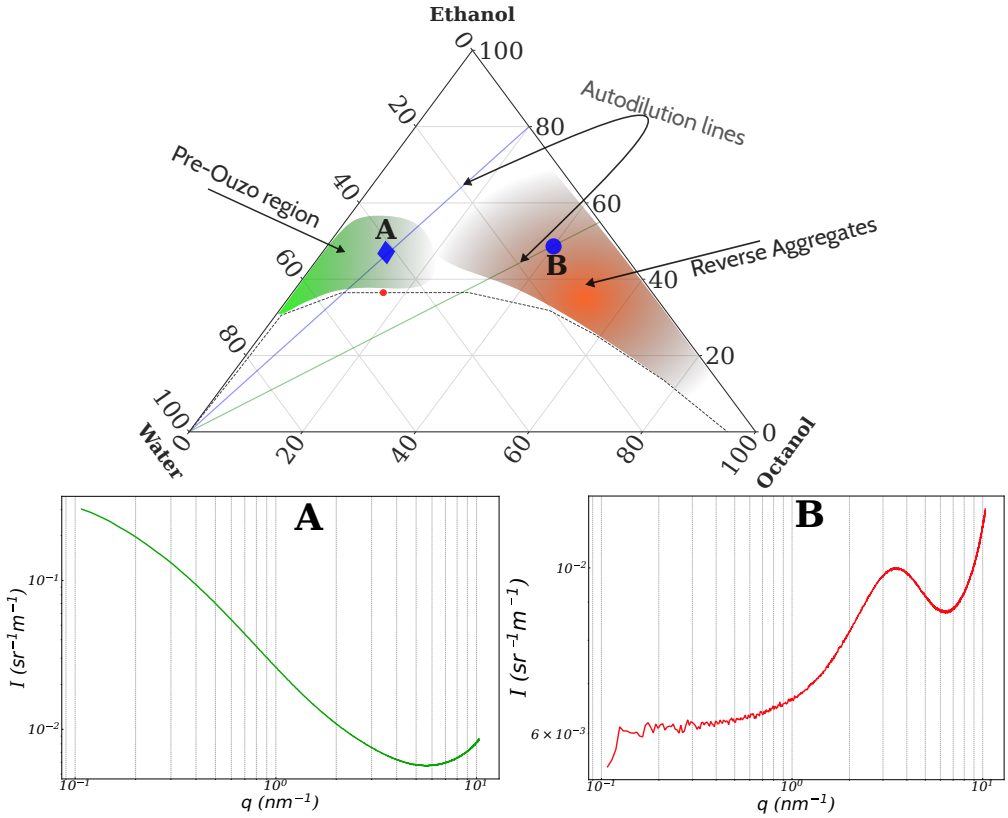

Figure 3.3: *(**Top**) The octanol-ethanol-water phase triangle illustrates the pre-Ouzo region and the zone where reverse aggregates are formed. The critical point is marked (red dot) on the binodal line (from [156]). Two sample points: sample point A (blue diamond), located on the 20:80 octanol:ethanol dilution line within the pre-Ouzo region, and sample point B (blue circle), situated on the 35:65 dilution line in the reverse aggregate region. (**Bottom**) Scattering curves corresponding to the two points on the ternary phase diagram. **Left**: The scattering curve for the sample A (pre-Ouzo region) shows high intensity at lower q values, indicating pre-Ouzo aggregation. **Right**: The scattering curve for sample B (reverse aggregate region) features a peak at higher q values, reflecting oil-hydrotrope clusters in the form of reverse aggregates.*

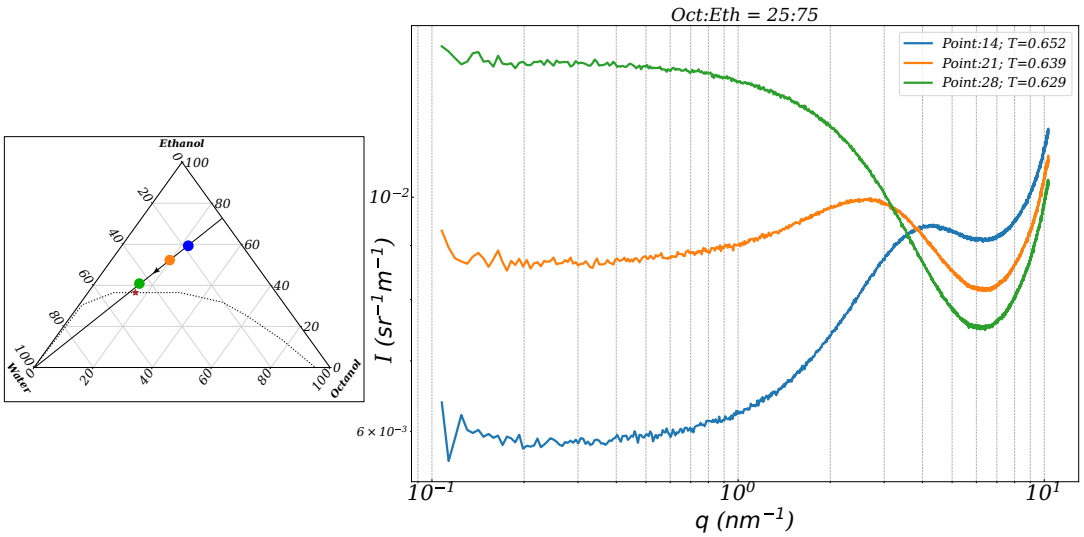

Figure 3.4: *I vs. q curve for three points along the 25:75 octanol-to-ethanol ratio line. The inset displays the ternary plot highlighting these points on the 25:75 autodilution line. The green curve shows pre-Ouzo structuration at low q, which is absent in the blue and orange curves. The blue curve features a broad pre-peak near* $4\,nm^{-1}$*. The legend provides the point number on the dilution line and the corresponding transmission coefficient (T).*

(blue) shows a pre-peak at higher q ($\sim 4\,\mathrm{nm}^{-1}$), indicating octanol-ethanol hydroxyl interactions that form inverse structures with water molecules interspersed.

As dilution continues, indicated by the orange curve, the intensity at higher q decreases while the intensity at lower q rises slightly, leading to an overall flatter curve. This change results from the increase in distance of the inverse aggregates as more water becomes incorporated within them, leading to a shift of the pre-peak to lower q values.

With further dilution, the system enters the pre-Ouzo region, where the scattering curves start to resemble the green line. This curve exhibits a notable increase in intensity at lower q values ($\sim 0.1\,\mathrm{nm}^{-1}$), signaling the formation of pre-Ouzo aggregates. These aggregates emerge as the inverse structures disintegrate, resulting in oil droplets dispersed within a continuous water phase, with hydrotrope present in both major phases. The pre-Ouzo droplets, encased by a loosely defined hydrotrope interface (ethanol in this case), typically measure a few nanometers in size ($\sim 2-4\,\mathrm{nm}$).

3.2.2 Structural Insights from Data Fitting

Based on the model proposed by Prevost et al. [120], each data point was fitted using a combination of appropriate functions derived from the four-term function (Eq. 3.8), which can be classified into I_{bkg} (Background intensity), OZ (Ornstein-Zernike), BP (Broad-peak or pre-peak), and Porod ($\mathrm{I} \propto q^{-4}$) terms (Eq. 3.9).

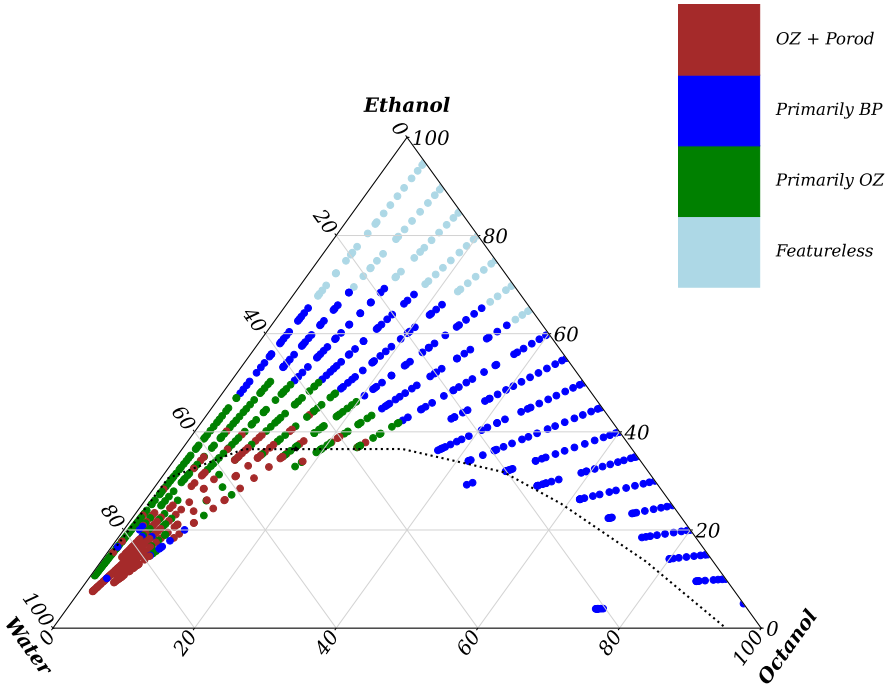

Figure 3.5: *Ternary phase diagram showing points corresponding to data acquired for different sample compositions, in terms of mass fraction, from the in situ SAXS autodilution experiment. Points are color-coded by fit type:* ***light blue*** *for no distinct features,* ***green*** *for OZ features (pre-Ouzo aggregates),* ***blue*** *for pre-peak features (oil structuration), and* ***brown*** *for a mix of OZ and Porod, typically in water-rich regions where larger structures form (details in Appendix A.1.3).*

$$I = I_{\text{bkg}} + \frac{I_{\text{OZ}}}{1 + (q\xi_{OZ})^2} + \frac{I_{\text{BP}}}{1 + [(q - q_{\text{BP}})\xi_{\text{BP}}]^2} + \alpha q^{-4} \tag{3.8}$$

$$I = I_{\text{bkg}} + \text{OZ} + \text{BP} + \text{Porod} \tag{3.9}$$

After the initial fit was completed, the data points were categorized into specific types to facilitate understanding of the overall features in the ternary system. This classification was based on certain criteria: for instance, if the signal contribution from OZ at q_{BP} exceeds the intensity of BP, the point is designated as an OZ point; otherwise, it is assigned as a BP point (further details in Appendix A.1.3). This classification process resulted in Figure 3.5. This figure provides a concise representation of the ternary phase diagram of *octanol-based* system, categorizing it into distinct regions, which are described as follows:

1. **Featureless (within the q-range):** Within the examined data range, certain initial points on the ternary phase diagram exhibit no distinct features or structures that could be associated with a pre-peak Lorentzian or an OZ function. During

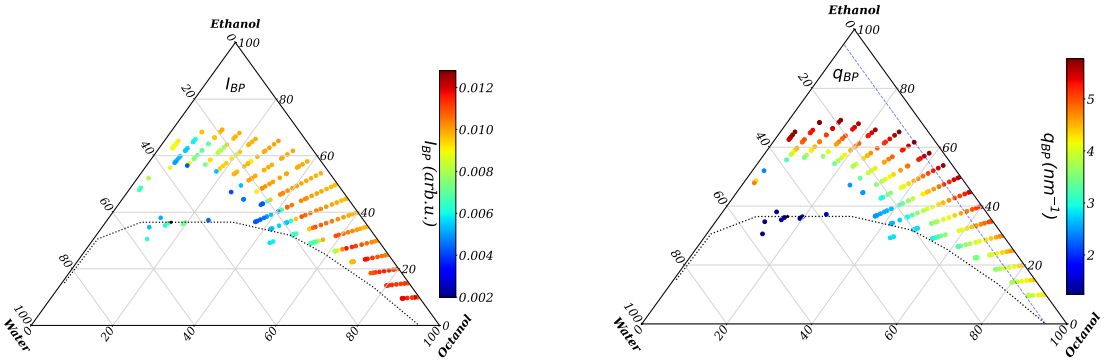

Figure 3.6: *Ternary phase diagram showing the fit parameters related to the pre-peak:* ***(Left)*** *I_{BP}: Intensity of the pre-peak* ***(Right)*** *q_{BP}: Parameter related to peak position. The dashed blue line acts as a guide for the eye to mark the line of constant water concentration, along which the pre-peak position shifts to a lower q with increasing octanol content.*

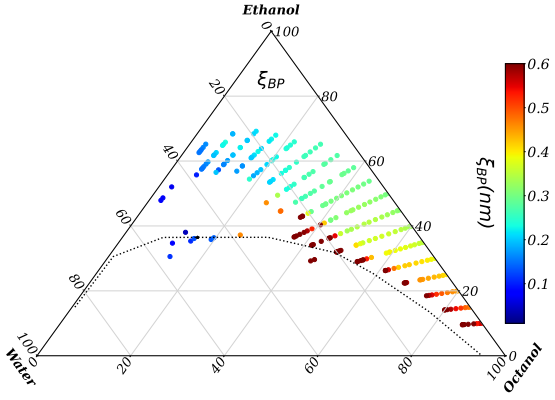

Figure 3.7: *Ternary phase diagram with points indicating ξ_{BP}, a parameter associated with the width of the pre-peak. A larger ξ_{BP} corresponds to a sharper peak.*

the data fitting process, these points are modeled using the fit function: (BP + I_{bkg}), which combines a pre-peak term with a background. However, the pre-peak position for these points falls outside the q-range of our analysis and is therefore referred to as featureless, based solely on the limitations of our q-window.

2. **BP (pre-peak or broad-peak):** In the lower water content region, most of the points display a *pre-peak* in the scattering curve. This pre-peak is characterized by a Lorentzian with q_{BP} representing the peak position and ξ_{BP} representing the peak sharpness, indicating the presence of octanol-ethanol clusters swollen by water molecules.

   In Figure 3.6 (Right), where q_{BP} represents the spacing between these structures in inverse space (nm^{-1}), we observe two key trends. First, along a constant water line, the value of q_{BP} decreases with increasing octanol. This indicates that the size of the oil-ethanol cluster increases as more oil is added. In contrast, higher ethanol

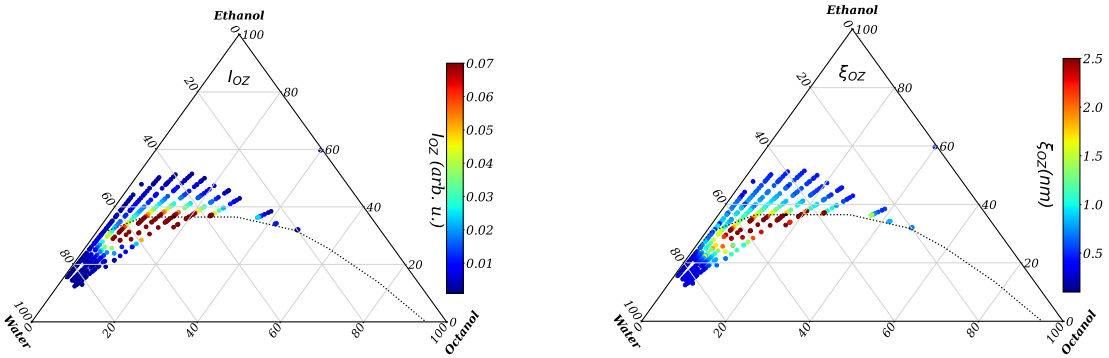

Figure 3.8: *Ternary phase diagram showing the fit parameters related to pre-Ouzo droplets:* ***(Left)*** *I_{OZ}: Intensity of Ornstein-Zernike term* ***(Right)*** *ξ_{OZ}: Length scale of the pre-Ouzo aggregates (in nm)*

content enhances the solubility and results in smaller and fewer well-defined reverse aggregates. This manifests as a decrease in ξ_{BP} (Figure 3.7).

Additionally, for a constant octanol-ethanol ratio, as the water content increases, the spacing between the aggregates also increases due to the additional water now residing in the core. This swelling of the aggregate results in them occupying more space, causing the centers of the cores to move farther apart. Due to the contrast difference between the hydroxyl group and alkyl part, when the water-rich center moves apart it manifests as the position of the *pre-peak* shifting to lower q [157].

3. **OZ (Ornstein-Zernike):** Figure 3.8 illustrates the points on the ternary phase diagram where the scattering curves are modeled by a Lorentzian function, specifically the OZ term, centered at $q = 0$. These points predominantly correspond to the formation of pre-Ouzo structures, which emerge near the critical point.

   Pre-Ouzo droplets are thermodynamically stable microemulsions, typically a few nanometers in size. As the system approaches the biphasic region within the pre-Ouzo domain, the size of these droplets (represented by ξ_{OZ} in Figure 3.8- Right) continues to grow (upto $\sim 2.5 - 4\,\mathrm{nm}$). However, after a certain point (at the binodal line), there is a gradual reduction in droplet size. This decrease occurs when some pre-Ouzo droplets, which had been expanding due to the addition of water, exceed a thermodynamic threshold and transition into much larger Ouzo emulsions. This transformation is not captured by the OZ term but is instead characterized by a q^{-4} Porod relaxation term at relatively lower q values, leading to a reduction in the intensity of the OZ term.

   As shown in Figure 3.8 (Left), the intensity of the OZ term increases as the system approaches the critical point. Pre-Ouzo droplets extend beyond the binodal line into the biphasic region, indicating a coexistence of pre-Ouzo microemulsions and Ouzo emulsions [120]. Notably, a pre-Ouzo signature persists well within the biphasic region, suggesting that while some droplets coalesce into larger Ouzo

emulsions, others remain, gradually merging as dilution progresses to form increasingly structured Ouzo droplets.

4. **Porod Region (αq^{-4}):** For certain points on the phase diagram, the I vs. q scattering curve exhibits a q^{-4} dependence, indicative of Porod scattering due to the large interface of the Ouzo emulsions. This function is most relevant in the biphasic region, where Ouzo droplets are present. Although these droplets are not always the dominant feature in the I vs q curve within our available q-range due to the lack of lower q values, their presence becomes evident once the binodal line is crossed.

Maxima of I_{OZ} and Phase Separation

In the octanol-based ternary system, a distinct characteristic is observed in the intensity of the OZ Lorentzian term across multiple dilution lines. By analyzing the curves of I_{OZ} as a function of water mass fraction along individual dilution lines—where each point represents a specific sample composition with a fixed octanol-to-ethanol ratio—a consistent maximum value of this parameter is noted. This behavior is similar to the findings of Prevost et al. [120] in their study of the 5:95 octanol:ethanol dilution line. For example, Figure 3.9 (Left) illustrates two dilution lines (for example) with initial octanol-to-ethanol ratios of 20:80 and 40:60, respectively. In these cases, I_{OZ} increases until it peaks at 56.57% and 38.28% water (by mass), respectively. This maximum represents a key point on the ternary phase diagram, appearing along autodilution lines where the oil concentration is relatively low.

These maxima indicate a phase transition in the ternary system, shifting from a single homogeneous phase to a biphasic state characterized by turbidity and non-homogeneity. This can be intuitively understood: the decrease in OZ intensity suggests that pre-Ouzo aggregates are disintegrating and forming a new structure—larger Ouzo emulsions. As previously discussed, these larger Ouzo droplets are not modeled by the q^{-2} relation of the OZ term, leading to a reduction in OZ intensity after the phase transition. The peak in I_{OZ} serves as a clear marker of this transition, and when plotted on the ternary phase diagram, these points align with the binodal line (see Figure 3.9, right).

Jump in I_{BP} and the Lifshitz line

In Figure 3.10 (Left), the fit parameter I_{BP}, which represents the intensity of the *pre-peak*, is plotted against the mass fraction of water in the ternary system for two distinct dilution lines, each with a fixed octanol-to-ethanol ratio. This figure shows that, at a certain stage of dilution, the octanol-based ternary system undergoes a sudden drop in pre-peak intensity (I_{BP}). This decrease occurs at different points depending on the dilution line. The simplest explanation for this behavior is a structural reorganization within the ternary system, transitioning from a pre-peak-dominated arrangement to a different structural form. When these drop points are mapped onto the ternary phase

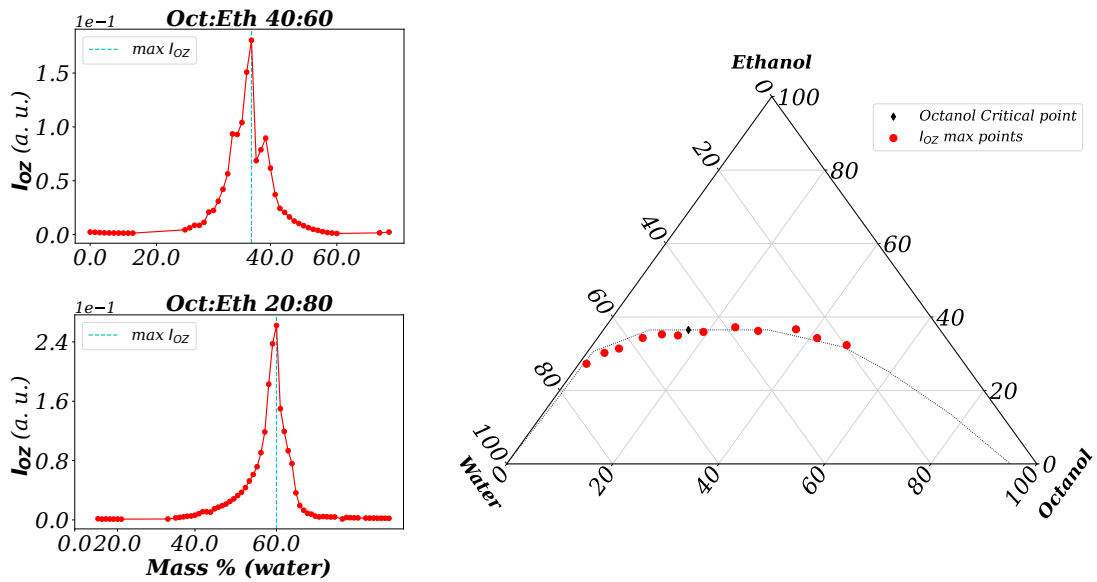

Figure 3.9: ***(Left)*** *OZ intensity plotted against the water mass fraction for two dilution lines, with initial octanol-to-ethanol ratio of 20:80 and 40:60, respectively.* ***(Right)*** *The red dots represent all the maxima of OZ plotted on the ternary phase diagram, tracing the binodal line. These points, known as phase separation points, signify a transition from a macroscopically homogeneous phase to a non-homogeneous phase.*

diagram, they form a line that closely resembles the proposed Lifshitz line (see Figure 3.10 Right) and thus we refer to it here as the "experimental LL".

In previous work by Prevost et al. [120], a Lifshitz line was proposed, marking the onset of pre-Ouzo aggregate formation as the octanol-ethanol binary is diluted. From the perspective of scattering curves and fitting models, this Lifshitz line represents the point beyond which the characteristic pre-peak pattern is no longer the only observed feature. At this stage, other patterns, such as the Ornstein-Zernike behavior, begin to appear in the SAXS data as the system approaches the pre-Ouzo domain. However, the experimental Lifshitz line does not align perfectly with the proposed one; instead, it exhibits a slight curvature in regions with lower octanol concentrations and higher ethanol content.

In this octanol-based ternary system, the Lifshitz line can be divided into two parts. In the lower region of the phase triangle, where the hydrotrope concentration is low and the binodal coincides with the LL, the system transitions during dilution from a state of structured inverse aggregates (water-in-oil) to a phase-separated state upon crossing the binodal. Beyond this point, phase separation occurs as the system moves toward a thermodynamically favorable state, minimizing free energy by forming coexisting macroscopic phases. Meanwhile, in the upper region, where the hydrotrope concentration is higher, the Lifshitz line marks the transition point indicating the onset of an organizational shift as the system undergoes dilution. Overall, this leads to defining the Lifshitz

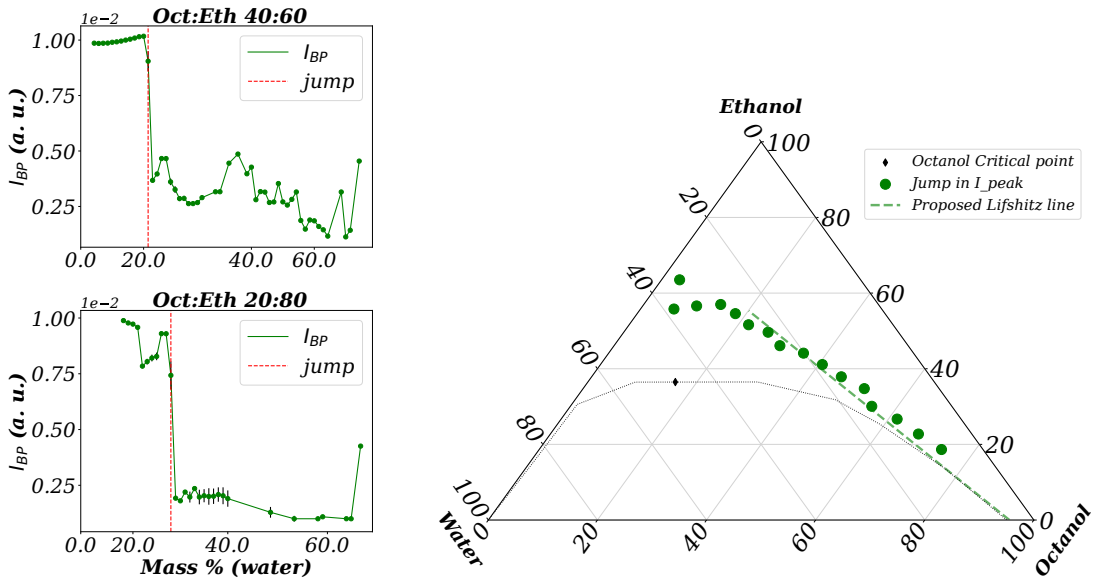

Figure 3.10: ***(Left)*** *Variation of the intensity of the pre-peak as a function of water mass fraction for two auto-dilution lines, with initial octanol-to-ethanol ratios of 20:80 and 40:60, respectively. These figures show a jump in I_{BP} as the system is diluted.* ***(Right)*** *Mapping these jumps onto the ternary phase diagram approximately retraces the Lifshitz line suggested by Prevost et al. [120], with a slight curvature at lower octanol concentrations in this experimental Lifshitz line.*

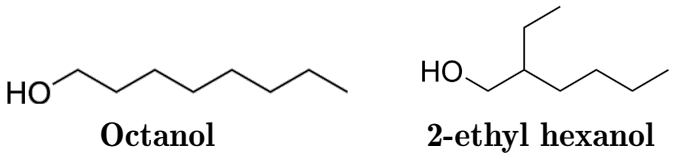

Figure 3.11: *Octanol and 2-ethyl hexanol*

line in this context as the transition point where the system shifts from one ordered phase to another ordered phase.

3.2.3 2-Ethyl Hexanol Substitution

The next phase of the experimental study involved substituting octanol with 2-ethyl hexanol in the ternary system. Octanol, due to its linear structure, forms worm-like aggregates in bulk through hydrogen bonding. When water is introduced, these molecules initially arrange themselves into a prolate ellipsoid core, which becomes more spherical as dilution progresses [157]. In contrast, 2-ethyl hexanol, with its branched structure (Figure 3.11), behaves differently in bulk, as the branching prevents the formation of extended structures typically seen with linear molecules. This structural difference is further reflected in their solubilization capacities, as evidenced by the binodal lines for their respective ternary systems at 25°C (see Figure 3.12). Octanol has a smaller bipha-

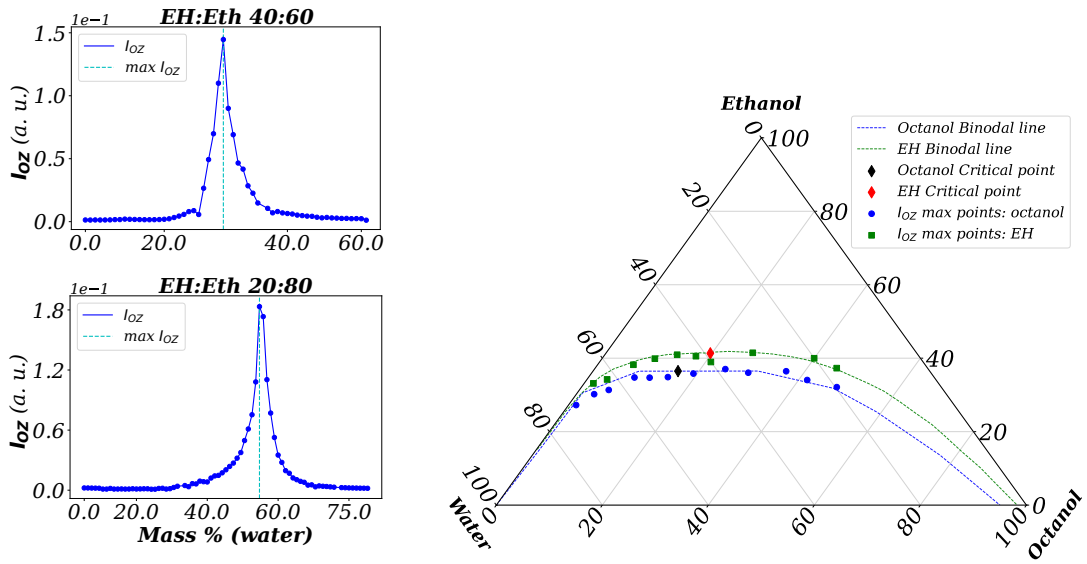

Figure 3.12: ***(Left)*** *OZ intensity as a function of water mass fraction for two dilution lines, starting with EH-to-ethanol ratios of 20:80 and 40:60.* ***(Right)*** *Binodal lines for octanol- and 2-ethylhexanol-based ternary systems at 25°C. The phase separation points, marked by the maxima of OZ intensity, are shown along the binodal line for both ternary system (green square for EH and blue dots for octanol).*

sic region, suggesting its capacity to incorporate higher amounts of water into stable arrangements before phase separation occurs. In contrast, 2-ethylhexanol exhibits a larger biphasic region.

Qualitatively, the trend of the **Ornstein-Zernike** (OZ) features associated with pre-Ouzo aggregates is similar in both systems along any dilution line. The intensity of the OZ term increases with dilution, reaching a maximum near the binodal line as the system approaches the pre-Ouzo region, after which I_{OZ} decreases. When mapping the maxima of I_{OZ} for different dilution lines over the phase triangle, the pattern for 2-ethyl hexanol retraces the binodal line, similar to the behavior observed in the octanol-based ternary system (see Figure 3.12).

However, when quantitatively comparing the OZ length parameter, ξ_{OZ}, for the EH and octanol-based ternary systems, subtle differences become apparent:

Difference 1a: For similar compositions in both octanol and EH ternary systems, the ξ_{OZ} values are generally higher in the EH ternary system when the ethanol content is relatively high. For instance, at approximately 10% oil, 41% ethanol, and 49% water, the ξ_{OZ} value in the EH system is 2.08 nm, while in the octanol system, it is around 1 nm (see Table A.4 for more comparisons). This emphasizes the contrasting behavior of oil droplets in a water-rich environment, where they act as pre-Ouzo structures. In the case of the 2-ethyl hexanol ternary system, when EH molecules are present in the water-rich phase forming pre-ouzo aggregates, their branching structure occupies more space compared to the octanol ternary system. Consequently, even with similar compositions,

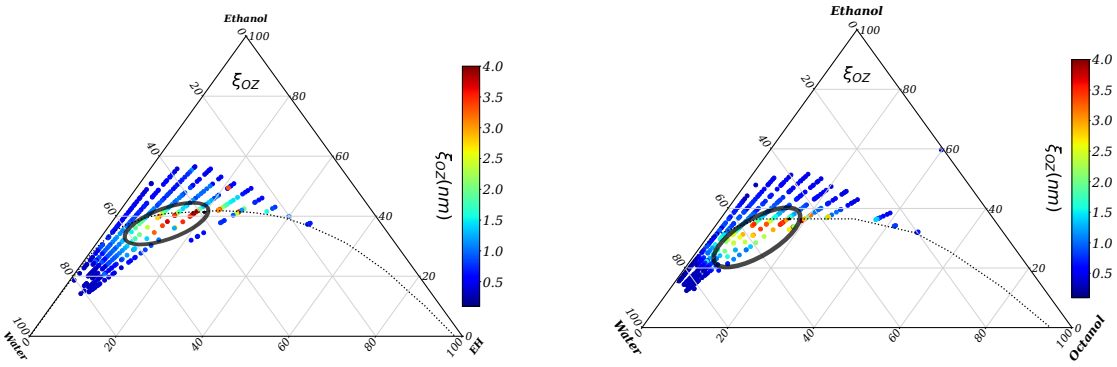

Figure 3.13: *Comparison of the ξ_{OZ} parameter for the **(Left)** 2-ethyl hexanol and **(Right)** octanol-based ternary systems. The octanol-based system exhibits a slightly larger area ($\sim$ 12%) of bigger pre-Ouzo droplets (greater than $\sim$ 2.5 nm) mixed within the Ouzo emulsions, compared to the 2-ethyl hexanol system.*

the EH pre-ouzo droplets take up a larger volume.

Difference 1b: Conversely, when the ethanol content is lower, for comparable compositions in both systems, the ξ_{OZ} value is higher in the octanol-based system. For instance, at approximately 10% oil, 29% ethanol, and 61% water, the ξ_{OZ} value in the EH system is 1.62 nm, while in the octanol system, it is around 2.39 nm (see Table A.5 for more comparisons). This may be because, within the biphasic region, pre-Ouzo aggregates formed in the EH system tend to break apart more easily compared to those formed with octanol, resulting in smaller droplets in the EH system.

Difference 2: In the EH ternary system, ξ_{OZ} values exceeding 2.5 nm are restricted to a narrow region near the binodal curve. Conversely, in the octanol-based system, these larger values extend slightly deeper into the metastable Ouzo region below the binodal curve (see Figure 3.13). This difference arises because EH pre-Ouzo aggregates are more unstable and tend to break more easily within the biphasic region compared to their octanol-based counterparts.

Further, once the system crosses the binodal line and enters the metastable state, the formation of Ouzo emulsions begins. In terms of scattering intensity, while the smaller pre-Ouzo aggregates are characterized by the q^{-2} dependence observed in the OZ term at $q \sim 0.1$ nm^{-1}, the larger Ouzo emulsions, however, display a q^{-4} dependence at even lower q values (< 0.1 nm^{-1}). Thus, during dilution process the OZ intensity increases up to a certain point, at which the system crosses the binodal line and Ouzo emulsification begins. After this, Ouzo emulsions become the dominant species, replacing the smaller pre-Ouzo aggregates. As the size of the species increases, it eventually falls outside the experimental q-range, causing I_{OZ} to decrease. Consequently, the pre-Ouzo aggregates shrink, leading to a decrease in the ξ_{OZ} parameter as well.

The larger area of higher ξ_{OZ} values in the octanol-based system, compared to the EH system, suggests that octanol-based pre-Ouzo aggregates are more resistant to breakdown and transition into Ouzo emulsions. This indicates that a greater amount of water is needed to break down most of the pre-Ouzo aggregates and form the Ouzo emulsions in

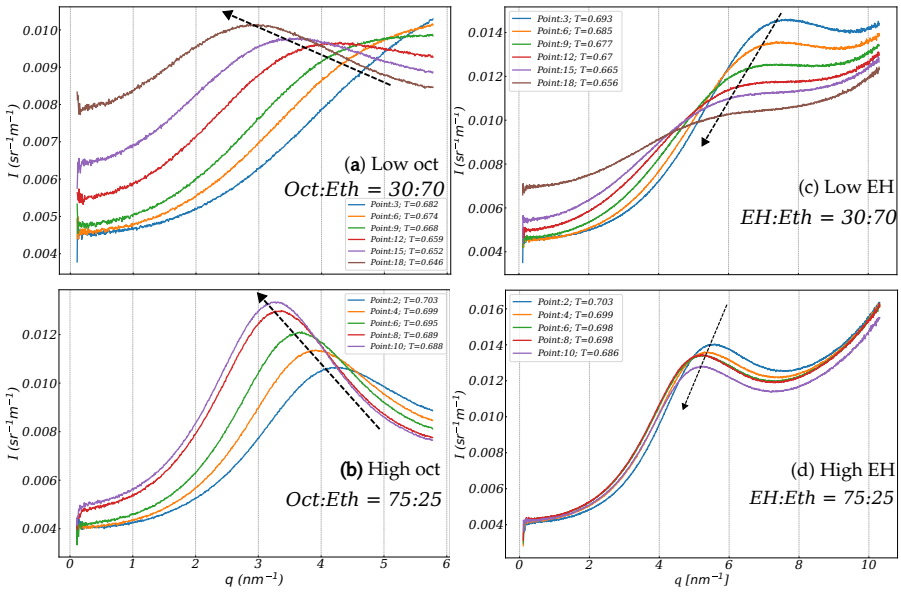

Figure 3.14: *Scattering curves for the octanol (**Left:** **a** and **b**) and 2-ethyl hexanol-based (**Right:** **c** and **d**) ternary systems, where a higher point number corresponds to a more diluted sample. Figures **a** and **c** show lower initial oil ratios, while figures **b** and **d** represent higher oil content. Although the center of the **broad peak** shifts to lower q values in all cases, its intensity decreases in the 2-ethyl hexanol system but increases in the octanol system.*

the octanol system.

When comparing the **pre-peak** between the octanol-based and EH-based ternary systems, two key differences emerge: the first concerns the shift in *pre-peak* position (q_{BP}) on the q-scale, while the second relates to variations in pre-peak intensity (I_{BP}).

Examining the scattering curves in Figure 3.14 for the octanol-based ternary system, the *pre-peak* shifts to a lower q value as the water content increases, indicating the evolution of reverse aggregates with dilution. In the octanol system, the peak position moves between $5\,\mathrm{nm}^{-1}$ and $2.5\,\mathrm{nm}^{-1}$ for lower octanol ratios and between $4.5\,\mathrm{nm}^{-1}$ and $3\,\mathrm{nm}^{-1}$ for higher octanol content. A similar trend is observed in the 2-ethyl hexanol-based ternary system, where the peak shifts from $8\,\mathrm{nm}^{-1}$ to $5.5\,\mathrm{nm}^{-1}$ for lower EH content and from $6\,\mathrm{nm}^{-1}$ to $4.5\,\mathrm{nm}^{-1}$ for higher EH content. In comparison, although dilution leads to the expansion of reverse aggregates in both oil-based ternary systems, the octanol-based aggregates are initially larger, as indicated by their smaller q values, compared to those in the EH-based system.

Another variation between the two systems lies in the behavior of the pre-peak intensity (I_{BP}): while its magnitude increases with dilution in the octanol system, it decreases in the EH system. This reflects differences in their reverse structures—octanol-based aggregates are more well-defined due to the linear structure of octanol molecules, which pack more efficiently per unit volume and exhibit stronger hydroxyl group interactions, allowing them to incorporate more water. The increasing intensity suggests that these

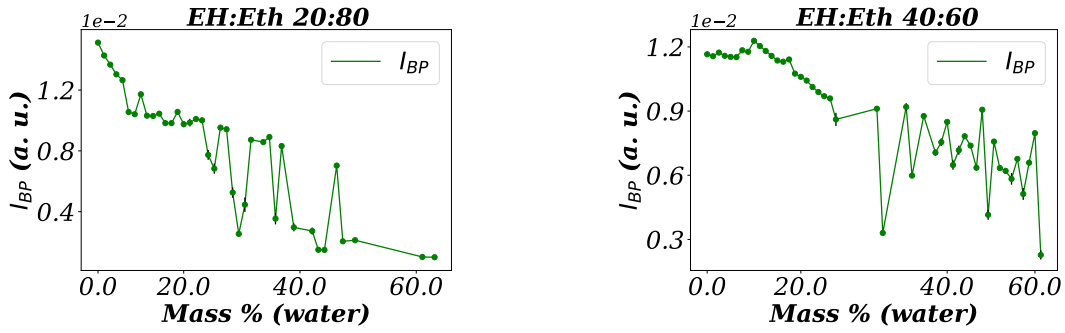

Figure 3.15: *Examples of intensity changes in the pre-peak for the 2-ethyl hexanol-based ternary system, displaying a gradual decrease rather than the sharp drop observed in the octanol-based ternary system.*

structured aggregates remain stable even as water is added to their cores. In contrast, EH-based (branched oil) aggregates start smaller and incorporate less water upon dilution before eventually breaking apart due to weaker hydroxyl group interactions.

Furthermore, Figure 3.15 shows that, unlike the octanol-based ternary system, the 2-ethyl hexanol system does not exhibit a sudden jump in *pre-peak* intensity. Instead, it displays a gradual decline. As a result, identifying the so-called 'experimental Lifshitz line' in the 2-ethyl hexanol ternary system based on the same criterion—a jump in I_{BP} as observed in the octanol system—was not possible. However, the transition from reverse aggregates to the pre-ouzo domain still occurs, and it can be described as a broader Lifshitz zone rather than a clear-cut line.

3.2.4 Invariant of OZ and BP

A more quantitative approach to delineating the pseudo-phases of OZ and BP on the ternary diagram is through the calculation of the Porod invariant, introduced in Chapter 2. Since the Porod invariant depends on the volume fraction rather than the particle size, it eliminates direct size effects while still retaining information about contrast, volume fraction, and overall morphology. This makes it a robust tool for distinguishing structural transitions without complications from size polydispersity. Additionally, as long as the scattering contrast remains unchanged, the Porod invariant allows for a consistent comparison of different phase regions, making it particularly useful in mapping phase boundaries in complex ternary systems.

For octanol ternary, the absolute invariant, computed separately for the OZ and BP terms, provides a clear quantitative distinction between the two regions dominated by each structural feature. The OZ-invariant (Figure 3.16) distinctly marks the pre-Ouzo region, making its boundaries more apparent. In contrast, the BP-invariant (Figure 3.17) highlights the region of reverse aggregates, where higher values indicate a stronger presence of these structures. The ratio of these two invariants is shown in Figure 3.18,

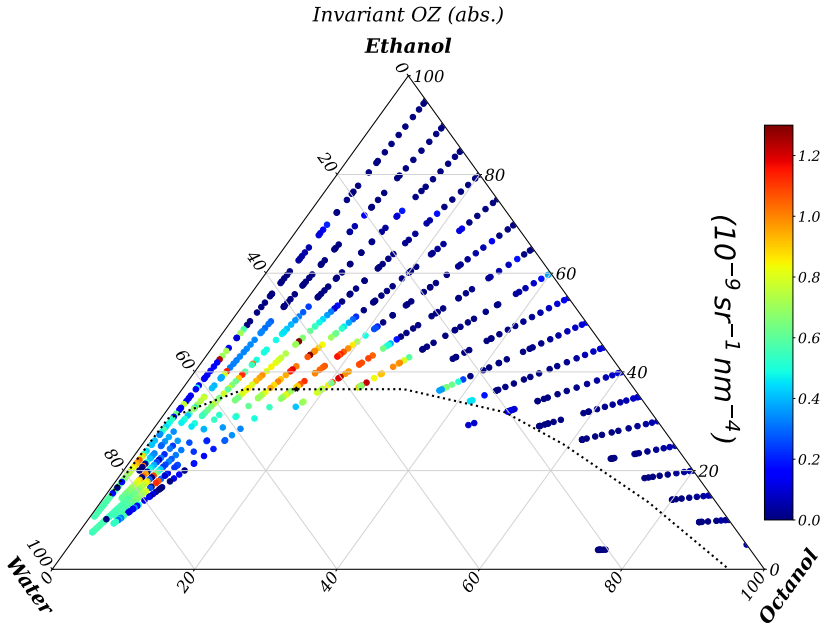

Figure 3.16: *Absolute invariant values for the OZ term in the octanol ternary system. The OZ invariant reveals a distinct boundary for the pre-ouzo domain, marking the region where a significant increase in OZ intensity is observed.*

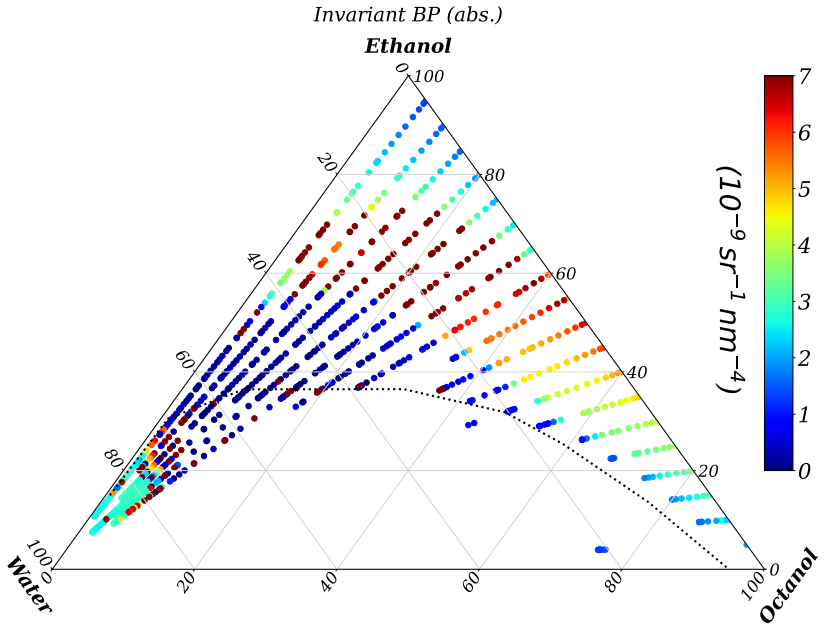

Figure 3.17: *Absolute invariant values for the BP term in the octanol ternary system. The BP invariant highlights the region in the lower part of the phase triangle where the pre-peak intensity is more pronounced, indicating stronger hydroxyl group interactions among the alcohols. In the upper portion of the ternary diagram, the pre-peak gradually shifts out of the experimental q-window, indicated by lower values of the corresponding invariant.*

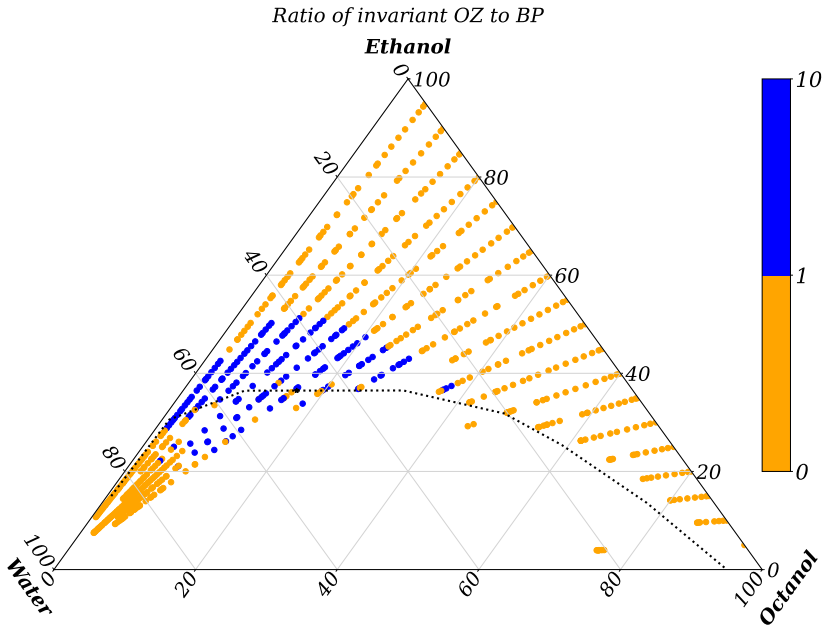

Figure 3.18: *Ratio of invariant OZ to invariant BP, indicating the regions where either OZ or BP dominates.*

highlighting the dominant contribution of either BP or OZ across the phase triangle.

In Figure 3.19, the boundary of the pre-ouzo domain is marked by identifying points where the OZ invariant becomes nonzero. When compared to the previously established experimental Lifshitz line (LL), both boundaries exhibit a similar curvature, albeit at different compositions. By analyzing these two newly identified lines alongside the previously highlighted fit parameter values, an inference can be made about an organizational transition occurring as one moves across the phase triangle from right to left.

At point A, on the right side, the system is in a pseudo-phase rich in oil, favoring the reverse aggregate structures (as discussed in the chapter on dynamics). As the system nears point B, positioned between the LL and the boundary marked as the 'onset of OZ,' it progressively shifts from an oil-continuous to a water-continuous phase. This region serves as a transitional zone, where residual alcohol-based structures persist while the early stages of pre-Ouzo aggregation emerge, though well-defined aggregates have yet to form. Finally, moving from point B to point C, within the pre-Ouzo boundary, well-defined pre-Ouzo aggregates become apparent.

An analysis of both the invariant (see Figure 3.20) along with the results of fitted data parameters of the EH ternary, reveals a fundamental difference in the structuring of reverse aggregates between the two ternary systems. On the oil-rich side, octanol-based reverse aggregates are larger, well-defined, and can incorporate more water into their cores, whereas EH-based reverse aggregates are smaller and less structured due to the branched nature of the molecules. Consequently, defining a clear Lifshitz line (the boundary between w/o and o/w regions) and a pre-ouzo boundary (the mesoscale structure domain upon dilution) is more challenging in the EH-ethanol-water ternary

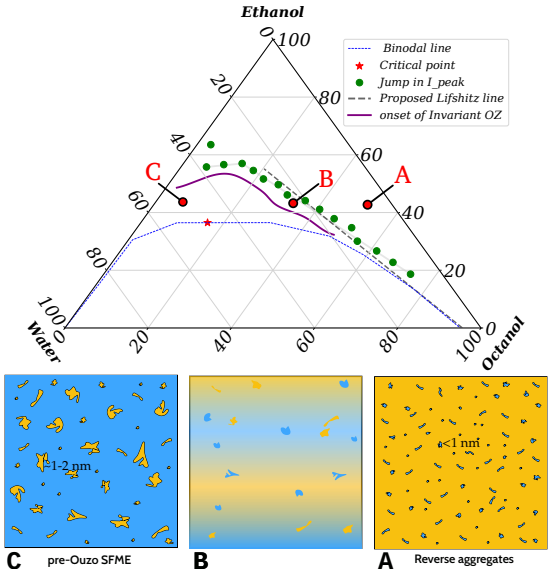

Figure 3.19: ***Top***: *Ternary plot depicting the experimental LL, identified by a jump in pre-peak intensity (I_{BP}), and the pre-ouzo boundary, marked by the onset of invariant OZ values.* ***Bottom***: *Schematic representation of three highlighted points on the ternary: A (located in the oil-rich phase, where reverse aggregates form), B (a transitional state with weakly defined mesoscale structures), and C (the pre-ouzo region, consisting of oil-ethanol clusters in a water-rich environment).*

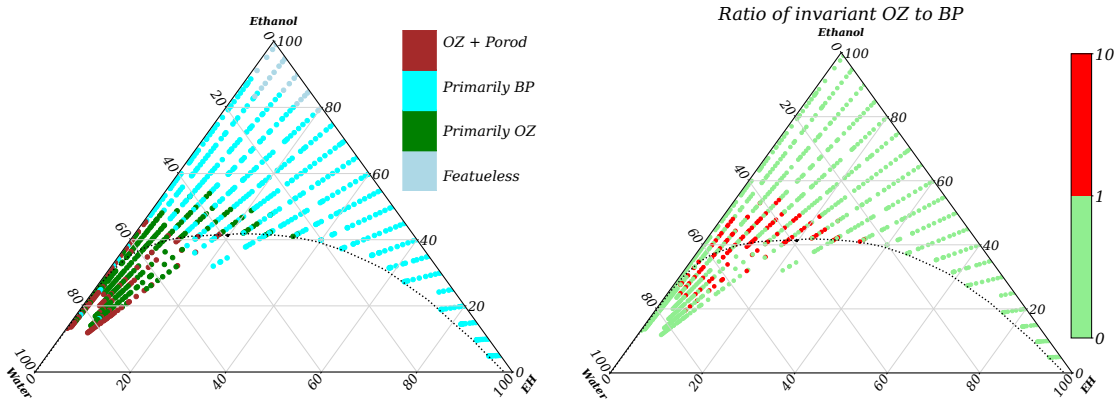

Figure 3.20: ***Left***: *Condensed representation of the fit functions used to define the main contributions from the OZ (pre-Ouzo) and BP (pre-peak) terms (note: "featureless" refers to the region where the pre-peak is outside the analyzed q-window for our case).* ***Right***: *The ratio of the OZ to BP invariant for the EH-based ternary system.*

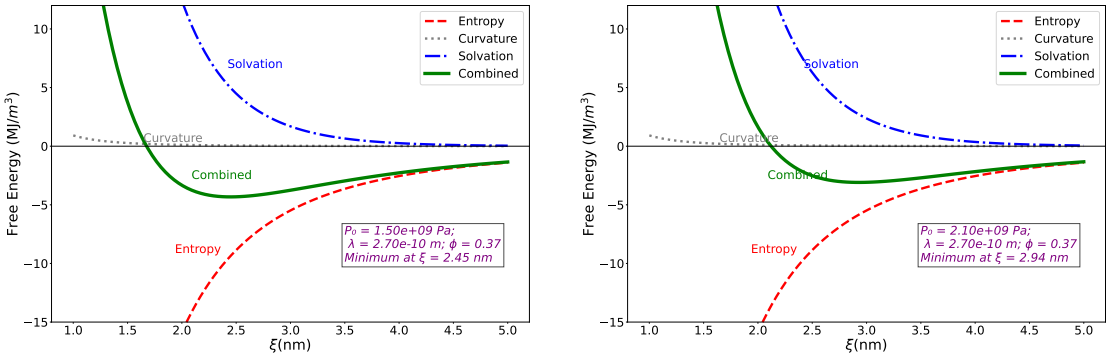

Figure 3.21: *Total free energy computed for a pre-Ouzo droplet containing 12% oil, 35% ethanol, and 53% water.* ***Left****: Octanol-based ternary system (ξ ∼ 2.51 nm).* ***Right****: EH-based ternary system (ξ ∼ 2.95 nm). The value of ξ is determined from experimental data (see Table A.6 for parameter values).*

system.

Free Energy Calculation for SFME

An attempt was made to calculate the free energy for pre-Ouzo structures following the approach of Zemb et al. [109]. In Figure 3.21, the total free energy for the octanol- and EH-based ternary systems are shown, based on SAXS experimental results from this work.

The total free energy includes contributions from solvation (or hydration) energy, entropy, and bending (or curvature) energy, as outlined in Chapter 1. The equilibrium of these factors stabilizes the pre-Ouzo aggregate, resulting in a free energy minimum.

Here, entropy depends solely on the correlation length, ξ, while hydration energy is determined by:

$$P_{hydration} = -P_0 e^{-u/\lambda} \tag{3.10}$$

where P_0, the contact pressure, is influenced by the binding and arrangement of water and ethanol molecules at the interface. The parameter λ represents the decay length associated with hydration and u is linked to the thickness of water-rich domains (see Appendix A.3 for details on the calculation).

To compare the forces involved in EH and octanol pre-Ouzo aggregates, we examine cases with similar compositions in both ternary systems (Figure 3.21). Using the parameters from Zemb et al. [109] for the octanol ternary system, we found that the calculated ξ value at the free energy minimum closely matches the experimental $\xi_{OZ_{oct}}$ from SAXS at a given composition. To match the SAXS-derived $\xi_{OZ_{EH}}$ value for EH, we adjusted the P_0 parameter while keeping all other parameters fixed. The results show that EH has a contact pressure 1.4 times higher than octanol at this composition, when its OZ length parameter is 1.18 times larger than that of octanol.

This preliminary exploration of free energy parameters provides insight into the rela-

tionship between the pre-Ouzo domain size (proportional to $\sim 4\xi$) and the hydration pressure (which keeps the pre-Ouzo domains separated). The result aligns with expectations, as hydration pressure acts as a repulsive force that prevents domain collapse—larger domain sizes correspond to higher contact pressures. However, this remains a preliminary calculation, and a more thorough analysis of both systems is necessary to establish a generalized trend linking free energy and domain size in pre-Ouzo SFME for 2-ethyl hexanol ternary systems.

3.3 Conclusion from SAXS Study

We identified distinct regions characterized by pseudo-phases: the pre-ouzo aggregates in the water-rich region, primarily described by the Ornstein-Zernike (OZ) term, and the oil-rich region defined by a pre-peak, where aggregates form through octanol-ethanol hydroxyl group interactions, with water residing inside. Further insights into their structure are revealed through dynamic studies in the following chapters.

An experimentally determined Lifshitz line was identified for the octanol-ethanol-water ternary, closely resembling the proposed LL but with a slight curvature. In this system, the well-defined wormlike reverse aggregates in the oil-rich region contribute to a high pre-peak intensity (I_{BP}). Upon dilution, at certain compositions, these structures break apart abruptly as a new pseudo-phase emerges, causing a sharp decrease in I_{BP}, which signifies the transition. However, such a distinct transition was not observed in the EH-based ternary. While reverse aggregates were present, they were comparatively shorter than those in the octanol system due to the branching ethyl group in EH, which limits hydroxyl interactions. As dilution progresses, these structures gradually disassemble, initiating the formation of the next pseudo-phase in a more continuous manner. This leads to a gradual decrease in I_{BP}, emphasizing the influence of EH's branching on structuration and phase transitions. Further molecular dynamics simulations of the EH-based ternary system could provide deeper insights into its structural organization.

The calculation of the invariant quantity offers a quantitative approach to identifying the pre-Ouzo boundary within the phase triangle. Additionally, the maxima of the I_{OZ} fit parameter, when mapped onto the ternary diagram, closely follow the binodal line reported in the literature from tie-line measurements, reinforcing the accuracy of the composition calculations, which are embedded in the transmission values obtained from the *in situ* measurements.

Furthermore, although critical fluctuations (CF) are expected in ternary systems near the critical point (CP), they were not observed in the SAXS experiments. The pre-Ouzo organization remained unaffected by these fluctuations, as indicated by the reasonable length scale parameter of the OZ term (ξ_{OZ}). This demonstrates the advantage of SAXS over light scattering techniques. In DLS, measurements are often taken at lower q values, where signals from large-scale critical fluctuations can dominate and potentially obscure contributions from smaller pre-Ouzo aggregates. SAXS, by contrast, operates at

higher q values, avoiding this issue and ensuring a clearer distinction between different length scales. This enables a more reliable characterization of the nanoscale structural organization within the pre-Ouzo regime.

Chapter 4

Temperature-Dependent Behavior of Pre-Ouzo

4.1 Introduction

The temperature of a solution is critical in determining the formation and stability of a system, making the understanding of thermal responses in SFME systems essential for optimizing their performance. Temperature variations enable the solubilization and desolubilization of components into different phases, facilitating the extraction of desired components. Temperature-dependent studies on SFMEs have revealed significant advancements in extraction processes. For instance, Zhang et al. [105] explored a novel SFME system with DMSO as an amphiphilic solvent, n-butanol as the non-polar phase, and water as the polar phase. Their findings showed that minor temperature changes near the boundary line triggered dramatic transitions from single-phase microemulsion (at high temperatures) to complete phase separation (at low temperatures), enabling complete demulsification. Unlike redox- or CO2-induced transitions in other systems, this temperature-induced transition in SFME was not confined to a specific sub-region (W/O, BC or O/W). When used as a nano-reactor, Ag NPs spontaneously separated into the lower phase upon cooling, simplifying collection. Additionally, Ag NPs from SFME exhibited higher catalytic activity compared to those from SBME, likely due to the absence of surfactant adsorption on their surface.

The study by Mingbo et al. [158] on the trans-anethol–ethanol–water system revealed that increasing the temperature expands the monophasic region, while both the refractive index and viscosity decrease monotonically. Notably, viscosity shows a significant exponential decay. Higher temperatures disrupt macroscopic stability, leading to an exponential reduction in scattering light intensity due to the disappearance of mesoscopic droplets (100 nm in size). These droplets, which contain minimal trans-anethol, demonstrate rapid nucleation and size recovery upon cooling, highlighting excellent reversibility. While droplet size remains relatively stable with temperature, their concentration decreases exponentially. These findings underscore the crucial role of mesoscopic structures

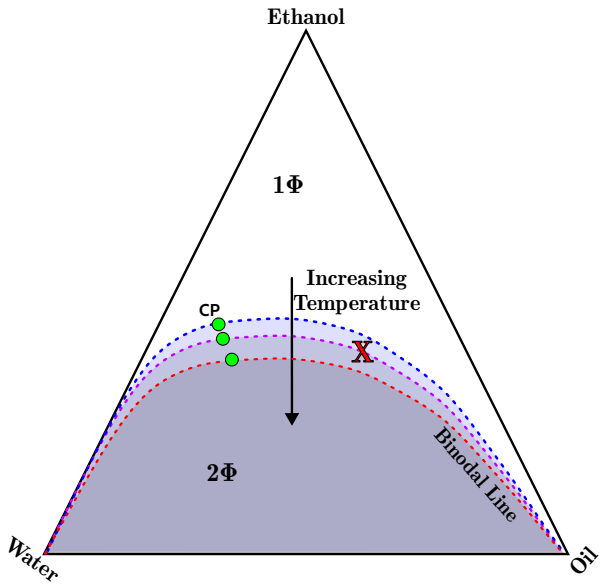

Figure 4.1: *Schematic representation of temperature-dependent variations in the biphasic region of an ethanol-based oil-water ternary system. With increasing temperature, the homogeneous (1ϕ) region expands as the binodal line shifts downward, while the critical point (green circles) moves slightly toward the oil-rich side. As a result, any given point X within the phase triangle may lie in either the single-phase (1ϕ) or biphasic (2ϕ) region, depending on the system's temperature.* *(This figure is derived from the findings for the 2-ethyl hexanol-ethanol-water ternary system presented in Figure 5.22.)*

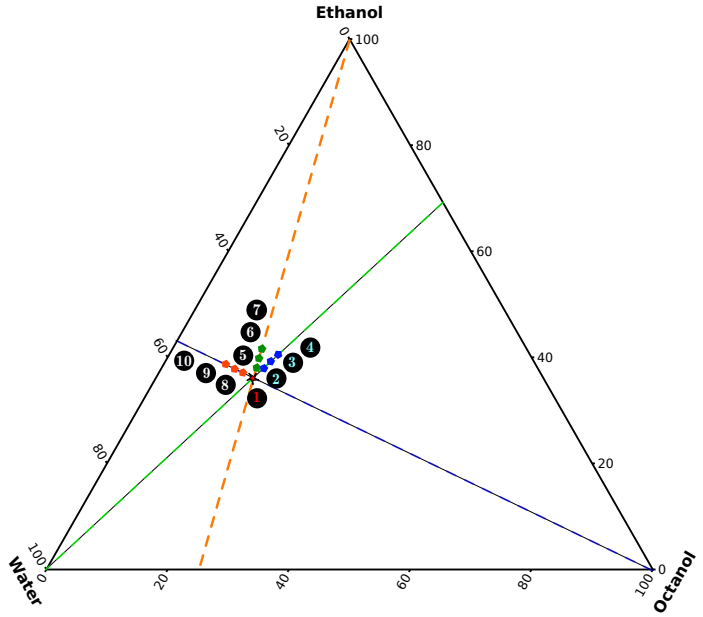

Figure 4.2: *Ternary plot showing the points for which temperature-dependent SAXS experiment was performed. Point 1 is the critical point, while the others are progressively positioned away from the critical point in terms of composition. (Note: the colored pentagon symbols are the actual points while the numbers in circle are there to help identify them.)*

in thermal responses within ternary surfactant-free systems. Further, understanding the temperature range of stability for SFMEs is crucial for their effectiveness in extraction applications. These results emphasize the importance of studying temperature behavior in SFMEs to fully harness their potential for various applications.

Each point on a phase triangle corresponds to a sample with a fixed composition; however, the features of the phase triangle, such as the binodal line and critical point, are temperature-dependent due to variations in the solubility of the ternary components (see Figure 4.1). For instance, in a ternary mixture of octanol, ethanol, and water, increasing temperature causes the binodal line to shift downward, expanding the homogeneous region in the phase diagram [158]. Similarly, in the octanol-ethanol-water ternary system, the critical point shifts closer to the oil phase with increasing temperature [159].

We conducted temperature-dependent SAXS measurements to investigate how the behavior of the ternary samples changes near the critical point. This study focused on examining the intensity of the Ornstein-Zernike (OZ) term as a function of temperature, which is characteristic of pre-Ouzo aggregation and its temperature dependence. This experiment builds upon the SAXS autodilution study discussed in the previous chapter, but in this case, we analyzed the ternary samples without any autodilution.

For the temperature-dependent investigation of the phase behavior in octanol-ethanol-water and 2-ethyl hexanol-ethanol-water ternary mixtures, a total of 20 samples were examined, with ten unique compositions prepared for each system. Details of the octanol-based samples are provided in Table A.7, and those of the ethyl hexanol-based samples in Table A.8. Each experiment began at 15°C, with the capillary gradually heated to 55°C while three SAXS measurements were taken at each temperature point. Afterward, the capillary was gradually cooled back to 15°C, with measurements taken during the cooling process in the same manner.

4.2 Results and Discussions

Figure 4.1 illustrates the downward shift of the binodal line with increasing temperature. Depending on the temperature, any point X could fall within the two-phase region or represent a single-phase sample. The temperature at which the sample point transitions into the two-phase region upon cooling is referred to as the Phase Separation Temperature (PST). As expected, the PST will vary for each point on the phase triangle, indicating the temperature at which it will intersect the binodal line.

Based on their temperature-dependent behavior, the samples can be divided into two groups: those positioned near the binodal line at room temperature and those farther away from it. Considering that 25°C is a reasonable approximation of room temperature and there is well-established literature data on the critical point and binodal line for the octanol-ethanol-water ternary system, we use this temperature as our reference point.

The Ornstein–Zernike (OZ) intensity reflects the presence of pre-Ouzo aggregates. A decrease in I_{OZ} with increasing temperature indicates improved solubilization, which

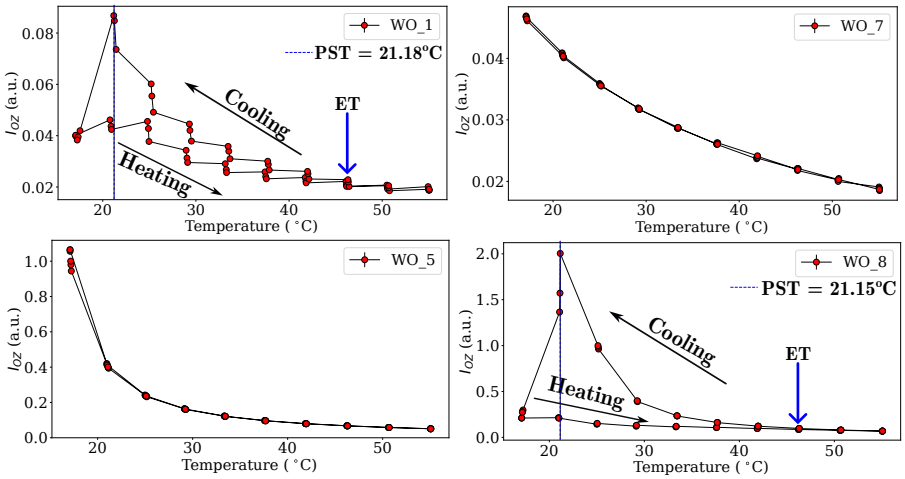

Figure 4.3: *I_{OZ} vs Temperature plots for octanol-based ternary samples as shown in Figure 4.2. (**Top Left**) For sample WO_1, representing the critical point, a hysteresis is observed in I_{OZ} during heating and cooling. (**Top Right**) and (**Bottom Left**) For samples WO_5 and WO_7, which are farther from the critical point in the vertical direction, no hysteresis is observed. (**Bottom Right**) Sample WO_8 exhibits a similar hysteresis pattern as WO_1 but shows higher I_{OZ} values, indicating stronger pre-Ouzo aggregation. The phase separation temperature (PST) and equalizing temperature (ET) are indicated on the figures.*

prevents spontaneous mesoscale structuring. Figure 4.3 illustrates the I_{OZ} vs temperature data obtained through OZ fitting for four different samples. These samples are named in the same order as listed in the phase triangle shown in Figure 4.2.

Samples with compositions closer to the binodal line (at 25°C) exhibit distinctive behavior during temperature changes. For example, the I_{OZ} vs. temperature curves for samples closer to the critical point and, consequently, the binodal line (such as WO_2 and WO_8 in Figure 4.3) in the octanol-based ternary system exhibit hysteresis. For these samples, the I_{OZ} typically starts at an intermediate value and decreases gradually as the temperature increases. During cooling process, the I_{OZ} value rises gradually, reaches a maximum at a specific temperature (PST), and then suddenly drops to a lower value below this temperature. Additionally, at a certain higher temperature (referred to here as ET for "Equalizing Temperature"), the I_{OZ} values for the heating and cooling paths converge and remain identical at higher temperatures.

The hysteresis observed in the I_{OZ} curve—where I_{OZ} follows different paths during heating and cooling—can be attributed to the shifting position of the system's binodal line, which moves upward as the temperature decreases. Since the samples were initially prepared according to the homogeneous phase at 25°C, a temperature drop below their PST during the experiment's initial phase causes the upward shift of the binodal line, moving these samples into the biphasic region, as their Phase Separation Temperature (PST) surpasses the current experimental temperature.

During heating, as the temperature increases and exceeds the PST, I_{OZ} is expected to show a sudden rise followed by a decline, corresponding to the formation of pre-

Ouzo aggregates and their subsequent breakdown with increasing temperature. However, incomplete mixing within the capillary can delay the aggregation process, causing I_{OZ} to decrease monotonously as the binodal line shifts away from the sample point.

Upon cooling, I_{OZ} increases at a different rate, likely due to improved sample homogeneity from better solubilization at higher temperatures. As indicated by the ET, this enhanced solubilization results in similar values at higher temperatures for both the heating and cooling paths.

During the cooling phase, the sample may re-enter the biphasic region upon reaching the binodal line, or its PST, as observed for sample WO_8 around 21.15°C and for WO_1 at 21.18°C. Additionally, the small variation in PST for samples close to the binodal line at 25°C hints to the curvature of the binodal line and underscores the differences in the proximity of the sample to the critical point (CP). For samples far from the CP or binodal line, however, this trend is not observed because the experimental temperature does not drop below their respective PSTs.

Furthermore, the magnitude of I_{OZ} is higher for samples positioned closer to the critical point (CP) in the pre-Ouzo region compared to those farther from CP. This trend reflects the extent of mesoscale aggregation and its dependence on temperature. Among the samples near 25°C-CP (WO_1, WO_2, WO_5, and WO_8), a noticeable variation in I_{OZ} values is observed. At 25°C, WO_8, located on the pre-Ouzo side, exhibits the highest I_{OZ} value (~ 1), followed by WO_2 on the right side of CP (~ 0.5). In contrast, WO_5 shows a significantly lower I_{OZ} value (~ 0.25), while WO_1 has the lowest (~ 0.05). The reduced I_{OZ} of WO_5 can be explained by its higher hydrotrope content, which increases its vertical distance from CP. However, WO_1 presents a more intriguing case. Despite having the lowest hydrotrope content among all samples, its behavior differs significantly due to its close proximity to CP at 25°C.

Samples positioned farther from the binodal line at 25 °C generally do not exhibit hysteresis, as they remain outside the biphasic region throughout the temperature cycle of the experiment. However, as the distance from the critical point increases in the upward direction, the overall Ornstein-Zernike intensity decreases. This is because the increased presence of hydrotrope facilitates solubilization, thereby hindering pre-Ouzo aggregation.

Similar trends are observed for the length scale parameter related to the Ornstein-Zernike intensity. In Figure 4.4, the ξ_{OZ} vs temperature plots are shown. For a sample closer to the binodal line at 25 °C (e.g., WO_8), hysteresis behavior is observed, where the length scale of the aggregates initially starts from an intermediate value at low temperatures and gradually decreases with heating. During cooling, the sample follows a different path, with higher ξ_{OZ} values below the ET. After reaching the PST, the size parameter drops to a lower value, returning to its original state before the experiment began.

In contrast, for a sample such as WO_7, which was never near the critical point (CP) and whose PST was never crossed during the experiment, both the heating and cooling

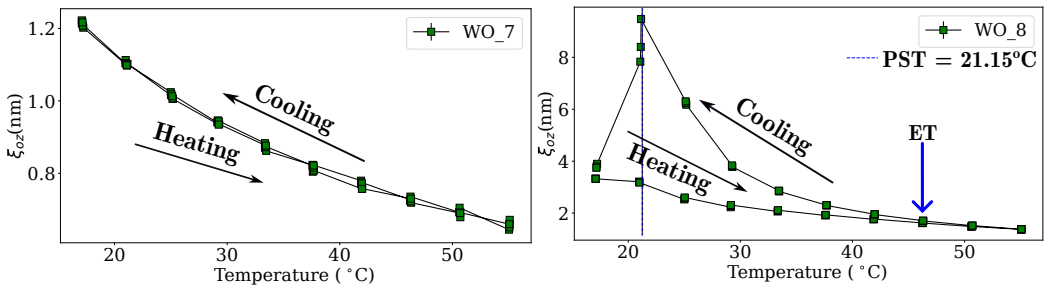

Figure 4.4: *Length scale parameter (ξ) extracted from the OZ fitting of SAXS data for the octanol-ethanol-water ternary system. The parameter shows a trend similar to the intensity of the OZ function: for samples relatively far from the critical point (CP) (e.g.,* ***Left****: WO_7), the curve follows the same path during heating and cooling. However, for samples closer to the CP (e.g.,* ***Right****: WO_8), a hysteresis effect is observed. Overall, parameter (ξ) decreases significantly with increasing temperature due to the enhanced solubilization of the components within the sample.*

paths show the same length scale parameter values, which continuously decrease with increasing temperature. In general, it can be assumed that the values obtained during the cooling path provide a better estimation of pre-ouzo formation, as aggregates form after the components are fully solubilized.

The sudden decrease in both the intensity and length scale of the OZ signal upon crossing the PST during cooling can be explained as follows: The OZ contribution originates from the smaller pre-Ouzo aggregates that predominantly exist in the homogeneous phase, as discussed earlier. However, once the system crosses the PST and enters the metastable region, spontaneous formation of Ouzo emulsion droplets occurs. These Ouzo emulsions, being significantly larger in size, do not contribute to the q^{-2}-dependent OZ term. Additionally, the formation of Ouzo droplets happens at the expense of the pre-Ouzo microemulsions, leading to a reduction in the OZ intensity. It is also noteworthy that trace amounts of pre-Ouzo aggregates remain present even within the Ouzo region, as highlighted in the previous chapter.

Figure 4.5 shows the ξ_{OZ} values for all 10 samples at both 21°C and 51°C, highlighting clear differences in I_{OZ} and ξ_{OZ} values when comparing the samples at the two temperatures.

At 21°C (lower temperature), ξ_{OZ} values differ between the cooling and heating paths, with higher values observed during the cooling path. This indicates enhanced aggregation during cooling. In contrast, at 51°C (higher temperature), the ξ_{OZ} values are similar for both the cooling and heating paths. Overall, the ξ_{OZ} values at 21°C are notably higher, ranging from approximately 1 to 10 nm, compared to the smaller range of 0.7 to 1.5 nm observed at 51°C. This difference is likely due to enhanced aggregation possibilities at lower temperatures.

For samples along the same dilution line (e.g., ethanol), increasing the distance from CP generally results in better solubilization and, consequently, poorer mesoscale struc-

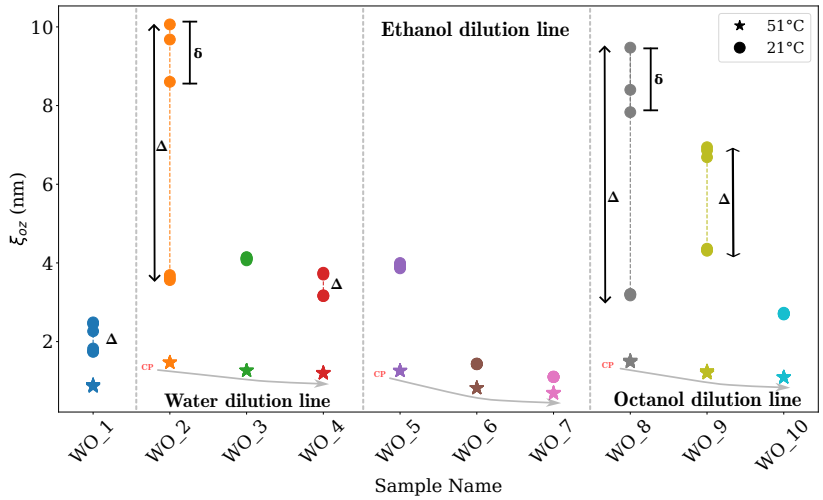

Figure 4.5: *Figure showing ξ_{OZ} values for 10 samples of the octanol-ethanol-water ternary at 51°C (star) and 21°C (circle). Three SAXS readings were taken during heating and cooling for each sample. The gray arrows indicate changes in ξ relative to the critical point (CP), with the dotted lines separating the water, ethanol, and octanol dilution categories. At higher temperatures, ξ values remain consistent across heating and cooling, while at lower temperatures, discrepancies (denoted by Δ) occur between the heating and cooling paths. Additionally, variations in ξ values (denoted by δ) are observed for the same temperature and cooling path across the three SAXS readings.*

turation at both temperatures. However, at 21°C, a distinct trend is observed: samples along the ethanol dilution line exhibit relatively lower ξ_{OZ} values compared to those along the octanol and water dilution lines. This difference is attributed to the curvature of the binodal line. Near CP, the binodal line has a flatter curvature, causing samples like WO_2 and WO_8 to be closer to the binodal line, while WO_5 is vertically farther from CP compared to the other two.

Similar observations were made for the 2-ethyl hexanol-ethanol-water ternary system, with the only difference being the magnitude of ξ_{OZ}. For example, comparing the samples near the 25°C-CP for both EH and octanol ternaries (WEH_1 and WO_1): the length scale for WEH_1 is around 5 nm at 25°C, while for WO_1, ξ_{OZ} is about 1.5 nm at its PST of 21.18°C, which is approximately 3.3 times smaller.

4.3 Conclusion from Temperature analysis

Overall, the SAXS analysis of SFME across varying temperatures provides insight into how pre-ouzo structuration evolves in relation to the temperature-driven binodal line and CP. When the sample becomes biphasic during heating or cooling, the size parameter sharply decreases due to the formation of ouzo emulsions at the expense of pre-ouzo microemulsions, as indicated by a sudden drop in the OZ intensity. Notably, the pre-ouzo region is not a static or well-defined area within the phase triangle; instead, it can be

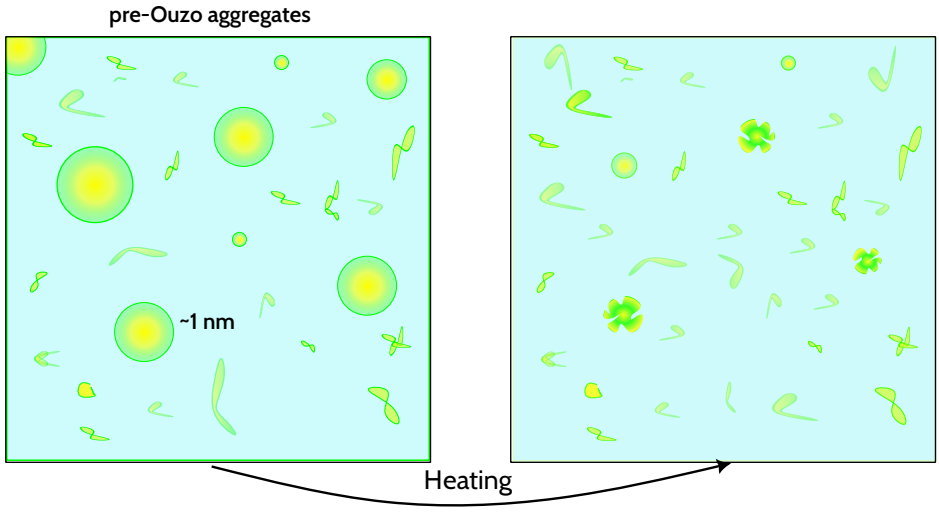

Figure 4.6: *Schematic representation of the pre-Ouzo microemulsions being resolubilized into the solution as smaller O/W droplets with increasing temperature.*

considered a thermodynamically responsive region of the phase diagram, with its extent changing based on temperature. From the perspective of a fixed sample composition, the degree of solubilization—and consequently the formation of pre-ouzo droplets—is temperature-dependent. This temperature sensitivity is illustrated in Figure 4.6.

Chapter 5

Dynamics of SFME Ternary System

The microscopic arrangement of molecules in liquid mixtures significantly influences their bulk properties, such as solubility, viscosity, and transport behavior. In this section, we aim to unravel the connection between molecular dynamics and macroscopic properties. To explore the dynamics and the effects of pre-Ouzo structuration in the ternary system, we utilized PFG-NMR, Neutron Spin Echo (NSE), and rheology, and compared our findings with classical molecular dynamics (MD) simulations conducted by D. Horinek (Univ. Regensburg). NSE and NMR provide complementary insights by measuring diffusion coefficients at different scales: NSE captures both individual and collective dynamics within small spatial domains over short timescales, while PFG-NMR focuses on self-diffusion dynamics at larger length scales over longer timescales.

We begin by exploring the dynamics of binary ethanol-water and ethanol-octanol mixtures to better understand the molecular interactions and diffusion processes that drive these systems [160]. Using a combination of NMR and NSE techniques, we investigate diffusion across a wide range of length scales, from nanometers to microns. This enables a detailed analysis of how dynamics evolve across different scales in complex mixtures. NMR reveals a well-known trend in complex systems, where dynamics slow down as the length scale increases [161].

Building on this, we extended our analysis to the octanol-ethanol-water ternary system, which is central to this study. To complement this, we performed rheology experiments to examine viscosity variations. For NSE, we expanded our investigation to include both octanol- and 2-ethyl hexanol (EH)-based ternary systems, allowing us to compare dynamics for these two types of hydrophobic components. This comparison enabled us to assess how substituting linear octanol with its branched counterpart influences the dynamics. NSE measurements were carried out using the IN15, IN11C and WASP instruments at ILL, which span different q-ranges and provide a comprehensive view across multiple length scales.

For the octanol-ethanol-water ternary system, we analyzed samples along three distinct dilution lines (see Figure 5.1). These lines were carefully chosen to encompass both samples within and outside the pre-Ouzo region, offering a thorough perspective on the

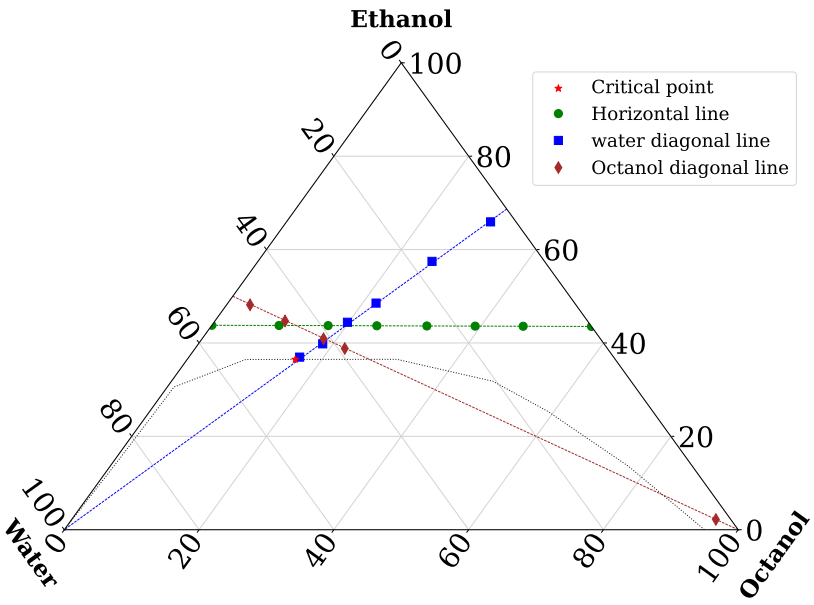

Figure 5.1: *Ternary phase diagram of the octanol-ethanol-water mixture, showing the different lines used for NMR analysis: the horizontal line (HL) with 8 samples, the diagonal line along the water vertex (DL_{water}) with 6 samples, and the diagonal line along the octanol vertex ($DL_{octanol}$) with 5 samples. All samples represent fully hydrogenated components, with compositions expressed as mass percentages.*

dynamic changes associated with pre-Ouzo aggregation: (a) *Horizontal Line:* This line includes 8 samples with a constant ethanol mass fraction and varying water-to-octanol ratios (details on compositions and calculations are provided in the Appendix section A.4). Moving from left to right across the phase triangle, the system transitions from a binary ethanol-water mixture to a ternary mixture with increasing octanol content, and finally to a binary octanol-ethanol mixture. (b) *Water Diagonal Line:* This line starts with a binary octanol-ethanol mixture, followed by successive dilution with water while maintaining a constant octanol-to-ethanol ratio. A total of 6 samples were analyzed along this line. (c) *Octanol Diagonal Line:* Along this line, the ethanol-to-water ratio remains constant, and samples with varying octanol content were prepared.

To isolate the dynamical signatures of individual components, we used deuterated compounds. For this purpose, we prepared three sets of each sample along the horizontal and water diagonal lines, where one component in each set was hydrogenated while the other two were deuterated. For example, in the first set, octanol was in its hydrogenated form ($C_8H_{18}O$), while ethanol and water were replaced with their deuterated forms (C_2D_6O and D_2O, respectively).

To gain further insights, we compared the octanol/EH-ethanol-based ternary system to the ethyl acetate-sodium salicylate-water system. In the latter, which is based on an electrolytic hydrotrope, there is no evidence of pre-Ouzo structuration or spontaneous emulsification (Ouzo effect) [162]. This comparison highlights the differences in dynamics

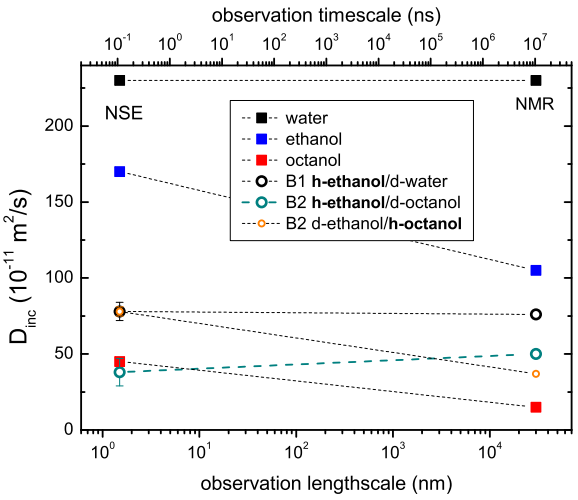

Figure 5.2: *Self-diffusion coefficients obtained from NSE and NMR measurements for pure compounds and binary mixtures at 298 K. In binary mixtures, the component being analyzed is highlighted in bold within the legend. The lines serve as visual guides. Notably, unlike the other components, the ethanol diffusion coefficient shows an increase between NSE and NMR measurements in the ethanol-octanol mixture.*

arising specifically from pre-Ouzo structuration in the former systems.

5.1 Pulse Field Gradient NMR Analysis of Octanol and EH Ternary Systems

Binary Ethanol-water and ethanol-octanol Mixture

For water, ethanol, and octanol in their pure, unmixed state, diffusion behavior varies significantly. Pure water maintains a consistent diffusion coefficient across different length scales due to its strong 3D hydrogen-bond network [163, 164]. In contrast, pure ethanol and pure octanol exhibit a noticeable slowing of diffusion as the length scale increases, driven by molecular clustering and hydrophobic interactions. These differences highlight how molecular structure and interactions influence diffusion dynamics.

In the ethanol-water binary mixture, ethanol's diffusivity is lower than that observed in pure ethanol, consistent with the solution's increased viscosity. At smaller length scales, corresponding to a few molecules probed by NSE, ethanol exhibits diffusion similar to that measured at larger distances by NMR. However, in the NSE data, there is a subtle dependence of diffusion on q, as indicated by the error bars in figure 5.2. In contrast, NMR results show that ethanol's diffusion stabilizes, influenced by the three-dimensional hydrogen-bond network of water, emphasizing the dominance of water's structure over macroscopic distances.

In the ethanol-octanol mixture, a contrasting behavior is observed. Octanol diffusion

slows at larger distances, consistent with the behavior of pure octanol. However, ethanol displays a surprising trend: its diffusion tends to increase at larger scales, behaving in a more bulk-like manner. This unexpected observation suggests that ethanol's dynamics at long distances are less hindered by the surrounding octanol molecules, which locally disrupt ethanol clusters. Meanwhile, octanol appears to be fluidized by the presence of ethanol, which disturbs the structural organization of octanol over short distances but preserves its effect at larger scales.

The dynamics in binary mixtures like ethanol-octanol reveal remarkable complexity and strong length-scale dependence, as evidenced by the significant disparity—over 60%—in diffusion coefficients measured using PFG-NMR and NSE. This contrast, spanning several orders of magnitude, highlights the subtle, long-range structuration in mono-alcohol systems, corroborated by dielectric spectroscopy observations of a pronounced Debye peak [165, 166]. These findings underline the intricate interplay between molecular structuring and dynamic behavior in these systems, paving the way for deeper insights into self-organization at varying scales.

Ternary System: Octanol-Ethanol-Water

We then extended the methodology to ternary mixtures. By examining the *horizontal dilution line* at 43 wt.% ethanol (see Figure 5.1, green line with circles), the composition of the octanol-ethanol-water ternary mixture spans the phase diagram from low octanol content on the left, characterized by mesoscale organization in the pre-Ouzo zone, to octanol-rich reverse aggregate mixtures on the right.

Unlike binary systems, the translational diffusion coefficients of individual species measured using NSE and NMR in the ternary mixtures were observed to show a notable degree of consistency. This agreement allowed the incoherent NSE data to be constrained by NMR diffusion coefficients. This initial analysis demonstrates that mesoscale organization in ternary systems prevents the formation of extended-range structures, allowing translational dynamics to be probed consistently at both nanoscale and microscale resolutions.

Figure 5.3 displays the diffusion coefficients measured by PFG-NMR along the horizontal line. Although the overall diffusion coefficient (derived from all hydrogenated samples) decreases by a substantial factor along this line, the diffusion behavior of individual species shows significant variation. Ethanol's self-diffusion coefficient remains constant throughout the range. In contrast, water's diffusion coefficient decreases as the composition of octanol increases i.e. shifts from the binary water-ethanol mixture (on the left side of the phase triangle) toward the ethanol-octanol binary (on the right). Conversely, octanol's diffusion coefficient exhibits an opposite trend, increasing as the octanol fraction in the ternary mixture rises. At the point where water and octanol reach equal mass fractions, water's diffusion coefficient drops further and stabilizes on the side where octanol is in excess. Meanwhile, octanol's diffusion coefficient remains relatively steady before this equal mass fraction point and then begins to increase on the other

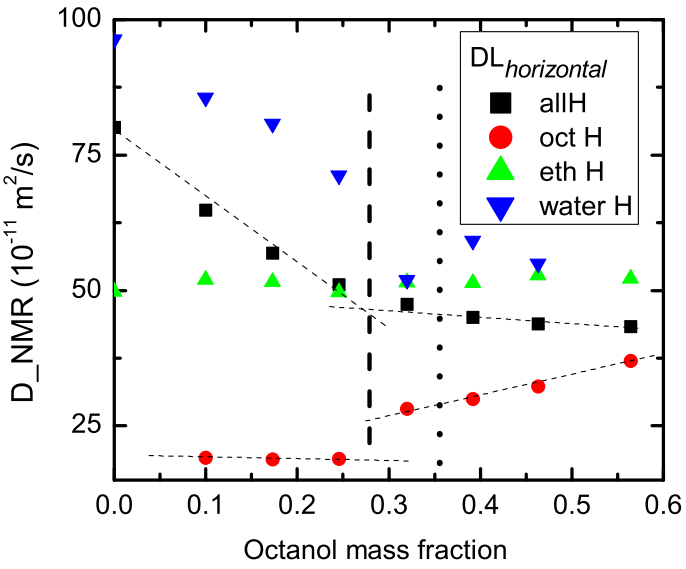

Figure 5.3: *Diffusion coefficients extracted from PFG-NMR (^1H) measurements along the horizontal dilution line. The legend refers to the hydrogenated species in the mixture: n-octanol, ethanol, or water, with the other two components deuterated. The vertical dotted line indicates the Lifshitz line proposed by Prevost et al. [120]; the dashed line indicates a mass ratio of octanol/water = 1. Error bars are smaller than the symbols. Dashed transversal lines are guides for the eye.*

side.

We also observe that when the ethanol mass fraction remains constant, its diffusion coefficient does not change during the transition between the oil-rich and water-rich regions, suggesting the presence of meso-structuration, where most of the ethanol exhibits dynamic behavior and is not strongly bound to other components. The behavior of the octanol diffusion coefficient differs as the system transitions from a pre-Ouzo domain to a reverse aggregate domain, leading to a reversal in the organization of octanol molecules. Notably, there is evidence of pre-Ouzo structuration, with oil molecules being trapped and exhibiting lower diffusion, as well as evidence of reverse structures where water is trapped. However, no signs of a transition to a bi-continuous phase are observed, where the dynamics of both major phases would typically become similar.

Classical molecular dynamics (MD) simulations along the same horizontal line showed excellent agreement with experimental diffusion coefficients, capturing both absolute values and trends (Figure 5.4). Minor discrepancies were observed for octanol diffusion, where (i) the slight inconsistent transition occurred for MD at a lower octanol fraction than in experiments, and (ii) the increase in diffusion coefficient of octanol was less linear at higher octanol ratio. The distinction between pre-Ouzo and non-Ouzo regions was particularly evident in the mean square displacement (MSD) slopes for octanol molecules (Figure 5.5). Additionally, log-log plots of MSD (Figure 5.6) highlight that octanol reaches a Fickian regime later than ethanol and water, especially at low

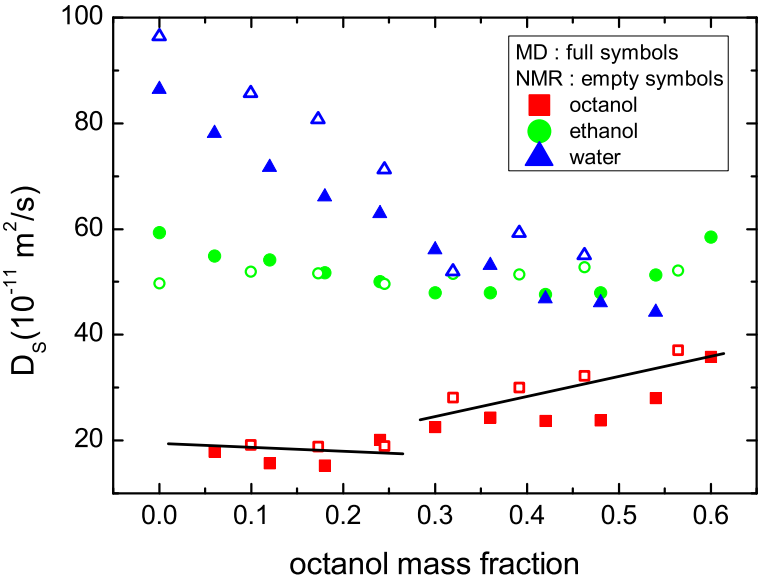

Figure 5.4: *Diffusion coefficients (solid symbols) of octanol, ethanol, and water from MD simulations along the horizontal line at a constant ethanol mass fraction ($w_E = 0.4$). Experimental values (empty symbols) from NMR measurements are shown for comparison. The black lines are guides for the eye.*

octanol content.

Additionally, PFG-NMR was used to examine two diagonal dilution lines (as shown in Figure 5.1). The water diagonal line (DL_{water}) corresponds to samples where an octanol-ethanol binary mixture is progressively diluted with water to create new ternary compositions; five such samples with varying water ratios were selected. The second line, the octanol diagonal line (DL_{octanol}), starts with a binary ethanol-water mixture, to which octanol is gradually added to form new ternary compositions. The corresponding diffusion coefficients are presented in Figure 5.7.

For the *water dilution line* (DL_{water}), which traverses the pre-Ouzo aggregation region at lower octanol concentrations, ethanol and octanol maintain relatively stable diffusion dynamics, whereas water's diffusion coefficient decreases with increasing octanol content. Beyond the Lifshitz line (LL), as octanol content rises, the diffusivity of both ethanol and octanol gradually increases, whereas water continues to diffuse more slowly.

Unlike the horizontal dilution line, where the mass ratio of octanol to ethanol increases, the ethanol-to-octanol ratio remains constant along (DL_{water}). As one moves from left to right in the phase triangle (increasing octanol content), ethanol content also rises. However, since only a limited fraction of ethanol strongly interacts with octanol, the presence of excess ethanol allows more free ethanol molecules to diffuse, leading to a subtle increase in its diffusivity, similar to octanol. This shift in ethanol's behavior, in contrast to the horizontal line where its diffusivity remains nearly constant, highlights the fraction of ethanol that strongly interacts with octanol.

For the second diagonal line ($DL_{octanol}$), analyzed using fully hydrogenated samples

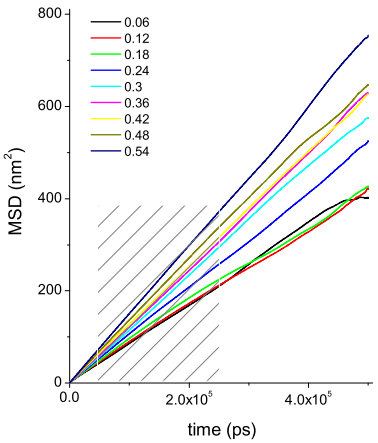

Figure 5.5: *Mean square displacement of octanol for different mass fraction along the horizontal line, obtained from MD simulations. The average is taken over all molecules. Further averaging is achieved by repeating the analysis,* $\Delta r_i^2(t) = (\mathbf{r}(t+\tau_i) - \mathbf{r}(\tau_i))^2$ *with the zero time* τ_i *in multiples of 100 ps. The region used for the computation is greyed out.*

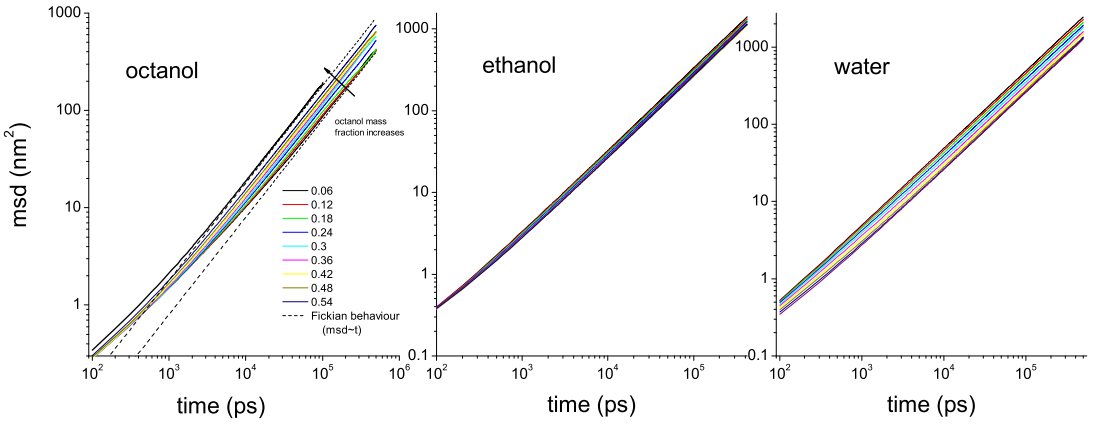

Figure 5.6: *Mean square displacement of octanol, ethanol and water obtained from MD simulations.*

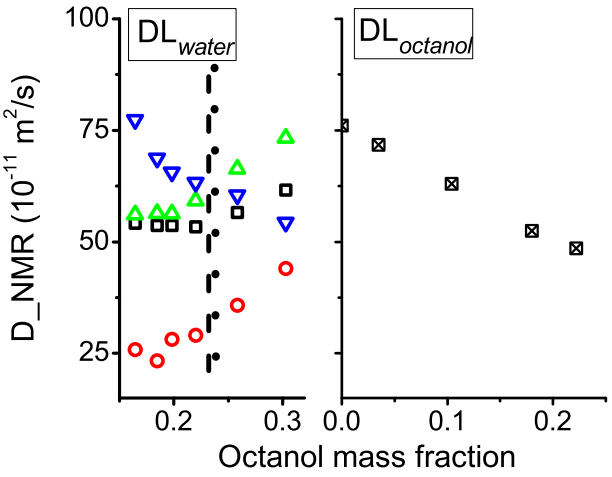

Figure 5.7: *Diffusion coefficient extracted from PFG-NMR (^1H) measurements on the two diagonals DL_{water} and $DL_{octanol}$ (left and right respectively). The black squares represent the all-hydrogenated samples, while the other symbols correspond to individual species: hydrogenated n-octanol (red circles), ethanol (green upward triangles), or water (blue downward triangles), with the other two components being deuterated. The vertical dotted line represents the Lifshitz line (LL) proposed by Prevost et al. [120], while the dashed line corresponds to a mass ratio of octanol to water equal to 1. Both lines nearly coincide for DL_{water} and fall outside the range for $DL_{octanol}$. Error bars are smaller than the symbols.*

only, the overall diffusivity gradually decreases with increasing octanol content, which aligns with the expected rise in viscosity along this path. Since most samples along this line fall within a similar composition range as the horizontal line and DL_{water}, individual characterization using deuterated mixtures of the three components was not deemed necessary.

To summarize, in the case of ethanol-water *binary mixture*, the dynamics are dominated by water's robust hydrogen-bond network, whereas the ethanol-octanol binary features weaker hydrogen bonding, resulting in enhanced ethanol diffusion at larger scales and fluidized dynamics for octanol.

In the octanol-ethanol-water *ternary system*, PFG-NMR data reveal distinct dynamic behavior in pre-Ouzo aggregates compared to non-pre-Ouzo ones. Water transitions from continuous to trapped dynamics, while octanol exhibits the opposite trend. Molecular dynamics simulations support this observation, emphasizing the role of mesoscale structuring in influencing system dynamics. The subtle transitions near the Lifshitz line further reinforce the direct link between mesoscopic structuration and dynamic properties, as demonstrated by the correlation between SAXS structural data and NMR measurements.

Characterizing specific interactions in ternary systems is challenging due to the coupled variations in composition. However, within the pre-Ouzo droplet region, which is believed to terminate at the Lifshitz line (LL), subtle dynamic changes at the molecular

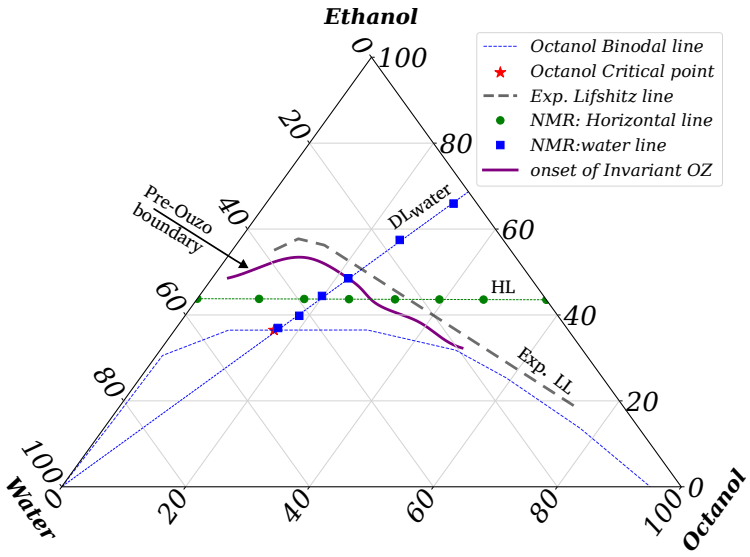

Figure 5.8: *Ternary phase diagram illustrating the intersection of the pre-Ouzo boundary with the NMR lines—the horizontal line (HL) and the water diagonal line (DL_{water})—which corresponds to the jumps in the diffusion coefficient shown in Figures 5.3 and 5.7.*

scale can be observed. Figure 5.8 shows the experimental LL position and the boundary of the pre-Ouzo region (as determined in the previous chapter from SAXS autodilution experiments), along with the locations of NMR samples along the horizontal line (HL) and the water diagonal line (DL_{water}). Notably, as the samples cross the pre-Ouzo boundary, distinct transitions in dynamics are revealed by NMR data, as indicated by changes in the diffusion coefficient (Figures 5.3 and 5.7). This shift marks the transition between pseudo-phases, a consistent trend observed across various samples. It suggests that at the onset of the pre-Ouzo region and the Lifshitz line, structural changes within the system influence the dynamics of the components.

5.2 Neutron Spin Echo Analysis

While PFG-NMR offers a reliable assessment of diffusion dynamics at larger length scales, Neutron Spin Echo (NSE) serves as an effective tool for probing dynamics at much shorter scales. *Coherent* neutron scattering results from the interference of waves scattered by different particles at distinct times, providing direct insights into translational dynamics relative to the structure, commonly referred to as collective motions. At small distances (high q values, corresponding to scales close to or smaller than molecular dimensions), the collective diffusion coefficient aligns with the self-diffusion coefficient. However, at larger distances, collective diffusion reflects the motion of groups of molecules and becomes influenced by characteristic correlation lengths. This distinction leads to differences between self and collective diffusion within aggregates. For a size distribution of aggregates, the corresponding distribution of collective diffusion coefficients, D_c, can be described using the Stokes-Einstein relation:

$$D_c = \frac{k_B T}{6\pi\eta R}. \tag{5.1}$$

In the mesoscale structured region, the droplet size significantly impacts collective diffusion, with smaller droplets exhibiting faster diffusion. Additionally, the intensity of coherent scattering is affected by the particle's form factor. For aggregates characterized by a wide size distribution, described by the Ornstein-Zernike (OZ) distribution with a mean value of 2–3 nm, the contribution to scattered intensity is dominated by larger aggregates probed at small q. As a result, these larger aggregates reduce the measured diffusion coefficient due to their slower motion.

To explore the effects of pre-Ouzo structuring at this scale, we conducted NSE measurements on the octanol-ethanol-water ternary systems. In the NSE fitting procedure, we use self-diffusion data from NMR to constrain incoherent diffusion, simplifying the fit function and improving the accuracy of the coherent diffusion data extracted from the fits.

Additionally, we use a combination of hydrogenated and deuterated compounds to enhance the contrast and isolate the diffusion dynamics more effectively.

5.2.1 NSE of Octanol-Ethanol-Water Ternary System

For the octanol-ethanol-water ternary system, Figure 5.9 shows the diffusion coefficient measured by NSE over the q-range of 0.02–0.5 Å^{-1}, corresponding to distances between 30 and 1 nm. Two points in the phase diagram were characterized: one in the pre-Ouzo region (left side), where large fluctuations occur, and one in the octanol-rich region, beyond the boundaries of the pre-Ouzo region (right side). The diffusion coefficients of all three components (water, ethanol, and octanol) at the point in the octanol-rich region are shown in the right plot of Figure 5.9, along with the intensity at zero time, which is directly proportional to $S(q)$. While the diffusion coefficients vary over q, the amplitude

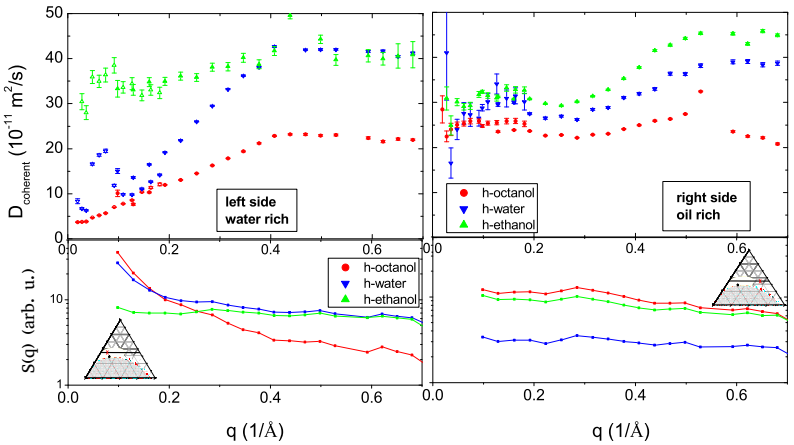

Figure 5.9: *Collective diffusion coefficient (**Top**) and corresponding intensity at zero time, S(q) (**Bottom**), measured by NSE as a function of momentum transfer for different contrasts. The measurements correspond to points on two sides of the phase diagram, each representing a different organizational state of the mixtures: **Left** - near the critical point in the pre-Ouzo domain; **Right** - outside the pre-Ouzo region. Data were collected on IN15 (empty symbols) and WASP (filled symbols) at the ILL, France. The same y-scales are used for both samples to facilitate direct comparison.*

of these variations is limited.

In colloidal solutions, the scale-dependent collective diffusion constant and the structure factor are typically related as:

$$D_c(q) = \frac{D_0}{S(q)}, \tag{5.2}$$

Where D_0 is the self-diffusion coefficient. A relationship known as de Gennes narrowing, stemming from de Gennes' research on quasi-elastic neutron scattering in liquids. For the point in the oil-rich side, a dip is observed at 0.3 $Å^{-1}$, indicating a slowdown in dynamics before the value rises again. This dip coincides with the broad peak in the structure factor $S(q)$, which reflects the de Gennes narrowing effect in the dynamics. In this context, the diffusion coefficient is expected to exhibit an inverse relationship with the intensity of the correlation peak in $S(q)$, as demonstrated in the lower part of figure 5.9.

In the left region, near the critical point/pre-Ouzo organization, we observe distinct behaviors among the three components. Water and octanol exhibit similar behaviors, which can be attributed to their contrast. Since octanol and water do not mix, the contrasts between hydrogen and deuterium (H/D or D/H) lead to similar signals. The diffusion coefficient varies by almost an order of magnitude across the probed q range. In the high-q limit, the plateau value differs, as the measured diffusion coefficient corresponds to the individual behavior of water and octanol. On the other hand, ethanol, which is distributed over both phases (inside and outside the droplets, although in different proportions), exhibits the de Gennes narrowing phenomenon only around 0.2-0.3

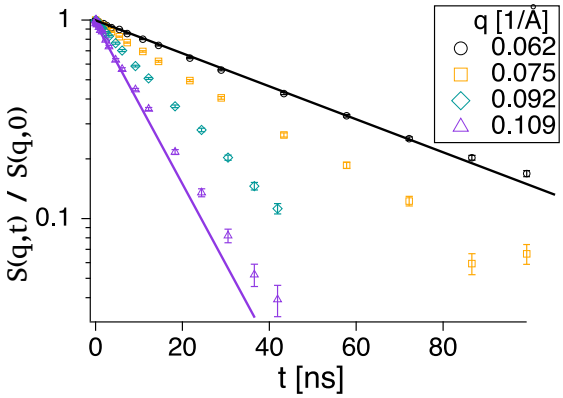

Figure 5.10: *$S(q,t)$ for different values of q of a sample in the pre-Ouzo region (sample on the left side of figure 5.9). The data deviates from single exponential (straight line) for q larger than $\sim$ 0.1 Å^{-1}.*

Å^{-1}.

Lifetime of the aggregates: The diffusion coefficient is determined by fitting an exponential decay to the data $S_{coh}(q,t)$ for various values of q. Well-chosen examples are presented in Figure 5.10. As noted by Roosen-Runge et al. [167], diffusion in heterogeneous media can be modeled in two extreme cases, corresponding to aggregates with either short or long lifetimes. If the aggregates have a *short lifetime* compared to the diffusion time, the measured diffusion coefficient, $\bar{D}$, represents an *average* of the individual diffusion coefficients D_i across different media. In this case, the signal follows a *single exponential decay*, expressed as:

$$S_{fast}(q,t) = \exp\left(-\sum_{i=0}^{N} c_i D_i q^2 t\right) = \exp\left(-\bar{D}q^2 t\right) \tag{5.3}$$

This equation represents the *sum of all intra-domain correlation functions*, where each term is weighted by the equilibrium fraction c_i of particles within a given domain. This is typically the case for the low q-range in our experiments, where the observation time is long due to the large distances involved. For our case, this holds true up to a wave vector of $q = 0.09$ Å^{-1}, where the characteristic diffusion time is about 30 ns.

On the other hand, if the lifetime of the aggregates is *longer* than the probed diffusion time, the signal is a *sum* of exponential terms originating from diffusion in different media.

$$S_{\text{slow}}(q,t) = \sum_{i=0}^{M} c_i \exp\left(-D_i q^2 t\right) \tag{5.4}$$

This results in a non-exponential signal, as observed in the high q-range (in Figure 5.10), i.e., above $\sim$ 0.1 Å^{-1}, with the diffusion characteristic time being approximately 10 nanoseconds at this distance. Based on these two limits, we can estimate the lifetime of the *pre-Ouzo* aggregates to be around 20 ns.

This timescale can be compared to cases involving stronger aggregation, such as the

lifetime of surfactant micelles. Pioneering work by Aniansson et al. [168] described the dynamics of surfactant micelles with two timescales: a 'fast' one associated with the exchange of molecules between adjacent aggregates and a 'slow' one related to the micellization/dissolution process. These timescales differ by two orders of magnitude, with the fast timescale in the microsecond range.

Close to the critical point, a timescale linked to critical fluctuations can also be defined, which is directly related to exchange and dissolution in a critical region where the two phases coexist. This timescale has been characterized in solutions similar to our study, such as the ternary mixture of dodecane/N,N'-dimethyl, N,N'-dibutyl tetra decyl malonamide (DMDBTDMA) and aqueous $Ce(NO_3)_3$ [169], where it is found to be in the microsecond range. Only one time constant is extracted, suggesting that critical fluctuations dominate the dynamics at this composition, encompassing all dynamical processes. In this context, our ultrasoft aggregates, composed of much smaller molecules, exhibit dynamics that are two orders of magnitude faster than those of classical surfactant micelles or metal-extractant complexes in oil.

While the pre-Ouzo aggregates exhibit a varying coherent diffusion across the q scale, the diffusion rates remain nearly constant on the right side of the phase triangle (see Figure 5.9), where W/O *reverse aggregates* dominate the system. The timescale of these diffusing entities can be estimated at relatively high q ($\sim 0.7\,\text{Å}^{-1}$) using the relation $T \sim \frac{1}{Dq^2}$, where the diffusion coefficient $D \approx 30 \times 10^{-11}\,\text{m}^2/\text{s}$ corresponds to a lifetime of less than 70 ps.

Dynamics of Hydrotrope (Ethanol) in Octanol-based Ternary System:

In the pre-Ouzo region, where the water content is higher than octanol, ethanol engages in stronger hydrogen bonding with water molecules. This interaction leads to similar diffusion behavior at smaller length scales (around $q = 0.6$ Å^{-1}; Figure 5.9, Top Left). However, at larger length scales ($q = 0.1$ Å^{-1}), ethanol diffuses more rapidly than both water and octanol. The flatter diffusion curve across length scales suggests that ethanol experiences fewer constraints from the oil phase, allowing relatively free movement. This behavior highlights ethanol's transient role as a dynamic interface between the oil core and the surrounding water medium, continuously moving in and out of the core.

In the oil-rich region, ethanol aligns with the behavior of octanol molecules within reverse aggregates. The hydroxyl group interactions between linear octanol and ethanol promote the formation of worm-like chains, compelling ethanol molecules to move in sync with octanol. Across both regions, ethanol diffuses faster than octanol due to its smaller size and less restricted motion. Further, in both the pre-Ouzo and oil-rich regions, ethanol consistently exhibits a higher diffusion coefficient than octanol.

Overall, the NSE experiment reveals distinct diffusion behaviors in ternary systems. For samples on the left side of the phase triangle and close to the critical point (CP) in octanol-based ternary system, the oil component exhibits a diffusivity trend similar to that of the trapped component i.e. the diffusion coefficient increases with q, indicating the presence of pre-Ouzo aggregates. On the right side of the phase triangle, outside the pre-Ouzo region, this trend is not observed. The overall magnitude of the diffusion coefficient is higher for non-pre-Ouzo samples, as the oil in the oil-rich region moves freely, in contrast to the constrained motion of oil molecules trapped and forming the pre-Ouzo droplets.

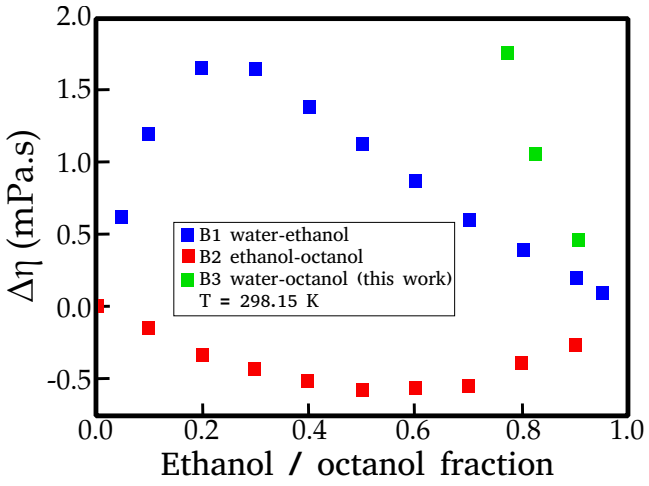

Figure 5.11: *Excess viscosity for the three binary mixtures in ethanol or octanol mole fraction in their miscibility range. Data for the water-ethanol and ethanol-octanol are taken from references [170] and [171] respectively.*

5.3 Investigation of Viscosity Behavior of SFME

To understand the macroscopic effects of SFME organization, we performed viscosity measurements for the octanol-ethanol-water system. Viscosity is a property directly related to the molecular dynamics and, consequently, the structural organization of the system components.

To visualize this, we calculate the excess viscosity ($\delta\eta$), which provides a good estimate of the deviation of viscosity in the mixture compared to its ideal value. The ideal viscosity, η_{ideal}, is given by:

$$\eta_{\text{ideal}} = \sum x_i \eta_i \tag{5.5}$$

where x_i represents the mole fraction of component i, η_i is the viscosity of the pure component i, and the sum runs over all components in the mixture. The excess viscosity $\delta\eta$ is then calculated as:

$$\delta\eta = \eta_{\text{measured}} - \eta_{\text{ideal}} \tag{5.6}$$

5.3.1 Results and Discussions

Binary Ethanol-Water/Octanol Mixture

At 20°C, octanol is much more viscous (7.36 mPa.s) compared to water and ethanol, which have viscosities of 1.0 and 1.2 mPa.s, respectively. In mixtures, the excess viscosity—a measure of how much the mixture's behavior deviates from ideal case—is similar in magnitude to the viscosities of the pure substances.

In the octanol-ethanol mixture, ethanol acts as a fluidizer, lowering the viscosity and resulting in negative excess viscosity. Conversely, the ethanol-water mixture exhibits pos-

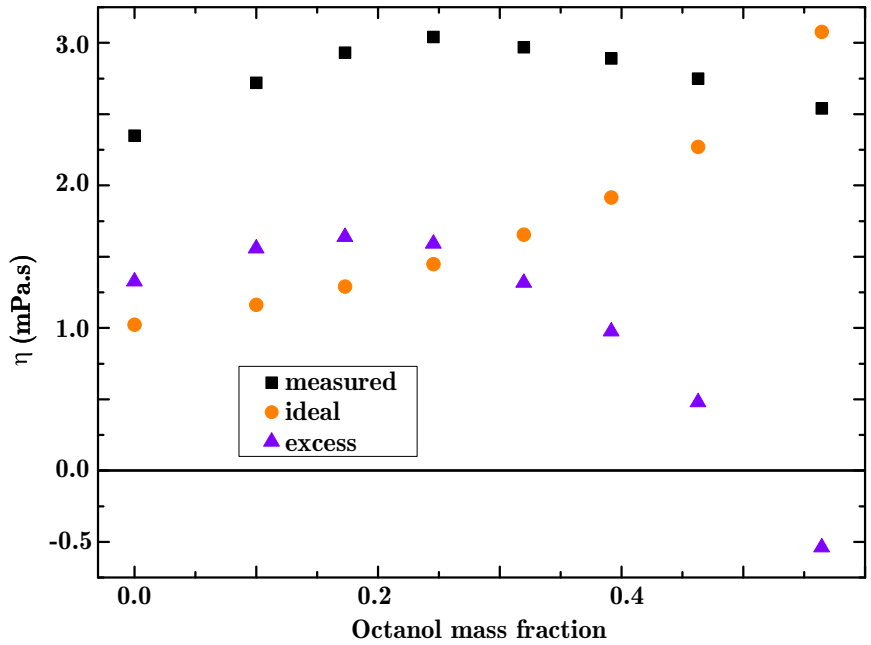

Figure 5.12: *Shear viscosity (black squares), ideal viscosity (orange circles) calculated as the weighted average of pure solvent viscosities, and the excess viscosity (violet triangles) showing deviations from the ideal values for the horizontal dilution line $DL_{horizontal}$ for the octanol-ethanol-water ternary.*

itive excess viscosity, likely due to water's strong hydrogen-bond network. These binary systems provide key insights into the nanoscale structure and dynamics of the ternary water-ethanol-octanol system, driven by the interactions between these components.

Rheology of the Ternary System

The shear viscosities of the octanol-ethanol-water ternary system are plotted against the octanol mass fraction in Figure 5.12. Along the horizontal line of the ternary diagram (corresponding to the green line in the phase triangle shown in Figure 5.1), the viscosity exhibits non-monotonic behavior as the octanol content changes. Specifically, moving from right to left along this line (as water content increases and octanol content decreases), the viscosity rises and reaches a maximum value more than twice that of an ideal solution.

Similarly, we measured the viscosity of the octanol ternary system along a different direction to validate our findings. The two selected diagonal lines follow a composition pattern similar to that described in the NMR section (Figure 5.1), where a binary mixture—either octanol-ethanol or water-ethanol—is progressively enriched with the third component to create new sample compositions. As observed for the samples along the horizontal line, viscosity increases near the pre-Ouzo region and close to the critical point, exhibiting a significant positive excess viscosity (Figure 5.13).

Positive excess viscosities are common in water-organic mixtures, such as water-alcohol or water-DMSO systems. For example, in water-ethanol mixtures, viscosity is

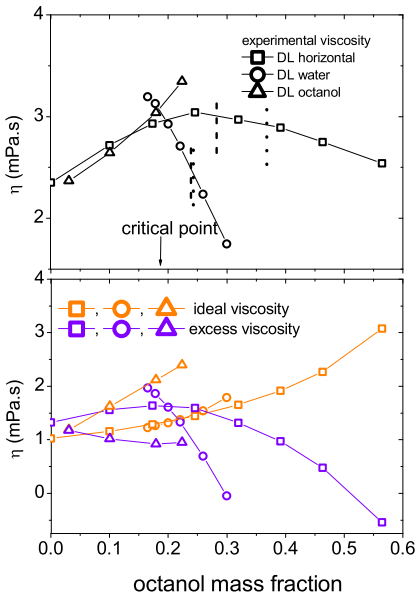

Figure 5.13: ***Top**: Shear viscosity measurements for the horizontal dilution line $DL_{horizontal}$ (squares), water dilution line DL_{water} (circles), and octanol dilution line $DL_{octanol}$ (triangles). Vertical dotted lines mark the estimated position of the dynamical Lifshitz line, with the critical point also highlighted. Dashed lines indicate the location where the octanol-to-water mass ratio equals 1.* **Bottom**: Ideal viscosity, calculated as the weighted average of the pure solvent viscosities, and the excess viscosity, showing deviations from the ideal values.*

inversely proportional to the diffusion coefficient, as predicted by the Stokes-Einstein relation, $D = \frac{k_B T}{6\pi\eta R}$, where R is the molecular size and η is the viscosity [172]. However, this relationship does not hold in the current system.

The observed viscosity increase can be compared to the effect of adding hard spheres to a solvent. According to Einstein's prediction, viscosity increases with the volume fraction, following the relation $\eta = \eta_0(1+2.5\phi)$, where ϕ is the volume fraction. For droplets composed of 20% octanol and 20% ethanol, this predicts a viscosity approximately twice that of the ethanol-water mixture ($\eta \sim 2.0$ mPa.s). While this estimate is likely high due to the transient and soft nature of the droplets, it is slightly larger than the measured value.

We propose that the positive viscosity excess, which reverses trend at the boundary between the pre-Ouzo and inverse aggregate region, arises from the structural organization of the solution. This suggests that viscosity in this system is not governed solely by the dynamics of individual molecules.

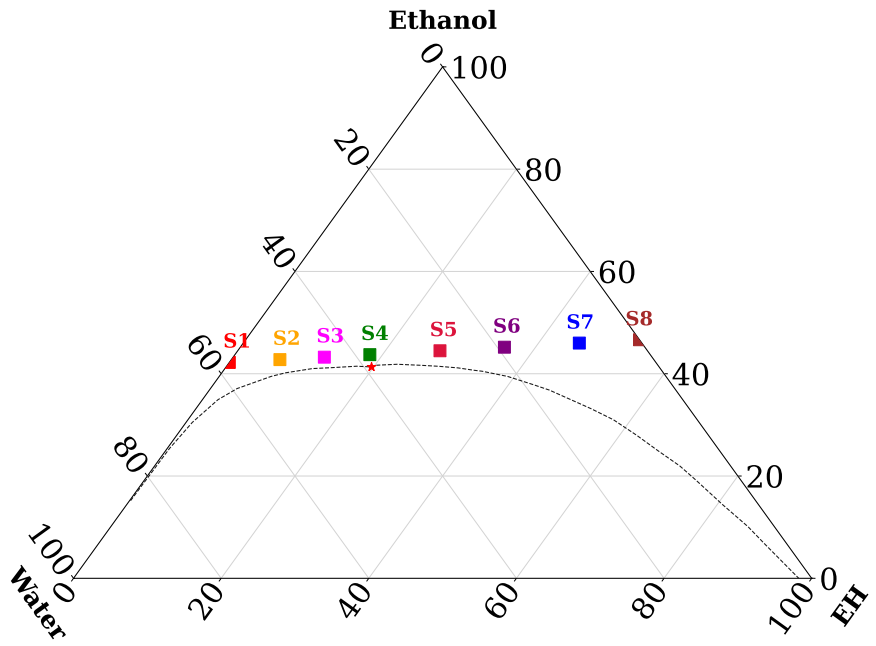

Figure 5.14: *NSE sample points for the EH-based ternary system plotted on the phase triangle. The samples are in mass fractions and correspond to fully hydrogenated compositions.*

5.4 Additional Investigations on Complementary Systems

In this section, we extend the investigation to two additional ternary systems to assess the universality of the pre-Ouzo phenomenon. This includes substituting the oil in the octanol-based ternary system to examine its influence and exploring a distinct ionic hydrotrope-based ternary system. While these preliminary explorations provide insight into broader trends, a more comprehensive analysis is necessary to fully establish the generality of the observed behavior.

5.4.1 NSE study of 2-Ethyl Hexanol-Ethanol-Water Ternary

After characterizing the dynamical properties of the octanol-ethanol-water ternary system, the next step involved replacing the oil component with 2-ethyl hexanol in the ternary mixture. This analysis aimed to explore how substituting a linear-chained oil with a branched counterpart affects dynamics, particularly due to pre-Ouzo structuration. This choice was driven by the same rationale that led to the use of 2-ethyl hexanol for SAXS structural analysis, as discussed in the previous chapter. NSE measurements for the 2-ethyl hexanol-ethanol-water ternary system were performed on the samples shown in Figure 5.14, all of which correspond to a constant ethanol volume fraction. For contrast-based studies in NSE, a combination of hydrogenated and deuterated samples was used. Samples S4 and S7 were analyzed on IN15 for both oil and hydrotrope con-

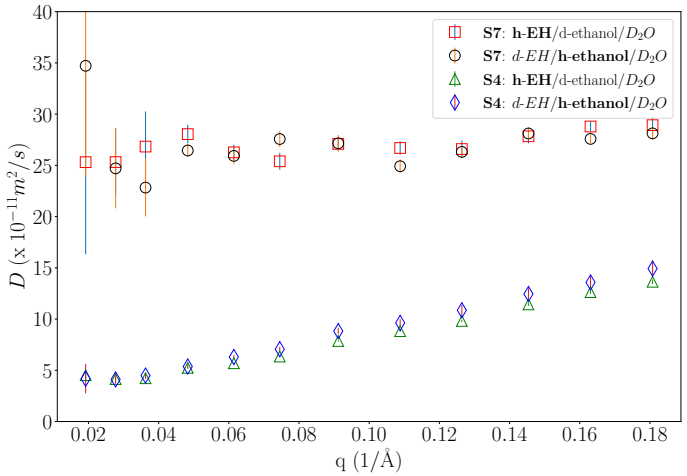

Figure 5.15: *Collective diffusion coefficient from IN15 analysis of the 2-ethyl hexanol-ethanol-water ternary system. The contrast naming format is oil-ethanol-water: HDD indicates hydrogenated oil with deuterated ethanol and water, while DHD represents deuterated oil and water with hydrogenated ethanol. For sample* S4 *(pre-Ouzo region), the diffusion increases with increasing q (decreasing length scale), suggesting faster dynamics at smaller length scales and trapped molecule dynamics at larger scales. In contrast, for sample* S7 *(oil-rich region), the diffusion coefficient of oil remains constant across all q, indicating a continuous oil medium.*

trasts, while the WASP analysis covered samples S2 to S8 in the oil contrast and samples S3, S5, and S7 in the ethanol contrast (composition details are provided in Table A.15).

Since the NSE data for 2-ethyl hexanol is fitted using a model with a free parameter, without incorporating the corresponding self-diffusion data from NMR analysis to constrain the incoherent diffusion coefficient, the interpretation should be considered with caution.

Samples inside the pre-Ouzo region: From Figures 5.15 and 5.16, it is evident that all samples near the critical point, i.e., those in the pre-Ouzo region (S2-S4), show an increase in the diffusion coefficient as q increases. This suggests that at larger length scales, the oil (EH) dynamics are slower, corresponding to the formation of pre-Ouzo droplets. As the length scale decreases, the molecular dynamics of the oil, which are faster, come into play. Furthermore, comparing the trends from IN15 to WASP, which cover a q-range from 0.019 Å^{-1} to 0.180 Å^{-1} and 1.04 Å^{-1} to 5.07 Å^{-1} respectively, we observe similar trends in the diffusion coefficient. In the lower q-range (up to 0.15 Å^{-1}), the diffusion coefficient spans from approximately 5×10^{-11} to 10×10^{-11} m^2/s. From $q = 0.15$ Å^{-1} to 0.5 Å^{-1}, D reaches a plateau value of 20×10^{-11} m^2/s. This behavior mirrors the dynamics of trapped molecules within droplets, indicating that the oil's dynamics are governed by the structuration within the ternary system.

Samples outside the pre-Ouzo region: For ternary samples that lie outside the pre-Ouzo region (S5-S7, Figure 5.16), the dynamics transition gradually from those of

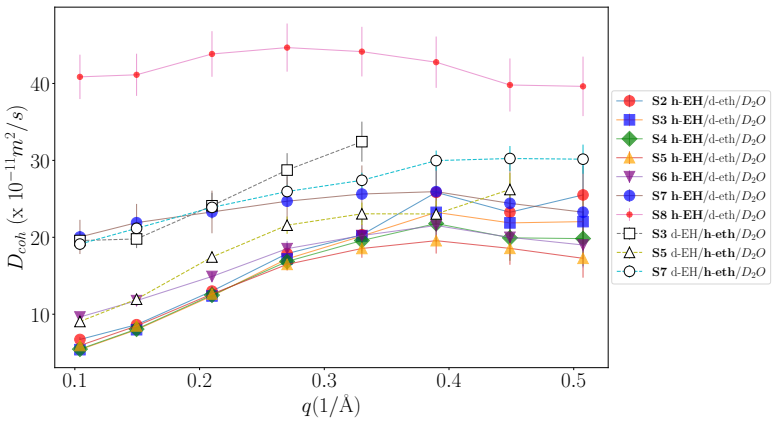

Figure 5.16: *Coherent diffusion coefficient from WASP analysis of the 2-ethylhexanol–ethanol–water ternary system. The contrast naming follows the oil–ethanol–water format, where 'h-' and 'd-' denote hydrogenated and deuterated species, respectively. For the oil contrast, diffusion increases slightly with q in the pre-Ouzo region, while* S7 *in the oil-rich region remains stable. Oil diffuses faster in the binary system (*S8*) than in ternary samples, indicating greater restriction in the ternary system. For the hydrotrope contrast, diffusion increases slightly with q across all samples. The sample near the critical point (*S5*) has a lower diffusion coefficient than those in the oil-rich (*S7*) or pre-Ouzo (*S3*) regions.*

a trapped oil molecule to those of a free and continuous oil medium. Specifically, for sample S7, located in the oil-rich region of the phase triangle, the oil dynamics remain relatively flat, indicating the continuous nature of the oil.

Behaviour of Hydrotrope in EH-Based Ternary: From Figure 5.15, at larger length scales (up to $q = 0.18$ Å^{-1}), the dynamics of ethanol molecules resemble those of EH molecules for sample S5 (near the critical point but slightly outside the pre-Ouzo region) and S7 (on the oil-rich side). However, for sample S3 (within the pre-Ouzo region), ethanol exhibits slightly higher diffusivity than EH even at lower q values.

From Figure 5.16, at smaller length scales ($q = 0.2$ Å^{-1} to $q = 0.5$ Å^{-1}), ethanol's diffusivity shows a slight increase with q, and its overall magnitude remains consistently higher than that of EH molecules across all samples, whether within the pre-Ouzo region or on the oil-rich side.

Overall, comparing the dynamics observed for oil, 2-ethyl hexanol ternary, and octanol, they follow a pattern similar to droplet formation for samples within the pre-Ouzo region. In contrast, samples outside this region exhibit more continuous dynamics, resembling a more oil-rich organization. The case of the hydrotrope, ethanol, is somewhat ambiguous for the EH system, and further NMR analysis of the components would help clarify the interpretation of the coherent dynamics.

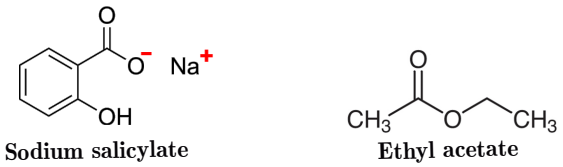

Figure 5.17: *Skeletal representation of sodium salicylate and ethyl acetate molecules*

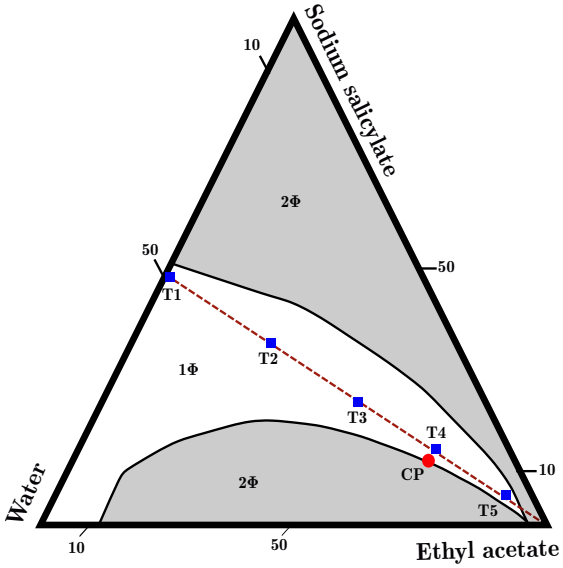

Figure 5.18: *Ternary phase diagram of the ethyl acetate-sodium salicylate-water system, where sodium salicylate functions as the hydrotrope, illustrating the five samples analyzed using NSE. The diagram highlights two distinct biphasic (2ϕ) regions separated by a homogeneous single-phase (1ϕ) region.*

5.4.2 Comparative Study: Ethyl Acetate-Sodium Salicylate-Water Ternary System

To broaden the scope of the research and provide a comparative framework for SFME-based ternary systems, we examined an alternative ternary system: ethyl acetate-sodium salicylate-water, where, Sodium salicylate (SoSa) acts as the hydrotrope. Unlike SFME systems, this system does not exhibit pre-Ouzo structuration near its critical point (CP), offering insights into the influence of hydrotropic interactions on phase behavior [162].

The ionic nature of sodium salicylate inhibits spontaneous emulsification (Ouzo effect) and pre-Ouzo aggregation, resulting in a distinct phase behavior compared to systems containing uncharged hydrotropes. When a water-SoSa mixture with sodium salicylate concentrations exceeding 1M is saturated with ethyl acetate, micellar-like structures form, resembling those observed in solutions of medium-chain surfactants such as sodium octanoate. Interestingly, this structural behavior is comparable to that observed when hydrotropic salts are introduced into classical ternary systems like octanol-ethanol-water [173].

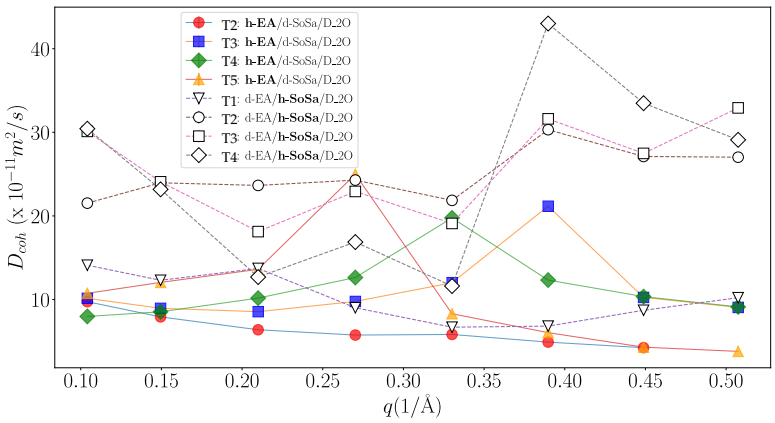

Figure 5.19: *Coherent diffusion coefficients obtained from WASP NSE analysis for both HDD and DHD contrast conditions. In the HDD contrast, 'h-EA' denotes hydrogenated ethyl acetate (EA), while Sodium salicylate (SoSa) and water are deuterated. Sample T2 exhibits a decreasing diffusion coefficient with increasing q, whereas T3 and T4 (the latter near the critical point) show an overall increasing trend with a sudden peak at intermediate q, followed by a return to initial values. In the DHD contrast, 'h-SoSa' represents hydrogenated Sodium salicylate, while EA and water are deuterated. Here, all samples display relatively flat diffusion coefficient distributions across the q-range, with no monotonic trend, indicating no trapped hydrotrope behavior. Sample T4 shows the largest deviation, likely due to critical fluctuations.*

Figure 5.19 presents diffusion data from WASP NSE analysis over a broader q-range. For the EA contrast, samples T3, T4, and T5 (closer to CP) show an abrupt doubling of the coherent diffusion coefficient (D_{coh}) at intermediate q, before returning to initial values. This behavior contrasts with sample T2, where D_{coh} decreases monotonically. In the hydrotrope contrast, samples farther from CP (T1, T2) exhibit monotonic trends, whereas closer to CP, a non-monotonic behavior suggests a freely diffusing hydrotrope. These findings confirm that, unlike SFME systems, the EA-SoSa-water ternary lacks pre-Ouzo aggregation near CP.

When comparing the NSE results from IN15 (Figure 5.20) for the ethyl acetate-based, octanol-based, and 2-ethyl hexanol (EH) based ternary systems: The diffusion coefficient vs q pattern of the ethyl acetate ternary sample (T4) resembles that of a non-pre-Ouzo sample in the octanol and EH-based ternary systems (i.e., sample S7), showing relatively constant diffusion rates across the given q range. In contrast, the pre-Ouzo samples (S2 and S4) from the octanol/EH ternary systems display a q-dependent diffusion pattern, which increases with q, resembling the dynamics of a confined oil droplet.

As alluded to earlier, near the critical point of a system, hydrotrope-based systems may exhibit two major factors contributing to an Ornstein-Zernike-type intensity profile. One arises from the correlation lengths associated with aggregate formation (pre-Ouzo), while the other stems from critical fluctuations.

Interestingly, the ethyl acetate-based ternary system shows an OZ intensity in the

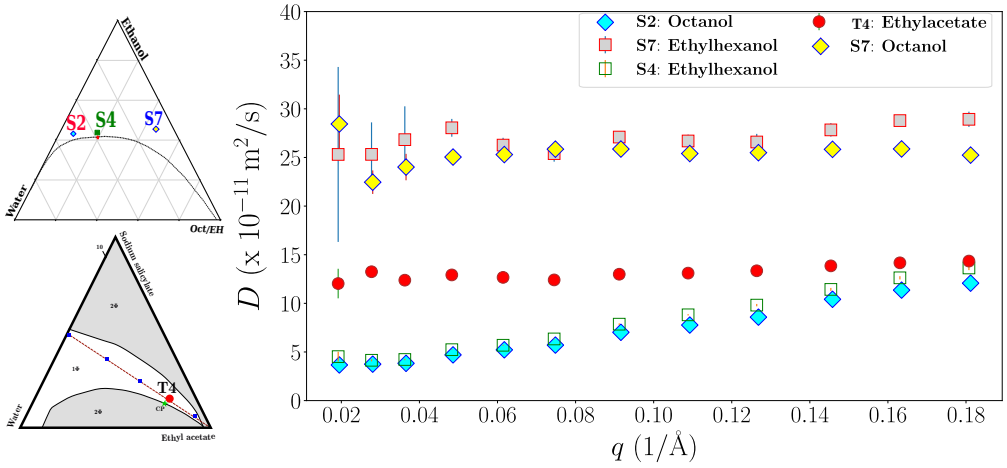

Figure 5.20: *Diffusion coefficients for the ethyl acetate -sodium salicylate-water ternary system, as determined from IN15. The sample near the critical point (T4: Ethyl acetate) of the ethyl acetate ternary shows a nearly constant diffusion rate with q, indicating its free, untrapped nature. This contrasts with the pre-Ouzo sample (S2: Octanol and S4: Ethyl hexanol) of the ethanol-based ternary system. All samples shown here correspond to the oil contrast of their respective ternary systems (ethyl acetate, octanol and 2-ethyl hexanol, respectively).*

SAXS data for sample T4, near its critical point, as studied by Asmae et al. [162]. These OZ intensity are results of critical fluctuations near the critical point rather than pre-Ouzo aggregates. Further, from the dynamics study, we observe that sample T4 does not exhibit pre-Ouzo structuring, as explained earlier. By comparing the dynamics of the ethyl acetate ternary with the octanol/EH-based ternary systems, we can reaffirm that the OZ intensity observed in the SAXS data for the octanol/EH ternary is indeed due to pre-Ouzo aggregation, not critical fluctuations.

While additional studies, such as NMR analysis, could offer more detailed insights into the role of ionic interactions in this ternary system, this investigation primarily served as a comparative study of the SFME pre-Ouzo system. The findings emphasize the crucial role of pre-Ouzo structuration in SFME-based ternary systems and underscore the impact of charged hydrotropes in influencing phase behavior. Furthermore, the differences in dynamics highlight the importance of microstructural organization in molecular diffusion within these systems.

Conclusion

In this thesis, we explored the structural and dynamical characteristics of octanol- and 2-ethyl hexanol-based ternary systems. These systems are capable of forming self-organized structures, including surfactant-free microemulsions (SFME), often referred to as pre-Ouzo aggregates, a term inspired by Ouzo emulsions. Structural analysis was conducted using *in situ* autodilution Small Angle X-ray Scattering (SAXS), while the dynamical properties were investigated across different length scales: Neutron Spin Echo (NSE) and Pulsed-Field Gradient NMR (PFG-NMR) provided insights at the microscopic level, and rheological measurements were used to probe the macroscopic dynamic behavior.

Several studies in the literature have explored ternary systems with a focus on the SFME structures. However, most research has either examined Ouzo emulsions in the biphasic region or characterized SFMEs in these systems using microscopy, Dynamic Light Scattering (DLS) and particle tracking methods [158, 174–176]. While DLS is a straightforward technique for identifying such structures, it becomes less reliable for pre-Ouzo mesoscopic structures, as even trace amounts of micron-sized impurities can complicate measurements. However, a comprehensive study of the different phases, particularly with a focus on mesostructuration, has been relatively unexplored in the literature. Prevost et al. [120] investigated an octanol–hydrotrope-based ternary system along a single dilution line using Small-Angle Scattering techniques, revealing that pre-ouzo droplets coexist with Ouzo emulsions within the metastable region of the phase triangle. Building on their work, this study mapped the complete phase triangle of a surfactant-free ternary system, providing a deeper understanding of the various pseudo-regions formed by the oil-water mixture with a hydrotrope.

Small-Angle X-ray Scattering (SAXS) proved to be an invaluable tool for investigating the structural organization of the octanol–ethanol–water ternary system, allowing us to map out distinct regions within the phase diagram. We identified the pre-Ouzo region on the water-rich side and the predominantly reverse aggregate region on the oil-rich side. Using the intensity maxima of the Ornstein-Zernike term, we were able to pinpoint the phase separation points along the binodal line. Additionally, our experimental analysis enabled the determination of the Lifshitz line (LL), which, interestingly, deviates from the previously proposed straight path and instead takes on a bent shape (see Figure 5.21).

Prevost et al. [120] previously proposed that the LL follows a straight path, assuming that the polar/unpolar partitions of the two coexisting microphases can be determined

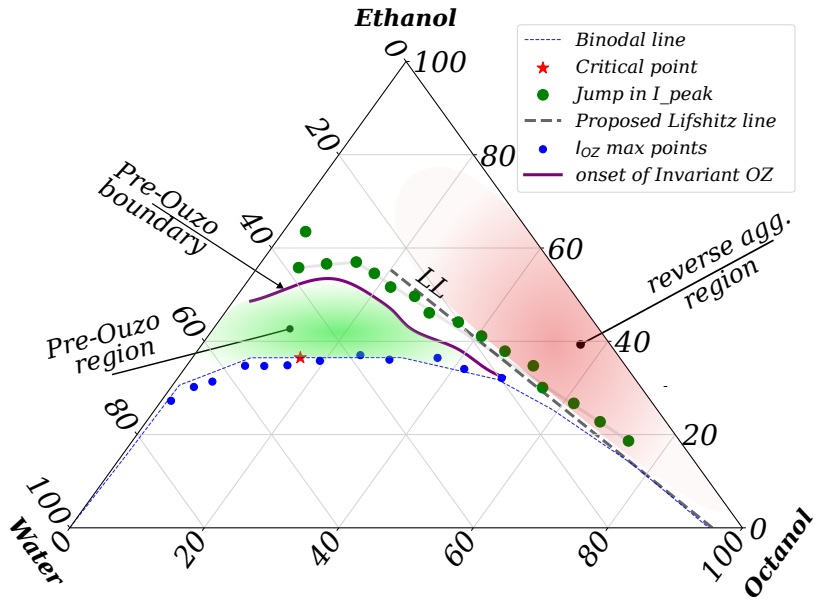

Figure 5.21: *Ternary phase diagram of octanol, ethanol, and water, summarizing key findings from the SAXS autodilution experiment: phase separation points (i.e., maxima of OZ intensity), the experimental Lifshitz line (i.e., jump points in pre-peak intensity), and the boundary of the pre-Ouzo region (marked by the onset of invariant values for the OZ term). The diagram also highlights the pre-Ouzo region and the reverse aggregate region, as observed in the dynamics study of the ternary system.*

by extending a tangential line to the binodal curve, starting from no hydrotrope point. In their framework, the LL acts as a transition boundary between a water-swollen, oil-rich domain (W/O), where the mixture retains characteristics of the binary alcohol solution, and a water-rich domain (O/W), where aggregates form without an amphiphilic film [121].

Our findings, however, indicate that the LL is not a straight line extending to the water-hydrotrope binary. Instead, it follows a curved trajectory, suggesting that the transition from W/O to O/W does not occur along a straight path. This deviation arises from the complex interplay between oil and water in the presence of a hydrotrope, which influences the structural organization of the system. Beyond the LL, the pre-Ouzo boundary—characterized by the onset of the OZ invariant quantity—marks the region where pre-Ouzo aggregates begin to form. Between these two lines, there exists a transition zone where the dominant reverse aggregate signature from alcohol molecules diminishes, but mesoscale aggregation is not yet sufficient to identify pre-Ouzo aggregates.

Furthermore, we observed subtle yet distinct structural differences arising from the presence of a branched oil molecule (2-ethyl hexanol). Unlike the octanol-based ternary system, which exhibits a sharp transition from reverse aggregates to the pre-Ouzo structure, this transition occurs more gradually in the 2-ethyl hexanol system. This behavior suggests that the emergence of the pre-Ouzo phase is influenced by a delicate balance

between the mesoscopic and nanoscopic organization of the oil, with molecular branching playing a key role in altering the system's structural evolution.

Another aspect of this study focused on exploring the effect of temperature on pre-Ouzo aggregates using SAXS. The results show that these aggregates tend to dissolve or shrink in size as the temperature increases, only to reassemble upon cooling. However, the proximity to the critical point and binodal line significantly influences the aggregation behavior. When the system is closer to the binodal line, the aggregate size follows a distinct hysteresis pattern—shrinking further upon heating but expanding beyond its original size upon cooling. This behavior is attributed to the initial transition of the sample into the biphasic region, which causes differences in the spontaneous mixing during heating and cooling cycles.

We then sought to identify the signature of the structuration through dynamics. Using PFG-NMR, we observed changes in the self-diffusion behavior of the components as the system crossed the pre-Ouzo boundary line, which had been previously identified from SAXS data. In the pre-Ouzo region on the water-rich side, octanol molecules exhibited lower self-diffusion rates than water, indicating their trapped nature. As the system shifted to the oil-rich side, octanol diffusivity increased slightly, while water molecules exhibited restricted diffusion, indicating the formation of reverse aggregates. In both pseudo-phases on either side of the phase triangle, ethanol diffused at a similar rate.

Neutron Spin Echo (NSE) data was useful in terms of revealing the dynamics of the system, with the incoherent signal providing insights similar to those observed by NMR. The coherent signal, on the other hand, highlighted collective behavior associated with the formation of oil aggregates. In the pre-Ouzo region, where oil molecules aggregate within the water-rich environment, oil diffusivity decreases as the probed length scale increases. In contrast, for samples that do not form pre-Ouzo aggregates, this trend is absent, and a flatter dependence on q is observed, indicating a continuous medium. This behavior was observed in both octanol- and 2-ethyl hexanol-based ternary systems.

To further complete the dynamics study of the ternary systems, we conducted rheological measurements. The results revealed an increased viscosity excess for the pre-Ouzo aggregates, indicating that the observed dynamical behavior is not solely governed by the individual molecular properties. Instead, the macroscopic organization of the system plays a significant role in influencing viscosity, a bulk property of the system.

Overall, this study provides valuable insights into the characterization of microemulsions formed using hydrotropes. While the findings are specific to water-monoalcohol ternary systems, they offer a foundational understanding of the diverse pseudo-phases that can exist within seemingly homogeneous ternary mixtures, paving the way for further exploration in similar systems.

Perspectives

Building on the findings of this thesis, there are several potential directions for further research into surfactant-free microemulsions (SFME) using hydrotropes, particularly in water-monoalcohol systems, which could deepen the understanding and broaden the applications of these systems.

Experimental Approach for Temperature-Dependent Studies, PFG-NMR analysis and Extraction Efficiency Testing

The figure 5.22 illustrates our simple temperature-based study of ternary sample preparation and the visual observation of phase transitions. In this experiment, we prepared hundreds of ternary mixtures of ethyl hexanol (EH), ethanol, and water in various ratios and observed their behavior at different temperatures using a thermalized water bath. A transparent homogeneous sample indicated the single-phase region, a turbid sample represented a metastable ouzo phase, and phase-separated samples corresponded to the biphasic region. By marking these observations on the ternary plot, we were able to construct a preliminary binodal line for three temperature cases: 4°C, 25°C, and 55°C. The reduction in the biphasic area with increasing temperature emphasizes the enhanced solubility in the system as the diffusion of components increases.

To better understand the dynamics and structural transitions, it would be beneficial to conduct temperature-dependent SAS studies at fixed temperatures (3-5 points) using a stopped-flow autodilution setup. This experimental approach could provide valuable insights into the reversibility of the phase transitions, particularly in relation to the crossing of the binodal line and the ability of the system to return to its original state at different temperatures. Such studies would offer a deeper understanding of the thermodynamic conditions influencing the formation and stability of pre-Ouzo and related aggregates.

Another method to examine the samples would be by using PFG NMR, where the Δ linked to diffusion times is varied, and the resulting variation in the individual sample components in the partially deuterated ternary mixture is observed. This would provide a detailed analysis of the diffusion behavior of each component over different time scales.

Further, testing the extraction efficiency of the octanol and 2-ethyl hexanol systems using simple temperature-dependent phase separation methods would allow for a direct comparison of their performance in extraction applications. This would provide practical

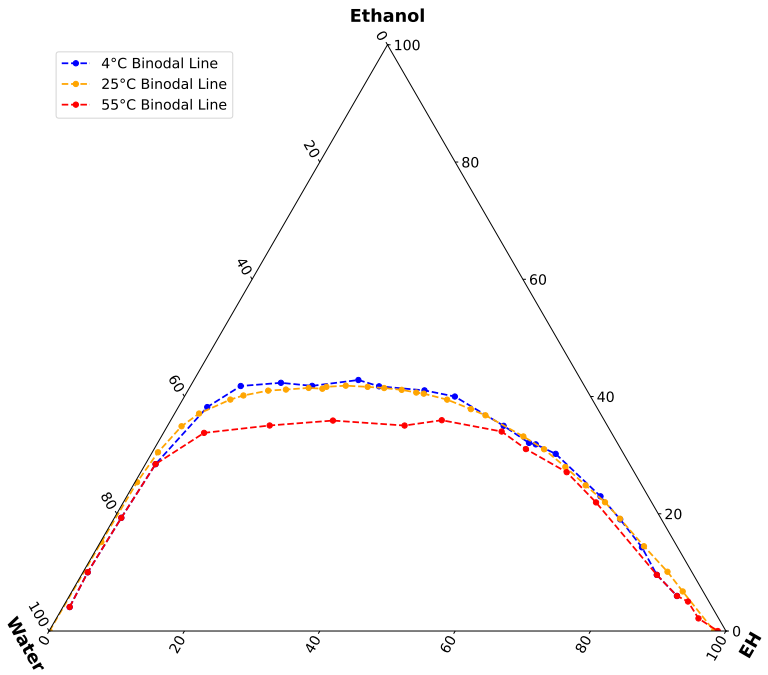

Figure 5.22: *The binodal line of the EH-based ternary shifts downward as temperature increases from 4°C to 25°C to 55°C, reflecting increased solubilization and a reduction in the biphasic region.* *(Note: Due to the limited number of samples studied, the curves for 4°C and 55°C appear less smooth, suggesting the need for further investigation with samples closer to the binodal lines at these temperatures. Few of the data points for 25°C was taken from reference [177].)*

data to assess the feasibility of using these systems in real-world processes and help optimize their formulation for specific applications.

Incorporation of a Fourth (Highly) Hydrophobic Component into the Hydrotrope-Based Ternary System

Incorporating a fourth, highly hydrophobic component, such as decalin, into the ternary system adds further complexity. This hydrophobic component may influence the phase behavior, potentially introducing a new critical point (CP) and giving rise to distinct structural organizations within the system. Understanding these formations and their impact on the phase diagram could be particularly valuable for extraction and solubilization processes, where the highly hydrophobic component is the one being extracted from the ternary mixture. To investigate this effect, studying the system's phase behavior under temperature variations with a trace amount of decalin in the ternary SFME system is beneficial.

A preliminary experiment was conducted to explore this behavior, examining two scenarios: a ternary system with 3% decalin in an octanol-based mixture (see Figure 5.23) and another with 20% decalin in a 2-ethyl hexanol-based mixture. The addition of the fourth component, as discussed earlier, is expected to modify the phase diagram, positioning the selected samples within the biphasic region. However, the precise loca-

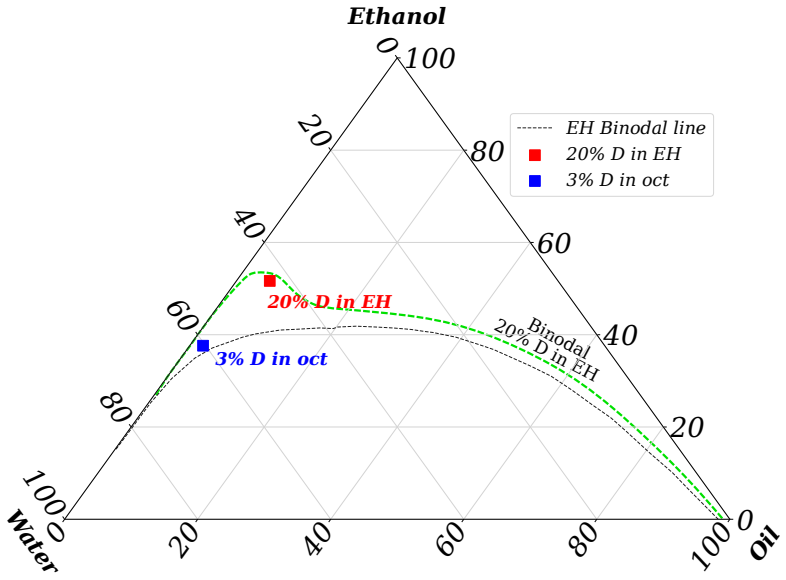

Figure 5.23: *Ternary diagram illustrating the samples containing decalin. The oil phase represents a mixture of the specified percentage of decalin in either 2-ethyl hexanol (EH) or octanol. The binodal line for the 20% decalin in EH ternary system (green dashed line), from [178], is also shown, highlighting a deviation from the standard pure EH-based binodal curve (black dashed line). This deviation places the sample within the biphasic region of this modified phase triangle.*

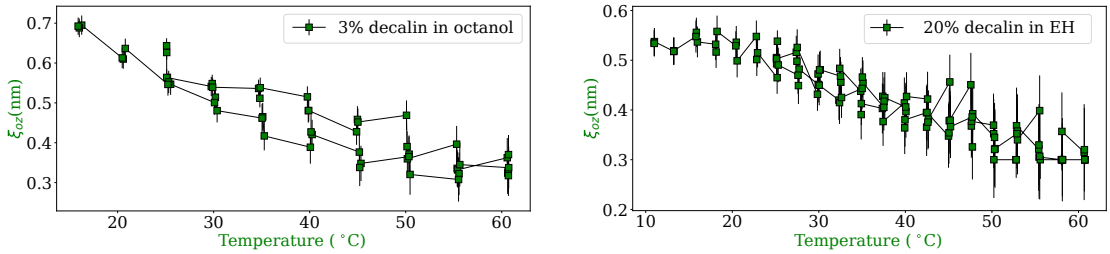

Figure 5.24: ***Left****: OZ length scale parameter for the quaternary system comprising octanol, decalin, ethanol, and water. The oil phase contains 3% decalin in an octanol-decalin mixture with a composition (wt%) of 2.00 oil (decalin + octanol), 37.62 ethanol, and 60.38 water. The ξ_{OZ} value decreases with increasing temperature.* ***Right****: OZ length scale parameter for the quaternary system comprising decalin, 2-ethyl hexanol, ethanol, and water. The oil phase contains 5.01% oil (a mixture of 2-ethyl hexanol and decalin), 51.66% ethanol, and 43.33% water by weight, corresponding to a sample with a total of 20% decalin in EH.*

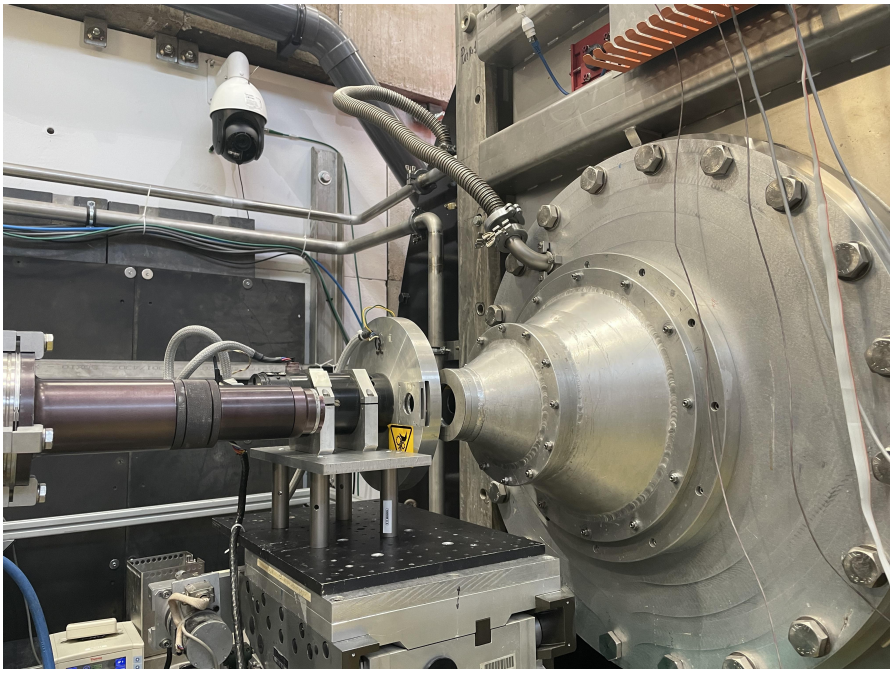

Figure 5.25: *In-situ SANS centrifuge measurement setup at the D22 instrument, ILL.*

tion of the critical point (CP) for this new quaternary system, specifically the octanol-decalin-based mixture, remains unclear. The results indicate relatively lower values of the Ornstein-Zernike (OZ) length scale parameter (ξ_{OZ}), suggesting minimal smaller pre-Ouzo aggregation in the system (see Figure 5.24). However, the ξ_{OZ} trend does not exhibit the smooth pattern seen in the SFME ternary system, likely due to unstable aggregation at this point. Even with increasing temperature, the ξ_{OZ} values did not rise, indicating that the samples either remain in the biphasic region or, if they transition to a monophasic state, the amount of pre-Ouzo aggregation is negligible.

Further investigation of the phase diagram for this quaternary system is required to better understand the influence of various parameters, such as how the phase triangle changes with the addition of a specific amount of the same hydrophobic component. It is also important to determine if sufficient mesoscale stabilization occurs near the system's new critical point (CP), and to examine the temperature-related variations.

Phase Aggregation Induced by Centrifugation: Investigation Using In-situ SANS

The application of external stimuli, such as centrifugal force, can induce phase aggregation, which is crucial for understanding the behavior of complex systems like microemulsions, where gravitational forces typically drive phase separation. In this context, centrifugal force serves as a mechanical driver that facilitates particle aggregation by effectively overcoming electrostatic repulsive forces that normally prevent particles from coming together.

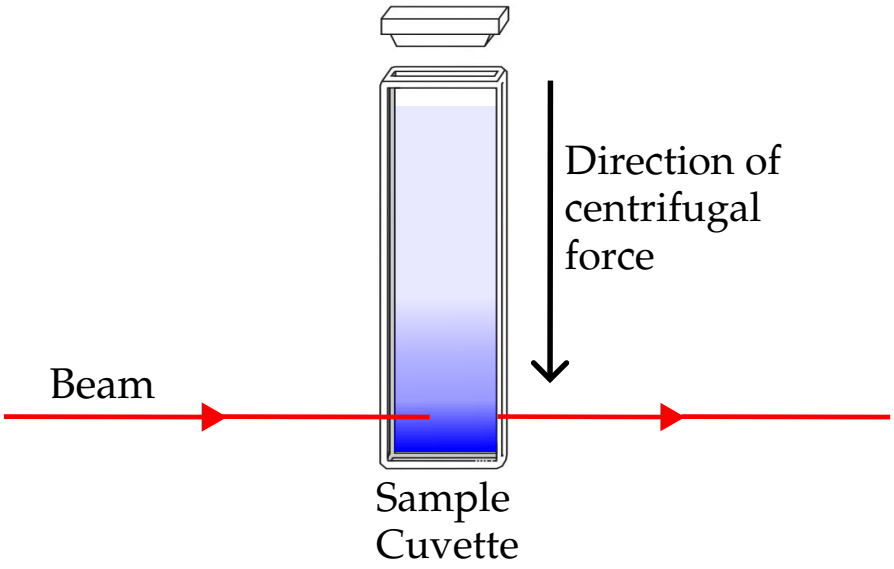

Figure 5.26: *Schematic illustration of a sample cuvette subjected to centrifugal force while positioned in the neutron beam. Aggregation predominantly occurs at the bottom end of the cuvette, where the force is strongest.*

Ultracentrifugation has been a fundamental analytical technique since its invention by Jean Perrin and Theodor Svedberg in 1926 [179], especially for the separation of microparticles and emulsions. However, its impact on microemulsions, particularly in ternary systems, remains an area of limited exploration. Early studies, such as those by Smith et al., have documented unexpected phenomena, including spontaneous emulsification in ternary solutions subjected to centrifugation [180–182]. Despite these observations, theoretical models that explain the behavior of ultraflexible microemulsions (UFME) under centrifugal conditions are still in development. To address this gap, Stemplinger et al. [183] proposed a unified theoretical framework for predicting centrifugation behavior in ternary systems. Their study, which focused on a ternary mixture of ethyl acetate, ethanol, and water, integrated both gravitational and thermodynamic gradients, resulting in a sedimentation/centrifugation map (CMap). This map provides an intuitive guide for understanding the effects of centrifugation in complex mixtures, identifying key features such as the Maceration point, Critical point, Pre-Ouzo region, and Meso-structured living network, thereby advancing our understanding of centrifugation efficiency and phase behavior.

Building on this concept, our study investigates the effect of centrifugal stimuli on particle aggregation in a system of Ludox silica nanoparticles, using in-situ small-angle neutron scattering (SANS) measurements (Figure 5.25). While Ludox particles may not directly resemble the ternary systems we aim to explore, they offer a valuable proof of concept for understanding aggregation under centrifugal forces.

Ludox silica particles are negatively charged due to the presence of silanol groups on their surface, which leads to electrostatic repulsion in pure water. This repulsion

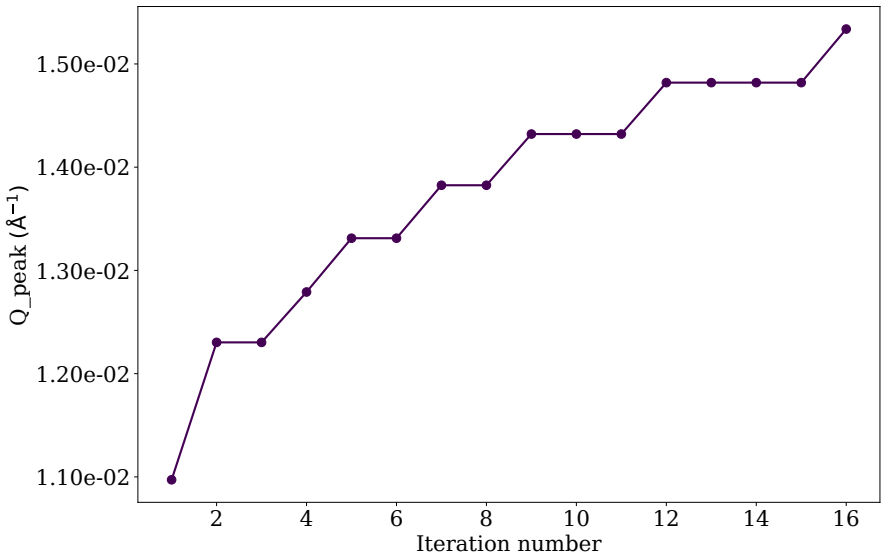

Figure 5.27: *Change in the peak position on the q-scale for silica particles in water observed in the in-situ SANS centrifuge experiment, measured at the far end of the sample cuvette, where the centrifugal force is maximal. With each successive iteration, the peak shifts to higher q-values, indicating that the particles are progressively moving towards the bottom of the cuvette and undergoing aggregation as the centrifugation cycle advances over time.*

prevents aggregation, ensuring stable dispersions of silica. However, introducing ions from salts such as NaCl or NaOH alters this behavior by screening the electrostatic repulsion, reducing the particles' effective charge and allowing them to approach one another. This reduction in repulsion facilitates aggregation, which is further enhanced under centrifugal force. In this experiment, we take advantage of these properties to promote aggregation and observe the process under centrifugation (see Figure 5.26).

In the in-situ SANS centrifugation experiment, a progressive shift in the peak position on the q-scale was observed (see Figure 5.27). At the far end of the cuvette, where the centrifugal force is most intense, the peak associated with aggregation shifted to higher q-values over time, indicating that as centrifugation progresses, the particles are moving towards this region and aggregating. This change in peak position suggests that centrifugal forces are effectively driving the aggregation of silica particles in the system.

While this study offers valuable insights into the effects of centrifugation on phase behavior, its applicability to our SFME ternary system is limited. For Ludox particles, the presence of a structural peak within the SANS range enables the study of silica particles. However, this approach becomes challenging for the octanol-ethanol-water ternary system. Additionally, the significant density difference between silica particles (2 g/cm^3) and water (1 g/cm^3) facilitates aggregation under centrifugal forces. In contrast, the minimal density difference between octanol (0.824 g/cm^3) and ethanol (0.789 g/cm^3) makes phase aggregation during centrifugation more difficult, especially when a pre-Ouzo droplet of octanol-ethanol in water forms. Despite these challenges, this experiment

provided valuable insights that can help refine the SFME system and further investigate its behavior under external stimuli.

By further exploring these directions, we can enhance the fundamental understanding of SFME systems, enabling the refinement of theoretical models and the expansion of their applications in various fields, such as green chemistry, energy, and biomedicine.

Résumé

Dans cette thèse, nous explorons les systèmes ternaires sans tensioactifs, composés de monoalcool et d'eau, en nous concentrant sur la structuration à l'échelle mésoscopique avec une attention particulière aux agrégats pré-ouzo. Ces agrégats ressemblent aux émulsions trouvées dans des boissons comme l'Ouzo ou le Pastis, mais sont considérablement plus petits (2–10 nm) par rapport aux émulsions d'Ouzo de taille micrométrique, et sont dans un état thermodynamiquement stable. Notre étude examine les mélanges d'alcools à longues chaînes (comme l'octanol, qui agit comme une huile), d'eau et d'éthanol, où l'éthanol est un hydrotrope qui facilite le mélange entre l'eau et l'huile autrement immiscibles. En variant les rapports des composants, nous observons la formation de différentes organisations. En utilisant des techniques telles que la Diffraction des Rayons X à Petit Angle (SAXS), l'Écho de Spin Neutronique (NSE) et la PFG-NMR, nous analysons les changements microscopiques structuraux et dynamiques dans ces mélanges. De plus, nous analysons l'effet de la température, contribuant à une compréhension approfondie des systèmes eau-alcool et de leur potentiel pour la conception de solvants novateurs.

Chapitre 1

Le Chapitre 1 introduit les concepts fondamentaux, en commençant par l'importance de l'étude des solutions dans diverses applications. Nous abordons ensuite l'importance des techniques de séparation et les principes derrière leur mise en œuvre. Nous explorons ensuite les systèmes ternaires composés d'huile, d'eau et d'un troisième agent solubilisant permettant leur mélange, ce qui conduit à une explication des émulsions et des microémulsions, qui dépendent des tensioactifs pour leur stabilité. Nous introduisons ensuite l'hydrotropie et une classe unique de systèmes appelés microémulsions sans tensioactifs (SFME), où la stabilité est atteinte grâce à un hydrotrope plutôt qu'un tensioactif. Ce phénomène est observé dans des boissons comme l'Ouzo, où des émulsions d'Ouzo et des microémulsions pré-Ouzo peuvent se former naturellement lors de la dilution avec de l'eau. Nous examinons plus en détail les propriétés des systèmes ternaires huile-hydrotrope-eau, mettant en évidence des éléments clés du diagramme de phase tels que les régions huile-dans-eau et eau-dans-huile, la ligne binodale et la ligne de Lifshitz. Enfin, nous passons en revue les études précédentes caractérisant les structures pré-Ouzo à l'aide de techniques telles que la diffusion à petit angle et les simulations de dynamique

moléculaire.

Chapitre 2

Dans le Chapitre 2, nous présentons un aperçu des différentes techniques expérimentales utilisées, ainsi que des détails sur les dispositifs spécifiques et les méthodes de préparation des échantillons. Nous commençons par expliquer les principes fondamentaux de la diffusion de rayonnement, puis plus spécifiquement la diffusion aux petit angle pour détailler les techniques de SAXS (rayons-X) et la SANS (neutrons). Les éléments essentiels sur l'interprétation des données dans les expériences de diffusion aux petits angles et la pertinence des calculs de l'invariant de Porod dans de tels contextes sont aussi exposés. Nous décrivons l'installation de l'instrument ID02 (ligne de SAXS à l'ESRF) telle qu'elle s'applique à notre étude.

Nous introduisons ensuite les techniques d'écho de spin neutronique, mettant en avant les instruments IN15 et WASP à l'ILL à Grenoble, France. Après cela, nous présentons les bases de la RMN à Gradient de Champs Pulsé (PFG-NMR) et l'appareil utilisé. Enfin, des détails techniques concernant les mesures de rhéologie sont donnés, et nous concluons par une brève description du processus de préparation des échantillons.

Chapitre 3

Dans le Chapitre 3, nous explorons les études expérimentales du système ternaire octanol, éthanol et eau en utilisant la diffusion de rayons-X aux petits angles avec autodilution in-situ. Nous collectons des données sur l'ensemble du diagramme de phase et les analysons à l'aide de scripts Python adaptés au gros volume de données. Les résultats préliminaires révèlent des structures mésoscopiques distinctes, y compris des agrégats pré-ouzo dans la région riche en eau près du point critique et des agrégats inverses du côté riche en huile du diagramme de phase.

Une analyse plus approfondie avec le modèle d'ajustement et les calculs invariants permet de définir la région pré-ouzo, correspondant principalement à la région du *pré-pic* des monoalcool, et identifie expérimentalement la ligne de Lifshitz (LL). La LL est observée comme étant courbée, contrairement à la ligne droite théorique proposée précédemment. De plus, nous remarquons une différence lorsqu'on utilise la version ramifiée de l'octanol, le 2-éthyl hexanol, qui montre un décalage progressif du domaine des agrégats inverses vers le domaine pré-ouzo, contrairement au système ternaire à base d'octanol où la transition entre ces régions est plus abrupte et intense.

Chapitre 4

Dans le Chapitre 4, nous présentons les résultats de l'étude SAXS en fonction de la température des systèmes ternaires à base d'octanol et de 2-éthyl hexanol. Le changement d'intensité du terme Ornstein-Zernike (OZ) et le paramètre de longueur d'échelle correspondant indiquent comment la structuration pré-ouzo varie avec la température. A

température fixe, la taille des agrégats dépend de la distance, en terme de composition, de l'échantillon par rapport au point critique. Plus sa composition est éloignée, plus la taille diminue. Globalement, l'augmentation de la température conduit à une réduction de la taille des agrégats pré-ouzo, reflétant la solubilité du système. La position de la ligne binodale, ou transition vers un état biphasique, change aussi avec la température. Lorsque l'échantillon devient biphasique lors du chauffage ou du refroidissement, le paramètre de taille diminue brusquement en raison de la formation d'émulsions d'Ouzo au détriment des microémulsions pré-ouzo, avec une diminution supplémentaire lors du chauffage. Cependant, les agrégats se reforment une fois l'échantillon refroidi. Plus l'échantillon est éloigné du point critique, moins l'effet est marqué.

Chapitre 5

Le Chapitre 5 se concentre sur l'étude des dynamiques moléculaires, principalement du système ternaire à base d'octanol. En utilisant la PFG NMR, nous identifions un changement de régime dans la diffusion de l'octanol et de l'eau, subtil mais réel, observé lors du passage de la ligne de Lifshitz. Cette observation est en accord avec les résultats de l'étude structurale et montre le lien subtil entre la dynamique et la structuration mésoscopique. Des simulations de dynamique moléculaire corroborent également les résultats de la RMN.

De plus, les techniques d'écho de spin neutronique fournissent des informations supplémentaires sur la variation des coefficients de diffusion collectifs sur une échelle de distances allant de quelques dizièmes à quelques dizaines de nanomètres. Nous observons un régime de dynamique qui révèle la nature piégée de l'octanol dans les agrégats pré-ouzo et sa nature continue dans la mélanges riches en huile.

Enfin, les propriétés macroscopiques non idéales des agrégats pré-ouzo sont démontrées par des mesures de rhéologie, montrant que l'excès de viscosité des mélanges dans la zone pré-ouzo est plus élevé qu'ailleurs.

Une étude comparative a été menée sur le système ternaire 2-éthylhexanol afin d'identifier les différences de SFME dues au ramification de l'huile, ainsi que sur un autre système ternaire sans phase Ouzo (acétate d'éthyle–salicylate de sodium–eau) afin de distinguer la structuration associée au point critique de celle de la région pré-Ouzo.

Conclusions et perspectives

Dans l'ensemble, cette étude fournit des informations précieuses sur la caractérisation des microémulsions formées à l'aide d'hydrotropes, avec des applications potentielles dans l'extraction et la solubilisation. Bien que les résultats soient spécifiques aux systèmes ternaires eau-monoalcool, ils offrent une compréhension fondamentale des diverses pseudophases qui peuvent exister au sein de mélanges ternaires apparemment homogènes, ouvrant la voie à de futures explorations dans des systèmes similaires.

Plusieurs piste son proposées pour de futures explorations: des mélanges quater-

naires, dans lesquels l'ajout d'une molécule ultra hydrophobe pourrait porter à la présence d'un second point critique ; l'utilisation de la centrifugation pour générer des agrégats pré-ouzo ou séparer les deux phases.

Bibliography

[1] J. W. McBain and H. E. Martin. Studies of the constitution of soap solutions: the alkalinity and degree of hydrolysis of soap solutions. *Journal of the Chemical Society, Transactions*, XCII, 1914.

[2] Fredric M. Menger. The structure of micelles. *Accounts of Chemical Research*, 12(4):111–117, 1979.

[3] D. J. McClements. *Food emulsions: principles, practices, and techniques*. CRC Press, 2004.

[4] D. J. McClements. Protein-stabilized emulsions. *Current Opinion in Colloid & Interface Science*, 9(5):305–313, 2004.

[5] S. Akula, A. K. Gurram, and S. R. Devireddy. Self-microemulsifying drug delivery systems: An attractive strategy for enhanced therapeutic profile. *International Scholarly Research Notices*, 2014:1–11, 2014.

[6] M. Alwadei, M. Kazi, and F. K. Alanazi. Novel oral dosage regimen based on self-nanoemulsifying drug delivery systems for codelivery of phytochemicals - curcumin and thymoquinone. *Saudi Pharmaceutical Journal*, 27:866–876, 2019.

[7] E. Atef and A. A. Belmonte. Formulation and in vitro and in vivo characterization of a phenytoin self-emulsifying drug delivery system (sedds). *European Journal of Pharmaceutical Sciences*, 35:257–263, 2008.

[8] M. Kazi, A. Alqahtani, A. Ahmad, O. M. Noman, M. S. Aldughaim, A. S. Alqahtani, et al. Development and optimization of sitagliptin and dapagliflozin loaded oral self-nanoemulsifying formulation against type 2 diabetes mellitus. *Drug Delivery*, 28:100–114, 2021.

[9] A. A.-W. Shahba, F. K. Alanazi, and S. I. Abdel-Rahman. Stabilization benefits of single and multi-layer self-nanoemulsifying pellets: A poorly-water soluble model drug with hydrolytic susceptibility. *PLoS ONE*, 13:e0198469, 2018.

[10] S. Gibaud and D. Attivi. Microemulsions for oral administration and their therapeutic applications. *Expert Opinion on Drug Delivery*, 9:937–951, 2012.

[11] N. Suhail, A. K. Alzahrani, W. J. Basha, N. Kizilbash, A. Zaidi, J. Ambreen, and H. M. Khachfe. Microemulsions: Unique properties, pharmacological applications, and targeted drug delivery. *Frontiers in Nanotechnology*, 3:754889, 2021.

[12] J. Flanagan and H. Singh. Microemulsions: a potential delivery system for bioac-

tives in food. *Critical Reviews in Food Science and Nutrition*, 46(3):221–237, 2006.

[13] Lirio Quintero and Norman F. Carnahan. Chapter 2 - microemulsions for cleaning applications. In Rajiv Kohli and K.L. Mittal, editors, *Developments in Surface Contamination and Cleaning*, pages 65–106. William Andrew Publishing, Oxford, 2013.

[14] Huapeng Liu, Xiyuan Wang, Youqian Zhai, and Tingting Xu. Application and development of chemical heat washing technology in petroleum oily sludge treatment: A review. *Separations*, 11(1):26, 2024.

[15] Edgar J. Acosta, Jeffrey H. Harwell, John F. Scamehorn, and David A. Sabatini. 7 - application of microemulsions in cleaning technologies and environmental remediation. In Ingegärd Johansson and P. Somasundaran, editors, *Handbook for Cleaning/Decontamination of Surfaces*, pages 831–884. Elsevier Science B.V., Amsterdam, 2007.

[16] M. L. Klossek, D. Touraud, T. Zemb, and W. Kunz. Structure and solubility in surfactant-free microemulsions. *ChemPhysChem*, 13(18):4116–4119, 2012.

[17] Olivier Diat, Michael L. Klossek, Didier Touraud, Bruno Deme, Isabelle Grillo, Werner Kunz, and Thomas Zemb. Octanol-rich and water-rich domains in dynamic equilibrium in the pre-ouzo region of ternary systems containing a hydrotrope. *Journal of Applied Crystallography*, 46(6):1665–1669, 2013.

[18] N. Grimaldi, P. E. Rojas, S. Stehle, A. Cordoba, R. Schweins, S. Sala, and et al. Pressure-responsive, surfactant-free co_2-based nanostructured fluids. *ACS Nano*, 11:10774–1084, 2017.

[19] R. F. Hankel, P. E. Rojas, M. Cano-Sarabia, S. Sala, J. Veciana, A. Braeuer, and et al. Surfactant-free co_2-based microemulsion-like systems. *Chem. Commun.*, 50:8215–8218, 2014.

[20] C. Breil, M. Abert Vian, T. Zemb, W. Kunz, and F. Chemat. "bligh and dyer" and folch methods for solid–liquid–liquid extraction of lipids from microorganisms. comprehension of solvatation mechanisms and towards substitution with alternative solvents. *International Journal of Molecular Sciences*, 18(4):708, 2017.

[21] A. V. Radushev, A. V. Plotnikov, and V. N. Tyryshkina. Regeneration methods of decontamination of phenol-containing waste waters. *Theoretical Foundations of Chemical Engineering*, 42:781–794, 2008.

[22] K. Binnemans, P. T. Jones, B. Blanpain, T. Van Gerven, Y. Yang, A. Walton, and M. Buchert. Recycling of rare earths: a critical review. *Journal of Cleaner Production*, 51:1, 2013.

[23] S. E. Kentish and G. W. Stevens. Innovations in separations technology for the recycling and re-use of liquid waste streams. *Chemical Engineering Journal*, 81:149, 2001.

[24] H. Shen and E. Forssberg. An overview of recovery of metals from slags. *Waste Management*, 23:933, 2003.

[25] V. Camel. Extraction techniques. *Analytical and Bioanalytical Chemistry*, 372:39, 2002.

[26] F. M. Doyle. Ion flotation-its potential for hydrometallurgical operations. *International Journal of Mineral Processing*, 72:387, 2003.

[27] D. Bitas, A. Kabir, M. Locatelli, and V. Samanidou. Food sample preparation for the determination of sulfonamides by high-performance liquid chromatography: State-of-the-art. *Separations*, 5(2):31, 2018.

[28] S. A. Khatibi, S. Hamidi, and M. R. Siahi-Shadbad. Application of liquid-liquid extraction for the determination of antibiotics in the foodstuff: Recent trends and developments. *Critical Reviews in Analytical Chemistry*, pages 1–16, 2020.

[29] A. S. Lorenzetti, C. E. Domini, and A. G. Lista. A simple and new reverse liquid-liquid microextraction for the automated spectrometric determination of doxycycline in chicken fat. *Food Chemistry*, 237:506–510, 2017.

[30] Payman Hashemi, Fatemeh Raeisi, Ali Reza Ghiasvand, and Akram Rahimi. Reversed-phase dispersive liquid–liquid microextraction with central composite design optimization for preconcentration and hplc determination of oleuropein. *Talanta*, 80(5):1926–1931, 2010.

[31] S. Otles and V. H. Ozyurt. Sampling and sample preparation. In *Handbook of Food Chemistry*, pages 151–164. Springer, 2015.

[32] C. S. Parinos, C. D. Stalikas, Th. S. Giannopoulos, and G. A. Pilidis. Chemical and physicochemical profile of wastewaters produced from the different stages of spanish-style green olives processing. *Journal of Hazardous Materials*, 145(1-2):58–63, 2007.

[33] Elena De Marco, Maria Savarese, Antonello Paduano, and Raffaele Sacchi. Characterization and fractionation of phenolic compounds extracted from olive oil mill wastewaters. *Food Chemistry*, 104(2):858–867, 2007.

[34] M. Jayne Lawrence and Gareth D. Rees. Microemulsion-based media as novel drug delivery systems. *Advances in Colloid and Interface Science*, 45(1):89–121, 2000.

[35] Miloslav Pekař and Ivan Samohýl. *The Thermodynamics of Linear Fluids and Fluid Mixtures*. Springer Cham, 1 edition, 2013. Published: 02 December 2013, eBook ISBN: 978-3-319-02514-8, Softcover ISBN: 978-3-319-34467-6, Copyright Springer International Publishing Switzerland 2014.

[36] Alain P. Foucault. Solvent systems in centrifugal partition chromatography. In *Centrifugal Partition Chromatography*, Chromatographic Science Series, page 72. Taylor & Francis, 1994.

[37] D. J. McClements. Critical review of techniques and methodologies for characterization of emulsion stability. *Critical Reviews in Food Science and Nutrition*, 47(7):611–649, 2007.

[38] D. J. McClements. *Food emulsions: principles, practices, and techniques*. CRC Press, Boca Raton, FL, 2015.

[39] Eric Dickinson. Food emulsions and foams: Stabilization by particles. *Current Opinion in Colloid & Interface Science*, 15(1):40–49, 2010.

[40] N. Widlak, R. W. Hartel, and S. Narine. *Crystallization and solidification properties of lipids*. The American Oil Chemists Society, Champaign, IL, 2001.

[41] C. C. Akoh and D. B. Min. *Food Lipids: Chemistry, Nutrition, and Biotechnology*. CRC Press, 2008.

[42] T. Kinyanjui, W.E. Artz, and S. Mahungu. Emulsifiers | organic emulsifiers. *Encyclopedia of Food Sciences and Nutrition*, pages 2070–2077, 1 2003.

[43] Krister Holmberg, Bo Jönsson, Bengt Kronberg, and Björn Lindman. *Emulsions and Emulsifiers*, chapter 21, pages 451–471. John Wiley & Sons, Ltd, 2002.

[44] E. A. Foegeding and J. P. Davis. Food protein functionality: A comprehensive approach. *Food Hydrocolloids*, 25(8):1853–1864, 2011.

[45] Holger Egger and Kathryn M. McGrath. Aging of oil-in-water emulsions: The role of the oil. *Journal of Colloid and Interface Science*, 299(2):890–899, 2006.

[46] Margaret M. Robins. Emulsions — creaming phenomena. *Current Opinion in Colloid & Interface Science*, 5:265–272, 11 2000.

[47] Margaret Robins, Andrew Watson, and Peter Wilde. Emulsions - creaming and rheology. *Current Opinion in Colloid & Interface Science*, 7:419–425, 11 2002.

[48] Johan Sjoblom. *Emulsions and Emulsion Stability: Surfactant Science Series/61*. CRC Press, Boca Raton, FL, 1996.

[49] F. Leal-Calderon and P. Poulin. Progress in understanding emulsion metastability and surface forces. *Current Opinion in Colloid & Interface Science*, 4:223–230, 6 1999.

[50] D. T. Wasan, A. D. Nikolov, and F. Aimetti. Texture and stability of emulsions and suspensions: role of oscillatory structural forces. *Advances in Colloid and Interface Science*, 108-109:187–195, May 20 2004.

[51] B. P. Binks and S. O. Lumsdon. Catastrophic phase inversion of water-in-oil emulsions stabilized by hydrophobic silica. *Langmuir*, 16(6):2539–2547, 2000.

[52] P. A. Winsor. Hydrotropy, solubilisation and related emulsification processes. *Transactions of the Faraday Society*, 44:376–398, 1948.

[53] MORTON ROSOFF. The nature of microemulsions. *Progress in Surface and Membrane Science*, 12:405–477, 1978.

[54] D.O. SHAH and R.S. SCHECHTER. Front matter. In *Improved Oil Recovery by Surfactant and Polymer Flooding*, page iii. Academic Press, 1977.

[55] Krister Holmberg, Bo Jönsson, Bengt Kronberg, and Björn Lindman. *Microemulsions for Soil and Oil Removal*, chapter 22, pages 473–492. John Wiley & Sons, Ltd, 2002.

[56] Krister Holmberg, Bo Jönsson, Bengt Kronberg, and Björn Lindman. *Chemical Reactions in Microheterogeneous Systems*, chapter 23, pages 493–517. John Wiley

& Sons, Ltd, 2002.

[57] W. Hou and J. Xu. Surfactant-free microemulsions. *Current Opinion in Colloid and Interface Science, 25, pp. 67–74.*, 2016.

[58] Makoto Harada, Noboru Shinbara, Motonari Adachi, and Yoshikazu Miyake. Liquid membrane operation with aid of microemulsion;separation of metal ions;. *JOURNAL OF CHEMICAL ENGINEERING OF JAPAN*, 23(1):50–57, 1990.

[59] F. J. Ovejero-Escudero, H. Angelino, and G. Casamatta. Microemulsions as adaptive solvents for hydrometallurgical purposes: A preliminary report. *Journal of Dispersion Science and Technology*, 8(1):89–108, 1987.

[60] V. C. Santanna, F. D. S. Curbelo, T. N. Castro Dantas, A. A. Dantas Neto, H. S. Albuquerque, and A. I. C. Garnica. Microemulsion flooding for enhanced oil recovery. *Journal of Petroleum Science and Engineering*, 66(3):117–120, January 2009.

[61] Husain N Kagalwala, Danielle N. Chirdon, Isaac N. Mills, Nikita Budwal, and Stefan Bernhard. Light-driven hydrogen generation from microemulsions using metallosurfactant catalysts and oxalic acid. *Inorganic chemistry*, 56 17:10162–10171, 2017.

[62] Debolina Mitra. Microemulsion and its application: An inside story. *Materials Today: Proceedings*, 83:75–82, 2023. Recent Advances in Material Science and Organic Synthesis.

[63] Ricky S.H. Lam and Michael T. Nickerson. Food proteins: A review on their emulsifying properties using a structure–function approach. *Food Chemistry*, 141(2):975–984, 2013.

[64] Beatriz Vieira da Silva, João C.M. Barreira, and M. Beatriz P.P. Oliveira. Natural phytochemicals and probiotics as bioactive ingredients for functional foods: Extraction, biochemistry and protected-delivery technologies. *Trends in Food Science & Technology*, 50:144–158, 2016.

[65] Muhammad Arshad, Rehan Ali Pradhan, Muhammad Zubair, and Aman Ullah. Chapter 13 - lipid-derived renewable amphiphilic nanocarriers for drug delivery, biopolymer-based formulations: Biomedical and food applications. In Kunal Pal, Indranil Banerjee, Preetam Sarkar, Doman Kim, Win-Ping Deng, Navneet Kumar Dubey, and Kaustav Majumder, editors, *Biopolymer-Based Formulations*, pages 283–310. Elsevier, 2020.

[66] Sabine Kosmella and Joachim Koetz. Polymer-modified w/o microemulsions - with tunable droplet-droplet interactions. *Current Opinion in Colloid & Interface Science*, 17(5):261–265, 2012.

[67] Edgar Acosta. Bioavailability of nanoparticles in nutrient and nutraceutical delivery. *Current Opinion in Colloid & Interface Science*, 14(1):3–15, 2009.

[68] Michael Gradzielski, Magali Duvail, Paula Malo De Molina, Miriam Simon, Yeshayahu Talmon, and Thomas Zemb. Using Microemulsions: Formulation Based

on Knowledge of Their Mesostructure. *Chemical Reviews*, 121(10):5671–5740, 2021.

[69] J. Marcus, M. L. Klossek, D. Touraud, and W. Kunz. Nano-droplet formation in fragrance tinctures. *Flavour and Fragrance Journal*, 28:294–299, 2013.

[70] Johannes Mehringer and Werner Kunz. Carl neuberg's hydrotropic appearances (1916). *Advances in Colloid and Interface Science*, 294:102476, 2021.

[71] A.M. Saleh and L.K. El-Khordagui. Hydrotropic agents: a new definition. *International Journal of Pharmaceutics*, 24(2):231–238, 1985.

[72] P. Bauduin, A. Renoncourt, A. Kopf, D. Touraud, and W. Kunz. Surfactant self-assembly and hydrotrope interaction in aqueous solutions. *Langmuir*, 21:6769–6775, 2005.

[73] T. K. Hodgdon and E. W. Kaler. Hydrotropic solubilization and its applications in colloid and interface science. *Current Opinion in Colloid and Interface Science*, 12:121–128, 2007.

[74] C. V. Subbarao, I. P. K. Chakravarthy, A. V. S. L. Sai Bharadwaj, and K. M. M. Prasad. Functions of hydrotropes in solutions. *Chemical Engineering & Technology*, 35(2):225–237, 2012.

[75] Deepa Subramanian, Christopher T. Boughter, Jeffery B. Klauda, Boualem Hammouda, and Mikhail A. Anisimov. Mesoscale inhomogeneities in aqueous solutions of small amphiphilic molecules. *Faraday Discuss.*, 167:217–238, 2013.

[76] C. Neuberg. Hydrotropische erscheinungen. *Biochem. Z.*, 76:107–176, 1916.

[77] V. Srinivas and D. Balasubramanian. When does the switch from hydrotropy to micellar behavior occur? *Langmuir*, 14:6658–6661, 1998.

[78] T. K. Hogdgon and E. W. Kaler. Hydrotropic solutions. *Curr. Opin. Colloid Interface Sci.*, 12:121–128, 2007.

[79] J. Eastoe, M. H. Hatzopoulas, and P. J. Dowding. Action of hydrotropes and alkylhydrotropes. *Soft Matter*, 7:5917–5925, 2011.

[80] Yong Cui, Chenyue Xing, and Yingqing Ran. Molecular dynamics simulations of hydrotropic solubilization and self-aggregation of nicotinamide. *Journal of Pharmaceutical Sciences*, 99:3048–3059, 7 2010.

[81] Werner Kunz, Krister Holmberg, and Thomas Zemb. Hydrotropes. *Current Opinion in Colloid and Interface Science*, 22:99–107, 2016.

[82] Vividha Dhapte and Piyush Mehta. Advances in hydrotropic solutions: An updated review. *St. Petersburg Polytechnical University Journal: Physics and Mathematics*, 1(4):424–435, 2015.

[83] Jonathan J Booth, Muhiadin Omar, Steven Abbott, and Seishi Shimizu. Hydrotrope accumulation around the drug: the driving force for solubilization and minimum hydrotrope concentration for nicotinamide and urea. *Physical Chemistry Chemical Physics*, 17(12):8028–8037, 2015.

[84] S. A. Vitale and J. L. Katz. Liquid droplet dispersions formed by homogeneous

liquid-liquid nucleation: The ouzo effect. *Langmuir*, 19(10):4105–4110, 2003.

[85] Rafael Muñoz-Espí and Olaia Álvarez Bermúdez. Application of nanoemulsions in the synthesis of nanoparticles. *Nanoemulsions: Formulation, Applications, and Characterization*, pages 477–515, 1 2018.

[86] Clément Goubault, Flavien Sciortino, Olivier Mongin, Ulrich Jarry, Mégane Bostoën, Hélène Jakobczyk, Agnès Burel, Stéphanie Dutertre, Marie Bérengère Troadec, Myrtil L. Kahn, Soizic Chevance, and Fabienne Gauffre. The ouzo effect: A tool to elaborate high-payload nanocapsules. *Journal of Controlled Release*, 324:430–439, 8 2020.

[87] Amanda Tibães Lopes, Bruna Lorena Figueiredo, Mariano Michelon, Sofia Santos Donaire Chura, Amanda Lélis de Souza, Letícia Morais Costa Teixeira, Guilherme Carneiro, and Franciele Maria Pelissari. Use of essential oil-loaded nanoemulsions in active food packaging. *Bio-Based Nanoemulsions for Agri-Food Applications*, pages 363–386, 1 2022.

[88] Abeeda Mushtaq, Sajad Mohd Wani, A. R. Malik, Amir Gull, Seema Ramniwas, Gulzar Ahmad Nayik, Sezai Ercisli, Romina Alina Marc, Riaz Ullah, and Ahmed Bari. Recent insights into nanoemulsions: Their preparation, properties and applications. *Food Chemistry: X*, 18:100684, 6 2023.

[89] Isabelle Grillo. Small-angle neutron scattering study of a world-wide known emulsion: Le pastis. *Colloids and Surfaces A: Physicochemical and Engineering Aspects*, 225:153–160, 9 2003.

[90] K. Roger. Nanoemulsification in the vicinity of phase inversion: Disruption of bicontinuous structures in oil/surfactant/water systems. *Current Opinion in Colloid & Interface Science*, 25:120–128, 2016.

[91] Ying Han, Ning Pan, Deqiang Li, Shuhui Liu, Bin Sun, Jinling Chai, and Dejie Li. Formation mechanism of surfactant-free microemulsion and a judgment on whether it can be formed in one ternary system. *Chemical Engineering Journal*, 437, jun 2022.

[92] Tobias Lopian, Sebastian Schöttl, Sylvain Prévost, Stéphane Pellet-Rostaing, Dominik Horinek, Werner Kunz, and Thomas Zemb. Morphologies observed in ultraflexible microemulsions with and without the presence of a strong acid. *ACS Central Science*, 2:467–475, 2016.

[93] Sebastian Schöttl, Tobias Lopian, Sylvain Prévost, Didier Touraud, Isabelle Grillo, Olivier Diat, Thomas Zemb, and Dominik Horinek. Combined molecular dynamics (MD) and small angle scattering (SAS) analysis of organization on a nanometer-scale in ternary solvent solutions containing a hydrotrope. *Journal of Colloid and Interface Science*, 540:623–633, 2019.

[94] Garland D Smith, Colleen E Donelan, and Roland E Barden. Oil-continuous microemulsions composed of hexane, water, and 2-propanol. *Journal of Colloid and Interface Science*, 60(3):488–496, 1977.

[95] N.F. Borys, S.L. Holt, and R.E. Barden. Detergentless water/oil microemulsions iii. effect of koh on phase diagram and effect of solvent composition on base hydrolysis of esters. *Journal of Colloid and Interface Science*, 71:526–532, 1979.

[96] D.K. Lavallee, E. Huggins, and S. Lee. Kinetics and mechanism of the hydrolysis of chlorophyll a in ternary solvent microemulsion media. *Inorganic Chemistry*, 21:1552–1553, 1982.

[97] B.A. Keiser and S.L. Holt. Reactions in detergentless microemulsions-incorporation of copper(ii) into meso-tetraphenylporphine ((tpp)h2) in a water/oil microemulsion. *Inorganic Chemistry*, 21:2323–2327, 1982.

[98] Mohamed EL-Hefnawy. Water in olive oil surfactantless microemulsions as medium for cds nanoparticles synthesis. *Modern Applied Science*, 6(4), 2012.

[99] J. Xu, L. Zhang, D. Li, J. Zhao, and W. Hou. Synthesis of mg2al–cl layered double hydroxide nanosheets in a surfactant-free reverse microemulsion. *Colloid and Polymer Science*, 291:2515–2521, 2013.

[100] Y.L. Khmelnistsky, A.K. Gladilin, I.N. Neverova, A.V. Levashov, and K. Martinek. Detergentless microemulsions as media for enzymatic reactions: catalytic properties of laccase in the ternary system hexane–2-propanol–water. *Collect Czech Chem Commun*, 55:555–563, 1990.

[101] C.J. O'Connor, A. Aggett, D.R. Williams, and R.A. Stanley. Candida cylindracea lipase-catalysed hydrolysis of methyl palmitate in detergentless microemulsion and paraffin/water biphasic media. *Australian Journal of Chemistry*, 44:53–60, 1991.

[102] C.J. O'Connor and D.R. Cleverly. Bile salt stimulated human milk lipase catalyzed ester hydrolysis in detergentless microemulsion media. *Biocatalysis and Biotransformation*, 12:193–204, 1995.

[103] M. Zoumpanioti, M. Karali, A. Xenakis, and H. Stamatis. Lipase biocatalytic processes in surfactant-free microemulsion-like ternary systems and related organogels. *Enzyme and Microbial Technology*, 39:531–539, 2006.

[104] J. Drapeau, M. Verdier, D. Touraud, U. Kröckel, M. Geier, and A. et al. Rose. Effective insect repellent formulation in both surfactantless and classical microemulsions with a long-lasting protection for human beings. *Chemistry and Biodiversity*, 6:934–947, 2009.

[105] Yongmin Zhang, Xuelian Chen, Bo Zhu, Yue Zhou, Xuefeng Liu, and Cheng Yang. Temperature-switchable surfactant-free microemulsion. *Langmuir*, pages acs.langmuir.0c00828–, 2020.

[106] A. Salabat, B.S. Mirhoseini, and F. Mirhoseini. Ionic liquid based surfactant-free microemulsion as a new protocol for preparation of visible light active poly(methyl methacrylate)/tio_2 nanocomposite. *Scientific Reports*, 14:15676, 2024.

[107] L. Song, H. Jia, F. Zhang, H. Jia, Y. Wang, Q. Xie, F. Fan, Q. Wang, and S. Wen. Sustainable utilization of surfactant-free microemulsion regulated by co_2 for treating oily wastes: An interpretation of the response mechanism. *Langmuir*,

40(1):960–967, Jan 2024. Published online: Dec 27, 2023.

[108] Xiaoyu Zhang, Miaomiao Song, Jinling Chai, Xiaocui Cui, and Jiao Wang. Preparation, characterization and application of a surfactant-free microemulsion containing 1-octen-3-ol, ethanol, and water. *Journal of Molecular Liquids*, 300:112278, 2 2020.

[109] Thomas N. Zemb, Michael Klossek, Tobias Lopian, Julien Marcus, Sebastian Schöettl, Dominik Horinek, Sylvain F. Prevost, Didier Touraud, Olivier Diat, Stjepan Marčelja, and Werner Kunz. How to explain microemulsions formed by solvent mixtures without conventional surfactants. *Proceedings of the National Academy of Sciences of the United States of America*, 113(16):4260–4265, 2016.

[110] Deepa Subramanian, Jeffery B. Klauda, Peter J. Collings, and Mikhail A. Anisimov. Mesoscale phenomena in ternary solutions of tertiary butyl alcohol, water, and propylene oxide. *The Journal of Physical Chemistry B*, 118(22):5994–6006, 2014.

[111] Zhiyong Li, He Cheng, Junyu Li, Jinkun Hao, Li Zhang, Boualem Hammouda, and Charles C. Han. Large-scale structures in tetrahydrofuran–water mixture with a trace amount of antioxidant butylhydroxytoluene (bht). *The Journal of Physical Chemistry B*, 115(24):7887–7895, 2011.

[112] M. L. Klossek, D. Touraud, and W. Kunz. Eco-solvents–cluster-formation, surfactantless microemulsions and facilitated hydrotropy. *Physical Chemistry Chemical Physics*, 15(26):10971–10977, 2013.

[113] F. M. Menger and D. W. Doll. On the structure of micelles. *Journal of the American Chemical Society*, 106(4):1109–1113, 1984.

[114] G. Lindau. Zur erklaerung der hydrotropie. *Die Naturwissenschaften*, 23:396–401, 1932.

[115] Andreas E. Robertson, Dung H. Phan, Joseph E. Macaluso, Vladimir N. Kuryakov, Elena V. Jouravleva, Christopher E. Bertrand, Igor K. Yudin, and Mikhail A. Anisimov. Mesoscale solubilization and critical phenomena in binary and quasi-binary solutions of hydrotropes. *Fluid Phase Equilibria*, 407:243–254, 2015.

[116] R. M. Hornreich, Marshall Luban, and S. Shtrikman. Critical behavior at the onset of **k**-space instability on the λ line. *Physical Review Letters*, 35(25):1678–1681, 1975.

[117] R. D. Koehler, K.-V. Schubert, R. Strey, and E. W. Kaler. The lifshitz line in binary systems: Structures in water/c4e1 mixtures. *Journal of Chemical Physics*, 101(12):10843–10849, 1994.

[118] Alexander Kudlay and Semjon Stepanow. On the behavior of the lifshitz line in ternary homopolymer/diblock-copolymer blends, 2001.

[119] Jean-Louis Bretonnet and Jean-Marc Bomont. Structure of self-assembly amphiphilic systems: Relation between phenomenological parameters and microscopic potential parameters. *Chemical Physics*, 539:110905, 2020.

[120] Sylvain Prévost, Sebastian Krickl, Stjepan Marčelja, Werner Kunz, Thomas Zemb, and Isabelle Grillo. Spontaneous Ouzo Emulsions Coexist with Pre-Ouzo Ultraflexible Microemulsions. *Langmuir*, 37(13):3817–3827, 2021.

[121] Sylvain Prévost and Thomas Zemb. Using weak aggregation for solubilization and separation. *Neutrons, X-rays, and Light*, pages 701–740, 1 2025.

[122] K. V. Schubert, R. Strey, S. R. Kline, and E. W. Kaler. Small angle neutron scattering near lifshitz lines: Transition from weakly structured mixtures to microemulsions. *The Journal of Chemical Physics*, 101:5343–5355, 1994.

[123] K. Roger, R. Botet, and B. Cabane. Coalescence of repelling colloidal droplets: A route to monodisperse populations. *Langmuir*, 29:5689–5700, 2013.

[124] P. Bauduin, F. Testard, and Th. Zemb. Solubilization in alkanes by alcohols as reverse hydrotropes or "lipotropes". *The Journal of Physical Chemistry B*, 112(39):12354–12360, 2008. PMID: 18774856.

[125] Sebastian Schöttl, Didier Touraud, Werner Kunz, Thomas Zemb, and Dominik Horinek. Consistent definitions of "the interface" in surfactant-free micellar aggregates. *Colloids and Surfaces A: Physicochemical and Engineering Aspects*, 480:222–227, 2015.

[126] C Tanford. The Hydrophobic Effect: Formation of Micelles and Biological Membranes . *Wiley, New York*, 1980.

[127] S. Schöttl, J. Marcus, O. Diat, D. Touraud, W. Kunz, T. Zemb, and D. Horinek. Emergence of surfactant-free micelles from ternary solutions. *Chem. Sci.*, 5:2949–2954, 2014.

[128] CEA - IRAMIS. What is measured in a small-angle x-ray scattering (saxs)?, 2024. Accessed: 2024-12-10.

[129] Roberto Verbeni, Giulio Monaco, Keijo Hämäläinen, Simo Huotari, and Tuomas Pylkkänen. Direct tomography with chemical-bond contrast. *Nature Materials*, 10(7):489–493, 2011.

[130] D. S. Sivia. *Elementary Scattering Theory: For X-ray and Neutron Users*. Oxford University Press, New York, 2011.

[131] C. J. Gommes, S. Jaksch, and H. Frielinghaus. Small-angle scattering for beginners. *Journal of Applied Crystallography*, 54(Pt 6):1832–1843, Nov 2021.

[132] Stuart A. Rice. Small angle scattering of x-rays. a. guinier and g. fournet. translated by c. b. wilson and with a bibliographical appendix by k. l. yudowitch. wiley, new york, 1955. 268 pp. *Journal of Polymer Science*, 19(93):594–594, 1956.

[133] Fabrice Cousin. Small angle neutron scattering. In *EPJ Web of Conferences*, volume 104, page 01004, CEA-Saclay, 91191 Gif-sur-Yvette, France, 2015. Laboratoire Léon Brillouin, CEA-CNRS, EDP Sciences.

[134] Thomas Zemb and Peter Lindner. *Neutrons, X-Rays and Light: Scattering Methods Applied to Soft Condensed Matter*. Elsevier, 1st edition, 2002.

[135] Cy M. Jeffries, Jan Ilavsky, Anne Martel, Stephan Hinrichs, Andreas Meyer,

Jan Skov Pedersen, Anna V. Sokolova, and Dmitri I. Svergun. Small-angle x-ray and neutron scattering. *Nature Reviews Methods Primers*, 1(1):70, 2021.

[136] Theyencheri Narayanan, Michael Sztucki, Pierre Van Vaerenbergh, Joachim Léonardon, Jacques Gorini, Laurent Claustre, Franc Sever, John Morse, and Peter Boesecke. A multipurpose instrument for time-resolved ultra-small-angle and coherent X-ray scattering. *Journal of Applied Crystallography*, 51(6):1511–1524, Dec 2018.

[137] Theyencheri Narayanan, Michael Sztucki, Thomas Zinn, Jerome Kieffer, Alejandro Homs-Puron, Jacques Gorini, Pierre Van Vaerenbergh, and Peter Boesecke. Performance of the time-resolved ultra-small-angle x-ray scattering beamline with the extremely brilliant source. *Journal of Applied Crystallography*, 55:98–111, 2022.

[138] B. Farago. The basics of neutron spin echo. Technical Report KFKI–1999-04/E, KFKI, Hungary, 1999. Available at: `http://inis.iaea.org/search/search.aspx?orig_q=RN:30054775`.

[139] F. Mezei. Neutron spin echo: A new concept in polarized thermal neutron techniques. *Zeitschrift für Physik*, 255:146–160, 1972.

[140] R. Cywinski. Neutron spin echo spectroscopy. In F. Hippert, E. Geissler, J.L. Hodeau, E. Lelièvre-Berna, and J.R. Regnard, editors, *Neutron and X-ray Spectroscopy*, pages 427–455. Springer, Dordrecht, 2006.

[141] W. Gavin Williams. *Polarized Neutrons*, volume 1 of *Oxford Series on Neutron Scattering in Condensed Matter*. Oxford University Press, Oxford, 1988.

[142] Institut Laue-Langevin. In15 instrument layout. `https://www.ill.eu/for-ill-users/instruments/instruments-list/in15/description/instrument-layout`.

[143] Institut Laue-Langevin. Wasp instrument layout. `https://www.ill.eu/for-all-users/instruments/instruments-list/wasp/description/instrument-layout`.

[144] E. L. Hahn. Spin echoes. *Physical Review*, 80:580–594, 1950.

[145] M. H. Levitt. *Spin Dynamics: Basics of Nuclear Magnetic Resonance*. John Wiley & Sons, Chichester, England, 2002.

[146] C. P. Slichter. *Principles of Magnetic Resonance*. Springer-Verlag, Berlin, 1996.

[147] R. Kimmich. *NMR: Tomography, Diffusometry, Relaxometry*. Springer, Berlin, 1997.

[148] E. O. Stejkal and J. E. Tanner. Spin diffusion measurements: Spin echoes in the presence of a time-dependent field gradient. *Journal of Chemical Physics*, 42:288, 1965.

[149] P. T. Callaghan. *Principles of Nuclear Magnetic Resonance*. Oxford University Press, Oxford, 1991.

[150] William S. Price. Pulse field gradient nmr. *Concepts in Magnetic Resonance*, 9(2):299–336, 1997.

[151] Physikalische Chemie Universität Münster. Praktikum - physikalische chemie - grundpraktikum, accessed 2024-12-16.

[152] K. S. Vahvaselkä, R. Serimaa, and M. Torkkeli. Determination of liquid structures of the primary alcohols methanol, ethanol, 1-propanol, 1-butanol and 1-octanol by x-ray scattering. *Journal of Applied Crystallography*, 28:189–195, 4 1995.

[153] N. P. Franks, M. H. Abraham, and W. R. Lieb. Molecular organization of liquid n-octanol: an x-ray diffraction analysis. *Journal of Pharmaceutical Sciences*, 82(5):466–470, May 1993.

[154] G. A. Martynov. The ornstein–zernike equation and critical phenomena in fluids. *Journal of Chemical Physics*, 129(24):244509, 2008.

[155] F. S. Carvalho and J. P. Braga. The ornstein-zernike equation: three distinct approaches. *Revista Brasileira de Ensino de Física (Rev. Bras. Ens. Fis.)*, 47, 2025.

[156] Alberto Arce, Antonio Blanco, Pilar Souza, and Isabel Vidal. Liquid-Liquid Equilibria of Water + Methanol + 1-Octanol and Water + Ethanol + 1-Octanol at Various Temperatures. *Journal of Chemical & Engineering Data*, 39(2):378–380, apr 1994.

[157] Justin L. MacCallum and D. Peter Tieleman. Structures of neat and hydrated 1-octanol from computer simulations. *Journal of the American Chemical Society*, 124(50):15085–15093, 2002.

[158] Mingbo Li, Yuki Wakata, Hao Zeng, and Chao Sun. On the thermal response of multiscale nanodomains formed in trans-anethol/ethanol/water surfactant-free microemulsion. *Journal of Colloid and Interface Science*, 652(PB):1944–1953, 2023.

[159] Yongmin Zhang, Xuelian Chen, and Xuefeng Liu. Temperature-Induced Reversible-Phase Transition in a Surfactant-Free Microemulsion. *Langmuir*, 35(44):14358–14363, 2019.

[160] Ingo Hoffmann, Firoz Malayil Kalathil, Tobias Lopian, Didier Touraud, Orsolya Czakkel, Marie Plazanet, and Christiane Alba-Simionesco. Unexpected molecular dynamics of ethanol in hydrogen-bonded binary mixtures, ethanol-octanol and ethanol-water. *EPJ Web of Conferences*, 272:01003, 2022.

[161] Q. Berrod, F. Ferdeghini, J.M. Zanotti, P. Judeinstein, D. Lairez, V. García Sakai, O. Czakkel, P. Fouquet, and D. Constantin. Ionic liquids: Evidence of the viscosity scale-dependence. *Scientific Reports*, 7:2241, 2017.

[162] Asmae El Maangar, Pierre Degot, Verena Huber, Jeremy Causse, Patrick Berthault, Didier Touraud, Werner Kunz, and Thomas Zemb. Pre-nucleation cluster formation upon ethyl acetate addition to an aqueous solution of an anionic hydrotrope. *Journal of Molecular Liquids*, 310:113240, 2020.

[163] A. Arbe, P. Malo de Molina, F. Alvarez, B. Frick, and J. Colmenero. Dielectric susceptibility of liquid water: Microscopic insights from coherent and incoherent neutron scattering. *Phys. Rev. Lett.*, 117:185501, Oct 2016.

[164] Jesper S. Hansen, Alexander Kisliuk, Alexei P. Sokolov, and Catalin Gainaru. Identification of structural relaxation in the dielectric response of water. *Phys. Rev. Lett.*, 116:237601, Jun 2016.

[165] S. K. Garg and C. P. Smyth. Microwave absorption and molecular structure in liquids. lxii. the three dielectric dispersion regions of the normal primary alcohols1. *The Journal of Physical Chemistry*, 69(4):1294–1301, 1965.

[166] Takaaki Sato and Richard Buchner. Dielectric relaxation processes in ethanol/water mixtures. *The Journal of Physical Chemistry A*, 108(23):5007–5015, 2004.

[167] Felix Roosen-Runge, Dominique J. Bicout, and Jean-Louis Barrat. Analytical correlation functions for motion through diffusivity landscapes. *The Journal of Chemical Physics*, 144(20):204109, 05 2016.

[168] E. A. G. Aniansson, S. N. Wall, M. Almgren, H. Hoffmann, I. Kielmann, W. Ulbricht, R. Zana, J. Lang, and C. Tondre. Theory of the kinetics of micellar equilibria and quantitative interpretation of chemical relaxation studies of micellar solutions of ionic surfactants. *The Journal of Physical Chemistry*, 80(9):905–922, 1976.

[169] D. Sheyfer, Qingteng Zhang, J. Lal, T. Loeffler, E. M. Dufresne, A. R. Sandy, S. Narayanan, S. K. R. S. Sankaranarayanan, R. Szczygiel, P. Maj, L. Soderholm, M. R. Antonio, and G. B. Stephenson. Nanoscale critical phenomena in a complex fluid studied by x-ray photon correlation spectroscopy. *Phys. Rev. Lett.*, 125:125504, Sep 2020.

[170] Begoña González, Noelia Calvar, Elena Gómez, and Ángeles Domínguez. Density, dynamic viscosity, and derived properties of binary mixtures of methanol or ethanol with water, ethyl acetate, and methyl acetate at T=(293.15, 298.15, and 303.15)K. *The Journal of Chemical Thermodynamics*, 39(12):1578–1588, dec 2007.

[171] Marco A. F. Faria, Rosana J. Martins, Márcio J. E. M. Cardoso, and Oswaldo E. Barcia. Density and viscosity of the binary systems ethanol + butan-1-ol, + pentan-1-ol, + heptan-1-ol, + octan-1-ol, nonan-1-ol, + decan-1-ol at 0.1 mpa and temperatures from 283.15 k to 313.15 k. *Journal of Chemical & Engineering Data*, 58(12):3405–3419, 2013.

[172] Tilo Seydel, Robert M. Edkins, and Katharina Edkins. Picosecond self-diffusion in ethanol–water mixtures. *Physical Chemistry Chemical Physics*, 21(18):9547–9552, 2019.

[173] J. Marcus, D. Touraud, S. Prévost, O. Diat, T. Zemb, and W. Kunz. Influence of additives on the structure of surfactant-free microemulsions. *Phys. Chem. Chem. Phys.*, 17:32528–32538, 2015.

[174] Maria A. Vratsanos, Wangyang Xue, Nathan D. Rosenmann, Lauren D. Zarzar, and Nathan C. Gianneschi. Ouzo effect examined at the nanoscale via direct observation of droplet nucleation and morphology. *ACS Central Science*, 9(3):457–465, 2023.

[175] Clément Goubault, Déborah Iglicki, Robert A. Swain, Benjamin F.P. McVey, Bertrand Lefeuvre, Ludivine Rault, Céline Nayral, Fabien Delpech, Myrtil L. Kahn, Soizic Chevance, and Fabienne Gauffre. Effect of nanoparticles on spontaneous ouzo emulsification. *Journal of Colloid and Interface Science*, 603:572–581, 12 2021.

[176] Déborah Iglicki, Clément Goubault, Mouktar Nour Mahamoud, Soizic Chevance, and Fabienne Gauffre. Shedding light on the formation and stability of mesostructures in ternary "ouzo" mixtures. *Journal of Colloid and Interface Science*, 633:72–81, 2023. HAL Id: hal-03886976.

[177] Horacio N. Solimo. Liquid–liquid equilibria for the water + ethanol + 2-ethyl-1-hexanol ternary system at several temperatures. *Canadian Journal of Chemistry*, 68(9):1532–1536, sep 1990.

[178] Francisco Ruiz, Vicente Gomis, and Rogelio F. Botella. Quaternary liquid—liquid equilibrium: water—ethanol—2-ethylhexanol—decalin at 25°c. unusual shape of the solubility surface. *Fluid Phase Equilibria*, 43:317–327, 12 1988.

[179] The Nobel Prize in Physics. The nobel prize in physics, 1926. `https://www.nobelprize.org/prizes/physics/1926/summary`, 1926. Accessed: 2025-01-05.

[180] J. L. Cole and J. C. Hansen. Analytical ultracentrifugation as a contemporary biomolecular research tool. *Proceedings of the National Academy of Sciences*, 96(3):1227–1234, 1999.

[181] S. Bulut, I. Åslund, D. Topgaard, H. Wennerström, and U. Olsson. Lamellar phase separation in a centrifugal field. a method for measuring interbilayer forces. *Soft Matter*, 6(22):4520–4527, 2010.

[182] Y. Zhang and Y. Feng. Stimuli-responsive microemulsions: State-of-the-art and future prospects. *Current Opinion in Colloid & Interface Science*, 49:27–41, 2020.

[183] Simon Stemplinger, Sylvain Prévost, Thomas Zemb, Dominik Horinek, and Jean François Dufrêche. Theory of ternary fluids under centrifugal fields. *Journal of Physical Chemistry B*, 125(43):12054–12062, nov 2021.

[184] Sylvain Prevost, Tobias Lopian, Maximilian Pleines, Olivier Diat, and Thomas Zemb. Small-angle scattering and morphologies of ultra-flexible microemulsions. *Journal of Applied Crystallography*, 49(6):2063–2072, Dec 2016.

[185] Mark James Abraham, Teemu Murtola, Roland Schulz, Szilárd Páll, Jeremy C. Smith, Berk Hess, and Erik Lindahl. Gromacs: High performance molecular simulations through multi-level parallelism from laptops to supercomputers. *SoftwareX*, 1-2:19–25, 2015.

[186] William L. Jorgensen, David S. Maxwell, and Julian Tirado-Rives. Development and Testing of the OPLS All-Atom Force Field on Conformational Energetics and Properties of Organic Liquids. *Journal of the American Chemical Society*, 118(45):11225–11236, January 1996.

[187] Shirley W. I. Siu, Kristyna Pluhackova, and Rainer A. Böckmann. Optimization

of the OPLS-AA Force Field for Long Hydrocarbons. *Journal of Chemical Theory and Computation*, 8(4):1459–1470, April 2012.

[188] J. L. F. Abascal and C. Vega. A general purpose model for the condensed phases of water: TIP4P/2005. *The Journal of Chemical Physics*, 123(23):234505, 12 2005.

[189] In-Chul Yeh and Gerhard Hummer. System-Size Dependence of Diffusion Coefficients and Viscosities from Molecular Dynamics Simulations with Periodic Boundary Conditions. *The Journal of Physical Chemistry B*, 108(40):15873–15879, October 2004.

Appendix A

Supplementary Material

A.1 SAXS Autodilution

A.1.1 Data teatment and analysis

$$I = I_{bkg} + \frac{I_{OZ}}{1 + (q\xi)^2} + \frac{I_{BP}}{1 + [(q - q_{BP})\xi_{BP}]^2} + \alpha q^{-4} \tag{A.1}$$

The raw data were obtained in terms of I vs. q and background subtraction was performed by removing the empty cell background from the initial datasets. For data fitting, a model proposed by Prevost et al. [120] was employed, as represented by Equation A.1. This model comprises four distinct terms, each capturing unique physical phenomena observed in the system.

The first term, I_{bkg}, represents a flat background intensity, providing a baseline scattering level not attributed to any specific structural features within the sample. This term isolates the contributions of other components in the fitting function.

The second term, $\frac{I_{OZ}}{1+(q\xi)^2}$, corresponds to the Ornstein-Zernike function. This Lorentzian term, centered at $q = 0$, captures scattering from critical fluctuations or small pre-Ouzo droplets within the system. Physically, it reflects the influence of density or composition fluctuations on scattering intensity, particularly near the phase separation critical point, where the correlation length ξ is crucial.

The third term, $\frac{I_{BP}}{1+[(q-q_{BP})\xi_{BP}]^2}$, represents a Lorentzian peak observed at higher q values, associated with scattering from smaller, well-defined structures, such as droplets or aggregates. In this system, it reflects octanol-ethanol clusters formed through hydrogen bonding interactions. The peak position q_{BP} corresponds to the inverse spacing of these structures, with ξ_{BP} related to peak sharpness, where $FWHM = 2/\xi_{BP}$.

Lastly, the αq^{-4} term accounts for the rapidly decreasing intensity at higher q values, known as Porod scattering. The q^{-4} dependence is characteristic of scattering from large objects or interfaces, in accordance with the Porod law, observed here for Ouzo emulsions.

Together, these four terms form a comprehensive model describing the scattering intensity over a broad range of length scales, effectively capturing the various physical

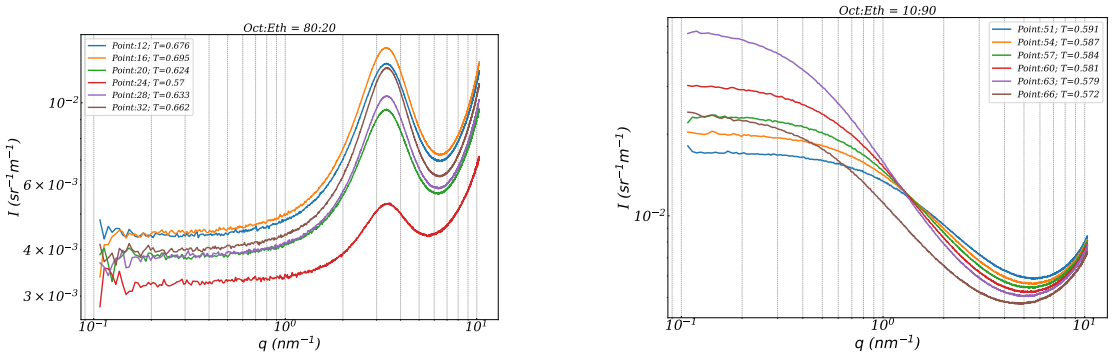

Figure A.1: *Types of I vs. q plot with different oil to ethanol starting ratio.* ***(Left)****: The pre-peak corresponds to smaller oil structuration at relatively higher q, indicating a smaller length scale. This occurs at a higher octanol ratio, making the pre-peak clearly visible.* ***(Right)****: With reduced octanol content and sufficient water, we see the emergence of aggregates namely the pre-Ouzo droplets.*

processes and structures within the system, as derived from the works of Prevost et al. [184].

Fitting Procedure: Given the vast number of points on the ternary phase diagram for which SAXS data was measured (each point representing a specific ratio of octanol, ethanol, and water), changes in the component ratios lead to variations in the system. These variations are reflected in the I vs. q data, resulting in changes to the basic profile of the curve and complicating the analysis or fitting of the raw data. To address this complexity, we employed the following procedure using Python:

- *Step 1:* Each I vs. q plot was fitted with various combinations of the terms from Eq. A.1, such as the 1^{st} and 2^{nd} term or the 1^{st}, 2^{nd}, and 3^{rd} term and so on.

- *Step 2:* After fitting the dataset with 10 different combinations independently, the best fit was selected based on the reduced chi-square value with the minimum number of terms possible. (The reduced chi-squared (χ^2) value quantifies how well the model fits the data per degree of freedom. A value of χ^2 close to 1 indicates a good fit, suggesting that the model adequately explains the observed data within the uncertainty. If χ^2 is significantly greater than 1, it suggests that the model does not fit the data well, possibly indicating that the model is overly simplistic or that the uncertainties in the data have been underestimated. Conversely, if χ^2 is much less than 1, it may indicate overfitting, where the model is too complex for the available data.)

- *Step 3:* Further, a list of the data points along with the best-fit function used and all other fit parameters is generated. This list has all seven parameters from the fitting function and the corresponding error values.

- *Step 4:* All the data points were plotted on a ternary phase diagram according to

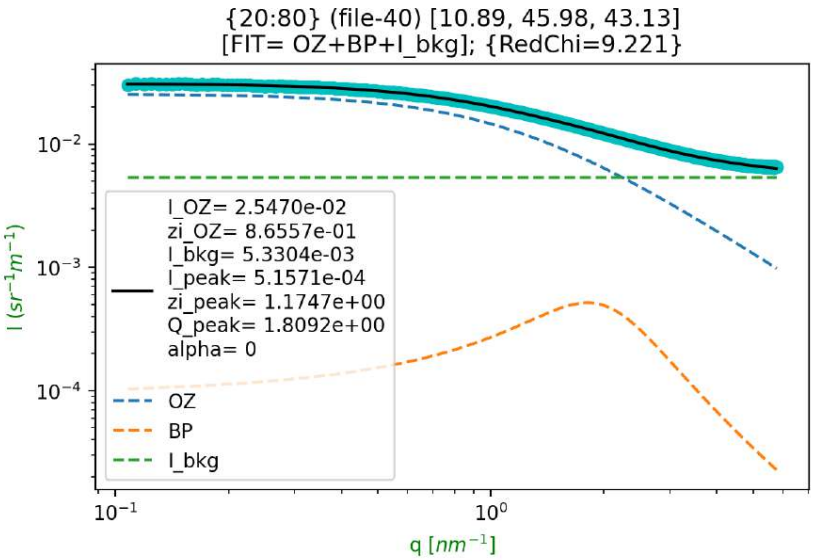

Figure A.2: *An example of data fitting using a combination of different terms from the main fit function, including the Ornstein-Zernike term, the pre-peak Lorentzian term, and a background amplitude, all displayed as separate components.*

the composition of those points. (Further simplification of the phase diagram was done as explained in the next section)

A.1.2 Composition Calculation:

The oil-ethanol mixture is treated as a pseudo component with extinction coefficient ϵ_{12} and volume fraction ϕ_{12}. The transmission of the ternary system upon dilution with water reads:

$$T_x = \exp\left[-\{\epsilon_{12}\phi_{12} + \epsilon_3(1-\phi_{12})\}t\right] \tag{A.2}$$

where the extinction coefficient of water ϵ_3 is determined from a measurement of pure water. Eq.A.2 can be solved for ϕ_{12} to obtain the composition of each sample:

$$\phi_{12} = \frac{\ln\left(\frac{T_x/T_0}{t}\right) + \epsilon_3}{\epsilon_3 - \epsilon_{12}} \tag{A.3}$$

In doing so, we assume that the sample $\phi_{12} + \phi_3 = 1$ and the ratio ϕ_1/ϕ_2 remains constant.

Moreover, as shown in Figure A.3, data in the biphasic region is largely absent along most dilution lines. This absence is due to phase separation within the sample, causing varying, uncontrolled ratios of oil-ethanol and water to enter the capillary. Consequently, this leads to fluctuations in the transmission coefficient, making it impossible to assign a definitive composition to that data.

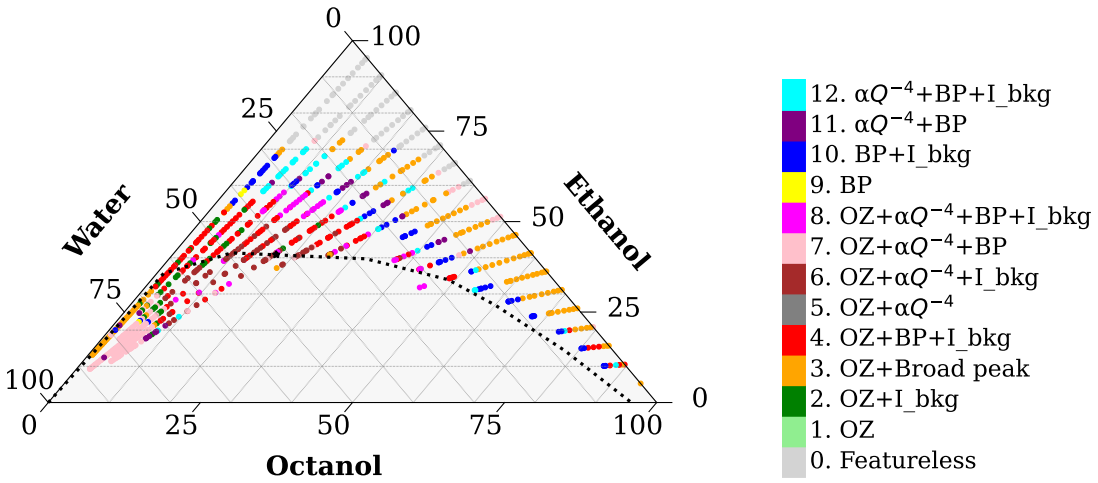

Figure A.3: *Initially generated ternary plot depicting different combination fit functions used for individual points on the autodilution line.*

A.1.3 Condensing the fit-functions on octanol ternary plot

Rewriting Eq. A.1 as:

$$I = Bkg + OZ + BP + Porod \tag{A.4}$$

The steps used to generate the condensed version of the ternary plot showing fit functions (Figure 3.5) from the initially generated, raw fit-function ternary plot (Figure A.3) are as follows:

1. **Featureless (Light blue points):**
   - For points with low oil and water concentrations, no distinct features are observed within the given q range. These points are initially fitted using a BP term, but as the peak position (q_{BP}) reaches the boundary of the fit range, they are classified as featureless.
2. **Primarily pre-peak (Blue points):**
   - For initial fit functions corresponding to '*3. OZ+BP*' or '*4. OZ+BP+I_bkg*': When the OZ intensity at the peak position is less than the pre-peak intensity, i.e.,
   $$\left(\frac{I\_OZ}{1+(q\_BP \cdot zi\_OZ)^2}\right) < I\_BP,$$
   and the water concentration $water\_conc \leq 50\%$, the fit predominantly reflects a pre-peak contribution on the oil-rich side, as observed in the scattering curves.
   - If the fit is *7. OZ+αq^{-4}+BP* or *8. OZ+αq^{-4}+BP+I_bkg* and the OZ intensity is less than the peak intensity, and water concentration $water\_conc \leq 50$, it is *10. BP+I_bkg* ($fit = 10$).

- If the fit is *11.* αq^{-4}*+BP* or *12.* αq^{-4}*+BP+I_ bkg* and water concentration $water\_conc \leq 50$, it has negligible Porod effect.

3. **Primarily Ornstein-Zernike (Green points):**

- For initial fit functions corresponding to '*3. OZ+BP*' or '*4. OZ+BP+I_ bkg*': When
$$\left(\frac{I\_OZ}{1+(q\_BP \cdot zi\_OZ)^2}\right) > I\_BP,$$
and if $water\_conc \leq 50\%$, The fit primarily exhibits an Ornstein-Zernike (OZ) contribution with a subtle presence of the pre-peak.
- For initial fit functions corresponding to '*3. OZ+BP*' or '*4. OZ+BP+I_ bkg*': If $water\_conc > 50\%$, the fit is also classified as primarily Ornstein-Zernike.
- If the fit was previously *'5. OZ+*αq^{-4}*'* or *'6. OZ+*αq^{-4}*+I_ bkg'* and the following threshold is satisfied at $q = 0.05nm^{-1}$, which is a relatively low value where we can observe remnants of both Porod relaxation and OZ:
$$\left(\frac{I\_OZ}{1+(0.05 \cdot zi\_OZ)^2}\right) > \alpha \cdot 0.05^{-4}$$
- If the fit is *'7. OZ+*αq^{-4}*+BP'* or *'8. OZ+*αq^{-4}*+BP+I_ bkg'* and the OZ intensity exceeds the peak intensity, and water concentration $water\_conc \leq 50\%$ where we don't have any noticeable Porod effect.

4. **Porod and OZ (Brown points):**

- If the fit was previously *'5. OZ+*αq^{-4}*'* or *'6. OZ+*αq^{-4}*+I_ bkg'* and the following threshold is satisfied at $q = 0.05nm^{-1}$, then the final fit is set to be *'6. OZ+*αq^{-4}*+I_ bkg'*, representing a mix of Porod and OZ where Porod relaxation is not very subtle:
$$\left(\frac{I\_OZ}{1+(0.05 \cdot zi\_OZ)^2}\right) < \alpha \cdot 0.05^{-4}$$
- If the fit is *'7. OZ+*αq^{-4}*+BP'* or *'8. OZ+*αq^{-4}*+BP+I_ bkg'* and the OZ intensity exceeds the peak intensity and water concentration exceeds 50% where the Porod effect is not subtle.

Table A.1: *Components of the fit-function used. Here, OZ: Ornstein-Zernike; BP: pre-peak; αq^{-4}: Porod relaxation; I_bkg: background amplitude*

#	**Fit Type**
1	OZ
2	OZ + I_bkg
3	OZ + BP
4	OZ + BP + I_bkg
5	OZ + αq^{-4}
6	OZ + αq^{-4} + I_bkg
7	OZ + αq^{-4} + BP
8	OZ + αq^{-4} + BP + I_bkg
9	BP
10	BP + I_bkg
11	αq^{-4} + BP
12	αq^{-4} + BP + I_bkg

Table A.2: *Refining of Fit Function*

Initial Fits	**Condition**	**Final Category**
1. BP *2. BP + I_bkg*	No distinct features, low oil and water concentrations. q_{peak} reaches the boundary of the fit range	**Featureless (Light blue)**
3. OZ+BP *4. OZ+BP+I_bkg*	$I\_OZ/(1+(q\_BP \cdot zi\_OZ)^2) < I\_BP$ $water\_conc \leq 50\%$ (Dominated by BP on oil-rich side)	**Primarily pre-peak (Blue)**
7. OZ+αq^{-4}+BP *8. OZ+αq^{-4}+BP+I_bkg*	$I\_OZ/(1+(q\_BP \cdot zi\_OZ)^2) < I\_BP$ $water\_conc \leq 50$ (Negligible Porod relaxation)	**Primarily pre-peak (Blue)**
11. αq^{-4}+BP *12. αq^{-4}+BP+I_bkg*	$water\_conc \leq 50\%$ (negligible Porod effect)	**Primarily pre-peak (Blue)**
3. OZ+BP *4. OZ+BP+I_bkg*	$I\_OZ/(1+(q\_BP \cdot zi\_OZ)^2) > I\_BP$ $water\_conc > 50\%$ (Dominated by OZ in water-rich region)	**Primarily OZ (Green)**
5. OZ+αq^{-4} *6. OZ+αq^{-4}+I_bkg*	At $q = 0.05nm^{-1}$: $I\_OZ/(1+(0.05 \cdot zi\_OZ)^2) > \alpha \cdot 0.05^{-4}$.	**Primarily OZ (Green)**
7. OZ+αq^{-4}+BP *8. OZ+αq^{-4}+BP+I_bkg*	$I\_OZ/(1+(q\_BP \cdot zi\_OZ)^2) > I\_BP$ $water\_conc \leq 50\%$ (Negligible Porod effect)	**Primarily OZ (Green)**
5. OZ+αq^{-4} *6. OZ+αq^{-4}+I_bkg*	At $q = 0.05nm^{-1}$: $I\_OZ/(1+(0.05 \cdot zi\_OZ)^2) < \alpha \cdot 0.05^{-4}$ Mix of Porod and OZ	**Porod and OZ (Brown)**
7. OZ+αq^{-4}+BP *8. OZ+αq^{-4}+BP+I_bkg*	$I\_OZ/(1+(q\_BP \cdot zi\_OZ)^2) > I\_BP$ $water\_conc > 50\%$ (Porod effect not subtle)	**Porod and OZ (Brown)**

Table A.3: *Summary of Forces Involved in the Stabilization of Pre-Ouzo Structures*

Force	Description in context of pre-Ouzo
Entropy-driven dispersion	Favors smaller, polydisperse domains, preventing phase separation and ensuring dynamic equilibrium.
Hydration forces	Arise between octanol-rich domains due to structured water at high-density OH interfaces, preventing coalescence.
Van der Waals forces	Negligible in comparison to hydration and entropy effects due to weaker interaction strength.
Bending energy	Minimal due to high curvature of domains, indicating ultraflexible microemulsions.

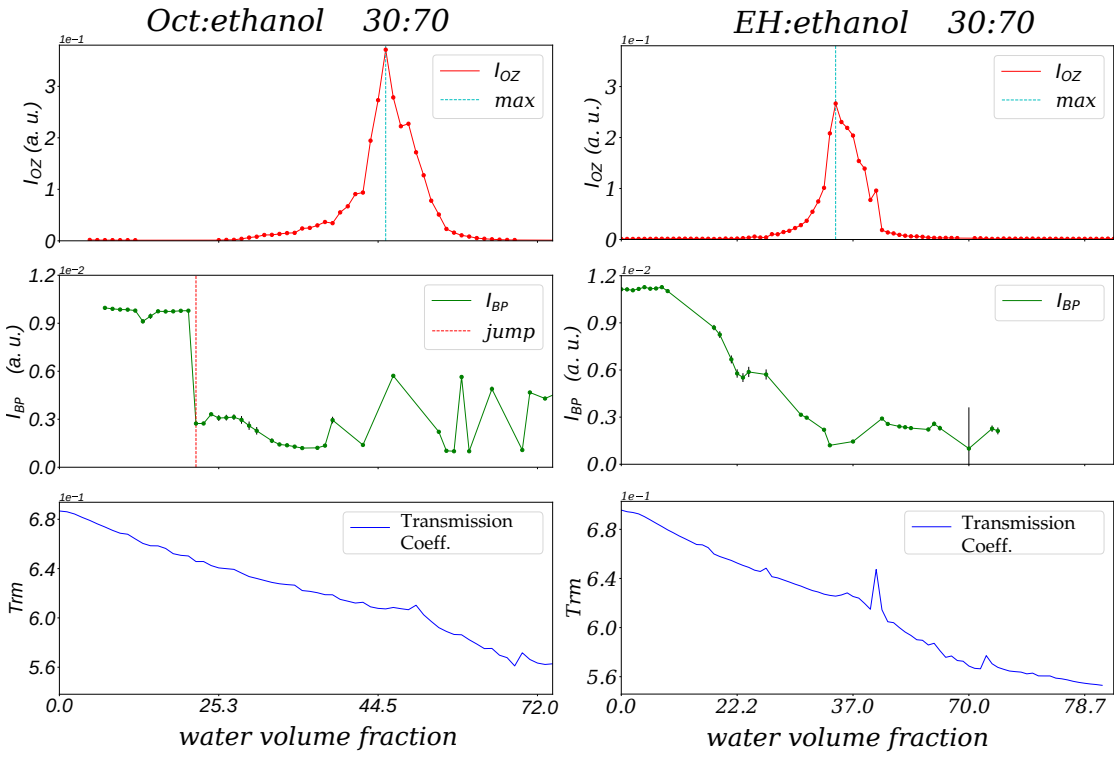

Figure A.4: *Comparison of* ***(left)*** *the octanol-based ternary system and* ***(right)*** *the EH-based ternary system in terms of OZ intensity (I_{OZ}), pre-peak intensity (I_{BP}), and the corresponding transmission values from SAXS measurements along the 30:70 oil to ethanol autodilution line.*

Table A.4: *Samples where $\xi_{OZ_{EH}} > \xi_{OZ_{Oct}}$. These samples show a higher oil and ethanol content, while water content generally correlates inversely with oil content. Higher oil percentage tends to favor higher $\xi_{OZ_{EH}}$ values compared to $\xi_{OZ_{Oct}}$. The compositions are rounded off to the nearest integer values.*

Oil%	**Eth%**	**Water%**	$\xi_{OZ_{EH}}$	$\xi_{OZ_{Oct}}$
10	41	49	2.0826	1.0053
17	40	43	4.0000	1.0313
13	40	47	3.2552	1.1130
10	39	51	2.7168	1.0523
26	39	35	1.9671	1.0263
16	38	46	3.1631	1.1867
13	38	49	3.3028	1.2644
7	38	55	1.9294	1.0152
9	37	54	2.2346	1.4347
12	37	51	3.3606	1.5634
16	37	47	2.6880	1.8192
6	36	58	1.8587	1.1849
12	35	53	2.9566	2.5097
6	35	59	1.5250	1.0845
4	33	63	1.3921	1.1733
4	32	64	1.1318	1.1256
9	27	64	1.4376	1.2583

Table A.5: *Samples where $\xi_{OZ_{EH}} < \xi_{OZ_{Oct}}$. These samples generally have a lower ethanol content (typically 3%-7%), and the ethanol content spans a wide range. Water content tends to be higher in this group, particularly when oil content is lower, and this favors lower $\xi_{OZ_{EH}}$ values compared to $\xi_{OZ_{Oct}}$.*

Oil%	**Eth%**	**Water%**	$\xi_{OZ_{EH}}$	$\xi_{OZ_{Oct}}$
16	36	48	2.6880	3.0269
9	34	57	1.9913	2.8222
11	33	56	1.4029	3.4107
6	33	61	1.2489	1.6112
14	32	54	1.0767	2.9372
5	31	64	1.0686	2.5767
8	31	61	1.4607	2.9103
3	31	66	1.3184	1.4732
8	30	62	1.2621	2.5582
5	30	65	1.1059	2.3860
3	30	67	1.3104	1.4069
10	29	61	1.6282	2.3907
7	29	64	1.4987	2.3916
7	28	65	1.1595	2.4016
9	26	65	1.1070	2.0660
7	21	72	1.0008	1.6792

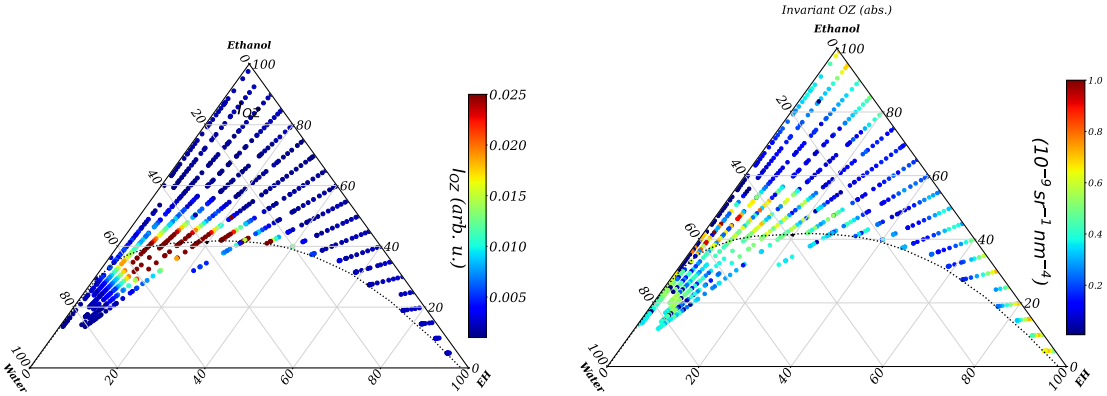

Figure A.5: ***Left****: Intensity of the OZ term (I_{OZ}),* ***Right****: OZ invariant for the 2-ethyl hexanol ternary system, based on the calculation in Equation A.5. In some oil-rich regions, although the exact I_{OZ} is very small, the invariant at the same sample points shows significant values. Since the Porod invariant depends on density difference and volume fractions rather than aggregate size, certain reverse aggregates exhibit notable values.*

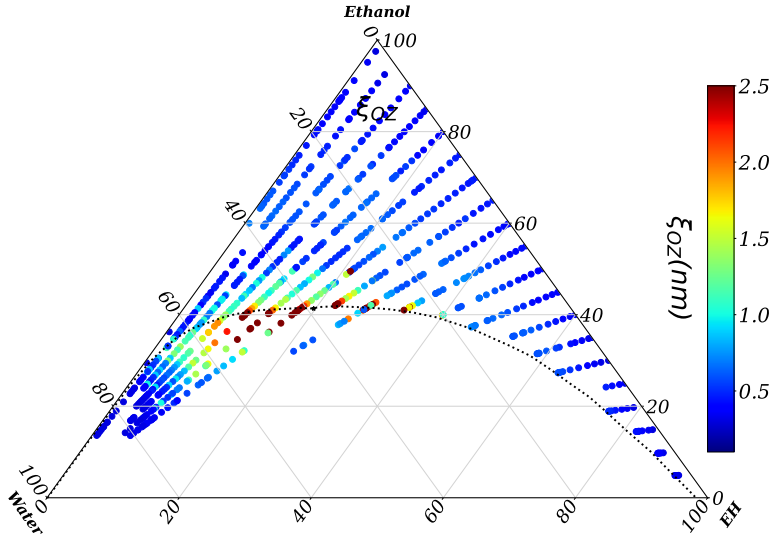

Figure A.6: *The length scale parameter ξ_{OZ} for the EH ternary system, showing pre-Ouzo aggregates near the critical point and the absence of significant aggregation on the oil-rich side.*

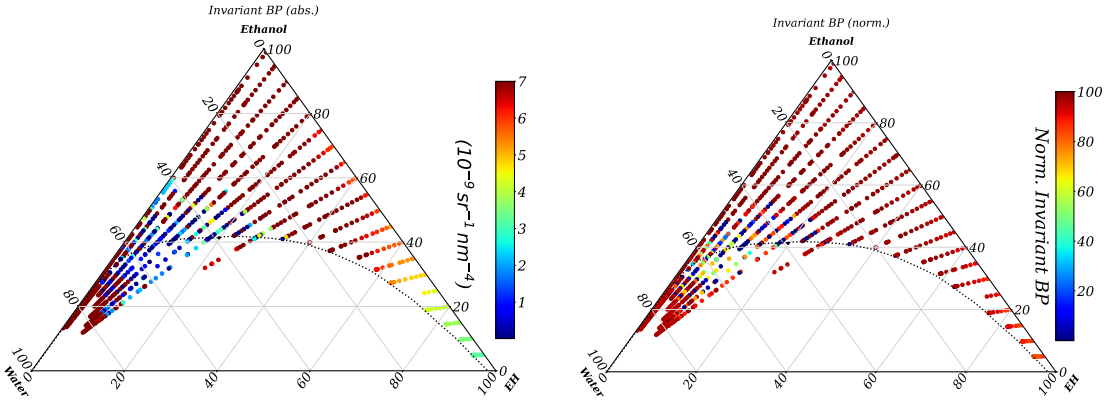

Figure A.7: *Comparison of* ***(left)*** *absolute BP invariant (based on equation A.7) and* ***(right)*** *normalized BP invariant (based on equation A.10) for EH based ternary.*

A.2 Invariant Oct and EH

The following equations describe the calculation of invariants from the scattering intensity, integrating over a defined q-range. These invariants provide a measure of the contribution from different structural components in the system.

Ornstein-Zernike (OZ) Invariant

$$\text{Invariant}_{\text{OZ}} = \int_{q_{\text{start}}}^{q_{\text{end}}} \frac{I_{\text{oz}} q^2}{1 + q^2 \xi_{\text{oz}}^2}\, dq \tag{A.5}$$

The associated uncertainty is determined using error propagation:

$$\sigma_{\text{OZ}} = \sqrt{\left(\frac{\partial \text{Invariant}_{\text{OZ}}}{\partial I_{\text{oz}}} \Delta I_{\text{oz}}\right)^2 + \left(\frac{\partial \text{Invariant}_{\text{OZ}}}{\partial \xi_{\text{oz}}} \Delta \xi_{\text{oz}}\right)^2} \tag{A.6}$$

Broad Peak (BP) Invariant

$$\text{Invariant}_{\text{BP}} = \int_{q_{\text{start}}}^{q_{\text{end}}} \frac{I_{\text{BP}} q^2}{1 + (q - q_{\text{BP}})^2 \xi_{\text{BP}}^2}\, dq \tag{A.7}$$

The uncertainty considers variations in intensity, peak position, and correlation length:

$$\sigma_{\text{BP}} = \sqrt{\left(\frac{\partial \text{Invariant}_{\text{BP}}}{\partial I_{\text{BP}}} \Delta I_{\text{BP}}\right)^2 + \left(\frac{\partial \text{Invariant}_{\text{BP}}}{\partial q_{\text{BP}}} \Delta q_{\text{BP}}\right)^2 + \left(\frac{\partial \text{Invariant}_{\text{BP}}}{\partial \xi_{\text{BP}}} \Delta \xi_{\text{BP}}\right)^2} \tag{A.8}$$

For octanol/EH mixtures, integration is carried out over the range $q_{\text{start}} = 0$ nm^{-1} to $q_{\text{end}} = 30$ nm^{-1}.

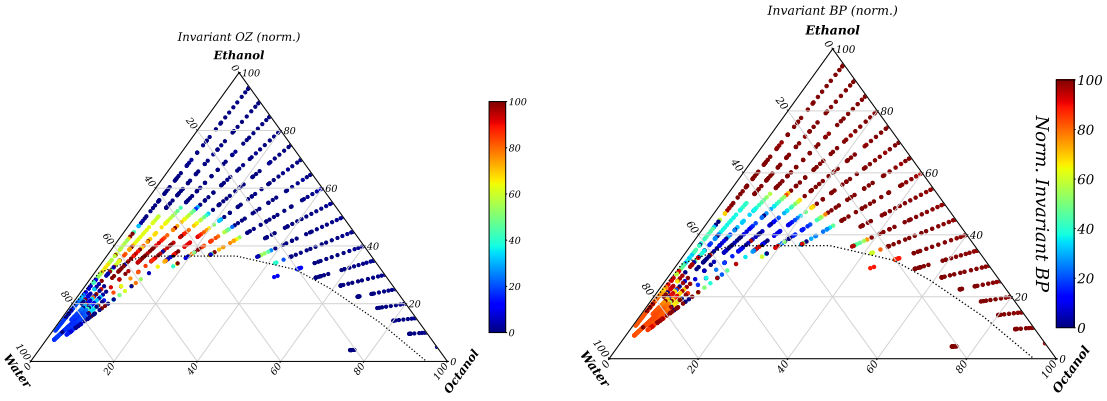

Figure A.8: ***(Left)*** *normalized OZ invariant (from equation A.9) and* ***(right)*** *normalized BP invariant (from equation A.10) for octanol based ternary.*

Normalization

The invariants are normalized to express their relative contributions as percentages, allowing for a direct comparison between the OZ and BP terms.

$$\text{Normalized}_{\text{OZ}} = \frac{\text{Invariant}_{\text{OZ}}}{\text{Invariant}_{\text{OZ}} + \text{Invariant}_{\text{BP}}} \times 100 \tag{A.9}$$

$$\text{Normalized}_{\text{BP}} = \frac{\text{Invariant}_{\text{BP}}}{\text{Invariant}_{\text{OZ}} + \text{Invariant}_{\text{BP}}} \times 100 \tag{A.10}$$

This ensures that the contributions from the different scattering components are directly comparable.

A.3 Mathematical Formulations of Free Energy Calculations

Entropy:

All formulations presented here are based on the work of [109], with special thanks to Thomas Z. and Stjepan M. for their invaluable assistance.

Entropy depends on the *Ornstein-Zernike* (OZ) correlation length (ξ) because ξ determines the spatial correlations in density fluctuations, shaping the disorder of the system. In a *random Gaussian field* with the OZ spectrum, a level cut near zero creates a disordered network of oil- and water-rich domains. Since ξ dictates how these fluctuations decay over distance, it directly influences the entropy of the surface distribution. A larger ξ results in more structured, lower-entropy configurations, while a smaller ξ leads to greater disorder and higher entropy. This relationship holds for both sharp and diffuse interfaces, as long as the density fluctuations follow the OZ spectrum.

The *Ornstein-Zernike* (OZ) spectrum is given by the equation:

$$v(k,\xi) = \frac{1}{1+k^2\xi^2} \tag{A.11}$$

where k is the wavevector.

To normalize the spectrum, we introduce a normalization constant that depends on the cut-off wavenumber k_c and the correlation length ξ. The normalized spectrum $v_0(k,\xi)$ is given by:

$$v_0(k,\xi) = \frac{2\pi^2}{(1+k^2\xi^2)\int_0^{\frac{2\pi}{\xi}} \frac{k^2}{1+k^2\xi^2}\,dk} \tag{A.12}$$

Here, the denominator contains an integral that accounts for the cut-off at $k_c = \frac{2\pi}{\xi}$, beyond which fluctuations are not considered.

The entropy function is defined as:

$$S_{\text{entropy}}(\xi) = \frac{1}{2\pi^2}\int_0^{\frac{2\pi}{\xi}} k^2 \log(v_0(k,\xi))\,dk \tag{A.13}$$

Free Energy of Hydration (or Solvation Energy):

The free energy of solvation is expressed as:

$$\text{solvationFE}(\xi, P_0, \lambda, \phi) = 10^6 \cdot \frac{S}{V}(\xi) \cdot f_{\text{hydration}}(P_0, \lambda, \xi, \phi) \tag{A.14}$$

$$f_{\text{hydration}}(P_0, \lambda, \xi, \phi) = \int_{\infty}^{\text{up-lim}} -P_0 e^{-u/\lambda}\,du \tag{A.15}$$

In this expression, the integrand represents the hydration pressure, where P_0 is the contact pressure, dependent on the binding and positioning of water and ethanol molecules at the interface. Additionally, λ is the decay length related to the hydration.

The upper limit of the integral corresponds to the surface separation h_T, given by:

$$h_T(\xi,\phi) = \frac{1-\phi}{A/V(\xi)} \tag{A.16}$$

In this expression, ϕ denotes the oil-rich volume fraction, and $A/V(\xi)$ is a function that characterizes the surface area per unit volume of the level-cut Gaussian random field, which contributes to the hydration force. Specifically, $A/V(\xi)$ is given by:

$$\frac{A}{V}(\xi) = \frac{2}{\pi}\sqrt{\frac{\langle k^2\rangle(\xi)}{3}} \tag{A.17}$$

where $\langle k^2\rangle(\xi)$ is calculated as:

$$\langle k^2\rangle(\xi) = \frac{\int_0^{\frac{2\pi}{\xi}} k^4 v_0(k,\xi)\,dk}{2\pi^2} \tag{A.18}$$

Ternary	ξ (nm)	ϕ	P_0 (Pa)	λ (m)
Oct	1.57	0.36	1×10^9	2.75×10^{-10}
EH	3.38	0.36	2.9×10^9	2.75×10^{-10}

Table A.6: *Parameters for octanol and EH at 12% oil, 37% ethanol, and 51% water, used to calculate the corresponding combined free energy for the optimal ξ (OZ correlation length) based on SAXS experiments. This suggests that, for the given composition in the EH and octanol ternary system, the contact pressure for EH is 2.9 times higher due to a larger pre-Ouzo aggregate.*

Curvature or Bending Free Energy:

The free energy associated with curvature is defined as:

$$\text{CurvatureFE}(k_c, \xi, \phi) = k_c \cdot 3.31356096 \times 10^{-23} \cdot \pi \cdot \rho(10^{-9}\xi, \phi) \tag{A.19}$$

where the density function is expressed as:

$$\rho(r, \phi) = \frac{3\phi}{4\pi r^3} \tag{A.20}$$

Here, a conservative upper bound of the bending constant (k_c) of 0.1 kBT is used, because bending constants are close to 1 kBT for C12 chains. The bending constants scale like the cube of the "film thickness" and are reduced in the presence of short-chain alcohols; therefore, the real value is certainly below that value.

Total Free Energy

Therefore, the total free energy is expressed as:

$$\text{TotalFE}(\xi) = S_{\text{entropy}}(\xi) + \text{solvationFE}(\xi, P_0, \lambda, \phi) + \text{CurvatureFE}(k_c, \xi, \phi) \tag{A.21}$$

Table A.7: *Composition of octanol based samples (% Volume fraction) used for the temperature dependant SAXS study*

SAMPLE	Octanol	Ethanol	Water
WO_1	17.29	40.71	42.00
WO_2	17.83	41.97	40.20
WO_3	18.37	43.23	38.40
WO_4	18.70	44.02	37.28
WO_5	16.51	43.36	40.13
WO_6	15.89	46.12	37.99
WO_7	15.28	47.75	36.98
WO_8	15.21	41.84	42.95
WO_9	13.33	42.77	43.90
WO_10	11.24	43.80	44.96

Table A.8: *Composition of EH based samples (% Volume fraction) used for the temperature dependant SAXS study*

SAMPLE	Octanol	Ethanol	Water
WEH_1	20.56	45.24	34.19
WEH_2	22.61	49.74	27.65
WEH_3	22.10	48.62	29.28
WEH_4	21.51	47.33	31.16
WEH_5	19.37	48.86	31.77
WEH_6	18.08	51.77	30.15
WEH_7	17.50	54.04	28.46
WEH_8	18.26	46.82	34.92
WEH_9	16.36	47.91	35.73
WEH_10	14.28	49.10	36.62

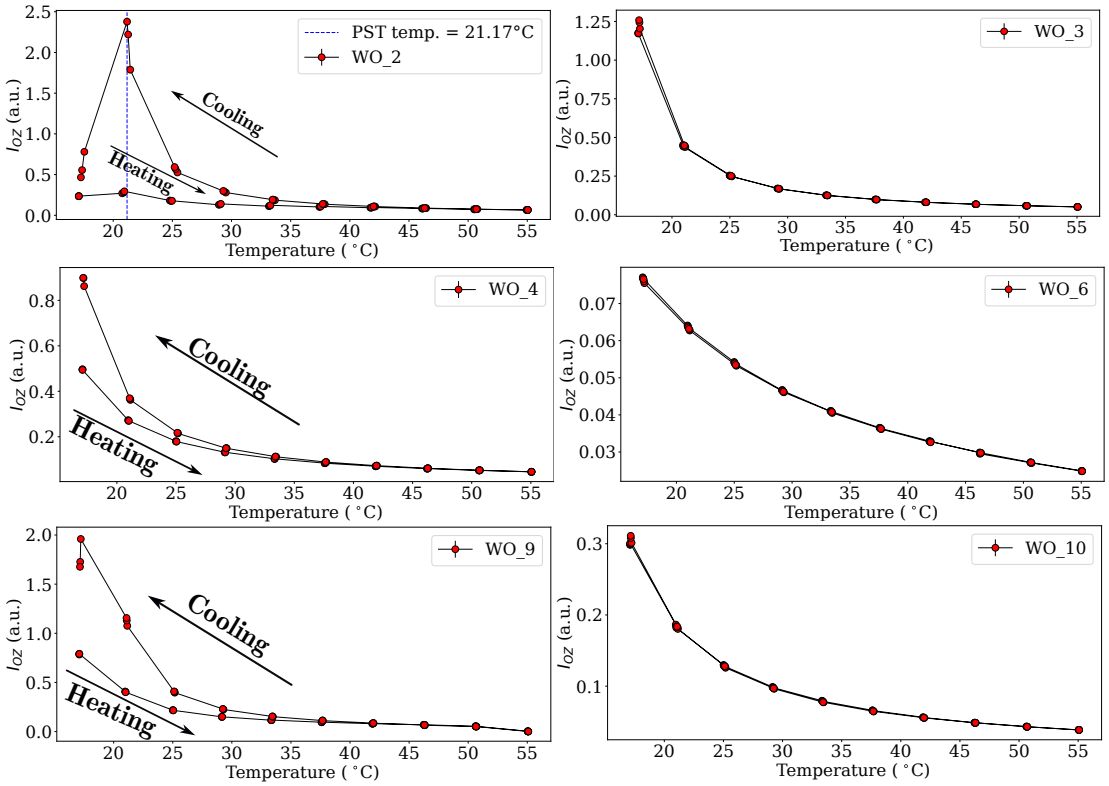

Figure A.9: *I_{OZ} vs. temperature plots for octanol-based ternary samples (WO_2, WO_3, WO_4, WO_6, WO_9, and WO_10) as shown in Figure 4.2.*

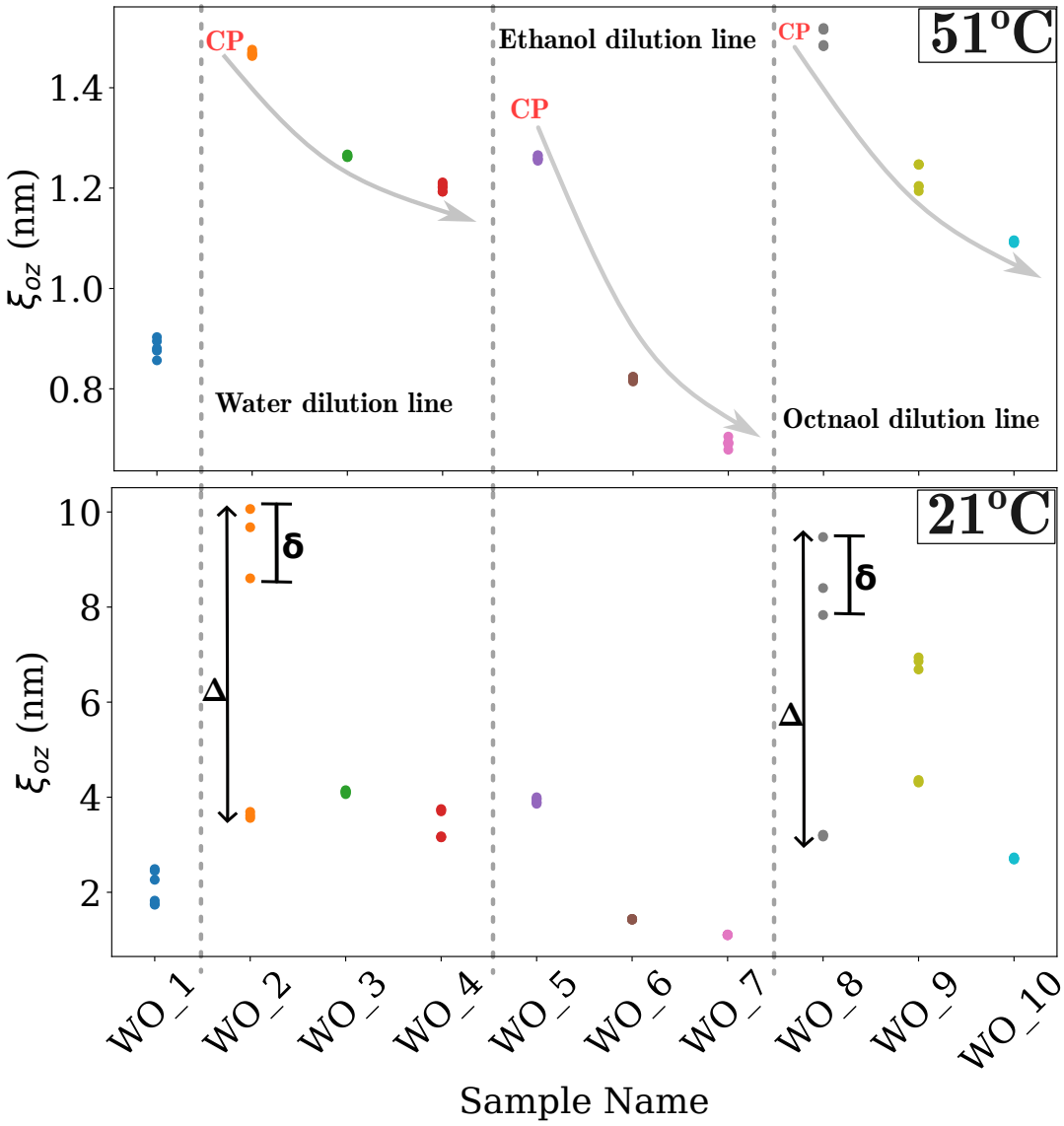

Figure A.10: *Figure showing the ξ_{OZ} values for all 10 samples analyzed for the octanol-ethanol-water ternary at 51°C (**Top**) and 21°C (**Bottom**). For each sample, three SAXS readings are taken during heating and three during cooling. The gray curved arrows serve as a guideline for the change in ξ value with increasing distance of the samples relative to the critical point (CP). The dotted lines distinguish the three categories of dilution lines for the samples with respect to CP, namely the water, ethanol, and octanol lines. At higher temperatures, the ξ values remain largely unchanged regardless of whether the sample follows the heating or cooling path. However, at lower temperatures, discrepancies in the ξ values between heating and cooling paths are observed, represented by Δ. Additionally, for the same temperature and cooling path, there can be variations in the ξ values corresponding to the three SAXS readings, denoted by δ.*

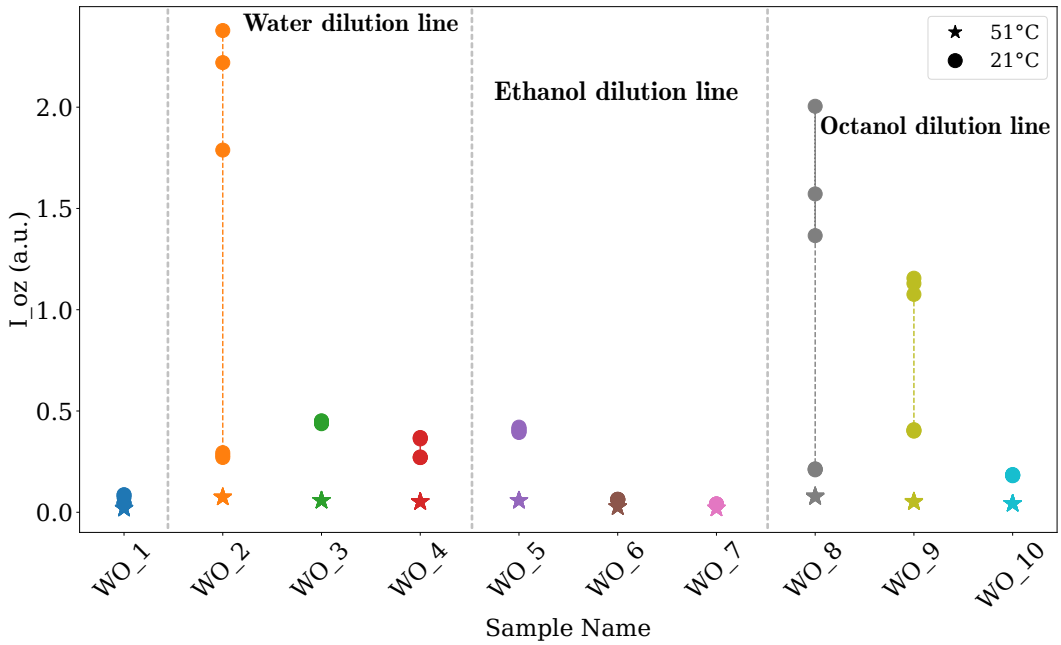

Figure A.11: *I_{OZ} for 10 samples along the three dilution lines near the critical point (CP) of the octanol-ethanol-water ternary system. The I_{OZ} value for sample WO_1 remains lower than that of the other samples at both temperatures.*

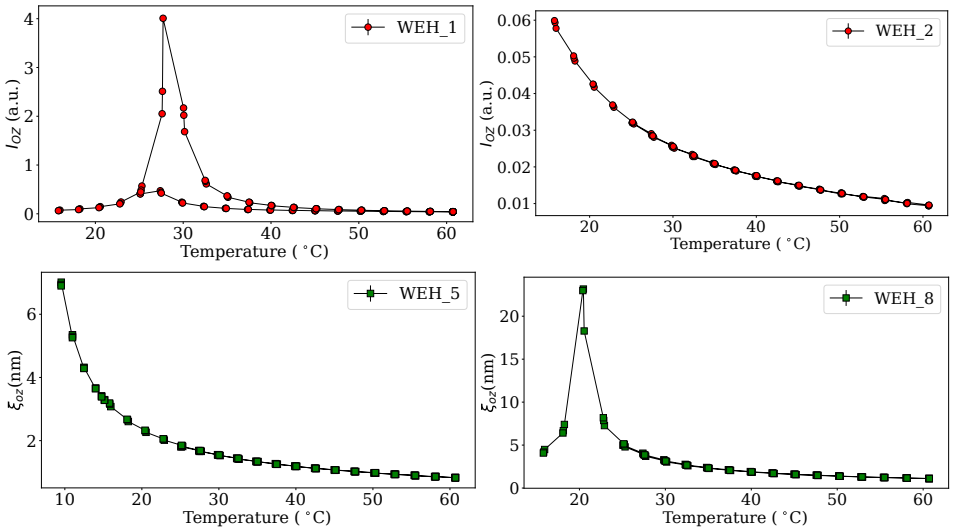

Figure A.12: *I_{OZ} **(top)** and ξ_{OZ} **(bottom)** as a function of temperature for several samples of the 2-ethyl hexanol-ethanol-water ternary system. The samples are numbered in the same order as shown in Figure 4.2 relative to the critical point (CP) of EH ternary.*

Table A.9: *Mass and mole percentage of the components used in the eight samples corresponding to all-H contrast for PFG-NMR study*

Sample	Mass Fraction (%)			Mol Fraction (%)		
	W_{Oct}	W_{Eth}	W_{H2O}	X_{Oct}	X_{Eth}	X_{H2O}
HL1	0.00	43.79	56.21	0.00	23.35	76.65
HL2	9.99	43.74	46.26	2.14	26.42	71.45
HL3	17.29	43.72	38.99	4.09	29.23	66.68
HL4	24.54	43.68	31.78	6.50	32.69	60.82
HL5	31.98	43.64	24.38	9.64	37.21	53.15
HL6	39.16	43.61	17.23	13.65	42.96	43.40
HL7	46.30	43.58	10.12	19.08	50.77	30.15
HL8	56.46	43.54	0.00	31.45	68.55	0.00

A.4 PFG NMR calculations

A.4.1 Horizontal line

For the NMR experiments, three distinct sets of samples (**P1**, **P2**, and **P3**) were prepared using different combinations of deuterated and protonated components, defined as follows:

- **P1**: H-Oct + D-Eth + D_2O
- **P2**: D-Oct + H-Eth + D_2O
- **P3**: D-Oct + D-Eth + H_2O

Table A.9 provides the compositions of the eight all-H samples used for NMR, arranged along the 'horizontal line' (refer to Figure 5.1). These mole fractions serve as a reference for calculating the corresponding mass fractions, which are used for sample preparation across the three different contrasts (P1, P2, and P3).

Figure A.13 and Table A.10 present the diffusion coefficients obtained from the NMR experiments for all eight samples across the three sets (P1, P2 and P3).

Mentioned below are the steps to Calculate Individual Diffusion Coefficients from Raw NMR Data (demonstrated using set P1):

1. **Determine Moles of Labile Species (H/D):**

$$\text{H-Octanol:} \quad X_{\text{labile-Hoct}} = \text{Moles of octanol in the ternary mixture} \tag{A.22}$$

$$\text{D-Ethanol:} \quad X_{\text{labile-Deth}} = \text{Moles of ethanol in the ternary mixture} \tag{A.23}$$

$$D_2O: \quad X_{\text{labile-D2O}} = 2 \times (\text{Moles of } D_2O \text{ in the ternary mixture}) \tag{A.24}$$

2. **Calculate the Fraction of Labile H:**

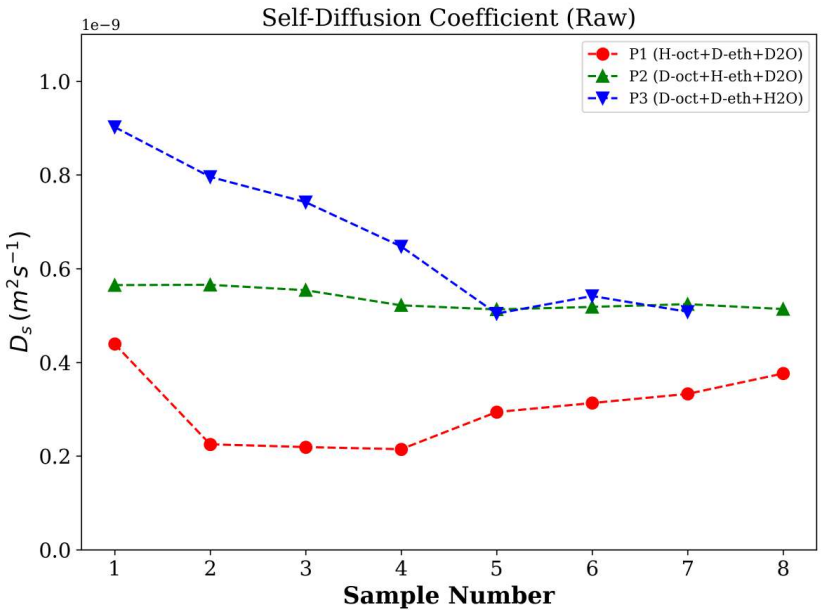

Figure A.13: *Raw diffusion coefficient of the 8 samples along the horizontal line for the different contrasts: P1, P2 and P3*

Table A.10: *Raw data for diffusion coefficients (D_{raw}) in m^2/s for the 8 samples corresponding to the 3 contrasts: p1, P2 and P3.*

Sample No.	$D_{\text{P1-raw}}$	$D_{\text{P2-raw}}$	$D_{\text{P3-raw}}$
HL1	4.3919×10^{-10}	5.6494×10^{-10}	9.0215×10^{-10}
HL2	2.2522×10^{-10}	5.6554×10^{-10}	7.9586×10^{-10}
HL3	2.1933×10^{-10}	5.5398×10^{-10}	7.4187×10^{-10}
HL4	2.1474×10^{-10}	5.2174×10^{-10}	6.4743×10^{-10}
HL5	2.9396×10^{-10}	5.1296×10^{-10}	5.0411×10^{-10}
HL6	3.1323×10^{-10}	5.1840×10^{-10}	5.4159×10^{-10}
HL7	3.3270×10^{-10}	5.2424×10^{-10}	5.0805×10^{-10}
HL8	3.7621×10^{-10}	5.1377×10^{-10}	-

$$f_{\text{labile-H}} = \frac{X_{\text{labile-Hoct}}}{X_{\text{labile-Hoct}} + X_{\text{labile-Deth}} + X_{\text{labile-D2O}}} \tag{A.25}$$

3. **Determine Non-Labile H:**

$$\text{H-Octanol:} \quad X_{\text{non-labile-Hoct}} = 17 \times X_{\text{labile-Hoct}} \tag{A.26}$$

$$\text{D-Ethanol:} \quad X_{\text{non-labile-Deth}} = 0 \tag{A.27}$$

$$D_2O: \quad X_{\text{non-labile-D2O}} = 0 \tag{A.28}$$

4. **Calculate Total H for Each Component:**

$$\text{H-Octanol:} \quad X_{\text{total-Hoct}} = X_{\text{labile-Hoct}} \times f_{\text{labile-H}} + X_{\text{non-labile-Hoct}} \tag{A.29}$$

$$\text{D-Ethanol:} \quad X_{\text{total-Deth}} = X_{\text{labile-Deth}} \times f_{\text{labile-H}} + X_{\text{non-labile-Deth}} \tag{A.30}$$

$$D_2O: \quad X_{\text{total-D2O}} = X_{\text{labile-D2O}} \times f_{\text{labile-H}} + X_{\text{non-labile-D2O}} \tag{A.31}$$

5. **Determine Mole Fractions of H for all the 3 contrasts:** The mole fractions of H ($X^i_{Pj-Oct/Eth/H2O}$) for all three components are calculated for each sample (HL1–HL8) in each set (P1, P2, P3). Where i = 1 to 8 (corresponding to the 8 samples) and j= 1,2,3 for each contrast set.

6. **Solve for Individual Diffusion Coefficients:** Using the mole fractions ($X^i_{Pj-Oct/Eth/H2O}$) and mean diffusion coefficients ($D_{Pj-\text{raw}}$) from the raw NMR data for each set, the following equations are solved:

$$X^i_{\text{P1-Oct}} \cdot D_{s-\text{Oct}} + X^i_{\text{P1-Eth}} \cdot D_{s-\text{Eth}} + X^i_{\text{P1-Wat}} \cdot D_{s-\text{H}_2\text{O}} = D_{\text{P1-raw}} \tag{A.32}$$

$$X^i_{\text{P2-Oct}} \cdot D_{s-\text{Oct}} + X^i_{\text{P2-Eth}} \cdot D_{s-\text{Eth}} + X^i_{\text{P2-Wat}} \cdot D_{s-\text{H}_2\text{O}} = D_{\text{P2-raw}} \tag{A.33}$$

$$X^i_{\text{P3-Oct}} \cdot D_{s-\text{Oct}} + X^i_{\text{P3-Eth}} \cdot D_{s-\text{Eth}} + X^i_{\text{P3-Wat}} \cdot D_{s-\text{H}_2\text{O}} = D_{\text{P3-raw}} \tag{A.34}$$

Solving these equations yields the individual diffusion coefficients ($D_{s-oct/Eth/H2O}$) of the components along the horizontal line of the ternary phase diagram, as summarized in Table A.11 and illustrated in Figure A.14.

A.4.2 Diagonal lines

The calculated diffusion coefficients for each of the three components in the ternary system are presented (Table A.12) for the six samples along the line extending toward the water vertex in the ternary phase diagram, as determined using the steps outlined above. Additionally, the diffusion coefficient for the fully hydrogenated sample near the octanol vertex in the ternary phase diagram is included (Table A.13).

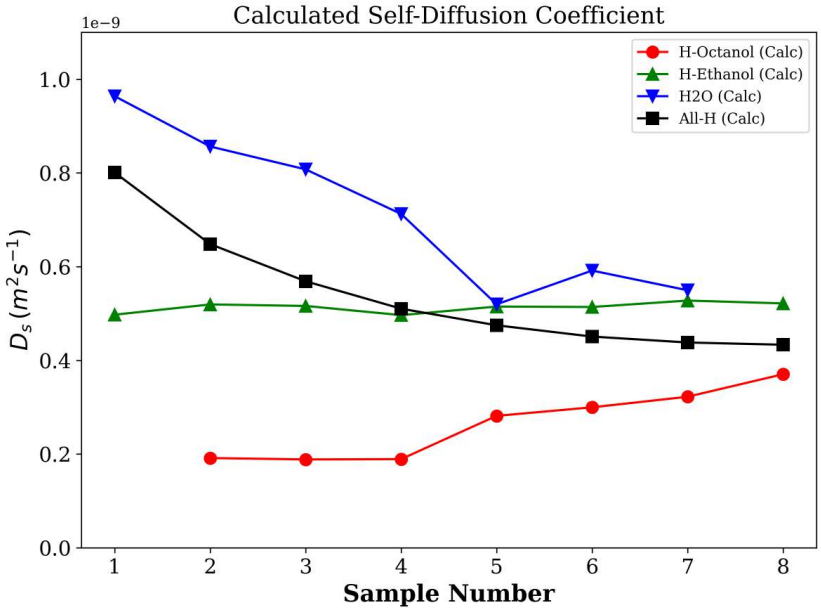

Figure A.14: *Self-Diffusion coefficient of the 3 components calculated as per above method and the raw diffusion coefficients for the samples with all hydrogenated species (black squares) along the horizontal line.*

Table A.11: *Calculated data for diffusion coefficients (in m^2/s) of all the components, in mixed H/D contrast as well as all_H case, for the 8 samples along the horizontal line.*

Sample No.	$D_{\text{s-Oct}}$	$D_{\text{s-Eth}}$	$D_{\text{s-Wat}}$	$D_{\text{s-All H}}$
HL1	-	4.9749×10^{-10}	9.6372×10^{-10}	8.0086×10^{-10}
HL2	1.9163×10^{-10}	5.1939×10^{-10}	8.5644×10^{-10}	6.4811×10^{-10}
HL3	1.8863×10^{-10}	5.1618×10^{-10}	8.0760×10^{-10}	5.6887×10^{-10}
HL4	1.8928×10^{-10}	4.9655×10^{-10}	7.1251×10^{-10}	5.1032×10^{-10}
HL5	2.8164×10^{-10}	5.1484×10^{-10}	5.1961×10^{-10}	4.7486×10^{-10}
HL6	2.9986×10^{-10}	5.1392×10^{-10}	5.9166×10^{-10}	4.5080×10^{-10}
HL7	3.2240×10^{-10}	5.2762×10^{-10}	5.4963×10^{-10}	4.3818×10^{-10}
HL8	3.7045×10^{-10}	5.2163×10^{-10}	-	4.3335×10^{-10}

Table A.12: *Diffusion coefficient (m^2/s) for Octanol, Ethanol, Water, and all Hydrogen cases for the water dilution line (DL_{water}).*

Sample No.	$D_{\text{s-Oct}}$	$D_{\text{s-Eth}}$	$D_{\text{s-Wat}}$	$D_{\text{s-All H}}$
DLW_1	2.2813E-10	5.2046E-10	8.1887E-10	5.4220E-10
DLW_2	2.0649E-10	5.4025E-10	7.2462E-10	5.3721E-10
DLW_3	2.6019E-10	5.4518E-10	6.9466E-10	5.3703E-10
DLW_4	2.7113E-10	5.8435E-10	6.6373E-10	5.3381E-10
DLW_5	3.4361E-10	6.7354E-10	5.9060E-10	5.6555E-10
DLW_6	4.3315E-10	7.6988E-10	-2.3610E-10	6.1669E-10

Table A.13: *Diffusion coefficient (m^2/s) for the octanol dilution line ($DL_{Octanol}$) with all hydrogenated components.*

Sample No.	$D_{\text{s-All H}}$
DLO_1	7.18E-10
DLO_2	6.31E-10
DLO_3	5.25E-10
DLO_4	4.86E-10
DLO_5	2.16E-10

Table A.14: *Compositions of the simulated systems for the octanol-ethanol-water ternary. In all systems the mass fraction of ethanol is $w_E = 0.4$.*

w_Octanol	N_Octanol	N_Ethanol	N_H2O
0	0	1401	5374
0.06	74	1401	4836
0.12	148	1401	4299
0.18	223	1401	3761
0.24	297	1401	3224
0.3	371	1401	2687
0.36	446	1401	2149
0.42	520	1401	1612
0.48	594	1401	1074
0.54	669	1401	537
0.6	743	1401	0

A.5 Molecular Simulation Data

We thank Dominik H. for conducting the simulation modeling and acknowledge his contribution to this work.

Ternary systems with an ethanol mass fraction of $w_E = 0.4$ were studied. The composition of the simulated systems are shown in Table A.14. All simulations were carried out using GROMACS 2023.2 [185]. Octanol and ethanol were described by the OPLS/AA force field [186] with L-OPLS dihedral potential corrections [187] for n-octanol, in conjunction with TIP4P/2005 water model [188]. Ethanol and n-octanol hydrogen atoms were represented by virtual interaction sites. The electrostatic interactions were calculated with the smooth PME method. A cutoff of 1.0 nm was used for the Lennard-Jones interactions, where the truncation error correction was applied to the energy and pressure.

After equilibration, the ternary systems were simulated for 500 ns and the two binary systems for 100 ns. The time step was 5 fs. The temperate was set to 300 K using a stochastic velocity rescaling thermostat, and the pressure was set to 1 bar using stochastic cell rescaling.

The diffusion coefficients of the three species were determined from Einstein plots using the "gmx msd" routine of GROMACS. The range from 50 ns to 250 ns was used for the fitting of the diffusion constants of the ternary systems, for the binary systems the range from 10 ns to 90 ns. The resulting errors in the diffusion constants are below $2.6 \cdot 10^{-11} \mathrm{m}^2/\mathrm{s}$.

For comparison to experimental data, the diffusion coefficients from MD are corrected for finite size effects following the approach of Yeh and Hummer. [189]

Table A.15: *NSE Sample Composition Data for the 8 samples on the EH phase triangle figure 5.14*

Sample	EH	Ethanol	Water
S1	0.00	42.21	57.79
S2	6.58	42.76	50.66
S3	12.36	43.24	44.40
S4	18.28	43.73	37.99
S5	27.40	44.49	28.11
S6	35.78	45.19	19.03
S7	45.53	46.00	8.48
S8	53.35	46.65	0.00

Table A.16: *Mass fractions (%) of components in Ethyl acetate (EA), Sodium Salicylate (NaSal) and Water ternary samples.*

Sample	EA (%)	NaSal (%)	Water (%)
ENa_1	0.00	49.86	50.14
ENa_2	38.14	30.84	31.02
ENa_3	59.17	20.36	20.47
ENa_4	69.26	15.33	15.41
ENa_5	88.93	5.52	5.55

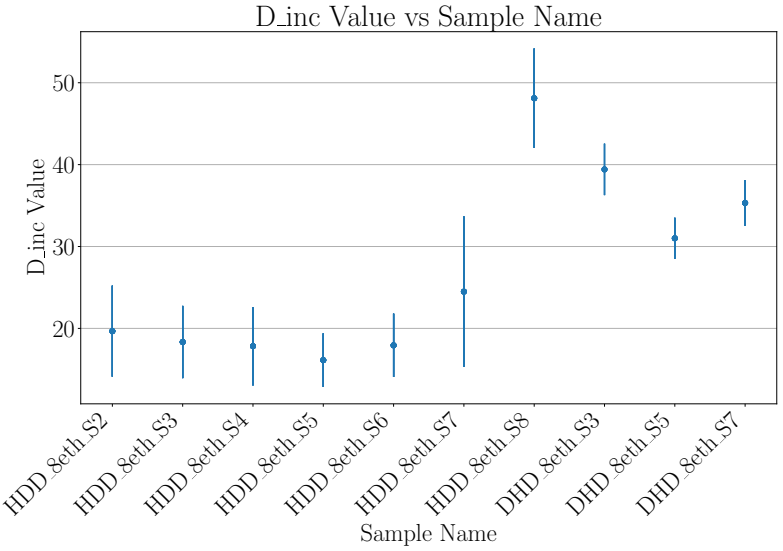

Figure A.15: *$D_{incoherent}$ from WASP analysis of 2-ethyl hexanol (EH) + ethanol + water ternary. The contrast naming format is oil-ethanol- water, where HDD refers to hydrogenated oil with deuterated ethanol and water and DHD refers to hydrogenated ethanol with deuterated oil and water.*

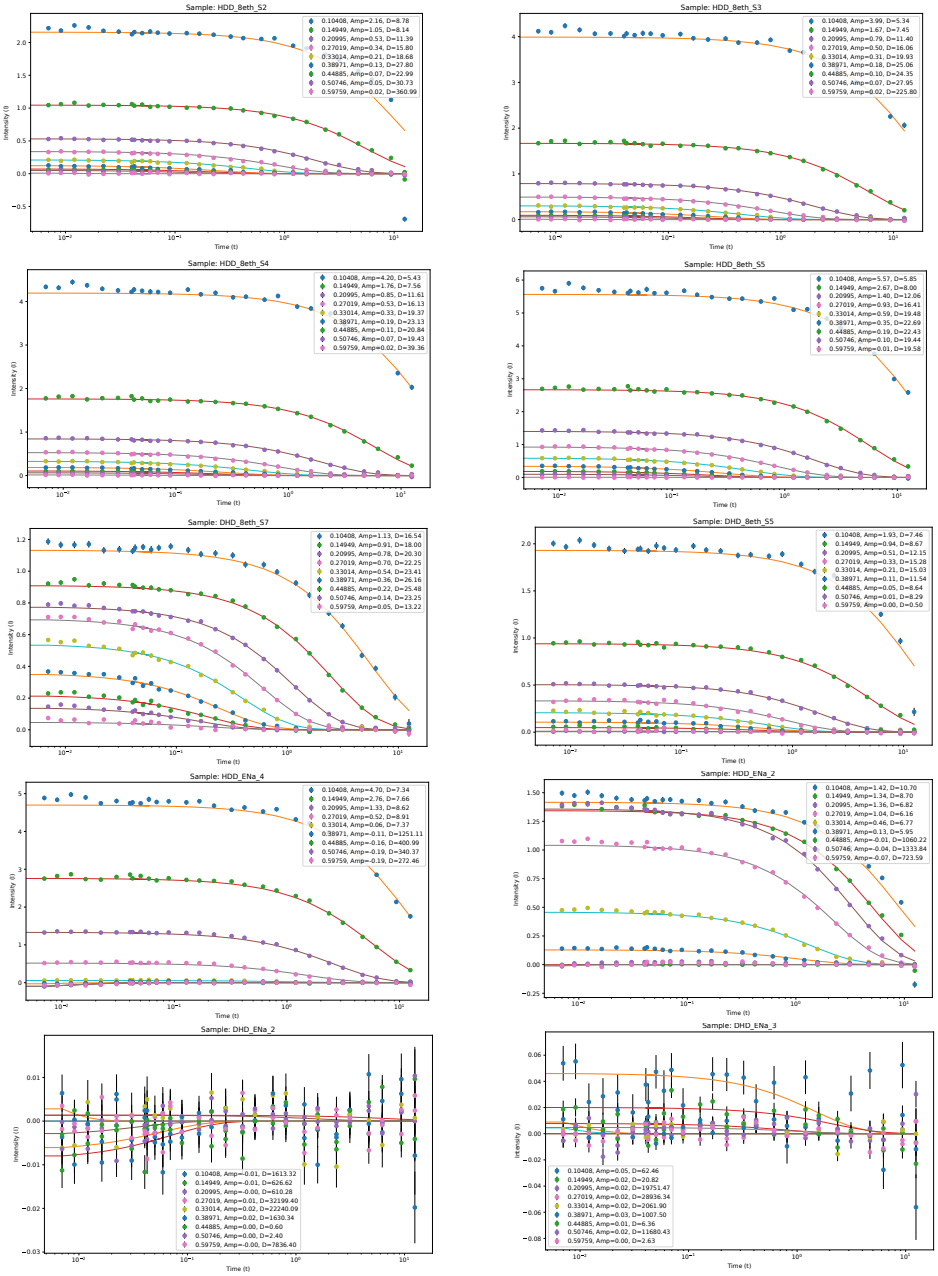

Figure A.16: *Intermediate scattering function $I(q,t)/I(q,0)$ versus time plots from NSE experiments. Here,* ***8eth*** *refers to the ethyl hexanol ternary,* ***ENa*** *to the ethyl acetate ternary.* ***HDD*** *indicates a system with hydrogenated oil and deuterated hydrotrope and water, whereas* ***DHD*** *refers to hydrogenated hydrotrope with deuterated oil and water.*

Table A.17: *Viscosity and Mass Fractions for Samples along the Horizontal Line (HL)*

Sample Name	Viscosity	Mass Fraction (%)		
		Octanol	Ethanol	Water
HL1	2.35	0	43.79	56.21
HL2	2.72	9.99	43.74	46.26
HL3	2.93	17.29	43.72	38.99
HL4	3.04	24.54	43.68	31.78
HL5	2.97	31.98	43.64	24.38
HL6	2.89	39.16	43.61	17.23
HL7	2.75	46.3	43.58	10.12
HL8	2.54	56.46	43.54	0

Table A.18: *Viscosity and Mass Fractions for Samples along the Water Diagonal Line (DLW)*

Sample Name	Viscosity	Mass Fraction (%)		
		Octanol	Ethanol	Water
DLW_1	3.20	16.52	36.65	46.82
DLW_2	3.13	18.04	40.03	41.93
DLW_3	2.93	20.08	44.54	35.38
DLW_4	2.71	22.02	48.85	29.13
DLW_5	2.24	26.06	57.81	16.13
DLW_6	1.75	30.05	66.66	3.29

Table A.19: *Viscosity and Mass Fractions for Samples along the Octanol Diagonal Line (DLO)*

Sample Name	Viscosity	Mass Fraction (%)		
		Octanol	Ethanol	Water
DLO_1	2.37	3.07	48.5	48.43
DLO_2	2.65	10.04	45.01	44.95
DLO_3	3.04	17.93	41.06	41.01
DLO_4	3.35	22.35	38.85	38.80
DLO_5	6.64	95.76	2.12	2.12

Appendix B

Algorithms: Python scripts

B.1 Stepwise Summary of Data Fitting Process for SAXS Autodilution Experiment

1. Initialization of Parameters and Data Preparation: In the first stage, the initial parameters for fitting are set up:

- The values for I_{oz0}, z_{oz0}, I_{bkg0}, I_{BP0}, z_{BP0}, q_{BP0}, and α_0 are initialized using the `set_initial_parameters` function.
- The data corresponding to y (intensity) and y_{err} (error) are extracted from the dataset.
- A function for model fitting, `function_selector`, is chosen and applied to the data.

2. Composition Calculation from Transmission Values:

- Transmission values for the empty capillary (`T_emptycap`) and the binary system (`T_binary`) are used to calculate the scattering cross-sections for water and oil.
- An initial oil ratio is set based on predefined volume fractions of octanol and ethanol.
- For each transmission measurement, the oil weight fraction (`w_oil`) is calculated, and the compositions of octanol, ethanol, and water are derived from it.

3. Model Setup and Fitting: Once the parameters are initialized, the model fitting begins:

- A combined model function, `whole_func_model`, is defined to fit the data.
- The `lmfit` model fitting library is used to perform the fitting process with the initial values.

- The error in the data is incorporated into the fitting process by applying weights based on the error values.

4. Results Processing and Plotting: After the fitting process, the results are processed:

- The parameters obtained from the fit are stored for each plot number.
- The error values for each parameter are computed and stored.
- The fitting plots are generated, showing the data points and the fitted curve along with the individual components of the model.

5. Model Updates and Iterations: After each fit, the model parameters are updated:

- The parameters from the current fit are assigned as initial values for the next fit, allowing the model to adapt as it progresses through the dataset.
- If certain conditions are met, the process iterates through the dataset, adjusting the initial conditions dynamically.

Sorting and Extracting Best Fit Data:

- The data files for each oil ratio are loaded, and entries are sorted by the second column (plot identifier).
- A sorted file is created with a heading that details the columns (e.g., oil ratio, fit type, parameters, and their errors).
- A new file is generated to store the "best fit" results for each dataset: - The best fit is determined by identifying the minimum reduced chi-squared (`RedChi`) value for similar plot identifiers and the combination of terms from the model with least free parameters, to avoid overfitting of the data. - The corresponding best-fit parameters are written to the output file.
- The process repeats for all oil ratios, ensuring all results are well-organized and the best fits are extracted systematically.

6. Final Output and Writing to File: Finally, after completing the fits:

- The results, including fitting parameters and statistical values (e.g., reduced chi-squared), are written to an output file.

B.2 WASP Data Analysis Algorithm

- **Input Data:** Experimental data is loaded from `COMBI_FILE.txt`, with key columns including sample names, q_i, t, intensities (I, I_{coh}, I_{inc}), and errors.

- **Fitting Function:** The following custom function models the physical behavior of the system:

$$\begin{aligned}\texttt{fit\_value} = \texttt{Prefak} \times \Big(I_{\text{coh\_current}} \times \big(\texttt{inel\_dyn} \cdot e^{-300 \cdot t_{\text{current}}} \\ + (1 - \texttt{inel\_dyn}) \cdot \big((1 - \texttt{el\_bkg}) \cdot e^{-D_{\text{coh}} \cdot q^2_{\text{current}} \cdot t_{\text{current}}} \\ + \texttt{el\_bkg} \big) \big) - 0.33 \cdot I_{\text{inc\_current}} \cdot \big(\texttt{amp\_inc} \cdot e^{-D_{\text{inc}} \cdot q^2_{\text{current}} \cdot t_{\text{current}}} \big) \Big)\end{aligned}$$

- **Minimization:** The script minimizes residuals using `lmfit.minimize`, fitting parameters such as `D_inc`, `D_coh`, `Prefak`, `inel_dyn`, `el_bkg`, and `amp_inc`.
- **Parameter Initialization:** D_inc parameter are either reused from previous fits or initialized with values based on NMR diffusion coefficients.
- **Outputs:**
  - Optimized parameters and their errors are saved to `optimized_parameters.txt`.
  - Detailed fit reports are written to `Reult_prettyPrint.txt`.
  - Fitted curves and experimental data for each sample are plotted against t (log-scale) for different q values, saved in `fit_plots.pdf`.

B.3 IN15 Data Analysis Algorithm

- The fitting process is based on the equation:

$$I(t) = a \cdot e^{-D_{\text{eff}} \cdot q^2 \cdot t}$$

  where $I(t)$ is the intensity at time t, a is a scaling parameter, D_{eff} is the effective diffusion coefficient, and q is the scattering vector magnitude.
- The `lmfit` library is used to perform non-linear least squares fitting to determine the parameters D_{eff}, a, and q.
- The calculated D_{eff} values and their uncertainties are used to study the diffusion behavior as a function of q.
- The results are visualized as a plot of D_{eff} vs. q, with error bars indicating uncertainties.

Fin

A heartfelt thank you to all my teachers who have guided me throughout this journey.

To my supervisors, **Ingo HOFFMANN** and **Marie PLAZANET** — your mentorship has been exceptional. Beyond the science, it was the friendly conversations and your constant support that helped me grow with each challenge you entrusted to me. You've shown me that a kind and approachable mentorship is truly the key to doing good science.

A special shoutout to **Sayantan Majumdar Sir** for introducing me to the world of soft matter physics — that first spark of interest really stuck with me.

Big thanks to **Sidhartha Jena Sir** for welcoming me into his lab — my second home at NITR. Your calm, thoughtful guidance and the way you shared your knowledge made a big difference and kept me going through this journey.

Also, a big thank you to **Anushree Roy Ma'am** — working under you helped me learn how to take responsibility in the lab, make decisions around instruments, and become more self-sufficient. You taught me those behind-the-scenes aspects of doing science that no one really talks about, but are so important.

And finally, a **huge, huge thanks to Maity Sir**. Right from my higher secondary days, you've shaped the way I look at science — making it practical, fun, and approachable. Your humility, depth of knowledge, and the way you always made yourself available to us really inspired me. You made me realize that it's not just about understanding science, but also about communicating it in a simple and effective way. You've helped me grow — both as a person and as a researcher.

Thank you all, truly, for everything.

"What we call the beginning is often the end. And to make an end is to make a beginning. The end is where we start from." – T.S. Eliot